The Development of Electrochemical Sensors Based on The Use of Different Forms of Carbon Materials

Korbua Chaisiwamongkhol

Wolfson College, University of Oxford

A thesis submitted for the degree of Doctor of Philosophy in Physical and Theoretical Chemistry

Trinity Term, 2019

The Development of Electrochemical Sensors Based on The Use of Different Forms of Carbon Materials

Korbua Chaisiwamongkhol

Wolfson College, University of Oxford

A thesis submitted for the degree of D.Phil. in Physical and Theoretical Chemistry

Trinity Term, 2019

Abstract

This thesis presents experimental work with the main aim of the development of chemical sensors using electroanalytical methods for applications in the food industry and for medical diagnosis. The first chapter introduces the principles and techniques of electrochemistry. Chapter 2 provides information on the experimental procedures and chemical/reagents used in the studies.

In this thesis, carbon based materials such as pyrolytic graphite; carbon nanotubes and carbon fibre have been used for a number of analytical and fundamental investigations. The first research aim of this thesis is to develop sensors for the detection of chemical compounds in ginger and turmeric. Chapter 3 and 4 demonstrate the capability of multiwalled carbon nanotubes modified electrodes for adsorptive stripping voltammetric determination of gingerol and curcumin along with the possibility for commercialisation. An extension of the first project to compare different types of carbon electrode materials including multiwalled carbon nanotubes, carbon black, graphene nanoplatelets, screen-printed carbon electrode and carbon paste electrode for the AdsSV technique is presented in Chapter 5. General principles to offer guidance in the optimal choice of carbon electrodes for AdsSV are established.

Chapter 6 investigates the reaction mechanism of atmospheric oxygen with an edge plane pyrolytic graphite electrode to generate surface quinone functionality. The results presented in Chapter 6 are evidenced as photochemical in nature and to likely involve singlet oxygen.

As a possible biomarker of salivary pH for diseases such as gingivitis and dental caries, the next aim of this thesis is to develop sensors for pH measurement in saliva. Chapter 7 reports the development of a micro-sized pH probe exploiting the pH dependence of surface quinones on micro carbon fibres for pH measurement of saliva. Applications in human saliva without any pre-treatment are highlighted.

In Chapter 8, amperometric pH sensing in samples of sheep's blood is investigated. At the beginning, surface quinones on graphite electrode are used in the study. However, in terms of signal size and the lack of robustness of the developed electrodes, micro-disc carbon fibre electrodes appeared to be less than optimal to use for study in biological samples with complex matrices such as blood. The investigation and exploitation of metal/metal oxide specifically iridium oxide electrodes for amperometric pH sensing in sheep's blood are carried out, shown to be superior, and are described in Chapter 8.

Finally, Chapter 9 presents overall conclusions.

Acknowledgements

First and foremost, I would like to express my deep gratitude to my wonderful supervisor, Professor Richard Compton, for having me in his research group and providing me with such amazing opportunities and experiences of doing research in electrochemistry. Thank him for his great support and encouragement since my day one in the Compton group. Thank you for your open-door policy and all the effort you spend on students. My enormous thanks must also go to Dr. Christopher Batchelor-McAuley who made huge contribution throughout my whole D.Phil in Oxford. Thank you Chris for your generous help and incredible patience for supervising me. I have learned a lot from both of you. This thesis would not have been possible without your guidance and help.

I would like to express my gratitude to the Royal Thai Government who provides full funding for my D.Phil study in the UK.

To Dia, Tulip, Lifu, Jake, Daisy, Xiuting, Ivana, Bertold, Collin, Rachel, Annie, Alex, Yuki Yuanzhe, Grace and many more, the Compton group members of past and present have always made me feel welcome and added fun to lab life. Many thanks to Dia for her help in all aspects during my time in the lab and Oxford. Thank you Lifu for his help when I bothered him with so many random questions especially with RGC's handwriting! Thanks Daisy and Bertold for emergency snacks.

I wish to thank all teachers who taught me in the past in all levels. All of you brought me here.

Thank you to the many Thai friends I have met here who help me maintain my work-life balance and making me not too lonely to live in Oxford.

Lastly, I would like to thank those special people in my life, my family, for their never-ending support and love. To P'Di, thank you for everything you have done for us and for believing in me when I doubt myself.

Contents

Glossary

Roman Symbols

Symbol	Meaning	Unit
a_i	activity of species *i*	unitless
A	electrode area	cm^2
A, B	species	
(aq)	aqueous solution	
C	concentration	mol cm^{-3}
C_{dl}	double layer capacitance	Farad cm^{-2}
D	diffusion coefficient	cm^2 s^{-1}
E	electrode potential	V
E^0	standard electrode potential	V
$E^{0'}$	apparent standard electrode potential	V
E_f^0	formal electrode potential	V
$E_{1/2}$	half-wave potential	V
E_{mid}	mid-point potential	V
E_p	peak potential	V
ΔE_p	peak-to-peak separation	V
F	Faraday constant (96485)	C mol^{-1}
I	current	A
I	ionic strength	mol kg^{-1} , mol L^{-1}
I_p	peak current	A

i	species	
J	flux	mol cm^{-2} s^{-1}
k^0	standard electrochemical rate constant	cm s^{-1}
$k_{ox};\ k_{red}$	oxidation, reduction rate constant	cm s^{-1}
K	Adsorption equilibrium constant	
m_T	mass transport coefficient	cm s^{-1}
m_{H^+}	molality of hydrogen ion	mol kg^{-1}
$m^{\ominus}$	standard molality	mol kg^{-1}
M	molar mass	mol cm^{-3}
n	number of electrons transferred	unitless
N	amount of formed product or consumed reactant	mol
Q	charge	C
R	universal gas constant (8.314)	J K^{-1} mol^{-1}
R_s	resistance of solution phase	Ω
t	time	s
T	temperature	K
v	potential scan rate	V s^{-1}
Z_i	charge of the ion	C

Greek Symbols

Symbol	Meaning	Unit
α, β	transfer coefficients	unitless

η	overpotential	V
γ	activity coefficient	unitless
$\gamma_{\pm}$	mean activity coefficient	unitless
Γ	surface coverage	mol cm^{-2}
Λ	Matsuda-Ayabe parameter	unitless
μ	chemical potential	J mol^{-1}
$\overline{\mu}$	electrochemical potential	J mol^{-1}
μ_i^0	Standard chemical potential	J mol^{-1}
ϕ	electrical potential	V
ϕ_M	electrical potential of the electrode	V
ϕ_S	electrical potential of the solution	V
δ	time-dependent diffusion layer thickness	
v	velocity	cm s^{-1}
υ	scan rate	V s^{-1}

Abbreviations

Abbreviation	Meaning
AdsSV	adsorptive stripping voltammetry
ASV	anodic stripping voltammetry
AuNP	gold nanoparticle
BPPGE	basal plane pyrolytic graphite electrode
CB	carbon black
CE	counter electrode
CNT	carbon nanotube

CNT-SPE	carbon nanotube modified screen printed electrode
CPE	carbon paste electrode
C-SPE	carbon screen printed electrode
CSV	cathodic stripping voltammetry
CV	cyclic voltammetry
DPV	differential pulse voltammetry
EDL	electrical double layer
EPPGE	Edge plane pyrolytic graphite electrode
FFTSWV	fast Fourier transform square wave voltammetry
GCE	glassy carbon electrode
GNP	graphene nanoplatelets
HMDE	hanging mercury drop electrode
HOPG	highly ordered pyrolytic graphite
IHP	Inner Helmholtz Plane
IR	infrared
IrOx	iridium oxide
LOD	limit of detection
LOQ	limit of quantitation
MWCNT	multiwalled carbon nanotube
OHP	Outer Helmholtz Plane
PTFE	polytetrafluoroethylene
RE	reference electrode
SCE	saturated calomel electrode
SEM	scanning electron microscope
SHE	standard hydrogen electrode
SPE	screen printed electrode
SWCNT	singlewalled carbon nanotube
SWV	square wave voltammetry
UV	ultraviolet
WE	working electrode
XPS	X-ray photoelectron spectroscopy

Chapter 1

Introduction to electrochemistry

This introductory chapter provides an overview of some of the fundamental concepts in electrochemistry and the electrochemical techniques which are relevant for the work presented in this thesis.

1.1 Electrochemical equilibrium: the Nernst equation

At the interface between a metallic electrode (metal) and a solution phase (aq), a general one-electron reduction can be described as:

$$A_{(aq)} + e^-_{(metal)} \rightleftharpoons B_{(aq)} \quad (1.1)$$

where A and B are the oxidised and reduced forms of a redox couple in an aqueous media. If the electrode is inserted into solution of both A and B, as a result of electron transfer between the two distinct phases, metal and solution, there is a creation of charge separation at the interface between the electrode and the solution. This gives rise to an electrode potential. The electrochemical equilibrium differs from a chemical equilibrium which is controlled by the chemical potentials of reactants and products since an electrochemical equilibrium represents a balance between chemical and electrical potentials. This distinction arises since the two phases of the electrode and the solution have different electrical potentials (ϕ_M and ϕ_S).

At equilibrium, the electrochemical potentials of reactant A and product B are equal. The electrochemical potential of species i ($\overline{\mu}_i$) is defined as:

$$\overline{\mu}_i = \mu_i + z_i F \phi_{M/S} \quad (1.2)$$

where μ_i is the chemical potential of species *i* and z_i is the charge of species *i*. *F* is the Faraday constant (96485 C mol^{-1}) indicating the charge passed per mole of electrons. ϕ is the electrical potential of the electrode (ϕ_M) or solution (ϕ_S).

For an equilibrium of eqn. (1.1), the balance of electrochemical potential is

$$(\mu_A + z_A F\phi_S) + (\mu_{e^-} - F\phi_M) = (\mu_B + (z_A - 1)F\phi_S) \quad (1.3)$$

Rearranging the eqn. 1.3 gives eqn. 1.4,

$$F\left(\phi_M - \phi_S\right) = \mu_A + \mu_{e^-} - \mu_B \quad (1.4)$$

The chemical potential (μ_i) is defined as

$$\mu_i = \mu_i^0 + RTlna_{i,0} \quad (1.5)$$

where μ_i^0 is the standard chemical potential. *R* is the molar gas constant (8.314 J K^{-1} mol^{-1}), *T* is the absolute temperature (K) and $a_{i,0}$ is the activity of species *i* at the electrode surface.

By substituting eqn. 1.6 and 1.7, eqn.1.4 can be rearranged to give

$$F\left(\phi_M - \phi_S\right) = (\mu_A^0 + \mu_{e^-} - \mu_B^0) + RTln\frac{a_{A,0}}{a_{B,0}} \quad (1.6)$$

$$\left(\phi_M - \phi_S\right) = \frac{\Delta\mu^0}{F} + \frac{RT}{F}ln\frac{a_{A,0}}{a_{B,0}} \quad (1.7)$$

where $\Delta\mu^0 = \mu_A^0 + \mu_{e^-} - \mu_B^0$

Equation 1.7 is the *Nernst equation* associated with a single electrode/solution interface. Here $\phi_M - \phi_S$ is an absolute value which cannot be measured. Rather a two-electrode system is required to form a circuit to make the measurement. When the content of solution at the second electrode/solution interface is maintained to be

constant, the measured potential difference between the two-electrodes (E) represents the potential of the electrode of interest. The second electrode where the potential is held constant is called a *reference electrode*.[1]

$$E = (\phi_M - \phi_S)_{test} - (\phi_M - \phi_S)_{reference} \quad (1.8)$$

For the *two-electrode* system, the Nernst equation becomes

$$E = E^0 + \frac{RT}{F} ln \frac{a_{A,0}}{a_{B,0}} \quad (1.9)$$

where E^0 is the standard electrode potential when the reference electrode is a standard hydrogen electrode or SHE (1atm, 298K, 1 unit activity) and the rest of the parameters have been previously defined. The activities for species *i* can be expressed with respect to their corresponding concentration,

$$a_i = \gamma_i c_i \quad (1.10)$$

where γ_i is the activity coefficient of species *i* (unitless).

To avoid any inconvenience to deal with activities in practice, the formal potential (E_f^0) is introduced to eqn. 1.11,

$$E = E_f^0 + \frac{RT}{F} ln \frac{c_{A,0}}{c_{B,0}} \quad (1.11)$$

where $c_{i,0}$ is the concentration of the species *i* at the electrode surface. The formal potential with respect to standard potential and activity coefficient is defined as

$$E_f^0 = E^0 + \frac{RT}{F} ln \frac{\gamma_A}{\gamma_B} \quad (1.12)$$

The above *Nernst equation* (eqn. 1.7, 1.9 and 1.11) provides a description of the electrode potential for a system under equilibrium. However, the establishment of electrochemical equilibrium requires fast electrode kinetics. Therefore, in the following section, the electrode kinetics will be considered and elaborated.

1.2 Electrode kinetics

In the previous section, electrochemical equilibrium was characterised by the Nernst equation. Thermodynamics describe the equilibrium state while kinetics quantitatively describes the evolution of chemical change. Moreover, experimentally, instead of allowing equilibrium to establish, electrochemists mostly disturb the equilibrium by application of a potential to the electrode in order to obtain information of the redox couple of interest. In this section, the rate of electron transfer at the interface is considered.

To discuss the rate of electron transfer, the simple example of a one electron reduction as presented in eqn. 1.1 is considered.

$$A_{(aq)} + e^-_{(metal)} \underset{k_{ox}}{\overset{k_{red}}{\rightleftarrows}} B_{(aq)} \qquad (1.13)$$

where A and B are the oxidised and reduced forms of a redox couple in an aqueous media and k_{red} and k_{ox} are the heterogeneous rate constants for the reduction and oxidation respectively. Note that reaction 1.13 differs from reaction 1.1 by substitution of harpoons by arrows, indicating an absence of equilibrium. The net current as a result of electron transfer may be described by the equation,

$$I = I_{red} + I_{ox} = nFAj \qquad (1.14)$$

where I is a net current passed, I_{red} and I_{ox} are the cathodic and anodic currents respectively, A is the electrode area and j is the flux at the electrode surface. The flux (j) is important quantity and can be predicted as the quantity of material (moles) reacting at unit electrode area per second. It can be thought as the rate of the electrochemical reaction:[2, 3]

$$j = k_q[reactant]_0^q \tag{1.15}$$

where q is the order of the reactant, k_q is a qth order rate constant and 0 as a subscript indicates the reactant concentration at the electrode surface.

Considering eqn.1.15 the current for oxidative and reductive components of reaction 1.13 can be written assuming, as is usual, first order process (q=1)

$$I_{red} = -FAk_{red}[A]_0 \tag{1.16a}$$

$$I_{ox} = FAk_{ox}[B]_0 \tag{1.16b}$$

The rate of electron transfer may be described via the Butler-Volmer equation.[4, 5] In particular, this equation describes the dependence of the rate constant on the potential applied (E), relative to a reference electrode

$$k_{red} = k^0 exp\left[-\frac{\alpha F}{RT}\eta\right] \tag{1.17a}$$

$$k_{ox} = k^0 exp\left[\frac{\beta F}{RT}\eta\right] \tag{1.17b}$$

where k^0 is the standard electrochemical rate constant (cm s^{-1}) representing the magnitude of k_{red} and k_{ox} at the formal potential, η is the overpotential (V) applied to the working electrode with $\eta = E - E_f^0$. α and β are the transfer coefficients ($\alpha + \beta = 1$) if, as in eqn.1.13, one electrode is transferred in the reaction. These equations show that the rate constants are exponentially dependent on the overpotential (η).

By combining eqn. 1.16a, 1.16b, 1.17a and 1.17b, the full expression for the rate of electron transfer as a function of potential is obtained and expressed as

$$I = FAk^0 \left(exp\left[\frac{+\beta F}{RT}\eta\right][B]_0 - exp\left[\frac{-\alpha F}{RT}\eta\right][A]_0 \right) \quad (1.18)$$

The Tafel Law can be derived based on Butler-Volmer kinetics. When the reduction process in reaction 1.13 is sufficiently fast that the oxidation reaction becomes negligible, the recorded current is equal to:

$$I = -FAk^0 exp\left[-\frac{\alpha F}{RT}\eta\right][A]_0 \quad (1.19)$$

Assuming $[A]_0$ is not greatly changed from a bulk concentration; eqn. 1.19 can be rearranged to be

$$ln|I| = -\frac{\alpha F}{RT}\eta + constant \quad (1.20)$$

A plot of $ln|I|$ against η is referred to a Tafel plot which will be linear. The Tafel plot can be used to determine transfer coefficient value from a gradient of the plot.

Similarly for an oxidation

$$ln|I| = +\frac{\beta F}{RT}\eta + constant \quad (1.21)$$

1.3 Mass transport

In the previous section, the rate of an electron transfer reaction taking place at a working electrode was considered. However, in order for an electrode reaction to occur, the reactant molecules need to be transported from the bulk solution to the electrode surface. At the same time the products will move away from the electrode

in the opposite direction. This movement is known as mass transport. There are three transport processes including diffusion, convection and migration which are discussed in more detail as follows.[3] The total mass transfer can be quantified by the one-dimensional form of the *Nernst-Planck Equation*:[1]

$$J_i(x) = -D_i \frac{\partial C_i(x)}{\partial x} + C_i v(x) - \frac{Z_i F}{RT} D_i C_i \frac{\partial \emptyset(x)}{\partial x} \qquad (1.22)$$

where $J_i(x)$ is the flux (mol cm^{-2} s^{-1}) and the rest terms on the right side of the equation are diffusional flux, convectional flux and migratory flux respectively.

1.3.1 Diffusion

Diffusion arises when a gradient of concentration exists in the system. When a suitable potential is applied, a reactant is consumed at the electrode surface, depleting the electroactive species concentration in vicinity of the electrode. Therefore, species from bulk solution diffuse to the electrode surface. This mass transfer by diffusion is described by Fick's laws.[6] Fick's first law, derived experimentally, relates the diffusional flux ($J_{D,i}$) to the concentration gradient as described in eqn. 1.23:

$$J_{D,i} = -D_i \frac{\partial C_i(x)}{\partial x} \qquad (1.23)$$

where $J_{D,i}$ is the diffusional flux, $\frac{\partial C_i(x)}{\partial x}$ is the concentration gradient at the point x and D_i is the diffusion coefficient of species *i*. Fick's first states that at a given point (x), the diffusional flux (mol cm^{-2} s^{-1}) is proportional to the diffusion coefficient and concentration gradient of the product. To relate the flux with the measured current

(I) according to the number of moles passing through a unit area in a unit time, the flux is expressed as:

$$j = \frac{I}{nFA} \tag{1.24}$$

where A is the electrode area, n is the number of electrons and F is the Faraday constant (96485 C mol^{-1}).

In the case of 'diffusion only' conditions, Fick's second law (Equation 1.25) which is derived from the first law via conservation of mass describes how the concentration varies as a function of time (t) in one dimension.

$$\frac{\partial C}{\partial t} = D_i \frac{\partial^2 C}{\partial x^2} \tag{1.25}$$

In three dimensions, the equation becomes

$$\frac{\partial C}{\partial t} = D_i \left(\frac{\partial^2 C}{\partial x^2} + \frac{\partial^2 C}{\partial y^2} + \frac{\partial^2 C}{\partial z^2}\right) \tag{1.26}$$

Importantly, the diffusion coefficient (D_i), describes how far a molecule can travel during a period of time. More precisely, the root mean square of the distance ($\sqrt{\langle x^2 \rangle}$) travelled by a particle in time (t) is related to the diffusion coefficient (D_i) by the Einstein-von Smoluchowski equation:[7, 8]

$$\sqrt{\langle x^2 \rangle} = \sqrt{2D_i t} \tag{1.27}$$

Similarly, for three-dimensional diffusion, the root mean square distance becomes

$$\sqrt{\langle x^2 \rangle + \langle y^2 \rangle + \langle z^2 \rangle} = \sqrt{6D_i t} \tag{1.28}$$

1.3.2 Convection

Convection is the movement of materials as a result of a mechanical force in the system. There are two broad types of convection; natural and forced convection. *Natural* convection occurs when a thermal or density gradient present in the solution, which is usually undesirable and can cause experimental irreproducibility.[9] To minimise this type of convection, the electrochemical cell is normally kept at a carefully controlled temperature to avoid temperature differences and the experimental time for measurement can be kept short in order to avoid the buildup of density gradients. *Forced* convection is caused by the external forces such as gas bubbling, stirring or pumping. It can be used in hydrodynamic studies (i.e. rotating disc electrodes or sonoelectrochemistry) where the convection is intentionally introduced in the system to eliminate the effect of natural convection and to boost the electrode signal over and above that from diffusion only. The flux due to convection is given by:

$$J_{c,i}(x) = C_i v(x) \tag{1.29}$$

where $v(x)$ is the solution velocity in the x direction (cm s^{-1}) and C_i is the concentration (mol cm^{-3}).

1.3.3 Migration

The third mass transport process, migration, arises due to the motion of a charged species in solution due to the difference of potential within the solution. The migratory flux ($J_{m,i}(x)$) at a point x is expressed as shown in eqn.1.30.

$$J_{m,i}(x) = -\frac{Z_i F}{RT} D_i C_i \frac{\partial \phi(x)}{\partial x} \tag{1.30}$$

The equation shows that the migratory flux is proportional to the diffusion coefficient (D_i, $cm^2\ s^{-1}$), the concentration of the ion (C_i, $mol\ cm^{-3}$), the charge of the ion (Z_i, C) and the gradient of the electric potential ($\frac{\partial \emptyset(x)}{\partial x}$, $V\ cm^{-1}$). In order to overcome this effect, experiments are often performed with solutions containing a high concentration of inert background electrolyte. Hence, most of the current is carried in the solution by the charged species (ions) from the supporting electrolyte due to their much higher concentration than the species under study and the contribution from migration of the species of interest is significantly reduced. Moreover, the use of high concentration of supporting electrolyte can offer several other benefits.[10] First, ohmic drop can be minimised as a result of the increasing of solution conductivity. Note that the ohmic drop between the RE and the WE will occur when current is flowing through an electrochemical cell (as described in section1.5). The ohmic potential drop in the solution should be reduced because it is characteristic of the bulk solution and not of the electrode reaction. Adding a high concentration of ions (excess supporting electrolyte) decreases the solution resistance resulting in a decrease of the IR drop between RE and WE. Second, the presence of electrolyte maintains a constant ionic strength in the solution during electrolysis thus fixing the formal potentials of redox couples. Lastly, the large excess of background electrolytes compresses the diffuse layer to within a distance of 10-20 Å from the electrode which the electron quantum tunnelling can take place because within this zone the electron wavefunctions of electroactive species and the electrode can overlap. For electrochemical experiments described in this thesis, 0.1 M KCl was used as supporting electrolyte in most of the work on aqueous solutions.

1.4 Faradaic and non-Faradaic processes

1.4.1 Faradaic processes

There are two different types of current that can occur at a working electrode surface during an electrochemical experiment, notably Faradaic and non-Faradaic processes.

The electroactive species can be oxidised or reduced at electrodes leading to the transfer of electron(s) across the interface. This process is described as Faradaic and is dictated by Faraday's law, that is, the amount of chemical reaction caused by the flow of current is proportional to the amount ('charge') of electricity passed.[11]

$$Q = nFN \tag{1.31}$$

where Q is charge passed through a cell, n is number of electron involved in the electrode process (A+ne$^-$ → B), F is the Faraday constant (96485 C mol^{-1}) and N is the amount of formed product or consumed reactant (mol). The generation of Faradaic currents requires molecules or ions to reach the electrode surface. This happens via mass transport towards the electrode surface as discussed in section 1.3.

1.4.2 Non-Faradaic processes or capacitative processes

A non-Faradaic process is defined as a charging process where there is no electron transfer at the electrode/solution interface when the potential is applied to an electrode in an electrolytic solution. Since charge does not cross the interface this results in the buildup of charge in the interfacial region. The process may be considered behaving in an analogous feature to a capacitor (see below). Changes of

potential lead to a current flow which is due to movement of ions within the solution phase and the electrode and/or the reorientation of dipole molecules of the solvent. This current is known as a non-Faradaic current, a capacitative current or a charging current. When a charged electrode surface is in contact with an electrolytic solution, the attraction of ions with opposite charge and repulsion of ions with the same charge are expected. Thus, opposite charge layers are developed at the electrode/solution interface.[12] This constitutes the Electrical Double Layer (EDL), as shown in Figure 1.1. When the potential applied at the electrode surface is more positive than that of the solution, anions and solvent molecules will move from the solution towards the charged electrode because of the electrostatic force. On the solution side of the double layer, there are thought to be several layers. [1] The closest layer to the electrode is called the *Inner Helmholtz, compact or Stern Layer*. This compact layer is occupied by the solvent molecule and the ions are typically desolvated and in direct contact with the electrode. They are said to be *specifically adsorbed ions*. The distance from the centres of the specifically adsorbed ions to the electrode surface is called the *Inner Helmholtz Plane* (IHP). Further out of the compact layer, the solvated ions move with Brownian motion in solution resulting in a *diffuse layer*.[3] The ions in this region can only approach the electrode to a certain distance and interact with the charged electrode via only long-range electrostatic forces. The position of the centres of the nearest solvated ions is called the *Outer Helmholtz Plane* (OHP). The OHP corresponds to the boundary between the compact and the diffuse layer. The decay of the electrostatic potential is shown schematically in Figure 1.1. Within the compact layer, the potential is predicted to drop linearly as a function of distance from the electrode surface. In contrast to the compact layer, the

potential decreases less rapidly in the diffuse layer to that of the bulk solution which is electro-neutral.

The charging current, I, caused by redistribution of ions in forming the double layer is described by,

$$I = \frac{dQ}{dt} = C_{dl} A \frac{dE}{dt} = C_{dl} A \nu \qquad (1.32)$$

where and C_{dl} is the double layer capacitance (F cm^{-2}), A is the electrode surface area (cm^2), and ν is the scan rate (V s^{-1}). The values of C_{dl} are found to be in the range of 10-40 μF cm^{-2} for aqueous solutions around room temperature. The capacitances of real capacitors are independent of the voltage. In contrast, the value of C_{dl} for the electrochemical interface typically varies as a function of the potential.[1]

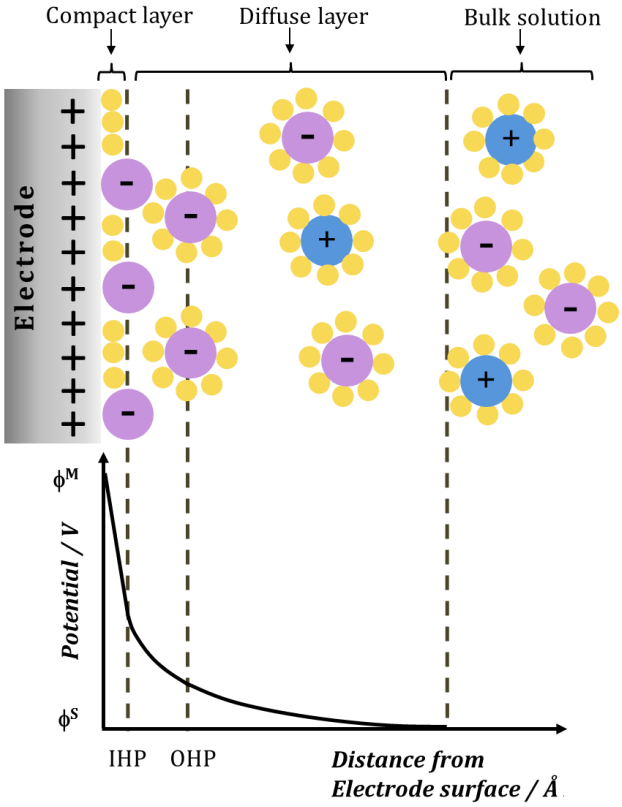

Figure 1.1 Schematic representation of the electrical double layer and potential profile through the solution side of the double layer.

1.5 Electrochemical cells

In order to measure the current at the electrode/solution interface and study an electrochemical system, an electrochemical cell containing several electrodes needs to be set up, such that a closed circuit is established. A typical electrochemical experiment is carried out using a three-electrode system, refer to Figure 1.2. This comprises a working electrode (WE), a reference electrode (RE) and a counter electrode (CE). The reaction of interest occurs at the interface of the *working electrode* and the solution. The use of a reference electrode is to enable the measurement and control of the potential of the working electrode when applying a potential. In all the experiments performed within the thesis, a potential is applied at the working electrode to observe voltammograms. The potential applied is with respect to the reference electrode. Normally, the reference electrode has a well-defined potential and is relatively stable provided no current passes through it. A third electrode, a counter electrode, is required to allow the current pass. Otherwise, the passage of the current through a reference electrode would induce Faradaic processes occur at the electrode surface and hence there would be an associated altered concentration of species next to the electrode surface. The Nernst equation (eqn. 1.11) shows that the electrode potential for a redox couple varies as a function of the concentration of the species in the potential determining equilibrium. Consequently if current passes through the reference electrode, the potential at the reference electrode is no longer constant. Moreover, the passage of current through both the working and reference electrode causes a potential drop (IR_s) between those electrodes since an electrical resistance exists in the bulk solution. As a result the working electrode potential would no longer be controlled.

$$Potential\ difference\ =\ (\phi_M - \phi_S)_{WE} -\ (\phi_M - \phi_S)_{RE} + IR_s \qquad (1.33)$$

Equation 1.33 shows the potential difference of a two-electrode system where $(\phi_M - \phi_S)_{WE}$ and $(\phi_M - \phi_S)_{RE}$ are the potentials at the working electrode interface and reference electrode interface respectively and IR_s term is the ohmic drop through the solution, when R_s being resistance of the solution phase. The term $(\phi_M - \phi_S)_{WE}$ is that controlling the rate of the electron transfer so that if the terms IR_s and $(\phi_M - \phi_S)_{RE}$ are variable and uncontrollable then this driving force is uncertain. Note that a two-electrode system in which the working electrode is a microelectrode[13, 14] and the other electrode is reference electrode can be often used because only a very small current (~10^{-9} A) passes through the system. The IR_s term is consequently minimised and can be neglected.

As shown in Figure 1.2, all the electrodes are controlled by a potentiostat. First the potentiostat imposes the fixed potential (E) between the working electrode and the reference electrode and only negligible current pass through the reference electrode. As the reference electrode serves a constant value of $(\phi_M - \phi_S)_{RE}$, any changes in the potential are reflected as a change in $(\phi_M - \phi_S)_{WE}$. The potential changes on the working electrode typically lead a current to flow and this current is measured. The potentiostat then drives the counter electrode to potential that is required to pass the current as flowing through the working electrode.

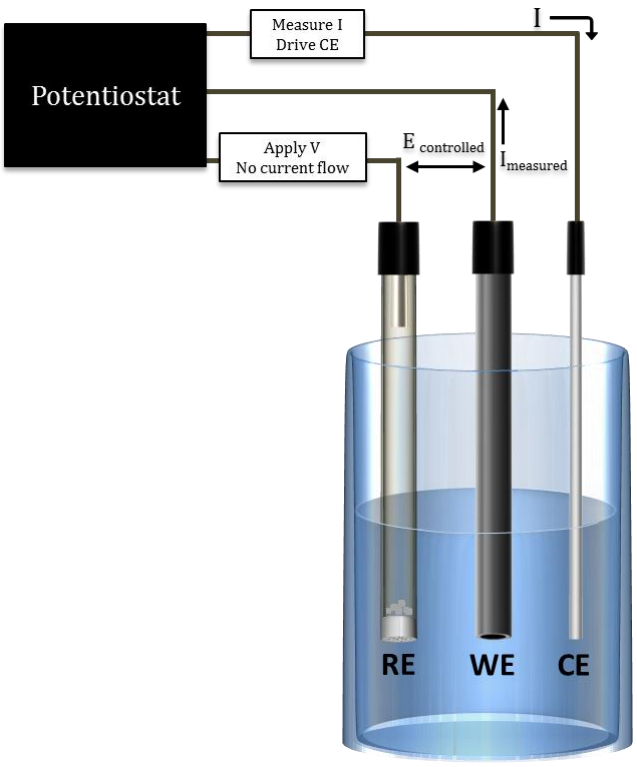

Figure 1.2 An electrochemical three-electrode cell set-up.

1.6 Electrochemical methods

This thesis utilises electrochemical methods in order to investigate electrochemical behaviour of analytes of interest and develop chemical sensors. This section introduces the background to cyclic voltammetry, square wave voltammetry, and stripping voltammetry.

1.6.1 Cyclic voltammetry

1.6.1.1 Diffusional systems

In cyclic voltammetry a potential is applied linearly at a constant scan rate (υ) to a working electrode. The typical waveform of cyclic voltammetry is illustrated in Figure 1.3(A). The potential is scanned from an initial value (E_1) to a final value (E_2) and then swept linearly back the initial potential (E_1).[15] The potential is decreased to

more negative for the study of a reduction process and increased to more positive for an oxidation process study. The initial potential is normally selected to be at a point where no reaction occurs, and the currents are near-zero. The only contribution to the current at the initial potential (E_1) is predominantly non-Faradaic or capacitative currents due to the built-up of charges at the electrode surface.[16] The potential E_2 where the scan is reversed is typically chosen to be at a high over potential ($\eta = E - E_f^0$). The current at the working electrode is recorded as a function of the applied potential and a current-potential plot is obtained known as a cyclic voltammogram. A typical cyclic voltammogram of a general reversible diffusional system (A + e^- ⇌ B) where the rate constant of electron transfer, k^0, is larger than the mass transport coefficient (see below) is shown in Figure 1.3(B).

The voltammogram relates to the simple one-electron reduction (A + e^- ⇌ B) where A is reduced to B. At the beginning as the applied potential, E, is more positive than the formal potential, E_f^0, no electron transfer occurs and there is no measured faradaic current. As the potential increases to more negative values, there is sufficient overpotential to reduce A to B and a large increase in current is observed. While A in the region near the electrode is consumed, the concentration of B builds up near the electrode surface. The flux starts to decrease when the surface concentration of A becomes close to zero, giving a peak-shaped response in the voltammogram.

In the reverse scan, the oxidation process (B ⇌ A + e^-) occurs when the potentials are sufficiently positive than the formal potential (E_f^0). An analogous peak is seen in the voltammogram as the formed product, B, is oxidised. There are thus two peaks of opposite currents in a cyclic voltammogram.

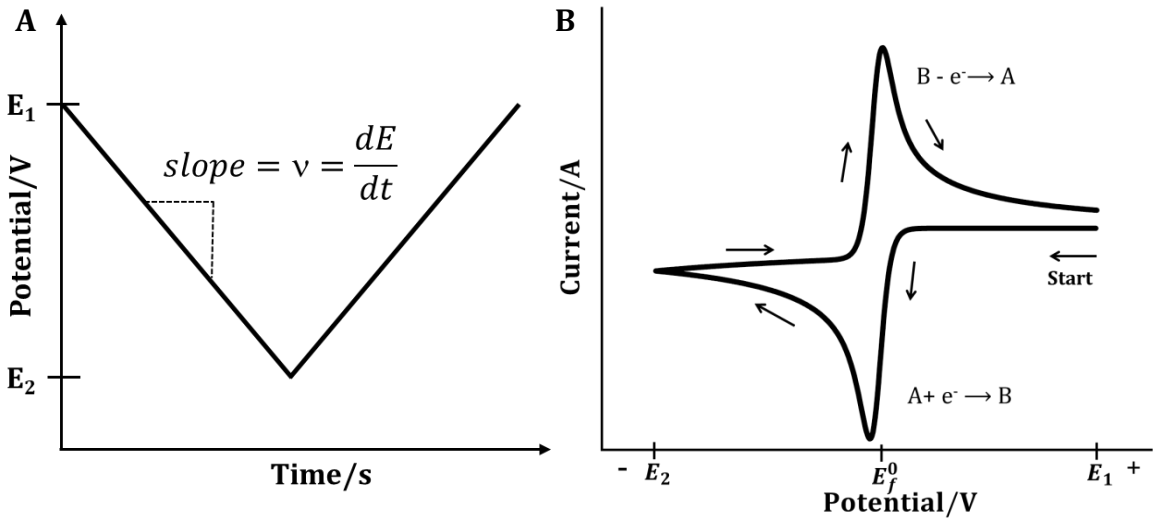

Figure 1.3 (A) The waveform of the potential applied during a cyclic voltammetry experiment and (B) a typical.

There are three general voltammetric profiles corresponding to reversible (black line), quasi-reversible (blue line) and irreversible (red line) systems (refer to Figure 1.4). Cyclic voltammetry can be used to provide information on the reversibility of the electrode reaction. The electrochemical rate constant (k^0) can be compared with the diffusional mass transport coefficient (m_T), which is defined as

$$m_T = \frac{D}{\delta} \tag{1.34}$$

where $\delta$is the time-dependent diffusion layer thickness ($\delta \sim \sqrt{2Dt}$).

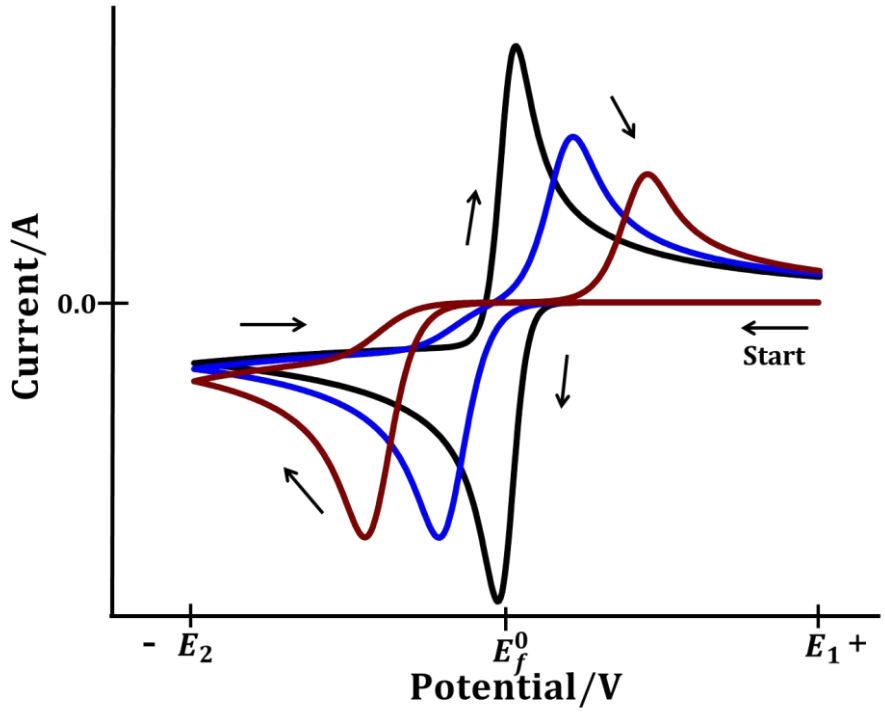

Figure 1.4 Cyclic voltammograms at a macrodisc electrode corresponding to reversible (black line), quasi-reversible (blue line), and irreversible systems (red line).

A system is classified as "reversible" when the standard electrochemical rate constant is sufficiently fast and outweighs the mass transport coefficient, $k^0 >> m_T$. The concentrations of the electroactive species at the electrode surface obey the Nernst equation. In agreement with Nernst equation, the peak-to-peak separation of the cyclic voltammogram is predicted to be ~57 mV (at 298K) and is independent of scan rate (refer to Figure 1.5). In contrary, for a system in the "irreversible" limit the electrode kinetics is relatively slow, $k^0 << m_T$. Due to the small k^0, the amount of the electroactive species consumed at the electrode is also relatively small at low overpotentials. The peak in the cyclic voltammetry occurs as the surface concentrations approaches zero and so a large overpotential is required to drive the electrode reaction: potential has to be applied in excess of the thermodynamic minimum, E_f^0. This consideration applies for both reduction and oxidation processes thus the peak-to-peak potential is larger than 57 mV (at 298K). In the case of

irreversible process, the peak-to-peak separation depends on scan rates (refer to Figure 1.6). At fast scan rates, the electroactive species can be reduced or oxidised in a short time resulting in a relatively thin diffusion layer. The mass transport to the electrode is hence efficient relative to the electrode kinetics, and the system is more irreversible (i.e. larger peak-to-peak separation). In practice, several systems are intermediate to these two extreme cases, known as a "quasi-reversible" system. At very slow scan rates, the systems behave more 'reversible-like', while at very fast scan rates the systems act as 'irreversible-like'.

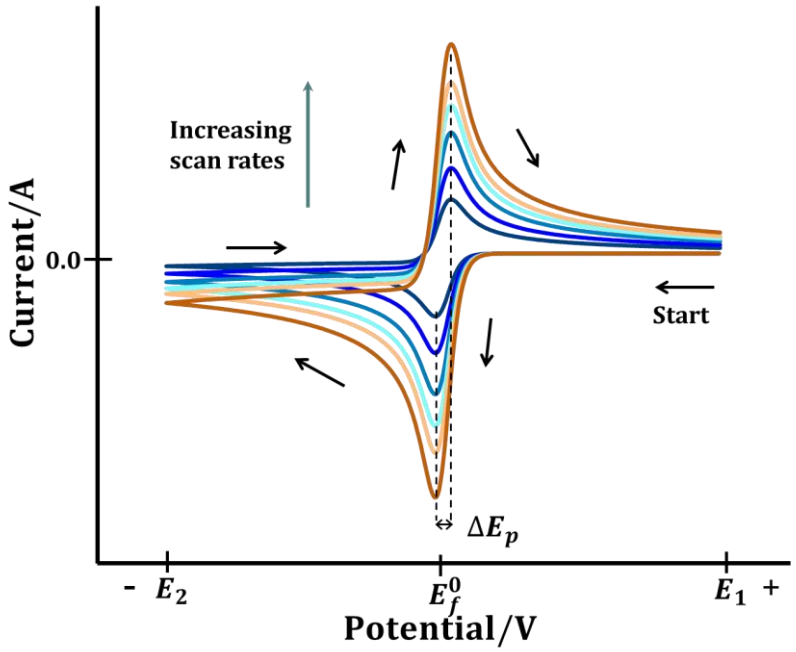

Figure 1.5 Cyclic voltammogram at a macrodisc electrode (A = 0.3 cm^2) of a one-electron transfer process ($A + e^- \rightleftharpoons B$; E_f^0=0 V, C_A = 1 mM, C_B = 0 mM, $D_A = D_B$ = 1x10^{-5} cm^2 s^{-1}) starting from cathodic scan at a range of scan rates (10-150 mV s^{-1}) for an *irreversible* process (large k^0 = 1x10^4 cm s^{-1}) showing constant peak to peak separation as the scan rate increases.

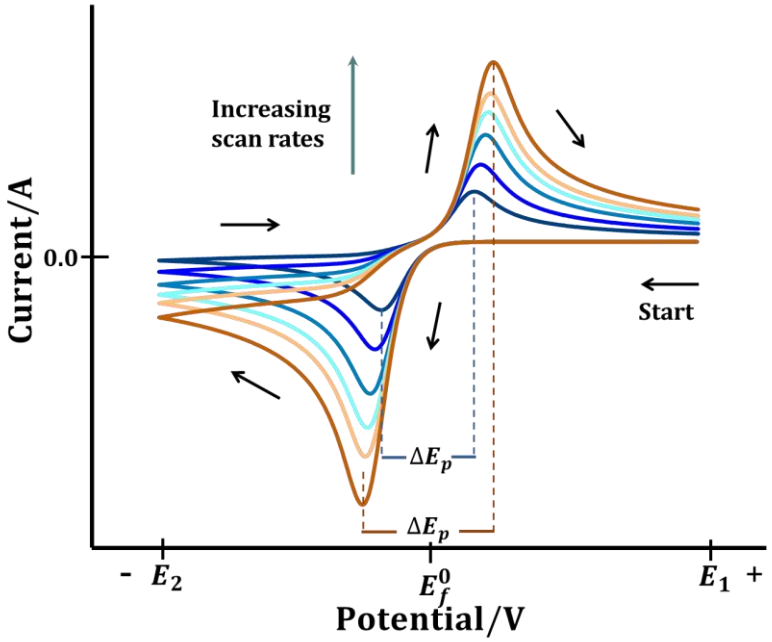

Figure 1.6 Cyclic voltammogram at a macrodisc electrode (A = 0.3 cm^2) of a one-electron transfer process (A + e^- ⇌ B; E_f^0=0 V, C_A = 1 mM, C_B = 0 mM, D_A = D_B = 1x10^{-5} cm^2 s^{-1}) starting from cathodic scan at a range of scan rates (10-150 mV s^{-1}) for an *irreversible* process (small k^0 = 1x10^{-4} cm s^{-1}) showing larger peak to peak separation as the scan rate increases.

Matsuda and Ayabe classified the system as reversible, quasi-reversible or irreversible according to a parameter Λ which was introduced and defined by them as:[2, 17]

$$\Lambda = \frac{k^0}{\sqrt{\frac{FD\upsilon}{RT}}} \tag{1.35}$$

This parameter summarises the interplay between the rate constant for electron transfer (k^0) and for (diffusional) mass transport. Table 1.1 shows the ranges of the parameter Λ for the three different classifications at macroelectrodes and the relation between k^0 and the scan rate (υ) which determines the electrochemical reversibility of a system.

Table 1.1 Criteria for the classification of electrochemical reversibility of macroelectrode voltammetry (where the numerical values relate to 298 K and α~0.5)

Types of electrochemical system	Classification boundary
Reversible	$\Lambda \geq 15$ or $k^0 \geq 0.3\upsilon^{0.5}$cm s^{-1}
Quasi-reversible	$15 > \Lambda > 10^{-3}$ or $0.3\upsilon^{0.5} > k^0 \geq 2\text{x}10^{-5}\upsilon^{0.5}$cm s^{-1}
Irreversible	$\Lambda \leq 10^{-3}$ or $k^0 \leq 2\text{x}10^{-5}\upsilon^{0.5}$cm s^{-1}

As described by the Randles-Ševčík equation, the peak current (I_p) for one electron reduction transfer process at a macroelectrode is related to the surface area of electrode (A, cm^2), the bulk concentration of species A ($[A]_{bulk}$, mol cm^{-3}), the diffusion coefficient of species A (D_A, cm^2 s^{-1}) and the scan rate (υ, V s^{-1}). α is the transfer coefficient.

For the reversible case, the Randles-Ševčík equation is given by,

$$I_p = 0.446FA[A]_{bulk}\sqrt{\frac{FD\upsilon}{RT}}, at\ 25°\text{C} \qquad (1.36)$$

In the irreversible limit, the Randles-Ševčík equation is given by,

$$I_p = 0.496\sqrt{\alpha}FA[A]_{bulk}\sqrt{\frac{FD\upsilon}{RT}}, at\ 25°\text{C} \qquad (1.37)$$

In both reversible and irreversible processes, the peak currents increase with the square root of the scan rate.

1.6.1.2 Surface bound systems

Hitherto, the discussion of this chapter has been focussed on diffusional process in which the reactants and products are in solution and diffuse towards the

electrode. In some cases which will be covered in this thesis, species can adsorb onto the electrode surface thus eliminating diffusion effects. Many experiments or electrochemical measurements using electroactive species adsorbed on electrode surface are investigated in various chapters of this thesis.

For a surface bound system, electroactive species A and B are considered to adsorb to the electrode surface throughout the redox process shown in eqn. 1.38.

$$A_{(ads)} + e^- \rightleftharpoons B_{(ads)} \tag{1.38}$$

The amount of species A and B on the electrode is quantified by the surface coverage (Γ, mol cm^{-2}). The total surface coverage (Γ_{total}) of the redox species is equal to sum of the surface coverages of the reduced and oxidised forms: $\Gamma_{total}=\Gamma_A + \Gamma_B$

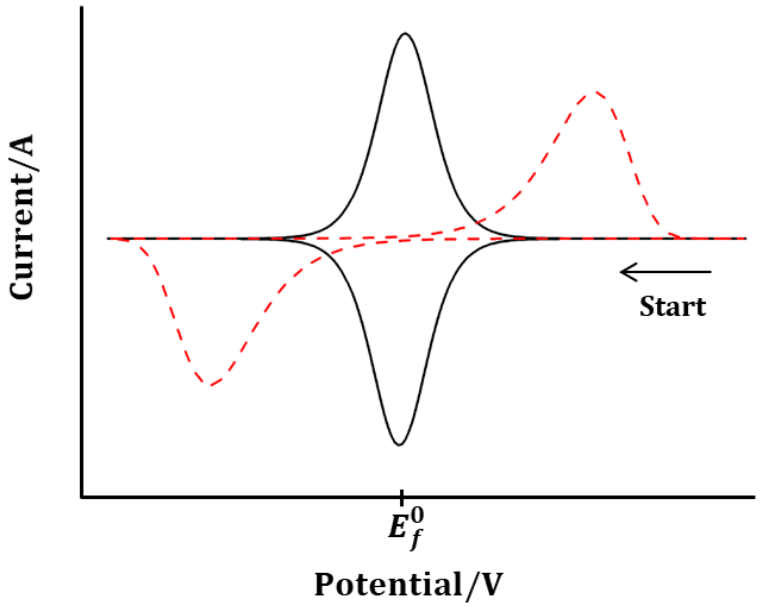

Figure 1.7 Cyclic voltammogram of an ideally adsorbed surface species showing a reversible process (solid line) and an irreversible process (dashed line).

For ideal behaviour of surface bound species, the forward and backward peak are symmetrical (ΔE_p=0) when the process is electrochemically reversible as shown in Figure 1.7 (black solid line). The current drops to zero at high overpotentials due to the electroactive species having been fully consumed. These main features are results of the finite quantity of the electroactive species on the electrode surface. Hence the wave shape is controlled only by the rate of electron transfer, but no diffusion is involved. Under ideal conditions, the Faradaic current (I_p) for a reversible process can be related to the surface coverage (Γ_{total}, mol cm^{-2}) which is given by the eqn. 1.39 (where n=1 is assumed):

$$I_p = \frac{F^2}{4RT} \upsilon A \Gamma_{total} \tag{1.39}$$

In the case of a slow electron transfer, the voltammetry is distorted with two asymmetric waves either side of the formal potential as shown in Figure 1.7 (dashed line). The peak current for a one-electron process is given by:[1]

$$I_p = \frac{\alpha F^2}{2.718RT} \upsilon A \Gamma_{total} \tag{1.40}$$

Furthermore, peak current is directly proportional to the scan rate in contrast to the case of diffusional systems where the peak current is a function of the square root scan rate.

1.6.2 Square wave voltammetry

Square wave voltammetry (SWV) is a pulse voltammetric technique which is commonly used to improve the sensitivity of voltammetry of an electrochemical process owing to its ability to reduce capacitative currents.[18] The waveform of SWV comprises of a symmetrical square wave pulse of amplitude superimposed on a

potential staircase as shown in Figure 1.8. The square wave is characterised by a pulse height, or square wave amplitude (ΔE_p), the staircase height (ΔE_s), the pulse time (t_p), and the cycle period (t_s). The pulse time can be expressed by terms of square wave frequency (f), $f = \frac{1}{2} t_p$.[2] The current measurement is made at two points of each cycle (I_1 and I_2 in Figure 1.8). These points represent the current at the end of the forward (I_1) and backward (I_2) pulses respectively, where the difference can be expressed as $\Delta I = I_2 - I_1$ in Figure 1.9.

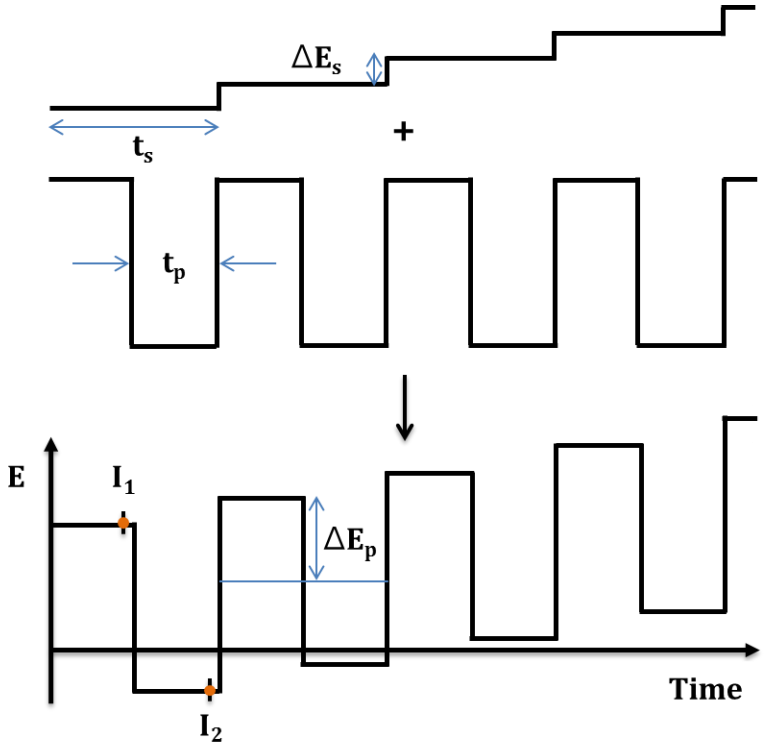

Figure 1.8 Square waveform and measurement schematic for SWV.

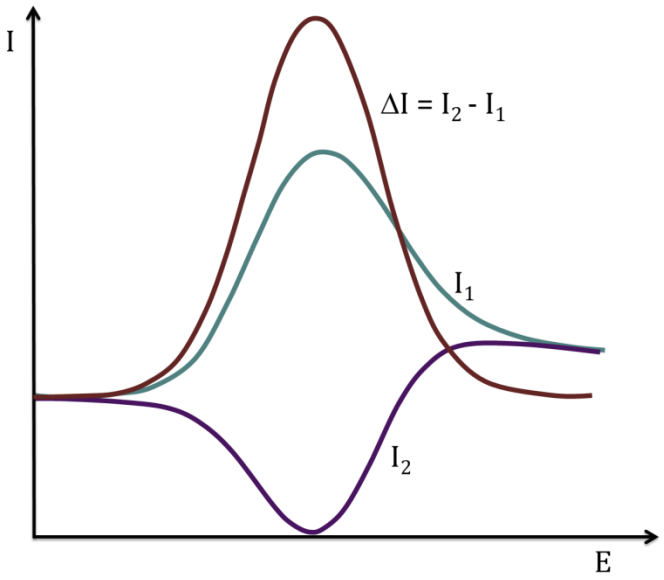

Figure 1.9 A typical square wave voltammogram.

This advantage of using square wave voltammetry is the subtraction of I_1 from I_2 if the potential steps between the forward and backward interval is small results in high measurement sensitivity and the cancellation of capacitative contributions. This is of particular importance in electroanalysis where the exclusion of such non-Faradaic currents allows more sensitivity. Due to its sensitivity and rapidity, the SWV method has been applied to numerous applications since its idea was first introduced by Barker et al.[19] and further developed by the Oysteryoungs in particular.[20] The low detection and determination limits allow the analysis of trace amount of analytes of interest. Due to these advantages of SWV, the technique has been elucidated for various applications in diagnostics, environmental monitoring, food analysis, pharmaceuticals determination and the measurement of enzymatic activity as reviewed by several researchers.[21-23] The use of SWV to improve signal sensitivity is explored in Chapter 8.

1.6.3 Stripping voltammetry

Stripping voltammetry is a powerful technique for the electroanalysis of a wide range of metals and organic substances which gives high sensitivity and is simple to use. The methodology is catagorised into three types; anodic (ASV), cathodic (CSV), and adsorptive (AdsSV) stripping voltammetry. Each has their own distinct features; however, all have two steps in common. In each case, the first involves the accumulation of target compound(s) onto a working electrode surface. This is called the *pre-concentration step*. During the second step, a potential sweep is performed resulting in the oxidation or reduction of the preconcentrated analytes on the electrode. The types of stripping voltammetry are summarised in Table 1.2.[2] In essence in ASV, the accumulated material is anodically oxidised in the second step whereas in CSV target analyte is cathodically reduced. In AdsSV the material is accumulated via adsorption.

Table 1.2 Summary of general step of stripping voltammetry

Techniques	Pre-concentration step	Stripping step
ASV	$M^{n+}_{(aq)} + ne^- \rightarrow M_{(electrode)}$	$M_{(electrode)} \rightarrow M^{n+}_{(aq)} + ne^-$
CSV	$M + L^{m-} \rightarrow M^{(n-m)-}_{(ads)} + ne^-$ $2M^{n+}_{(aq)} + mH_2O \rightarrow$ $M_2O_{m(electrode)} + 2mH^+ +$ $2(m-n)e^-$	$ML^{(n-m)}_{(ads)} + ne^- \rightarrow M + L^m$ $M_2O_{m(electrode)} + 2mH^+ +$ $2(m-n)e^- \rightarrow 2M^{n+}_{(aq)} + mH_2O$
AdsSV	$A_{(aq)} \rightarrow A_{(ads)}$ $M_{(aq)} + L_{(aq)} \rightarrow ML_{(ads)}$	$A_{(ads)} \pm ne^- \rightarrow B_{(aq)}$ $ML_{(ads)} \pm ne^- \rightarrow B'_{(aq)}$

Anodic stripping voltammetry and cathodic stripping voltammetry are widely used for trace metal analysis. Electrochemical analysis of "heavy" metals was traditionally performed using polarography where mercury was employed as a working electrode. However, due to the toxicity of mercury other alternatives such as ASV and CSV were developed. Table 1.3 shows some examples of the development of stripping voltammetry technique for metals analysis including the working electrodes used, the detection techniques and the limit of detection.

Table 1.3 Literature on anodic and cathodic stripping voltammetry

Elements	Stripping voltammetric technique	Working electrode	Stripping technique	LOD / M	Ref
As(III)	ASV	Silver	SWV	1.4×10^{-8}	24
As(III)	ASV	Gold film/glassy carbon	DPV	1.6×10^{-8}	25
Cu(II), Pb(II), Cd(II), Zn(II)	ASV	CNT fibres	SWV	Cu(II)0.27×10^{-9}, Pb(II) 1.5×10^{-9}, Cd(II) 1.9×10^{-9}, Zn(II) 1.4×10^{-9}	26
Cd(II), Zn(II)	ASV	Nanoporous bismuth	SWV	Cd(II)1.2×10^{-9}, Pb(II)7.1×10^{-9}	27
Se(IV)	CSV	Silver	DPV	2.5×10^{-9}	28
Se(IV)	CSV	Bismuth film/glassy carbon	DPV	1.3×10^{-9}	29
Se(IV)	CSV	AuNP/glassy carbon	SWV	8.1×10^{-9}	30
Ni(II)	CSV	Bismuth film/Cu	SWV	1.0×10^{-7}	31

DPV is differential pulse voltammetry.

Apart from trace metals, ASV and CSV are used for analysis of other compounds for example plant hormones or flavonoid glycosides in plants.[32, 33] Although, ASV and CSV facilitate the measurements of many electroactive species such as trace metals in particular, their utility for some analytical problems is restricted. Due to the electrolytic nature of the pre-concentration step, numerous

organic compounds cannot be electrodeposited. This thesis focusses on the use of adsorptive stripping voltammetry reflecting the nature of the analytes of interest as which will be presented in Chapters 3-5.

1.6.3.1 Adsorptive stripping voltammetry

Adsorptive stripping voltammetry (AdsSV) is similar to ASV and CSV with primary difference that the pre-concentration step is accomplished by adsorption of compounds onto the electrode surface rather than electrolytic accumulation.[34] The AdsSV is often the preferred method for organic analytes. Adsorptive stripping voltammetry is widely used in a number of applications to determine environmental carcinogens [35], additive dyes in food, and drugs[36]. Although AdsSV technique is mostly used for analysis of organic molecules, it can be used for trace metals determination via complexation with chelating agents adsorbed on the electrode surface.[37, 38] Table 1.4 represents the diversity and extent of the AdsSV techniques for analysis of a range of analytes.

Table 1.4 A range of substances analysed using adsorptive stripping voltammetry (AdsSV) at different electrodes.

Analytes	Working electrode	Stripping technique	LOD / M	Ref
Rifampicin	HMDE	SWV	9.8×10^{-9}	39
		DPV	6.1×10^{-9}	
	Lead film/GCE	SWV	9.0×10^{-11}	40
Dopamine	SPE-MWCNT	DPV	1.5×10^{-8}	41
Lamotrigine	Pyrolytic graphite electrode	CV	8.0×10^{-8}	42
Fulvestrant	Boron-doped diamond	DPV	2.4×10^{-7}	43
Viagra	MWCNT-g-PABS/GCE	SWV	4.7×10^{-12}	44
Hesperidin	MWCNT/BPPGE	CV	6.1×10^{-7}	45
		SWV	7.0×10^{-9}	
2,4,6-	MWCNT/GCE	LSV	2.6×10^{-9}	46

trinitrotoluene (TNT)				
Tannic acid	CPE	LSV	1.0×10^{-8}	47
Caffeine	MWCNT-Nafion/GCE	DPV	5.1×10^{-7}	48

DPV is differential pulse voltammetry and LSV is linear sweep voltammetry.

The general procedure of AdsSV is shown in Figure 1.10. Briefly, target compounds accumulate onto a working electrode by adsorption in the first step. Once a significant surface coverage has been obtained, a potential sweep is performed resulting in the oxidation or a reduction of the adsorbed species as a second step. Measurement of the charge (or current) from the stripping peak along with a suitable calibration curve gives rise to the quantification of the adsorbate in bulk solution. The electrochemical response of the surface bound species reflects the surface area of the electrode and the extent of adsorption. Therefore, the sensitivity of AdsSV based sensors can be enhanced by increasing the electrode surface area as well as using an optimum accumulation time during the pre-concentration step. Moreover, from using this approach, both qualitative and quantitative analysis can result.

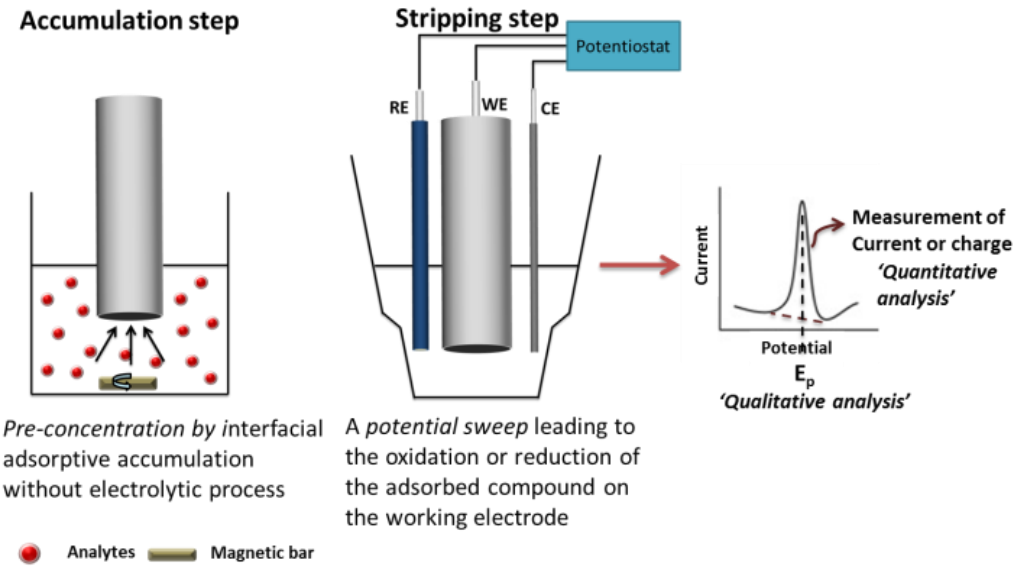

Figure 1.10 Schematic diagram of adsorptive stripping voltammetry; consisting of two important steps which are accumulation and stripping steps.

1.7 Electrode materials

The final section of this introduction focusses on the properties of electrode materials. Carbon based electrodes are used in most of the work presented in this thesis. As such, this section aims to give a brief overview of the properties and structure of the carbon-based materials used including pyrolytic graphite electrodes, screen printed electrodes, carbon paste electrodes, and carbon fibres.

1.7.1 Pyrolytic graphite electrodes

Pyrolytic graphite is a highly ordered graphite material. Basal plane and edge plane pyrolytic graphite electrodes are fabricated from this material. Considering a perfect crystal of graphite, as shown in Figure 1.11, there are two crystallographic planes on surface. A basal plane pyrolytic graphite electrode (BPPG) is produced by cutting parallel to the surface of the graphite layers. In contrast to the BPPG, the edge plane pyrolytic graphite electrode (EPPG) is fabricated from the layers of graphite which lie perpendicular to the basal planes.

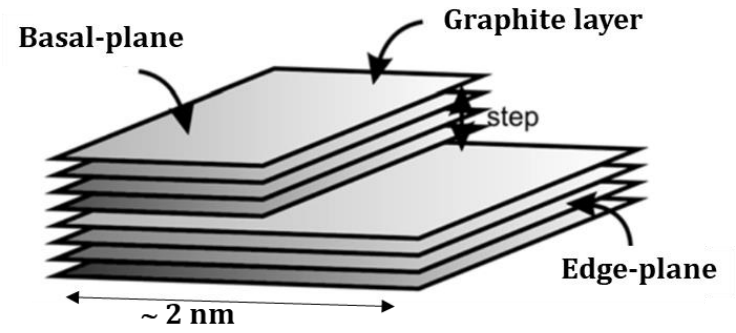

Figure 1.11 Schematic of the material structure of graphite highlighting the layered structure which exhibits both basal and edge plane sites.

Defects at the surface of BPPG electrodes occur in the form of steps exposing the edges of the graphite layers. According to the nature of the chemical bonding at

the edge of graphite layers, the two planes, edge and basal, exhibit different electrochemical properties.[49-51] For electrochemistry, the edge plane often manifests at least three orders of magnitude faster electrode kinetics in comparison with the basal plane which depends on redox couple.[52] Due to the highly active chemical sites of the edge plane, atmospheric oxygen and/or moisture can react resulting in these defect sites being decorated with a variety of surface oxo groups, most notably hydroxy, carboxylic acid, and quinone functional groups. These end groups are often considered responsible for the rapid electron transfer rates underpinning the electrochemical performance of EPPG electrodes.[53] The possible pathway of first generating and the second utilisation of the oxygen functionalities for electroanalysis are explored in Chapters 6 and 7. Furthermore, the BPPG electrode is employed to study the electrochemical behaviours of chemical compounds in spices and to use as a support for electrode modification with several carbon materials for adsorptive stripping voltammetry in Chapters 3-5.

1.7.2 Carbon paste electrodes

Carbon paste electrodes (CPE) are employed as a working electrode in experiments discussed in Chapter 5. In general, the electrodes are fabricated by mixing carbon materials with a non-electrolytic binder to produce a paste. The mixture is then packed into a well of an electrode holder (often a Teflon rod) which has a metal wire running through the holder as electrical contact. The diameter of the cavity can be adjusted to fit the needs of the researcher. Carbon paste electrodes offer an easily renewable surface, a relatively low cost to fabricate, and low background current contributions. Materials such as nanocarbon and polycrystalline graphite are generally selected as the Carbon components of making paste together with popular

organic pasting liquids or binders such as mineral oil or organic esters.[54, 55] Given their composition, carbon paste electrodes exhibit a hydrophobic surface, this being the most commonly reported property of this electrode.[56] Due to their hydrophobic surfaces, Carbon paste electrodes are common electrodes used for electroanalysis via adsorptive stripping voltammetry techniques.[57-62] In Chapter 5 of this thesis the carbon paste electrode is chosen for the optimisation of electrode materials for adsorptive stripping voltammetry.

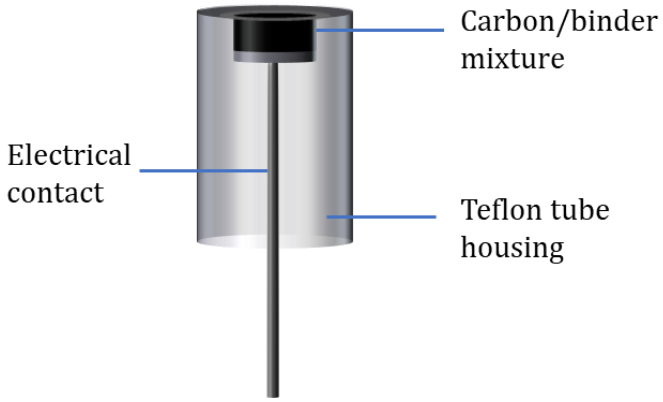

Figure 1.12 Schematic diagram of a Carbon paste electrode.

1.7.3 Carbon screen printed electrode

Electrode systems of a three electrode configuration can be fabricated onto a small piece of a solid substrate using a screen-printed technique. This type of electrode has gained popularity for the development of electrochemical sensors due to their disposable nature, easy integration into portable systems and the flexibility of modifying the surface. Moreover, the miniaturisation of the working electrode, counter electrode and reference electrode leads to the need of just a few microliters of sample.

SPEs can be produced by screen-printing layer-by-layer of ink onto a solid substrate which might be one of the various types of plastics or ceramics. The most commonly used pastes are silver ink for a conductive track or reference electrode and graphite based inks for the working and counter electrodes. Note that other materials including platinum, gold and silver based inks can also be used. The different formulations of ink paste can have strong effect on the electron transfer and the analytical performance of resulting carbon sensors.[63, 64] Modification of working electrode can be done by means of addition of modifier substances in the printing inks or by means of deposition of various materials on the electrode surface. Various types of substances have been reported as modifiers such as enzymes, polymers, electrochemical mediators, metal nanoparticles and carbon nanotubes. These are typically added to improve the sensitivity or selectivity of the SPEs. A wide variety of commercially available SPEs are provided by several companies e.g. Dropsens, PalmSens, Pine Research Instrumentation, eDAQ, Metrohm, Micrux Technologies, etc. The SPEs employed in Chapter 5 were purchased from DropSens (Asturias, Spain), refer to Figure 1.13. The electrodes consist of unmodified graphite or a multiwalled carbon nanotube modified carbon as a working electrode, a carbon counter electrode and a silver reference electrode printed onto a ceramic substrate.

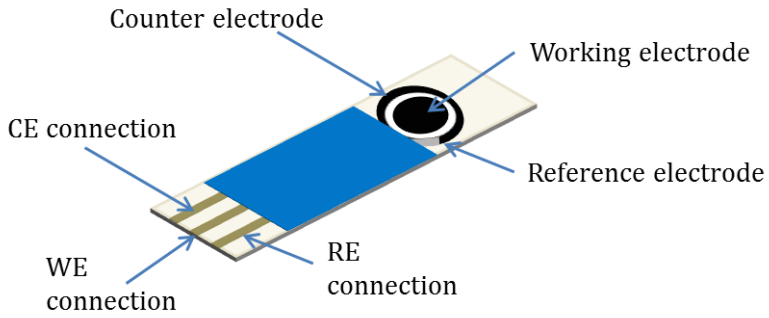

Figure 1.13 A typical screen-printed electrode from DropSens.

1.7.4 Carbon fibre electrode

Carbon fibres refer to fibres which contain over 90 wt% carbon. The carbon atoms are bonded together in microscopic crystals which are aligned parallel to the long axis of the fibre. The crystal alignment makes the fibre very strong for its size.[65] Carbon fibres range from 0.1 to 100 μm in diameter, with a common range being 5-25 μm. Due to the ultra-small size, the carbon fibre electrodes are of interest for applications in very small environments such as in a single cell or for an in vivo study. Apart from the advantage of the size, carbon fibre microelectrodes are biologically compatible and not toxic to cells. Also their electrochemistry has been well characterized and they have attractive electrochemical properties.[66] One primary application for carbon-fibre microelectrodes has been for in vivo real-time monitoring of neurotransmitter changes (especially in dopamine).[67]

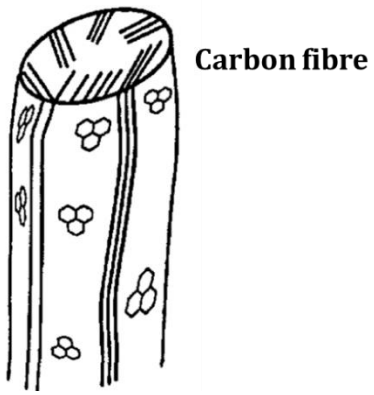

Figure 1.14 Schematic representations of general morphology of a carbon fibre showing that the graphitic plane generally is oriented along the fibre axis. Adapted from Ref.[68].

Due to the graphitic composition of carbon fibres, one would expect planes, basal and edge, to be appeared on fibres. Consequently, the oxygen-containing groups which mentioned earlier in section 1.7.1 must likely be presented on the carbon fibre surfaces. Note that the morphology, orientation, crystallite size, and tensile strength

of each fibre are different from type to type.[65] The scope for in vivo use and the presence of oxygen-containing functionalities on the carbon fibre surface lead us to explore the utilisation of carbon fibre electrode for development of an electrochemical sensor in Chapter 7.

Bibliography

1. A. J. Bard and L. R. Faulkner, *Electrochemical Methods: Fundamentals and Applications*, John Wiley & Sons, Inc, 2001.
2. R. G. Compton and C. E. Banks, *Understanding Voltammetry*, World Scientific, 2011.
3. A. C. Fisher, *Electrode Dynamics*, Oxford University Press, 1996.
4. J. A. V. Butler, *Transactions of the Faraday Society*, 1924, **19**, 729-733.
5. J. A. V. Butler, *Transactions of the Faraday Society*, 1924, **19**, 734-739.
6. A. Fick, *Annalen der Physik*, 1855, **170**, 59-86, in German. In English translation: *Journal of Science*, 1855, 16, 1830.
7. A. Einstein, *Annalen der Physik*, 1905, **322**, 549-560.
8. M. von Smoluchowski, *Annalen der Physik*, 1906, **326**, 756-780.
9. J. K. Novev and R. G. Compton, *Current Opinion in Electrochemistry*, 2018, **7**, 118-129.
10. C. H. Bamford, C. F. H. Tipper† and R. G. Compton, *Electrode Kinetics: Principles and Methodology*, Elsevier Science, 1986.
11. M. Faraday, *Philosophical Transactions of the Royal Society of London*, 1834, **124**, 77-122.
12. P. H. Rieger, *Electrochemistry*, Springer Netherlands, 1993.
13. E. I. Rogers, I. Streeter, L. Aldous, C. Hardacre and R. G. Compton, *Journal of Physical Chemistry C*, 2008, **112**, 10976-10981.
14. M. Fleischmann, F. Lasserre, J. Robinson and D. Swan, *Journal of Electroanalytical Chemistry and Interfacial Electrochemistry*, 1984, **177**, 97-114.
15. R. S. Nicholson and I. Shain, *Analytical Chemistry*, 1964, **36**, 706-723.
16. K. Cinková, M. Clark, S. V. Sokolov, C. Batchelor-McAuley, Ľ. Švorc and R. G. Compton, *Electroanalysis*, 2017, **29**, 1006-1013.
17. H. Matsuda and Y. Ayabe, *Zeitschrift für Elektrochemie, Berichte der Bunsengesellschaft für physikalische Chemie*, 1955, **59**, 494-503.
18. C. M. A. Brett and A. M. O. Brett, *Electrochemistry : principles, methods, and applications*, Oxford University Press, Oxford, 1993.
19. G. C. Barker and I. L. Jenkins, *Analyst*, 1952, **77**, 685-696.
20. J. G. Osteryoung and R. A. Osteryoung, *Analytical Chemistry*, 1985, **57**, 101-110.
21. V. Mirceski, R. Gulaboski, M. Lovric, I. Bogeski, R. Kappl and M. Hoth, *Electroanalysis*, 2013, **25**, 2411-2422.
22. B. Uslu and S. A. Ozkan, *Analytical Letters*, 2011, **44**, 2644-2702.
23. A. Chen and B. Shah, *Analytical Methods*, 2013, **5**, 2158-2173.
24. A. O. Simm, C. E. Banks and R. G. Compton, *Electroanalysis*, 2005, **17**, 1727-1733.
25. S. B. Rasul, A. K. M. Munir, Z. A. Hossain, A. H. Khan, M. Alauddin and A. Hussam, *Talanta*, 2002, **58**, 33-43.
26. D. Zhao, X. Guo, T. Wang, N. Alvarez, V. N. Shanov and W. R. Heineman, *Electroanalysis*, 2014, **26**, 488-496.
27. J. H. Hwang, X. Wang, D. Zhao, M. M. Rex, H. J. Cho and W. H. Lee, *Electrochimica Acta*, 2019, **298**, 440-448.
28. T. Ishiyama and T. Tanaka, *Analytical Chemistry*, 1996, **68**, 3789-3792.
29. Q. Zhang, X. Li, H. Shi, Hongzhou and Z. Yuan, *Electrochimica Acta*, 2010, **55**, 4717-4721.
30. A. O. Idris, N. Mabuba and O. A. Arotiba, *Journal of Electroanalytical Chemistry*, 2015, **758**, 7-11.
31. S. Legeai, S. Bois and O. Vittori, *Journal of Electroanalytical Chemistry*, 2006, **591**, 93-98.
32. M. H. Blanco, M. d. C. Quintana and L. Hernández, *Electroanalysis*, 2000, **12**, 147-154.
33. E. Reichart and D. Obendorf, *Analytica Chimica Acta*, 1998, **360**, 179-187.

34. A. J. Bard, *Electroanalytical chemistry : a series of advances. Volume 16*, Marcel Dekker, Inc., New York, 1989.
35. B. Jiri, P. Karolina and V. Vlastimil, *Current Analytical Chemistry*, 2008, **4**, 242-249.
36. J. C. Vire, J. M. Kauffmann and G. J. Patriarche, *Journal of Pharmaceutical and Biomedical Analysis*, 1989, **7**, 1323-1335.
37. J. Wang, J. Wang, J. Lu and K. Olsen, *Analytica Chimica Acta*, 1994, **292**, 91-97.
38. M. Grabarczyk and M. Adamczyk, *Journal of Analytical Methods in Chemistry*, 2017, **2017**, 1486497-1486497.
39. M. A. Alonso Lomillo, O. Domínguez Renedo and M. J. Arcos Martínez, *Electroanalysis*, 2002, **14**, 634-637.
40. K. Tyszczuk and M. Korolczuk, *Electroanalysis*, 2009, **21**, 101-106.
41. M. Moreno, A. S. Arribas, E. Bermejo, M. Chicharro, A. Zapardiel, M. C. Rodríguez, Y. Jalit and G. A. Rivas, *Talanta*, 2010, **80**, 2149-2156.
42. R.-S. Saberi and S. Shahrokhian, *Bioelectrochemistry*, 2012, **84**, 38-43.
43. B. Dogan-Topal, D. Kul, S. A. Ozkan and B. Uslu, *Journal of Applied Electrochemistry*, 2011, **41**, 1253.
44. A. I. Gopalan, K. P. Lee and S. Komathi, *Biosensors and Bioelectronics*, 2011, **26**, 3018-3022.
45. M. J. Sims, Q. Li, R. T. Kachoosangi, G. G. Wildgoose and R. G. Compton, *Electrochimica Acta*, 2009, **54**, 5030-5034.
46. J. Wang, S. B. Hocevar and B. Ogorevc, *Electrochemistry Communications*, 2004, **6**, 176-179.
47. L. Xu, N. He, J. Du and Y. Deng, *Electrochemistry Communications*, 2008, **10**, 1657-1660.
48. J. Zhang, L. P. Wang, W. Guo, X. D. Peng, M. Li and Z. B. Yuan, *International Journal of Electrochemical Science*, 2011, **6**, 997-1006.
49. R. L. McCreery, *Chemical Reviews*, 2008, **108**, 2646-2687.
50. M. Pumera, *Chemical Society Reviews*, 2010, **39**, 4146-4157.
51. M. Pumera, *Chemistry – A European Journal*, 2009, **15**, 4970-4978.
52. C. E. Banks, T. J. Davies, G. G. Wildgoose and R. G. Compton, *Chemical Communications*, 2005, DOI: 10.1039/B413177K, 829-841.
53. G. G. Wildgoose, P. Abiman and R. G. Compton, *Journal of Materials Chemistry*, 2009, **19**, 4875-4886.
54. I. švancara, K. Kalcher, W. Diewald and K. Vytřas, *Electroanalysis*, 1996, **8**, 336-342.
55. I. Švancara, J. Konvalina, K. Schachl, K. Kalcher and K. Vytřas, *Electroanalysis*, 1998, **10**, 435-441.
56. K. Kalcher, J. M. Kauffmann, J. Wang, I. Švancara, K. Vytřas, C. Neuhold and Z. Yang, *Electroanalysis*, 1995, **7**, 5-22.
57. R. Nissim and R. G. Compton, *Analyst*, 2014, **139**, 5911-5918.
58. S. Gutiérrez-Fernández, M. C. Blanco-López, M. J. Lobo-Castañón, A. J. Miranda-Ordieres and P. Tuñón-Blanco, *Electroanalysis*, 2004, **16**, 1660-1666.
59. N. E. Zoulis, D. P. Nikolelis and C. E. Efstathiou, *Analyst*, 1990, **115**, 291-295.
60. J. P. Hart, S. A. Wring and I. C. Morgan, *Analyst*, 1989, **114**, 933-937.
61. M. P. Kingsley, P. K. Kalambate and A. K. Srivastava, *RSC Advances*, 2016, **6**, 15101-15111.
62. M. M. Ghoneim, H. S. El-Desoky, A. Matsuda, T. Hattori and M. M. Abdel-Galeil, *RSC Advances*, 2015, **5**, 56086-56097.
63. P. Fanjul-Bolado, D. Hernández-Santos, P. J. Lamas-Ardisana, A. Martín-Pernía and A. Costa-García, *Electrochimica Acta*, 2008, **53**, 3635-3642.
64. J. Wang, B. Tian, V. B. Nascimento and L. Angnes, *Electrochimica Acta*, 1998, **43**, 3459-3465.
65. A. J. Bard, *Electroanalytical chemistry : a series of advances. Volume 17*, Marcel Dekker, Inc., New York, 1991.
66. M. L. Huffman and B. J. Venton, *The Analyst*, 2009, **134**, 18-24.
67. F. G. Gonon, C. M. Fombarlet, M. J. Buda and J. F. Pujol, *Analytical Chemistry*, 1981, **53**, 1386-1389.
68. R. L. McCreery, in *Voltammetric Methods in Brain Systems*, Springer, 1995, pp. 1-26.

Chapter 2

Experimental

This chapter outlines the experimental details of the reagents and instrumentation used throughout this thesis; specific descriptions of each experiment and/or reagents can be found in the relevant experimental sections of Chapters 3-8.

2.1 Chemicals, reagents and materials

All chemicals, reagents and materials described in this thesis can be found in Table 2.1 along with their purity and suppliers. All solutions were prepared using deionised water (Millipore, UK) with a resistivity of 18.2 MΩ cm at 298 K.

Table 2.1 List of chemicals, reagents and materials used in this thesis

Chemical name	Formula	Purity	Supplier
6-gingerol	$C_{17}H_{26}O_4$	98.90%	Carbosynth
Acetic acid	CH_3COOH	99.50%	BDH
Acetone	CH_3COCH_3		Merck Millipore
Alumina powder			Buehler
Bamboo-like multiwalled carbon nanotubes		>95%	NanoLab
Boric acid	H_3BO_3	99.50%	Aldrich
Capsaicin	$C_{18}H_{27}NO_3$		Sigma
Carbon dioxide gas	CO_2		BOC
Citric acid	$C_6H_8O_7$	≥99.0%	Sigma-Aldrich
Clearclad HSR electrophoretic paint			LSV Coating
Curcumin	$C_{21}H_{20}O_6$		Sigma-Aldrich

Defibrinated sheep's blood			TCS Biosciences Ltd
Duracal buffer pH10.01 ± 0.01			Hamilton
Duracal buffer pH4.01 ± 0.01			Hamilton
Duracal buffer pH7.00 ± 0.01			Hamilton
Graphene nanoplatelets			Strem Chemicals
Hydrochloric acid	HCl	AR grade	Fisher Scientific
Hydrogen peroxide (30%wt)	H_2O_2	ACS grade	Sigma-Aldrich
Mineral oil			Sigma-Aldrich
Nanocarbon			Cabot Performance
Nitric acid (70%)	HNO_3		Fisher Scientific
Nitrogen gas	N_2		BOC
Phosphoric acid	H_3PO_4	99.99%	Aldrich
Potassium chloride	KCl	≥99.0%	Sigma-Aldrich
Potassium dihydrogen phosphate	KH_2PO_4	≥99.0%	Sigma
Potassium hexachloroiridate(III)	K_3IrCl_6		Sigma-Aldrich
Potassium permanganate	$KMnO_4$	97%	Aldrich
Potassium thiocyanate	KSCN	≥99.0%	Honeywell Fluka
Sodium chloride	NaCl	>99.5%	Sigma-Aldrich
Sodium citrate monobasic	$Na_3C_6H_5O_7$	≥99.5%	Sigma
Sodium phosphate monobasic	NaH_2PO_4	≥99.0%	Sigma-Aldrich
Sodium hydrogencarbonate	$NaHCO_3$	99.5-100.5%	Sigma-Aldrich
Sodium hydroxide	NaOH	AR grade	Fisher Scientific
Sodium monohydrogen phosphate	Na_2HPO_4	≥99.0%	Sigma-Aldrich
Sulphuric acid (>95%)	H_2SO_4		Fisher Scientific
Synthetic saliva			Synthetic Urine e.K.

2.2 Biological samples

2.2.1 Saliva

Synthetic saliva was purchased from Synthetic Urine e.K. (Germany) manufactured according to a standardised production process in accordance with DIN 53160-1. DIN is an acronym that stands for Deutsches Institut für Normung e.V. (German Institute for Standardization). Specifically, the DIN 53160-1 is the standard procedure for testing the colourfastness of articles for common use with synthetic saliva.

For authentic saliva, samples were donated by consenting volunteers. Saliva samples were collected using a commercial device, namely the Salivette® (Sarstedt, Germany) which facilitates the collection of saliva, see Figure 2.1. A Salivette comprises of a conical swab made of cotton or synthetic material (such as polystyrene) for saliva absorption. The volunteers were given the swabs to gently chew for one minute. Recovery of saliva from the swab was retrieved by centrifugation of the Salivette at 2400 rpm for 15 min.

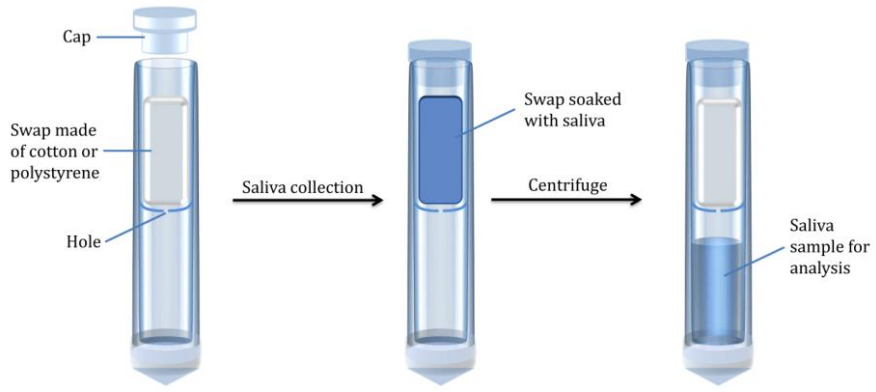

Figure 2.1 Schematic representation of saliva collection process using Salivette®

2.2.2 Blood

Defribrinated sheep's blood is used in Chapter 8 as a model for biological samples in general and blood samples in particular. The sheep's blood was purchased

from TCS Biosciences Ltd, UK. The blood sample was treated by the company to remove fibrin protein. Briefly, after collection the sample has been mechanically agitated this is commonly done in the presence of glass beads. As the blood clots the mechanical action and glass beads serve to physically remove the fibrin from blood and thus stops the coagulation of the blood sample without the need of anticoagulants or other additives.

2.3 Electrochemical set up

All electrochemical experiments were performed in a thermostated (25.0±0.2°C) Faraday cage with a uAutolab II potentiostat (Metrohm-Autolab BV, Utrecht, Netherlands). A standard three electrode set up was used throughout this thesis, consisting of a saturated calomel electrode (SCE +0.244 V vs. SHE, BASi Inc., Japan) as a reference electrode, a platinum mesh or platinum wire as a counter electrode, and a working electrode. The details of working electrodes used are different from chapter to chapter and will be discussed in the relevant chapter.

Chapter 3

Electrochemical Detection and Quantification of Gingerol Species in Ginger

Chapters 3-4 will focus on the development of electrochemical sensors for application in the food industry. Adsorptive stripping voltammetry (AdsSV) is used as a technique for the detection of gingerol in ginger (Chapter 3) and curcumin in turmeric (Chapter 4). Since the sensitivity of the AdsSV technique depends on the surface area of electrode, multiwalled carbon nanotubes (MWCNT) are chosen to modify the electrode due to their inherent high surface area.

In this chapter, we demonstrate the potential of electrochemical detection for the analysis of the 'strength' of ginger in ginger samples. This facile and fast detection method is aimed at quality control in food industry. Specifically, we report adsorptive stripping voltammetry (AdsSV) as a technique for the detection of gingerol compounds, the pungent components of ginger rhizome. Among the gingerols, 6-gingerol is the most abundant and is chosen as a model to characterise the behaviour of a wider range of related compounds. Multiwalled carbon nanotube modified basal plane pyrolytic graphite electrodes (MWCNT-BPPG electrode) are employed to enhance the sensitivity of the measurement. A linearity range from 1 μM to 50 μM with limit of detection of 0.21 μM and limit of quantification of 0.71 μM is obtained. Further, the simple and rapid extraction procedure by simply vortexing the ginger sample with ethanol is developed for extraction of gingerol related species.

The work presented in this chapter has been published in *Analyst*, 141, (2016), 6321-6328.[1]

3.1 Introduction

Zingiber officinale (ginger) is widely used around the world as a spice. This culinary product contains several different pungent and active ingredients; predominantly these are gingerol, shogaol, zingerone, and paradol which have the chemical structures shown in Figure 3.1.[2]

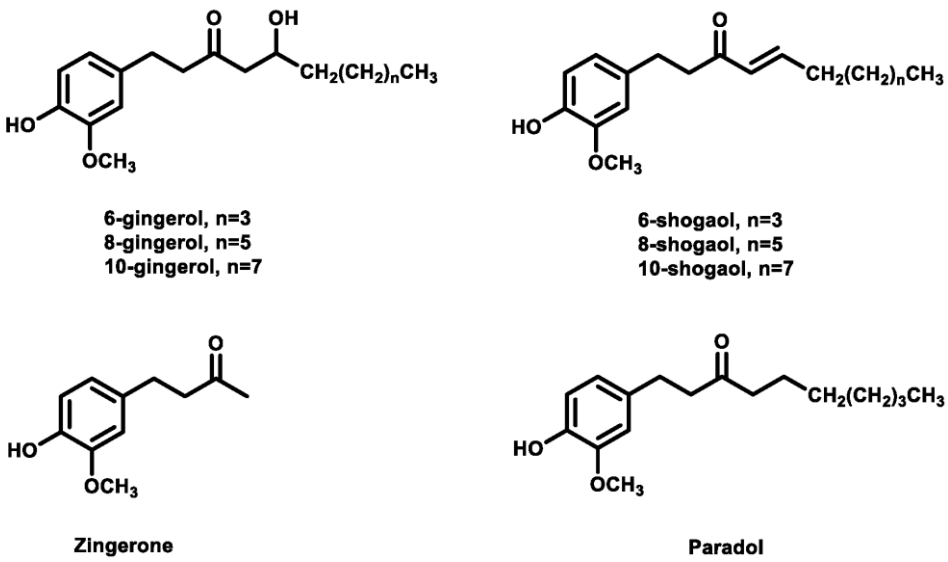

Figure 3.1 Chemical structures of pungent and active compounds in ginger.

The compounds in Figure 3.1 all contain a 2-methoxyphenol group and differ only in the structure of their side chain. Of these 6-gingerol was identified as the most abundant and pungent components in fresh ginger rhizome.[3, 4] Shogaol, a dehydrated form of gingerol mostly found in a dried or cooked ginger, is reportedly 'spicier' than gingerol (160,000 vs 80,000 Scoville Heat Units respectively).[5] However, fresh ginger contains much more gingerol than the other pungent compounds[6] and as such is used in this work as a model compound for the analysis of the 'strength' of ginger.

Beyond culinary uses gingerols have been shown to possess a variety of biological properties that can be beneficial for human health. They exhibit anti-inflammatory[7, 8], anti-platelet[9], anti-tumor[10], and high antioxidant properties.[11, 12] In addition, these active compounds have the possibility for use in cardiovascular disease treatment[13], and the prevention of nausea and vomiting during pregnancy and chemotherapy.[14-16]

The concentration of gingerol in ginger products has been shown to be related to the pungency level of ginger.[6] The degree of pungency is an important determinant of the value of the ginger products. However, the concentration of gingerol is found to vary with growing conditions, harvesting, processing of the ginger rhizome, and the extraction methodology.[17] From the reported literature, the concentration of gingerol related species in a variety of ginger samples (fresh ginger, ginger dietary supplements, ginger powder, and ginger beverage) is normally found between the limits of *ca.* 0.20 – 15.92 mg g^{-1}.[18,19]

Owing to their culinary and medicinal importance, a simple and accurate determination method of gingerol is desirable in the food industry. Hitherto, the major technique utilised for determine the concentration of gingerol is chromatography.[19-24] Gas chromatography (GC) has been used to analyse gingerol.[22, 23] Nonetheless, GC showed several disadvantages for analysing gingerol for instance the temperatures in the GC column have been shown to result in significant conversion of gingerol to shogaol because of its thermal instability which limits the application of this method.[21] High-performance liquid chromatography (HPLC) is by far the most popular technique to detect gingerol. However, the HPLC method is limited in terms of the high cost of the instrumentation and extensive necessary

sample preparation rendering the method inapplicable for use by non-skilled personnel and also time consuming and slow for frequent commercial use.

To address these problems of high cost instrumentation, complex sample preparation and to facilitate analysis by non-trained operators, we report a simple and sensitive electroanalytical detection of gingerol and related species at a multiwalled carbon nanotube modified basal-plane pyrolytic graphite electrode (MWCNT-BPPG electrode) using adsorptive stripping voltammetry (AdsSV). The adsorptive stripping voltammetry technique involves the accumulation of target compound(s) on the electrode surface. The electrochemical response obtained is highly dependent on the area of the electrode surface. Therefore, carbon nanotubes are chosen to modify the electrode due to their inherent high surface area (200 - 400 $m^2\ g^{-1}$)[25] which significantly increases the AdsSV response. In addition, we study real samples and develop a simple preparation method. Finally, we demonstrate the capability of the electrochemical detection to quantify gingerol related species in crushed ginger samples.

3.2 Experimental

3.2.1 Chemicals and reagents

All chemicals were of analytical grade and were used as received without further purification. 6-gingerol was purchased from Carbosynth (98.9% purity, Berkshire, UK). The bamboo-like multiwalled carbon nanotubes, b-MWCNTs (30±10 nm diameter, 5-20 μm length, >95% purity) were purchased from NanoLab (Brighton, MA, USA). All solutions were prepared with ultrapure water at a resistivity

of 18.2 MΩ cm at 298K (Millipore, USA). TESCO Ingredients Crushed Ginger was purchased from Tesco (Oxford, UK). The Britton-Robinson buffer, 0.05 M at pH 1.8, was prepared using boric acid (99.5% purity, Aldrich), phosphoric acid (99.99% purity, Aldrich) and acetic acid (99.5% purity, BDH).

3.2.2 Apparatus

All electrochemical experiments were performed using a three-electrode system in a Faraday cage held at 25 °C with a uAutolab II potentiostat (Metrohm-Autolab, Netherlands). A basal-plane pyrolytic graphite (BPPG) electrode was produced from pieces of the highly ordered pyrolytic graphite (HOPG) (Le Carbone, Sussex, UK). The electrode was set in an insulating PTFE housing with an electrical connection made using a stainless steel core. The BPPG electrode is used as a substrate for the modified electrode discussed below. The electrochemical cell was completed using a saturated calomel electrode, SCE, as the reference electrode (SCE +0.244 V vs SHE, BASi Inc., Japan) and a platinum mesh 99.99% (Goodfellow, UK) as the counter electrode.

The MWCNT modification of BPPG electrode was prepared using the drop casting method. The bamboo-like multiwalled carbon nanotubes were first dispersed in acetone (1 mg mL^{-1}). The solution was then sonicated in an ultrasonic bath for 10 minutes prior to drop casting. A 20 µL volume was drop-cast onto the BPPG electrode surface. This amount of MWCNT suspension yields the surface coverage which gives sufficiently enhanced electrochemical responses for detection of micromolar levels using AdsSV.[26] Evaporation of the acetone at room temperature then resulted in a nanotube modified electrode.[26, 27] The MWCNT-BPPG electrode was gently rinsed with acetone after each voltammetric scan prior to repeated use of the same drop-

cast electrode for further scans. Electrode refreshed in the manner could be used for 10-15 times before having to be replaced by a new drop cast. BPPG electrode surfaces were prepared by polishing the electrode surface on sand paper P2500 and P4000 grade respectively and then repeatedly pressing with cellotape (Henkel AG, Dusseldorf, Germany). The electrode was subsequently rinsed with acetone.[28]

3.2.3 Sample preparation

To facilitate analysis of real samples, gingerol species were extracted from commercially available crushed ginger. 1.0 g of sample was weighed (unless otherwise stated) and placed into a 15 mL centrifuge tube. 5 mL of ethanol was added as a solvent and the sample was vigorously shaken by a vortex mixer for 1 minute. The tube was then sonicated in the range of 0 – 20 minutes placed in an ultrasonic bath, and then the mixture was centrifuged at 4000 rpm for 10 minutes to remove solids. The supernatant was carefully collected.

3.2.4 Analytical procedure

A stock standard solution of 6-gingerol (2 mM) was prepared before diluting with a 0.05 M Britton-Robinson buffer at pH 1.8 to concentration of 1, 5, 10, 15, 20, 25, 30, and 50 μM as standard working solutions.

For voltammetric characterisation experiments using the MWCNT-BPPG electrode, the electrode was immersed in a solution containing the 50 μM 6-gingerol in a 0.05 M Britton-Robinson buffer at pH 1.8. In order to adsorb the 6-gingerol onto the electrode surface, the electrode was held at open circuit for one minute in the well-stirred solution. The electrode was then gently rinsed with deionised water and

transferred to the blank Britton-Robinson buffer solution at pH 1.8 for voltammetric analysis.

In order to investigate the influence of the scan rate on the voltammetric response of the gingerol, a 100 μM solution of 6-gingerol was used and analysed using the same procedure as discussed above. Note that, as will be seen later, for the voltammetric analysis two (or more) voltammetric cycles were performed as there is irreversible chemical change induced as a result of the fast scan, leading to reversible, and reproducible voltammetry on the second and subsequent scans.

For real sample analysis, extracts were diluted with 0.05 M Britton-Robinson buffer solution at pH 1.8 until the voltammetric response fell within the linear detection range (the dilution factors used were 25, 50, 100 and 200 for 0.25 g, 0.50 g, 0.75 and 1.0 g, and 2.0 g respectively). The detection of gingerol in the real sample was carried out by a standard addition method. The final standard solution concentrations of 6-gingerol in the diluted real sample solutions is 5, 10, 15, and 20 μM. The electrode was immersed in the solution and allowed to accumulate under stirring for one minute at the open circuit potential. The voltammetric analysis of the real sample was then recorded at a scan rate of 100 mV s^{-1}.

3.3 Results and discussion

In the following, first, the voltammetric response of 6-gingerol is investigated and characterised in Section 3.3.1. As discussed previously 6-gingerol is the predominant aromatic compound present in ginger providing its pungency and is used here as a model compound to characterise the behaviour of the wider family of species present in real samples containing the 2-methoxyphenol moiety. Second,

following the initial investigation of the electrochemical behaviour, in Section 3.3.2, the electrochemical redox response is evidenced to proceed via surface-controlled processes. Third, in Section 3.3.3, the accumulation time is optimised and the adsorption of 6-gingerol on the electrode surface is investigated. Next, the analytical performance of the modified electrode towards 6-gingerol is studied (Section 3.3.4). Finally in Section 3.3.5, the extraction procedure of 6-gingerol from a real sample is optimised, followed by the use of the developed electrochemical detection to quantify the 6-gingerol and other structurally related 2-methoxyphenol content in a real sample.

3.3.1 Voltammetric characterisation

The cyclic voltammetric response and electroactivity of 6-gingerol was initially explored at a bare BPPG electrode. In order to characterise the voltammetric profiles, 50 μM of 6-gingerol was adsorbed on the bare-BPPG electrode under open circuit conditions for one minute. Subsequently the oxidative voltammetric response of the electrode was recorded. The oxidative scan was started at 0.0 V and was initially scanned anodically to +1.2 V at which point the scan direction was subsequently reversed and the potential returned to 0.0 V. After the first scan (dashed line) a second (solid line) voltammetric cycle was recorded, the results of which are shown in Figure 3.2(A).

On scanning the first oxidative scan (dashed line) of the bare BPPG electrode a clearly defined peak is observed a peak at +0.68 V vs. SCE with peak current *ca.* 0.94 μA labelled as peak I. In the absence of the adsorption of 6-gingerol no voltammetric peak was observed as shown in the inlay of Figure 3.2(A). Upon reversing the scan direction from +1.2 V to 0.0 V, a reductive peak is observed at +0.37 V (peak II) with a

peak current of *ca.* 0.44 μA. On the second scan a new oxidative peak at +0.43 V is observed and labelled peak II' and a corresponding reductive peak recorded at +0.37 V with peak currents of 0.42 μA and 0.44 μA respectively. Notably on the second scan peak I is found to be absent. The voltammetric wave shapes associated with the redox processes indicates that the electroactive species and intermediates are surface bound; this will be further evidenced later in this chapter.

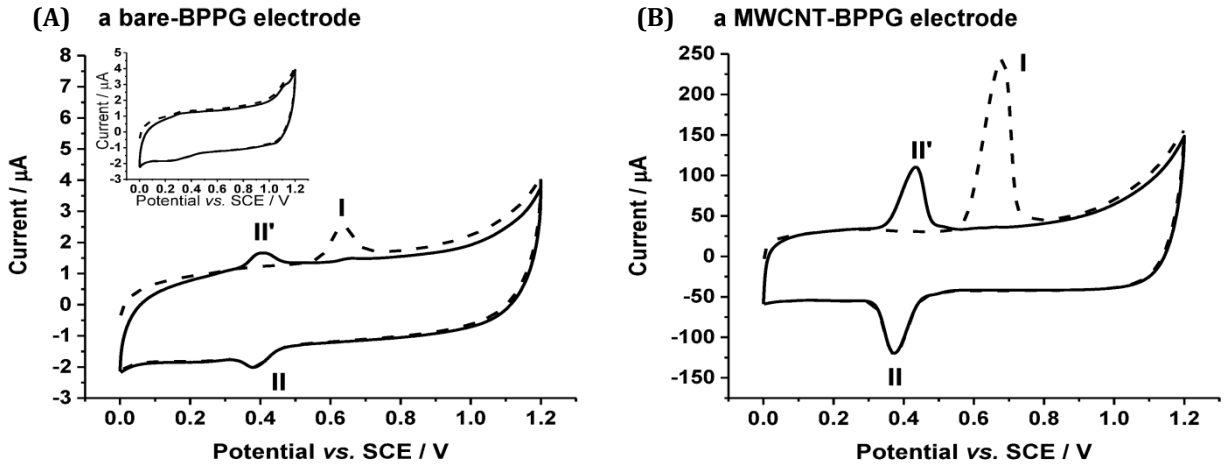

Figure 3.2 The overlaid first (dashed line) and second (solid line) cyclic voltammograms for the adsorptive stripping voltammetry of 50 μM 6-gingerol on (A) a bare-BPPG electrode and (B) a MWCNT-BPPG electrode recorded in a 0.05 M Britton-Robinson buffer solution pH 1.8, after open-circuit accumulation for 1 minute; scan rate 100 mV s^{-1}. Inset (A): cyclic voltammograms for no adsorption of 6-gingerol on a bare-BPPG electrode.

In order to seek to enhance the sensitivity of the voltammetric response towards the presence of gingerol, a BPPG modified electrode with multiwalled carbon nanotubes (MWCNT-BPPG) was investigated. The modified electrode was immersed into a 50 μM solution of 6-gingerol under open circuit conditions for one minute to allow the adsorption of 6-gingerol on the electrode surface. The voltammetric analysis was then recorded at a scan rate of 100 mV s^{-1}. The results shown in Figure

3.2(B) illustrate qualitatively similar cyclic voltammograms, however the magnitude of the voltammetric responses is very significantly enhanced as compared to the bare electrode. As measured from the peak currents of the peaks I, II, and II', the voltammetric signal on the MWCNTs is approximately 200 times larger. This distinct enhancement of peak heights when using the MWCNT-BPPG electrode is ascribed to the larger surface area of the modified BPPG electrode with MWCNT. The surface area of the modified electrode which was *ca.* 20 cm^2 as estimated from the amount of MWCNTs dropped on the BPPG electrode (Appendix A1) while the surface area of bare electrode was *ca.* 0.16 cm^2 which gives a ratio of surface areas of the same order of magnitude as the observed sensitivity difference of *ca.* 200. Consequently, all further experiments are reported on the MWCNT-BPPG electrode.

Turning attention to the electrochemical oxidation/reduction mechanism of 6-gingerol, the first cycle shows oxidation peak I at +0.68 V. In light of the literature on the oxidation of 2-methoxyphenol moieties[29], this peak is ascribed as being due to the oxidation of the 2-methoxyphenol substructure in the 6-gingerol (compound A in Scheme 3.1). On the reverse scan of the first cycle, the reduction peak II was observed at +0.37 V which results from electron transfer to the product from the chemically irreversible hydrolysis of the intermediate cation (compound B in Scheme 3.1) which forms an o-benzoquinone moiety (compound C in Scheme 3.1).[29, 30] After the first scan, peak I is no longer observable. Accordingly on the second scan, the reversible redox reaction (at +0.43 V and +0.37 V for oxidative and reductive peaks respectively) was exclusively seen and corresponds to the reversible redox process of o-benzoquinone and catechol (compounds C and D in Scheme 3.1) couple. This process is shown in the voltammograms as peaks II and II'.[31, 32] The proposed mechanism is illustrated and summarised in Scheme 3.1. The above electrochemical

results closely mirror those found for the electrooxidation of capsaicin. Capsaicin is closely structurally related to 6-gingerol and the electrochemical response has been previously reported by Kachoosangi *et al.* [26] However a notable contrast between the voltammetric responses of the two species arises upon consideration of the magnitudes of peak I and II as discussed below.

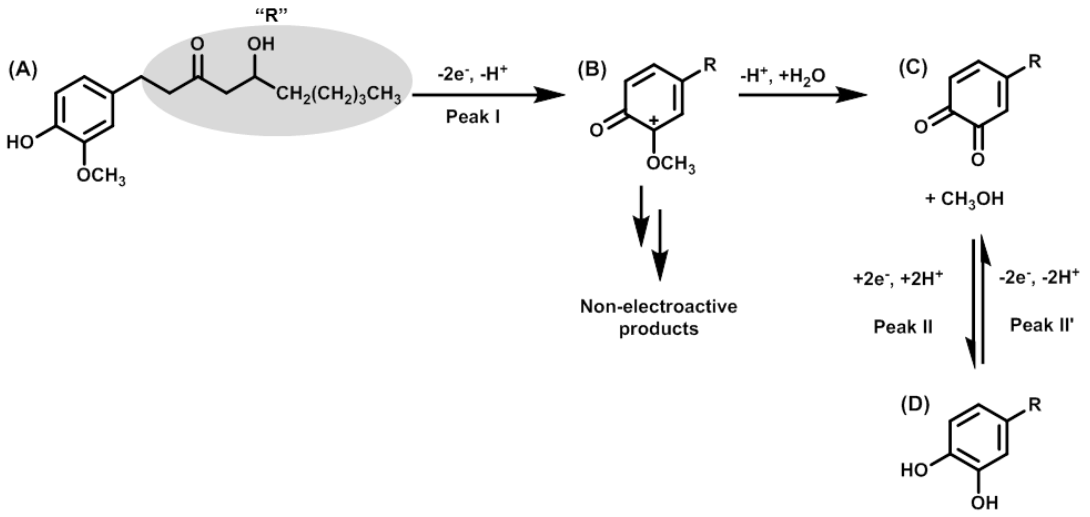

Scheme 3.1 The structure of 6-gingerol and the proposed mechanism for the electrochemical reaction of 6-gingerol.

The charge transferred during the voltammetry of 6-gingerol was studied by integration of the peak areas of peaks I and II from the adsorptive stripping voltammogram of 50 μM 6-gingerol measured after a 1 minute accumulation time. The charge transferred in peaks I and II was *ca.* 204 μC and 56 μC respectively. Hence, the ratio of peak I and II was found experimentally to be approximately 3:1. To enable direct comparison of these results with the electrochemical response of capsaicin, we conducted analogous experiments to those described above with capsaicin. In contrast, the peak areas for peaks I and II from redox reaction of capsaicin were found to be close to unity *ca.* 116 μC for peak I and *ca.* 101 μC for peak II. These results indicate that in the case of adsorbed capsaicin the oxidative product of peak I

is almost completely converted to the o-quinone species. Comparatively, from the result of 6-gingerol, we conclude that upon formation of the cation (compound B in Scheme 3.1) a second competing pathway exists in parallel to the irreversible hydrolysis reaction leading to the formation of the o-benzoquinone moiety. Moreover the products of this competing pathway are not electroactive in the electrochemical window being recorded since no other voltammetric peaks are observed experimentally. This second competing pathway included in the mechanism shown in Scheme 3.1.

3.3.2 Effect of voltage scan rate

The voltammetric method used in this work is adsorptive stripping voltammetry; this technique involves the accumulation of target analyte(s) on the electrode surface prior to conducting a voltammetric stripping analytical procedure. To confirm that the 6-gingerol is adsorbed on the MWCNT-BPPG electrode, the voltammetric response of the peaks II and II' were studied as a function of scan rate. The cyclic voltammograms were recorded in a 0.05 M Britton-Robinson buffer solution pH 1.8 at scan rates between 0.01 – 0.8 V s^{-1}. Note that before conducting this experiment the first scan was performed in each case in order to generate the redox couple prior to record the second voltammetric cycle. As shown in Figure 3.3**,** the wave shape of second scans is almost constant; however, at higher scan rates the peak-to-peak potential separation is larger. The magnitudes of the oxidative and reductive peak currents of 6-gingerol exhibit distinct deviations from linearity as plotted against the scan rate (Figure 3.3 inlay). Linearity of a voltammetric peak current with scan rate is commonly used as diagnostic for the presence of a surface bound redox process. In the present case the deviation away from linearity is likely to

predominantly reflect the non-idealities of the carbon nanotube modified electrode and the influence of uncompensated resistance of the cell that lead to voltammetric distortions (refer to section 1.5 in Chapter 1). In particular, the large capacitance of the substrate (arising from the large area) serves to distort the voltammetric response as partially reflected in the larger peak-to-peak separation observed at higher scan rates. It should be noted that integration of the redox peaks reveal the charge passed to be constant as a function of scan rate thus evidencing the surface bound nature of the redox couple.[33]

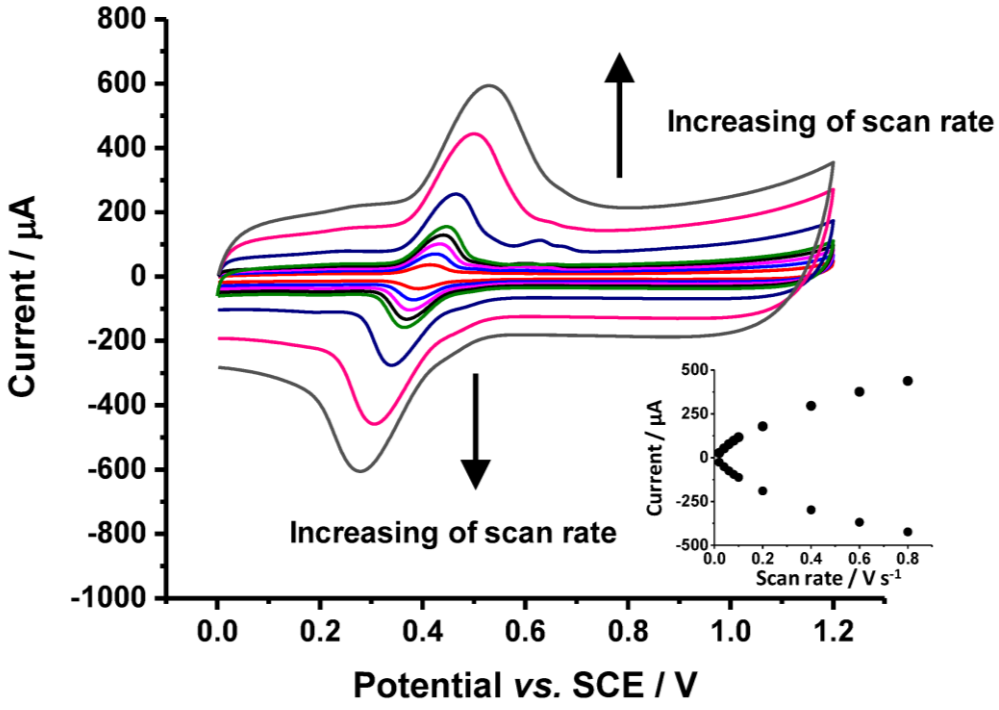

Figure 3.3 The second scans of cyclic voltammetry of 100 µM 6-gingerol on a MWCNT-BPPG electrode at varying scan rates in a 0.05 M Britton-Robinson buffer solution pH 1.8. Inset: plot of peak current versus scan rate.

3.3.3 Effect of accumulation time

Having studied the voltammetric response of the model compound 6-gingerol, the accumulation time is next optimised and the adsorption of 6-gingerol on the electrode surface is investigated. In order to optimise the accumulation time, we

performed adsorptive stripping voltammetry of 6-gingerol in the range of 10 – 100 μM at various accumulation times. The physical reasoning for the use of these different concentrations will be discussed below. The electrode was immersed in the solutions of varying 6-gingerol concentrations with accumulation times ranging from 0 to 12 minutes at an open circuit potential in the well-stirred solution. After adsorption of the analyte onto the electrode surface, the electrode was rinsed with deionised water and transferred to an electrochemical cell containing 0.05 M Britton-Robinson buffer solution pH 1.8 for voltammetric interrogation.

Figure 3.4(A) shows the plot of the responses of oxidative peak I as a function of time of adsorption 6-gingerol on the electrode surface. Considering the result from 10 μM 6-gingerol, on increasing the accumulation time from 0 to 5 minutes, the signal enhanced significantly. At longer adsorption times the peak area increases more slowly and reaches a plateau at *ca.* 8 minutes. The magnitude of this plateau region is sensitive to the concentration of gingerol in solution. Accordingly we conclude that at long adsorption times (>8 minutes) the extent of adsorption of gingerol on electrode surface is thermodynamically and not kinetically limited. As can be seen from the result, an accumulation time for 8 minutes would yield the highest sensitivity towards the presence of gingerol. However, in terms of facilitating the analytical procedure, a 1 minute accumulation time was selected for the further experiments as a compromise between a shorter analysis time and the sensitivity of the procedure.

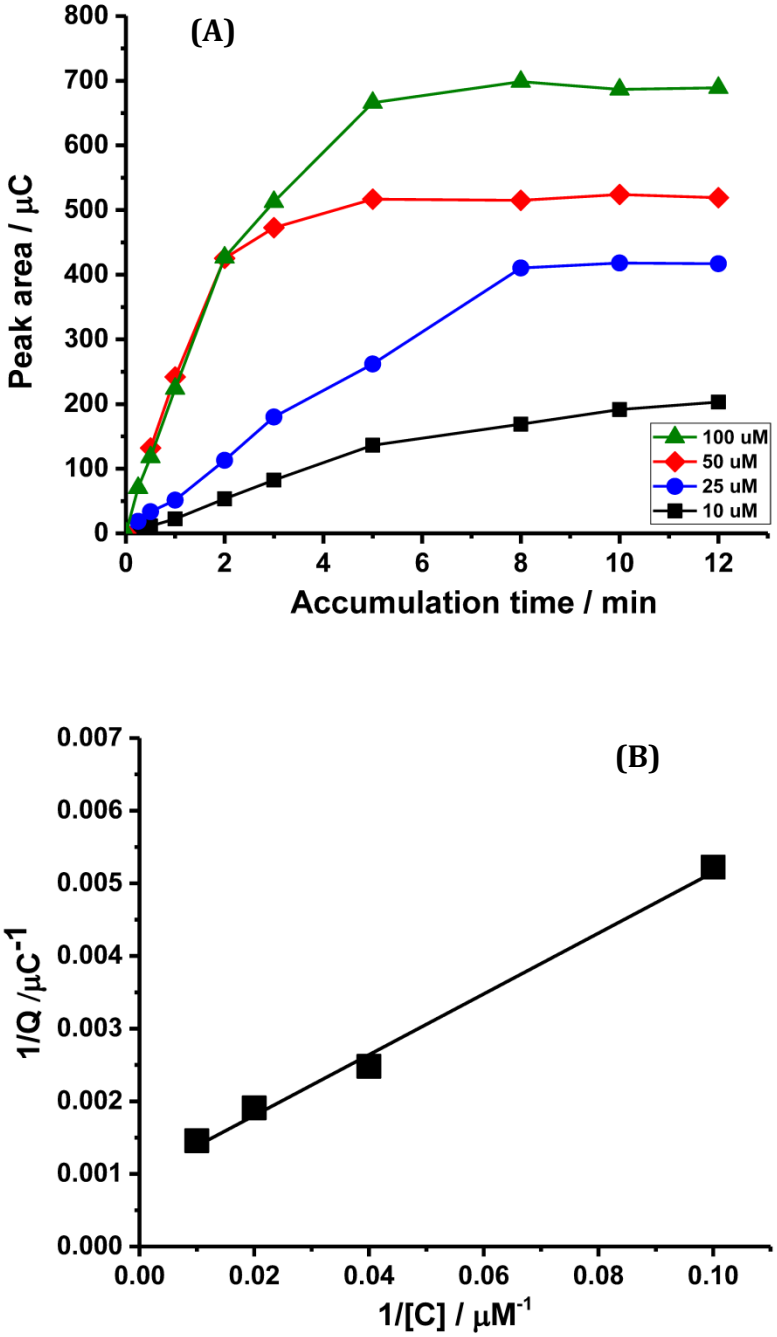

Figure 3.4 (A) The responses of oxidative peak I as a function of accumulation time in 10 µM (---■---), 25 µM (---●---), 50 µM (---◆---), and 100 µM (---▲---) of 6-gingerol. (B) The data plotted according to the linearised Langmuir isotherm.

Next the adsorption of 6-gingerol is analysed in terms of the Langmuir isotherm. The equilibrated surface coverage of the 6-gingerol is measured after 8 minutes accumulation.

Using the Langmuir adsorption isotherm, the fractional occupancy of the adsorption sites (θ) can be expressed as

$$\theta = \frac{K[C]}{1+\mathrm{K[C]}} \tag{3.1}$$

where K is the equilibrium constant which is $\frac{k_{ads}}{k_{des}}$ where k_{ads} and k_{des} are rate constant of adsorption and desorption respectively, and [C] is the concentration of 6-gingerol.[34]

$$\theta = \frac{Q}{Q_{max}} \tag{3.2}$$

where Q is the voltammetrically measured charge transferred during oxidation of the species at the concentration studied and Q_{max} is maximum charge transfer at saturation of the surface with gingerol.

Substituting equation (3.2) in (3.1) produces

$$\frac{Q}{Q_{max}} = \frac{K[C]}{1+\mathrm{K[C]}} \tag{3.3}$$

$$\frac{Q_{max}}{Q} = \frac{1}{\mathrm{K[C]}} + 1 \tag{3.4}$$

$$\frac{1}{Q} = \left(\frac{1}{\mathrm{K}Q_{max}}\right)\left(\frac{1}{[\mathrm{C}]}\right) + \frac{1}{Q_{max}} \tag{3.5}$$

The Langmuir isotherm predicts that a plot of 1/Q vs. 1/[C] should be linear. From this double reciprocal plot, the equilibrium constant and maximum charge transfer can be obtained from the slope and intercept respectively. As shown in

Figure 3.4(B), the plot is linear (R^2= 0.990) and the equilibrium constant and maximum charge transfer can be calculated *ca.* 0.023 μM^{-1} and 1035 μC respectively. Hence we conclude that the adsorption of gingerol is well-described by the Langmuir isotherm. The value of surface coverage (Γ) of the gingerol can be calculated using Faraday 1st law $\Gamma = Q/nFA$, where Q is the maximum charge transfer, n is the number of electrons (n=2), F is Faraday constant (96485 C mol^{-1}), and A is the surface area of the modified BPPG electrode (*ca.* 20 cm^2, refer to Appendix A1). The surface coverage was calculated to be *ca.* 2.7 x 10^{-10} mol cm^{-2} (or 1.6 x 10^{14} molecules cm^{-2}) which is fully consistent with monolayer formation of 6-gingerol on the MWCNT-BPPG electrode surface.[35]

In the study of accumulation time, we used the different concentrations of 6-gingerol. From the experimental Langmuir plot, the charge transfer corresponding maximum surface coverage is calculated to be *ca.* 1000 μC. From the charge transfer obtained from 100 μM 6-gingerol, the value of *ca.* 700 μC suggests that we achieve almost the maximum coverage which expected to make the surface of electrode become saturated at the higher concentration. Therefore, the analytical range studied needs to be below 100 μM.

3.3.4 Analytical response of MWCNT-BPPG electrode

Having investigated the adsorption of the model compound 6-gingerol we turn next to investigation the analytical response and analytical performance of the modified electrode towards 6-gingerol. With regard to study the analytical performance of the MWCNT-BPPG electrode towards 6-gingerol, we further performed the adsorptive stripping voltammetry of 6-gingerol of various concentrations. The experiment was conducted by first immersing the MWCNT-BPPG

electrode in standard solutions of 6-gingerol with concentrations in the range 1 – 50 μM using the optimised 1 minute accumulation time at an open circuit potential with stirring. After adsorption of the analyte, the same procedure as above was used before commencing the voltammetric scanning step. The cyclic voltammetric response as a function of the concentration of the 6-gingerol species is depicted in Figure 3.5. Notably, the small peak II' present on the overlaid voltammograms appears due to the repeated use of the electrode without renewal of the drop-cast carbon nanotubes. This repeated use of the electrode leads to the presence of the adsorbed o-benzoquinone and catechol couple from the previous experiment. In order to investigate the effect of repeatedly using the same MWCNT-BPPG electrode, the adsorptive stripping voltammetry of 50 μM 6-gingerol obtained using a fresh modified electrode was compared to that obtained using the electrode which has been used for three voltammetric scans. The peak areas of the oxidative peak I were investigated and compared. A *ca.* 5% difference in the charge transferred was observed. Therefore, the result indicated that there is no significant effect on the charge transferred of peak I that we use to quantify gingerol and related species. The inset depicts the calibration plot which is using the response of oxidative peak I of the first scan. The MWCNT-BPPG electrode reveals a linearity range of 1 - 50 μM (Q/μC = 2.97± 0.07[6-gingerol] (μM) – 1.05 ± 0.67 (μC), N=8, R^2 = 0.995). Using this procedure the limit of detection and limit of quantification were 0.21 and 0.71 μM respectively. The limit of detection was calculated based on 3σ/s and the limit of quantification was calculated based on 10σ/s where σ is the standard deviation and s is the sensitivity of the calibration curve.[36]

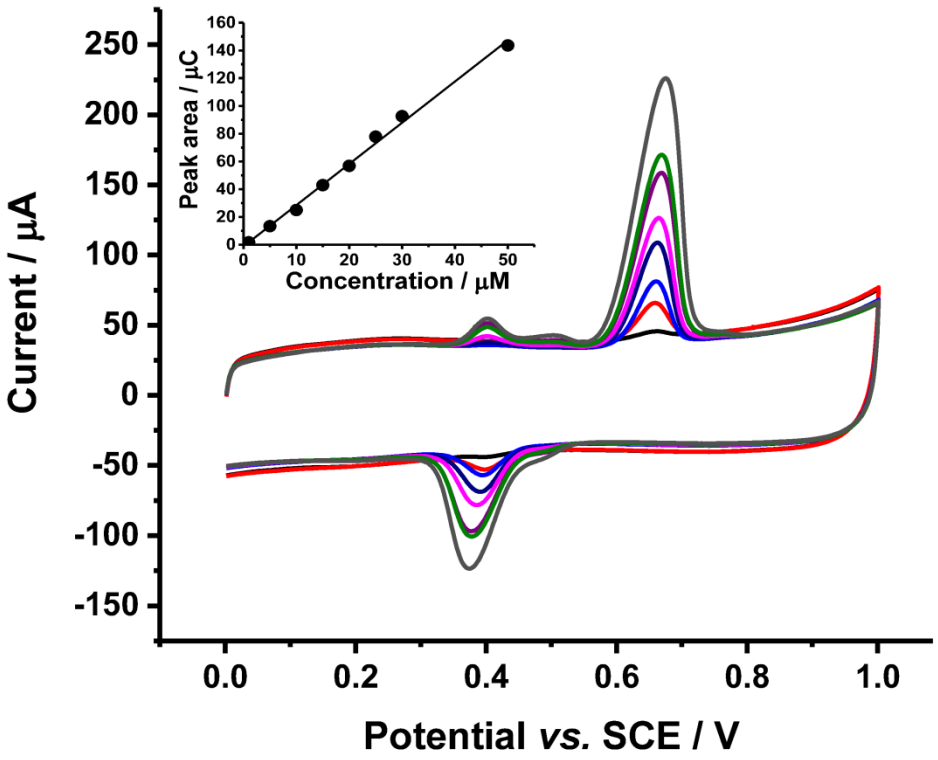

Figure 3.5 Adsorptive stripping cyclic voltammetric responses (first scans) of a MWCNT-BPPG electrode to increasing 6-gingerol concentrations from 1 to 50 µM in a 0.05 M Britton-Robinson buffer solution pH 1.8, after open-circuit accumulation for 1 minute; scan rate 100 mV s^{-1}. *Inset*: the corresponding calibration curve plot using the oxidation peak (I).

3.3.5 Analysis of a real sample on MWCNT-BPPG electrode

In order to assess the applicability of the method for the determination and quantification of the presence of the gingerol related species in a real sample, we first investigated the method for extraction of the analytes from a sample of ginger purchased from a local supermarket. In recent years, there have been various reports on extraction methods to obtain gingerol from ginger such as reflux[37], high-pressure Soxhlet extraction[38, 39] and ultrasonic extraction.[39-41] Among these mentioned methods, ultrasonic extraction is suggested to be the most rapid and simple technique in comparison with the other mentioned techniques. Moreover, it has been reported that gingerol species was converted to shogaol which is also pungent

compound in ginger at 80°C.[42] For reflux and high-pressure Soxhlet extraction, the process heats the solvent to boiling temperature which is equal to or higher than 80°C.[43] On the other hand, the heat caused by sonication is far less than that temperature (*ca.* 30°C measured from the experiment). Therefore, we selected ultra-sonication to extract the real sample in our work. The extraction procedure as fully described in experimental Section 3.2.3 was used. The extraction used the commercially available crushed ginger as purchased without any further processing prior to addition of the ethanol followed by mixing the sample and solvent using a vortex mixer. We studied the extracted yield at various sonication times which were 0, 5, 10, and 20 minutes. Note that 0 minute means that the sample was mixed with ethanol using a vortex mixer without sonication. The result showed that the concentration of gingerol related species from each sonication time was found in the range of 483 - 587 μM in the extracted solvent which was in the same range even with 0 minute sonication time, as shown in Figure 3.6(A). Although the result showed a slight decrease in the concentration of gingerol related species with time, the value still lie in the same range of the detection. From this result, we inferred that we can simplify the extraction method from using the sonication assisted extraction by simply shaking the sample with selected organic solvent, ethanol. The simplified extraction procedure we obtained consists of two steps which are mixing the samples with ethanol on a vortex mixer for 1 minute and centrifuge to remove solids. In the following experiment the simplified extraction method was used for the further extractions of a real sample.

Having simplified the extraction procedure we next turn to quantify the concentration of gingerol and related species in a real ginger sample. In order to determine the amount of analyte in the real sample, the mass of crushed ginger used

during the extraction process was varied from 0.25 g to 2.0 g. For each sample amount, three separate extractions were carried out and three repeat voltammograms were performed. The results showed that the amount of gingerol and related species extracted (μM) into the 5 mL ethanol increased proportionally to the amount of sample, as can be seen in Figure 3.6(B). We converted the concentration in extracted solvent to a concentration per a gram of sample. The concentration of gingerol related species extracted from the samples in the unit of μmol per gram of sample is illustrated in the inset of Figure 3.6(B). However, some small variation is observed between the different extractions as shown by the error bar in Figure 3.6(B). The likely cause of this variability occurs is variation in the extraction efficiency. Therefore, we further studied the extraction efficiency by multiple re-extractions from the extracted sample and calculated the extraction efficiency of the first extraction.

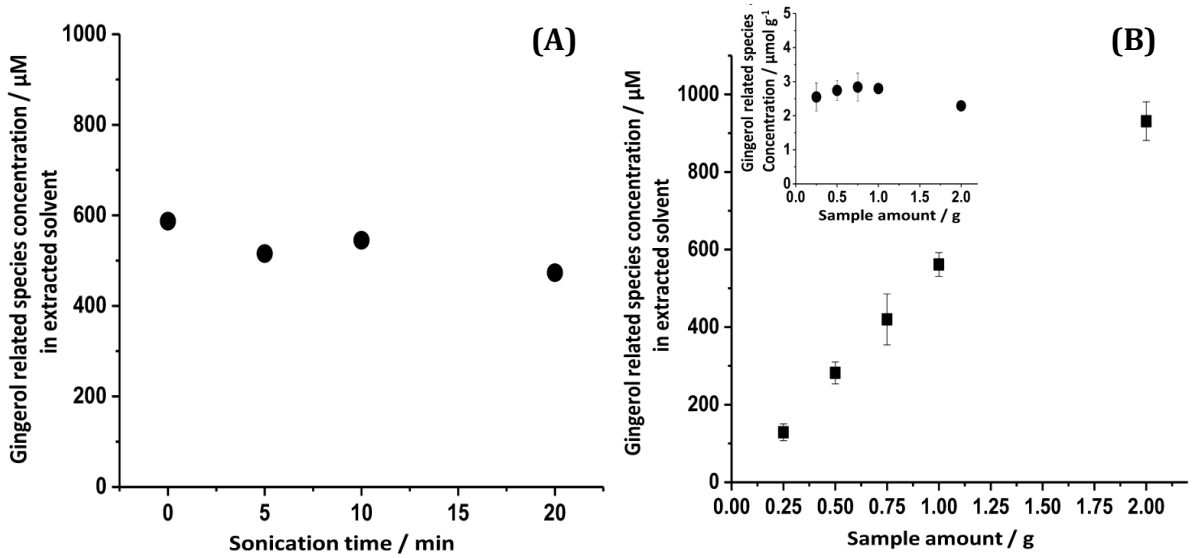

Figure 3.6 (A) Effective concentration of gingerol related species (μM) in the extracted solvent at different ultrasonic extractions time from 0 to 20 minutes. (B) Concentration of gingerol related species in the extracted solvent at different sample amounts. *Inset*: the plot of gingerol related species concentration after conversion to the concentration per gram of the sample and the amount of sample.

In order to assess the extraction efficiency of the extraction method, two sets of the experiments were performed as described next. 1.0 g of sample was weighed and placed into a 15 mL centrifuge tube. 5 mL of ethanol was added as a solvent and the sample was vigorously shaken by a vortex mixer for 1 min. The tube was then centrifuged at 4000 rpm for 10 min to remove solids. The supernatant was diluted (the dilution factor used was 100) and the voltammetric analysis was performed to quantify the concentration of gingerol related species. The extracted sample was re-extracted and quantified using the same procedure as described above. Re-extraction was conducted until the signal of sample was not observed. From the result, we calculated the extraction efficiency of the first extraction. The values obtained from the two repeated experiments were 85% and 87% extraction efficiency respectively as shown in Figure 3.7.

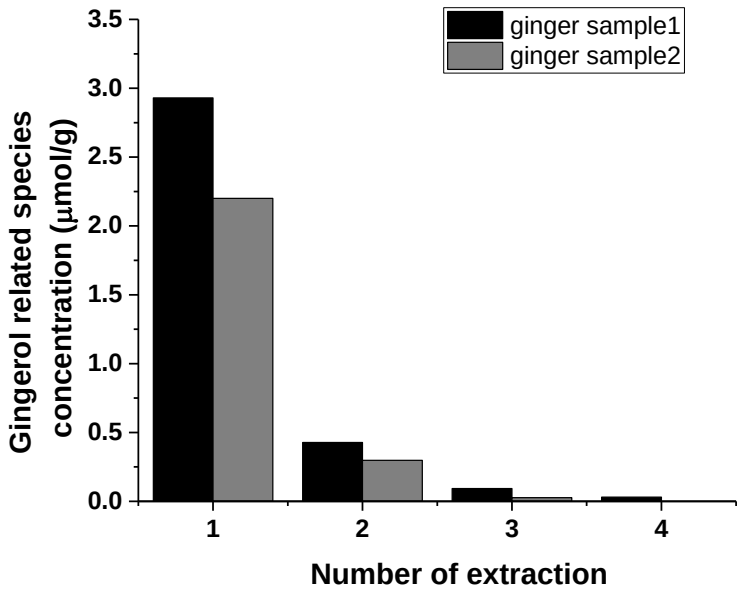

Figure 3.7 The comparison of gingerol related species (μmol g^{-1}) in ginger samples of the first extraction and multiple re-extractions of extracted ginger sample from 2 sets of extraction experiments.

The results showed that the extraction method gave *ca.* 85-87% extraction efficiency. From the result, we suggest that the variation of the result caused by the variability of different extraction efficiency. From the quantification result, we reported that the amount of gingerol related species found in the crushed ginger sample based on the first extraction was 2.64 ± 0.23 μmol g^{-1} or 0.78 ± 0.07 mg g^{-1} (n=3).

3.4 Conclusions

A MWCNT-BPPG electrode has been successfully utilised for the voltammetric determination of gingerol species in standard and real ginger samples. A good linearity range of 1 – 50 μM was obtained with a detection limit of 0.21 μM and a limit of quantification of 0.71 μM. The extraction of gingerol related species from real sample ginger can be achieved via a simple methodology using the ethanol and a vortex mixer, leading to a time saving sample preparation. To the best of the authors' knowledge, this proposed method is the first reported electrochemical method using for the detection of gingerol species. This fast and facile method of detection will be useful towards application in quality control of ginger products in the food industry.

Bibliography

1. K. Chaisiwamongkhol, K. Ngamchuea, C. Batchelor-McAuley and R. G. Compton, *Analyst*, 2016, **141**, 6321-6328.
2. A. H. Rahmani, F. M. A. Shabrmi and S. M. Aly, *International Journal of Physiology, Pathophysiology and Pharmacology*, 2014, **6**, 125-136.
3. V. A. Parthasarathy, Chempakam, B., Zachariah, T. J., *Wallingford: CABI* 2008.
4. C. C. Chen, M. C. Kuo, C. M. Wu and C. T. Ho, *Journal of Agricultural and Food Chemistry*, 1986, **34**, 477-480.
5. H. B. Heath, *New York: Van Nostrand Reinhold* 1981.
6. D. W. Connell and M. D. Sutherland, *Australian Journal of Chemistry*, 1969, **22**, 1033-1043.

7. M. Thomson, K. K. Al-Qattan, S. M. Al-Sawan, M. A. Alnaqeeb, I. Khan and M. Ali, *Prostaglandins Leukotrienes and Essential Fatty Acids*, 2002, **67**, 475-478.
8. H. Y. Young, Y. L. Luo, H. Y. Cheng, W. C. Hsieh, J. C. Liao and W. H. Peng, *Journal of Ethnopharmacology*, 2005, **96**, 207-210.
9. K. L. K. Koo, A. J. Ammit, V. H. Tran, C. C. Duke and B. D. Roufogalis, *Thrombosis Research*, 2001, **103**, 387-397.
10. S. K. Katiyar, R. Agarwal and H. Mukhtar, *Cancer Research*, 1996, **56**, 1023-1030.
11. I. Stoilova, A. Krastanov, A. Stoyanova, P. Denev and S. Gargova, *Food Chemistry*, 2007, **102**, 764-770.
12. Y. Masuda, H. Kikuzaki, M. Hisamoto and N. Nakatani, *BioFactors*, 2004, **21**, 293-296.
13. R. Nicoll and M. Y. Henein, *International Journal of Cardiology*, 2009, **131**, 408-409.
14. I. Lete and J. Allué, *Integrative Medicine Insights*, 2016, **11**, 11-17.
15. P. L. Palatty, R. Haniadka, B. Valder, R. Arora and M. S. Baliga, *Critical Reviews in Food Science and Nutrition*, 2013, **53**, 659-669.
16. T. Vutyavanich, T. Kraisarin and R. A. Ruangsri, *Obstetrics and Gynecology*, 2001, **97**, 577-582.
17. V. S. Govindarajan and D. W. Connell, *C R C Critical Reviews in Food Science and Nutrition*, 1983, **17**, 1-96.
18. H. A. Schwertner and D. C. Rios, *Journal of Chromatography B*, 2007, **856**, 41-47.
19. X. Shao, L. Lv, T. Parks, H. Wu, C. T. Ho and S. Sang, *Journal of Agricultural and Food Chemistry*, 2010, **58**, 12608-12614.
20. S. Saha, R. M. Smith, E. Lenz and I. D. Wilson, *Journal of Chromatography A*, 2003, **991**, 143-150.
21. X. G. He, M. W. Bernart, L. Z. Lian and L. Z. Lin, *Journal of Chromatography A*, 1998, **796**, 327-334.
22. D. J. Harvey, *Journal of Chromatography A*, 1981, **212**, 75-84.
23. D. W. Connell and R. McLachlan, *Journal of Chromatography A*, 1972, **67**, 29-35.
24. J. A. Aas, A. L. Griffen, S. R. Dardis, A. M. Lee, I. Olsen, F. E. Dewhirst, E. J. Leys and B. J. Paster, *Journal of Clinical Microbiology*, 2008, **46**, 1407-1417.
25. A. Peigney, C. Laurent, E. Flahaut, R. R. Bacsa and A. Rousset, *Carbon*, 2001, **39**, 507-514.
26. R. T. Kachoosangi, G. G. Wildgoose and R. G. Compton, *Analyst*, 2008, **133**, 888-895.
27. M. J. Sims, Q. Li, R. T. Kachoosangi, G. G. Wildgoose and R. G. Compton, *Electrochimica Acta*, 2009, **54**, 5030-5034.
28. M. Siswana, K. Ozoemena and T. Nyokong, *Sensors*, 2008, **8**, 5096.
29. M. Petek, S. Bruckenstein, B. Feinberg and R. N. Adams, *Journal of Electroanalytical Chemistry and Interfacial Electrochemistry*, 1973, **42**, 397-401.
30. L. Papouchado, J. Bacon and R. N. Adams, *Journal of Electroanalytical Chemistry and Interfacial Electrochemistry*, 1970, **24**, A1-A5.
31. D. Nematollahi, H. Goodarzi and E. Tammari, *Journal of the Chemical Society, Perkin Transactions 2*, 2002, DOI: 10.1039/B106794J, 829-834.
32. D. Nematollahi and M. Rafiee, *Journal of Electroanalytical Chemistry*, 2004, **566**, 31-37.
33. R. G. Compton and C. E. Banks, *Understanding Voltammetry (2nd ed.)*, Imperial College Press, 2011.
34. P. W. Atkins and J. D. Paula, Atkins' Physical Chemistry, Oxford University Press, 2010.
35. A. Bard and L. Faulkner, *Electrochemical Methods: Fundamentals and Applications*, John Wiley & Sons, Inc, 2001.
36. D. A. Skoog, S. Crouch, D. M. West and F. Holler, *London: Brooks Cole Publishing*, 2004.
37. A. Ghasemzadeh, H. Z. E. Jaafar and A. Rahmat, *BMC Complementary and Alternative Medicine*, 2015, **15**, 1-10.
38. S. Rai, K. Mukherjee, M. Mal, A. Wahile, B. P. Saha and P. K. Mukherjee, *Journal of Separation Science*, 2006, **29**, 2292-2295.
39. P. P. Said, O. P. Arya, R. C. Pradhan, R. S. Singh and B. N. Rai, *Journal of Food Process Engineering*, 2015, **38**, 107-114.
40. H. Wohlmuth, D. N. Leach, M. K. Smith and S. P. Myers, *Journal of Agricultural and Food Chemistry*, 2005, **53**, 5772-5778.
41. E. J. Choi, K. A. Lee, B. S. Kim and K. H. Ku, *Preventive Nutrition and Food Science*, 2012, **17**, 46-52.
42. S. Ok and W.-S. Jeong, *Preventive Nutrition and Food Science*, 2012, **17**, 166-171.
43. J. Redfern, M. Kinninmonth, D. Burdass and J. Verran, *Journal of Microbiology & Biology Education*, 2014, **15**, 45-46.

Chapter 4

Electrochemical Method for the Determination and Quantification of Curcumin in Turmeric

In the previous chapter, we evidenced the use of adsorptive stripping voltammetry (AdsSV) at a multiwalled carbon nanotube modified basal plane pyrolytic graphite electrode (MWCNT-BPPG electrode) for the determination of gingerol in ginger. In this chapter, we will focus on the exploitation of the MWCNT modified electrode for determination and quantification of curcumin in turmeric again using adsorptive stripping voltammetry (AdsSV). The voltammetric behaviour of curcumin on the modified electrode is examined and AdsSV shown to be a sensitive method for quantifying curcumin. The adsorption of curcumin on the electrode surface is evidenced to follow a Langmuir adsorption isotherm. A linear response to curcumin in the range of 2–100 μM was obtained with a detection limit of 0.45 μM and a limit of quantification of 1.49 μM. For application to real samples of turmeric, a one-step sample preparation in ethanol was developed providing a simple and rapid extraction procedure. The MWCNT-BPPG electrode with AdsSV allowed the determination of the curcumin equivalent in turmeric powder sample with recoveries in the range of 92–108 %. This facile and fast method will be useful for monitoring the quality of curcumin contained in commercial turmeric products.

The work presented in this chapter has been published in *Electroanalysis,* 29, (2017), 1049-1055.[1]

4.1 Introduction

The yellow-orange pigments extracted from rhizome of turmeric (Curcuma longa L.) consist of three curcuminoids: curcumin, demethoxycurcumin, and bisdemethoxycurcumin in an approximate ratio 2:1:1.[2, 3] Among these curcumin is the main ingredient and is by far the most investigated curcuminoid due to a wide range of biological and pharmacological properties including anti-oxidant, anti-inflammatory, anti-mutagenic, and anti-cancer behaviour.[4-6] Curcumin is reported to be a significantly more effective antioxidant than demethoxycurcumin and bisdemethoxycurcumin.[7, 8] Specifically, the chemical structure of curcumin comprises of two units of 2-methoxyphenol connected by an α,β-unsaturated diketone moiety which exhibits keto-enol tautomerism as depicted in Figure 4.1. The tautomer percentages are dependent on various parameters including solvent and temperature.[9] The enol form is more energetically stable in the solid phase and in ethanolic solution.[10]

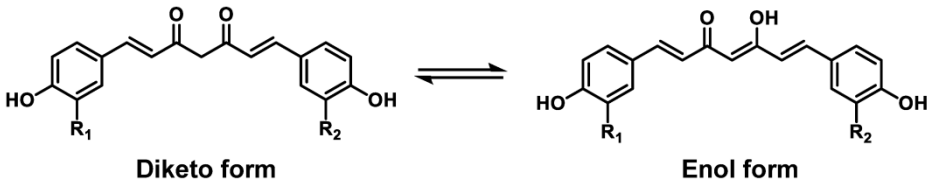

Compound	R_1	R_2
Curcumin	OCH_3	OCH_3
Demethoxycurcumin	OCH_3	H
Bisdemethoxycurcumin	H	H

Figure 4.1 Chemical structures of curcuminoids

Curcumin has a low solubility in aqueous solution and is highly unstable under basic conditions resulting from fast hydrolytic degradation to feruloylmethane and ferulic acid for example after only 5 minutes incubation in pH 8.5 phosphate buffer.[11]

The curcumin content of turmeric was found to vary depending on growing conditions, harvesting process, and extracting method.[12, 13] The percentage of curcumin content in commercially available turmeric products is reported to be between 0.5% and 5.7%.[14, 15] The content of curcumin is one of the primary factors in the quality control of commercial turmeric products.[12] Moreover, owing to the high cost of pure turmeric, turmeric powder can be, and often is, adulterated with different chemical compounds in order to mimic the appearance of curcumin. The major compounds which have been adulterated in turmeric spices are lead chromate as well as the dye metanil yellow.[13, 16-18] In October 2013, the US Food and Drug Administration (FDA) released a recall report of turmeric powder imported from one brand in Bangladesh. This recall was reportedly linked to contaminated turmeric powder with high lead levels that could cause very significant health problems to consumers. Moreover, children in a rural area in Bangladesh have been identified as having high blood lead concentrations. This lead exposure may originate from contaminated turmeric.[19]

Owing to threat of lead poisoning as well as other illnesses potentially caused by adulterated spices, food safety issues related to the possibility of contaminated turmeric powder are of concern to human health. Product quality assurance is essential including the quantification of curcumin content in commercially available turmeric products, since when the quantified amount of curcumin from the products is extremely low, we can infer that this product might be adulterated. A variety of techniques for the qualitative and quantitative analysis of curcumin has been proposed. Spectrometric methods have been employed for determination of curcumin content due to the high optical absorptivity of the compound at visible

wavelengths.[20] Another analytical method used is high-performance liquid chromatography coupled with various types of detector.[21-23] However, these methods require the use of relatively expensive instruments, complicated sample preparation steps, and well-trained personnel. Analysis via an electrochemistry based technique is potentially advantageous over the above mentioned techniques due to its simplicity, speed, sensitivity, cost effectiveness as well as possibly allowing testing outside of the laboratory. Curcumin offers an electrochemical response due to the 2-methoxyphenol moieties in the molecule. The 2-methoxyphenol moieties can be oxidised to a quinone-like structure, then this benzoquinone moiety subsequently exhibits the reversible redox behaviour typical of quinones.[24] There are several reports of curcumin detection using electrochemistry. A bare glassy carbon electrode with cyclic voltammetry was employed by Ziyatdinova *et al*.[25] and a carbon paste electrode (CPE) and hanging mercury drop electrode (HMDE) in combination with differential pulse voltammetry (DPV) were used for the detection of curcumin.[26] In these methods, they reported a low sensitivity but the electrochemical oxidation/reduction mechanism of curcumin at the electrode was not clarified. Another more sensitive electrochemical detection for the determination of curcumin was made by Daneshgar *et al*. [27] They employed carbon nanotubes or dysprosium nanowire modified carbon paste electrode in combination with fast Fourier transform square wave voltammetry (FFTSWV) but again the electrode reaction mechanism was not reported. In contrast to previous reports employing electrochemical techniques the present work in this chapter exhibits advantages in terms of the usage of simple cyclic voltammetry as well as a simple electrode modification procedure. Specifically, adsorptive stripping voltammetry is chosen to be the electrochemical tool for determination and quantification of curcumin. The

sensitivity of signal obtained from the AdsSV reflects the surface area of the electrode; hence multiwalled carbon nanotubes are a highly useful material for modifying the electrode surface owing to their extremely high surface area properties.[28]

We report an electrochemical method for curcumin detection using a multiwalled carbon nanotube modified electrode with a one-step sample preparation. The electrochemical behaviour of curcumin at the carbon nanotube modified electrode is investigated. The applicability of the developed method for detection and quantification of curcumin equivalent in a real sample of turmeric is demonstrated.

4.2 Experimental

4.2.1 Chemicals and apparatus

All chemicals were purchased at their highest available purity and were used without further purification. All solutions were prepared using deionised water at a resistivity of 18.2 MΩ cm at 25°C (Millipore, MA, USA). Curcumin was purchased from Sigma-Aldrich (St. Louis, MO, USA). The bamboo-like multiwalled carbon nanotubes (30±10 nm in diameter and 5-20 μm in length) were purchased from Nanolab (Brighton, MA, USA). The Britton-Robinson buffer solution was made using acetic acid (BDH), phosphoric acid and boric acid (Aldrich). Tesco Ground Turmeric was purchased from a local Tesco supermarket (Oxford, UK).

All voltammetric measurements were performed using an Autolab computer-controlled potentiostat uAutolab II (Metrohm-Autolab, Netherlands). The basal plane

pyrolytic graphite (BPPG, Le Carbone Ltd., Sussex, UK) electrode was prepared by securing the material inside an insulating PTFE housing with a stainless steel core for an electrical connection. A three-electrode configuration was used including a modified BPPG electrode (the preparation of the modified electrode is discussed below) as a working electrode, a platinum mesh 99.99% (Goodfellow, UK) as an counter electrode, and a saturated calomel electrode, SCE, as the reference electrode (SCE +0.244 V *vs* SHE, BASi Inc., Japan). All experiments were carried out in a Faraday cage held at a temperature of 25 ± 0.2°C.

The multiwalled carbon nanotube modified electrode was prepared by drop casting a suspension of MWCNTs in acetone onto the electrode surface. The MWCNTs were first suspended in acetone (1 mg mL^{-1}) through sonication for 10 minutes. A 20 μL aliquot of the casting suspension was dropped onto the BPPG electrode and the acetone allowed to evaporate.[29] The surface of the modified BPPG electrode was renewed between each scan. To expose a fresh surface prior to further modification with the MWCNTs, the BPPG electrode surface was renewed by polishing the surface of electrode on the sand paper P2500 and P4000 grade respectively. Subsequently, the electrode was repeatedly pressed on cellotape, and then subsequently rinsed with acetone.

4.2.2 Sample preparation

For real sample analysis, curcumin was extracted from turmeric powder prior to analysis using electrochemical detection. An aliquot of 10 mg of turmeric powder was weighed and placed into a 50 mL volumetric flask. Ethanol (unless otherwise stated) was used to make up the volume of 50 mL. The flask was shaken to mix the sample with the solvent, placed in an ultrasonic bath and sonicated for 10 minutes.

The solution was then used for electrochemical analysis without further filtration or dilution. For the optimisation of the extraction solvent, another set of samples were prepared following the procedure above but using acetonitrile in place of the ethanol. To optimise the sonication time, the sample was prepared in ethanol as described above. The flask was sonicated in the ultrasonic bath for different times between 0-20 minutes.

4.2.3 Analytical procedures

A curcumin stock standard solution of 1.00 mM was prepared before diluting to concentration of 2.0, 5.0, 10.0, 25.0, 50.0, 75.0, and 100.0 μM as standard working solutions. To prevent any possible decomposition of curcumin, all of the solution containers were wrapped with aluminium foil over the time range of experiment and kept in the dark. Note that curcumin has a low solubility in pure aqueous systems therefore pure ethanolic solutions were used.[9]

For the voltammetric characterisation experiments using a modified BPPG electrode, the electrode was immersed in a 50 μM curcumin standard solution prepared in ethanol. Adsorption accumulation was then performed under open circuit condition, with the electrode placed in a well-stirred curcumin solution for 1 minute before being gently rinsed with deionised water and transferred to the blank solution of 0.05 M Britton-Robinson buffer pH 1.8 for voltammetric analysis at a scan rate of 100 mV s^{-1}.

The effect of accumulation time was studied experimentally. The MWCNT-BPPG electrode was left in a well-stirred 50 μM curcumin solution again under open circuit conditions for different accumulation times in the range of 0-15 minutes. The

electrode was then moved to 0.05 M Britton-Robinson buffer pH 1.8. Cyclic voltammetric scans were recorded at a scan rate of 100 mV s^{-1}. For the study of the adsorption behaviour of curcumin on the electrode surface, a series of curcumin concentrations in the range of 0-1000 μM were used. The electrode was placed in the ethanol solution containing the desired curcumin concentration for 15 minutes to generate the equilibrated surface coverage. A similar procedure was used in order to record the cyclic voltammetric scans.

For the analysis of the real sample, the extracts from turmeric sample were used without dilution. The MWCNT-BPPG electrode was then immersed in the real sample matrix and allowed to accumulate at open circuit potential with stirring for 1 minute prior to commencing voltammetric analysis.

4.3 Results and discussion

In the following section, the electrochemical behaviour of curcumin adsorbed on a MWCNT-BPPG electrode is first explored. The voltammetric characterisation is reported in Section 4.3.1.1. In Section 4.3.1.2, the effect of accumulation time is studied and the adsorption of curcumin on the electrode surface is evidenced. Second, the analytical performance of the modified electrode towards curcumin detection is studied (Section 4.3.2), followed by the optimisation of real sample extraction procedure where the type of solvent and the time of sonication are optimised (Section 4.3.3). Finally, the use of the developed electrochemical detection methodology is used to quantify the curcumin equivalent in real samples of turmeric.

4.3.1 Electrochemical behaviour of curcumin on MWCNT-BPPG electrodes

4.3.1.1 Voltammetric characterisation

In order to characterise the cyclic voltammetric profiles of adsorbed curcumin, a 50 μM curcumin in ethanolic solution was employed and analyte adsorbed onto the MWCNT-BPPG electrode for 1 minute under open circuit condition. In order to record the voltammetric signal, the electrode was subsequently transferred to a 0.05 M Britton-Robinson buffer of pH 1.8. The cyclic voltammetry was scanned between +0.0 V and +1.0 V at 100 mV s^{-1}. As shown in Figure 4.2(A), on the first forward scan (solid line), a well-defined oxidative peak was observed at +0.74 V labelled as peak I and then a reductive peak (labelled as peak II) was measured at +0.45 V on the backward scan. Upon repeated cycling of forward scan (dash line), the oxidative peak I was no longer observable and was replaced by the oxidative peak III at +0.52 V. The reductive peak II at +0.45 V remained as seen on the first scan. A proposed mechanism for the electrochemical reaction of curcumin is shown in Figure 4.2(B). This is proposed on the basis of the literature reports of related molecules, especially capsaicin which ascribes the oxidative peak on the first scan to the two-electron, two-proton oxidation and the subsequent hydrolysis of the 2-methoxyphenol unit to form an ortho-benzoquinone unit (compound C Figure 4.2(B)).[30] Upon reversing the scan, the ortho-benzoquinone moiety is reduced, leading to the formation of an ortho-hydroquinone (compound D Figure 4.2(B)). Then for subsequent scanning the observed voltammetric responses correspond to the reversible redox behaviour of the ortho-hydroquinone/ortho-benzoquinone couple. As shown in the proposed mechanism, the electrochemical oxidation of curcumin involves two electrons per

one unit of 2-methoxyphenol. Therefore, the overall contribution of both parts of curcumin is a net four electron transfer. Under the investigated conditions, demethoxycurcumin can undergo a two electron oxidation process due to the single unit of 2-methoxyphenol contained in molecule while bisdemethoxycurcumin is not oxidised under our conditions.

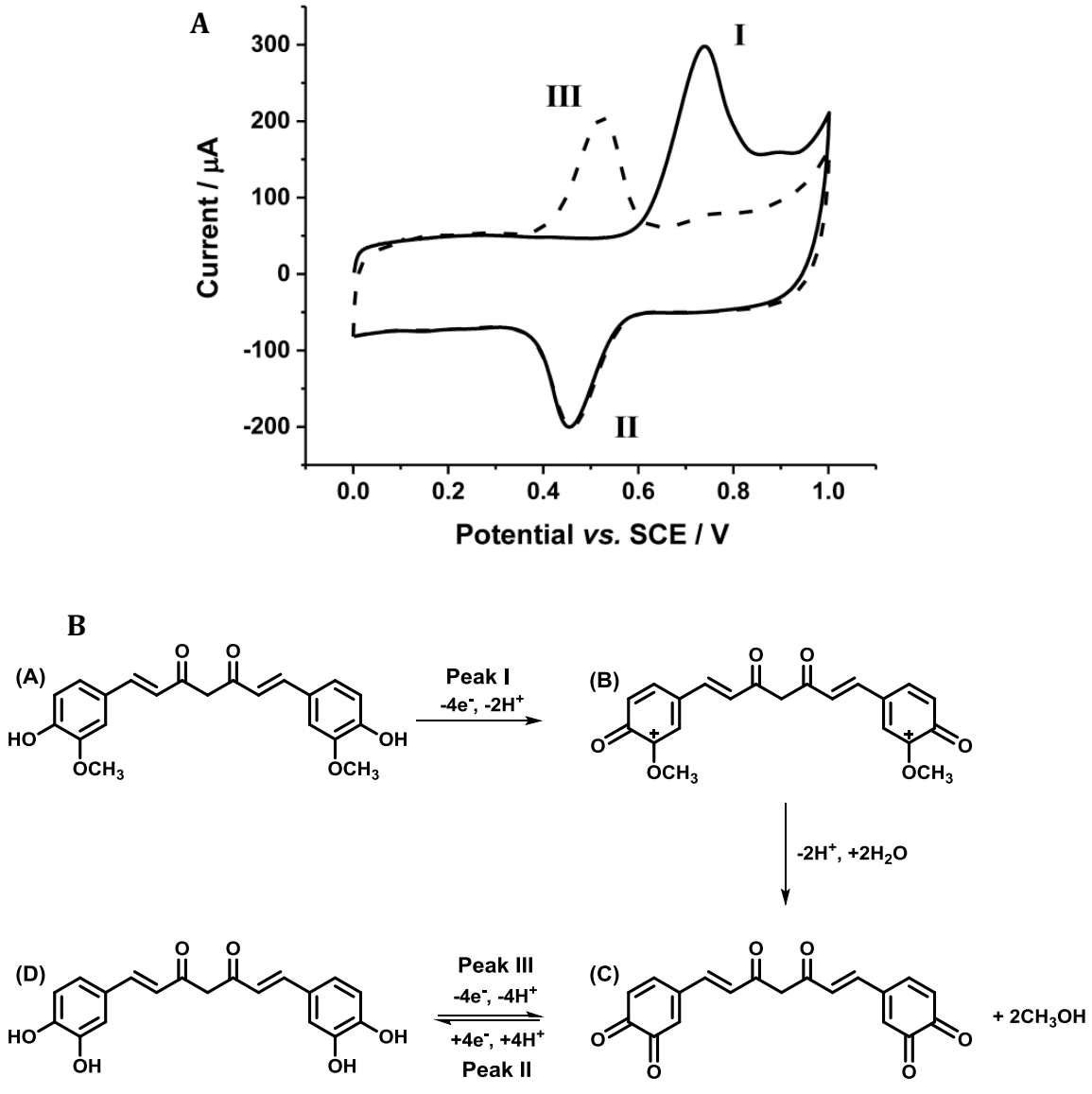

Figure 4.2 (A) The overlaid voltammetric responses of the 1st scan (solid line) and 2nd scan (dashed line) of curcumin adsorbed (open-circuit accumulation for 1 minute) on a MWCNT-BPPG electrode in 0.05 M Britton-Robinson buffer pH 1.8 at a scan rate of 100 mV s^{-1}. (B) The proposed mechanism for the electrochemical oxidation/reduction of curcumin.

4.3.1.2 Effect of accumulation time

In order to optimise the accumulation time of curcumin adsorbed onto electrode surface under open circuit conditions, the dependence of the adsorptive peak area of curcumin in 50 μM was investigated as a function of the accumulation time. The modified BPPG electrode was immersed into the standard curcumin solution for various accumulation times from 0 to 15 minutes (see section 4.2.3) and then transferred to record the voltammetric responses in 0.05 M Britton-Robinson buffer, as above.

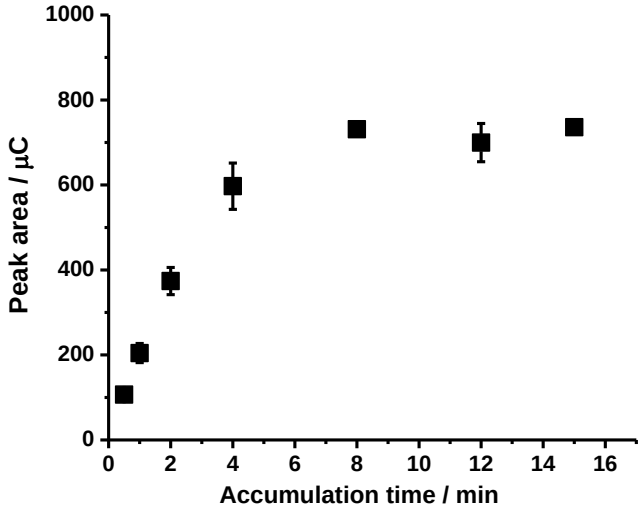

Figure 4.3 The change of oxidative peak I as a function of the accumulation time from 50 μM of curcumin.

The results are shown in Figure 4.3. The voltammetric peak area of the curcumin oxidation signal increases significantly on extending the accumulation time from 0 to 4 minutes, consistent with increased curcumin adsorption on the surface of electrode. At longer times beyond 4 minutes, the peak area enhances less rapidly and reaches a maximum plateau after *ca.* 8 minutes, indicating that the adsorbed curcumin on the electrode surface reaches saturation. To obtain the highest

sensitivity, 8 minutes accumulation therefore reports an optimal time. However, to facilitate a rapid analytical procedure, unless otherwise stated, a one minute accumulation was employed for all subsequent experiments as a compromise between high sensitivity and short analysis time.

Having explored the adsorption kinetics of curcumin onto the electrode surface, the stripping signal of curcumin was investigated as a function of the analyte concentration. Varying curcumin concentrations in the range of 0-1000 μM were used. In each case, the modified electrode was immersed in the curcumin solution for 15 minutes to allow curcumin to adsorb onto the electrode surface and to fully equilibrate. Subsequently, the electrode was placed in 0.05 M Britton-Robinson buffer to perform the voltammetric analysis.

The results of this experiment are depicted in Figure 4.4. The obtained charge transfer enhances with increasing curcumin concentration reaching a plateau at *ca.* 1000 μM curcumin. The experimental data was analysed using the Langmuir adsorption isotherm model. The general equation of the Langmuir isotherm is represented by the following equation[31]:

$$\theta = \frac{K[C]}{1+ K[C]} \qquad (4.1)$$

where θ is the fractional coverage, K is the adsorption equilibrium constant, and [C] is the curcumin concentration.

The Langmuir isotherm, Eq. (4.1), can be rearranged to obtain the following expression:

$$\frac{1}{\theta} = \frac{1}{K[C]} + 1 \qquad (4.2)$$

θ is the fractional coverage which can be calculated from the ratio $\frac{Q}{Q_{max}}$ where Q is the voltammetrically measured charge transferred during the oxidation of the surface adsorbed curcumin at the concentration studied and Q_{max} is maximum charge transfer at saturated surface with curcumin. For this experiment, the voltammetrically charge transferred during the oxidation of curcumin adsorbed at concentration of 1000 μM was measured to be *ca.* 1150 μC and this is assigned to be the maximum charge transfer.

The Langmuir isotherm predicts that a straight line should be obtained when $\frac{1}{\theta}$ is plotted against $\frac{1}{[C]}$ and the value of y-intercept should equal 1. As shown in Figure 4.4 inset, the Langmuir plot provided a good linearity (R^2 = 0.995) and interception of y-axis is close to 1 (y-intercept = 1.04±0.02). This suggests that the adsorption of curcumin from ethanol on the modified BPPG electrode likely obeys the Langmuir adsorption isotherm. The value of equilibrium constant (K) obtained from the slope of a straight-line fit was 0.041μM^{-1}. The surface of MWCNT-BPPG electrode becomes saturated at *ca.* 1000 μM curcumin concentration. The surface coverage of curcumin was calculated using Faraday's 1st law $\Gamma = Q/nFA$ where the charge (Q) was determined by integrating under the oxidative peak of 1000 μM curcumin, n is the number of electrons (n=4), F is the Faraday constant (96485 C mol^{-1}), and A is the surface area of the modified BPPG electrode (*ca.* 20 cm^2, see Appendix A1). The surface coverage was calculated to be *ca.* 1.5 x 10^{-10} mol cm^{-2} (or 9.0 x 10^{13} molecules cm^{-2}) which suggests that the curcumin forms a monolayer on the surface of MWCNT-BPPG electrode.[32] Implicit in the Langmuirian nature of the adsorption is that the latter is a reversible process where the curcumin is dissolved in ethanol. In contrast

when the electrode is transferred into water after adsorption in ethanol the curcumin remains irreversibly adsorbed.

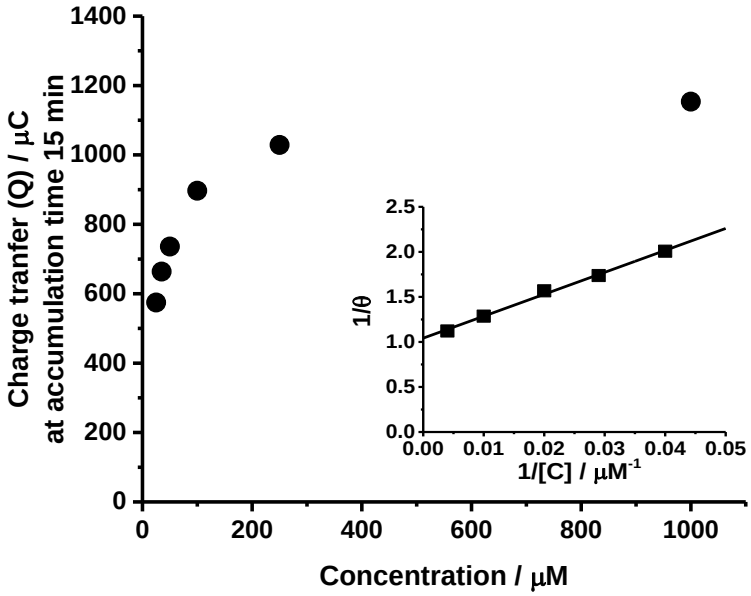

Figure 4.4 Langmuir plot showing the surface coverage against the concentration for adsorption of curcumin onto electrode surface.

4.3.2 Analytical response of the MWCNT-BPPG electrode

Having characterised the voltammetric responses of curcumin at MWCNT-BPPG electrode, optimised the accumulation time and investigated the adsorption of curcumin on the electrode surface, we next evaluated the applicability of the BPPG modified electrode with multiwalled carbon nanotubes for the analytical purposes of detecting the curcumin. The optimised accumulation time, 1 minute, was used to perform the adsorption of curcumin onto the electrode surface by open circuit adsorption. We first immersed the MWCNT-BPPG electrode to the solution of differing curcumin concentrations over the range of 2-100 μM in ethanol. The electrode was gently rinsed with deionised water and was placed in 0.05 M Britton-Robinson buffer pH 1.8 to perform the adsorptive stripping voltammetry. The

volammetric signal was recorded as a function of the curcumin concentrations as depicted in Figure 4.5. The analytical response of MWCNT-BPPG electrode towards curcumin was determined by integrating the peak area of oxidative peak of the 1st scan (peak I). As shown in the inset of Figure 4.5, the plot of peak area of curcumin oxidation peak versus curcumin concentrations revealed a linear response in the concentration range of 2-100 μM with a correlation coefficient of 0.999 (N=7). The calibration equation is Q/μC = (4.26±0.04)[curcumin](μM) – 8.53±2.41 (μC) with a limit of detection of 0.45 μM (based on 3σ/S) and a limit of quantification of 1.49 μM (based on 10σ/S) where σ is standard deviation and S is a sensitivity of calibration plot. The three repeated drop-cast modifications of the BPPG electrode with MWCNT exhibited a good reproducibility, with a relative standard deviation of less than 7%, as measured by the variation in peak area measured of 10 and 50 μM curcumin standard solutions.

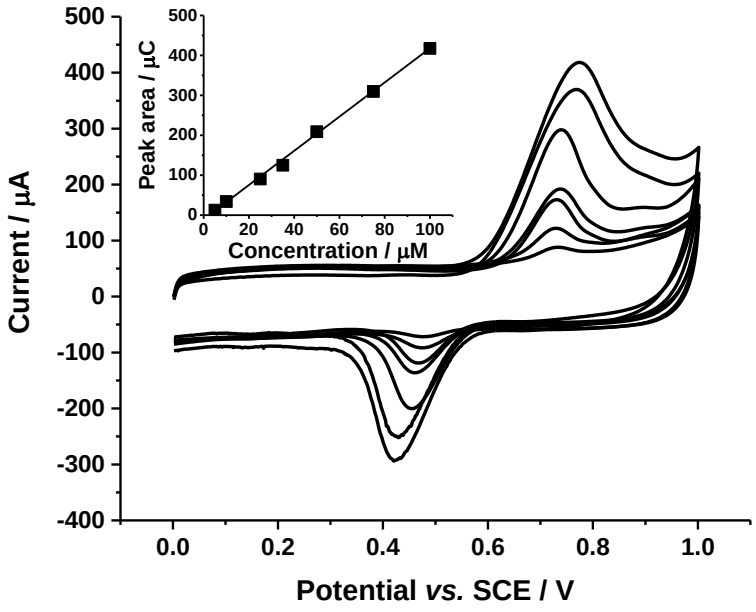

Figure 4.5 Adsorptive stripping cyclic voltammetric responses (1st scans) of a MWCNT-BPPG electrode to increasing curcumin concentrations from 2 to 100 μM in a 0.05 M Britton-Robinson buffer solution pH 1.8, after the open-circuit accumulation for 1 minute; scan rate 100 mV s^{-1}. Inset: the corresponding calibration curve plot using the oxidation peak (I).

4.3.3 Analysis of a real sample

The real sample employed in this work is in the form of turmeric powder which was purchased from a local supermarket. Finding a suitable solvent for extracting or dissolving the analyte of interest from real samples is the first step in any extraction method. Organic solvents, especially ethanol, methanol, acetone and acetonitrile, have been widely used to extract compounds from botanical and herbal samples.[33] Among these solvents acetonitrile and ethanol have been commonly used in order to extract curcumin in previous reports.[34, 35] Hence, a choice was made between these two different solvents namely acetonitrile and ethanol to select the best solvent for curcumin extraction. 10 mg of turmeric powder sample was dissolved in 50 mL of acetonitrile and ethanol separately. For each solvent, triplicate extractions were performed. After sonicating the sample mixture for 10 minutes, the extracted sample was detected directly without further filtration or dilution. The AdsSV analysis for curcumin was performed in 0.05 M Britton-Robinson buffer at pH 1.8. The efficiency of acetonitrile and ethanol on the extraction of the curcumin from turmeric powder sample was compared, where the results have been expressed as the curcumin equivalent (%w/w) of the original sample. The result are shown in Figure 4.6, it can be seen that the use of acetonitrile and ethanol resulted in 0.90±0.10%w/w and 1.02±0.08%w/w of curcumin equivalent respectively. The curcumin equivalent obtained from both solvents shows approximately similar extraction results. Although acetonitrile has been used as an extraction solvent for curcumin extraction in several previous literature reports and also gave roughly the same extraction result compared to ethanol in the present study, the toxicity of acetonitrile is a concern especially in the context of food.[36, 37] Therefore, ethanol was chosen as the extraction solvent for the further study of real samples.

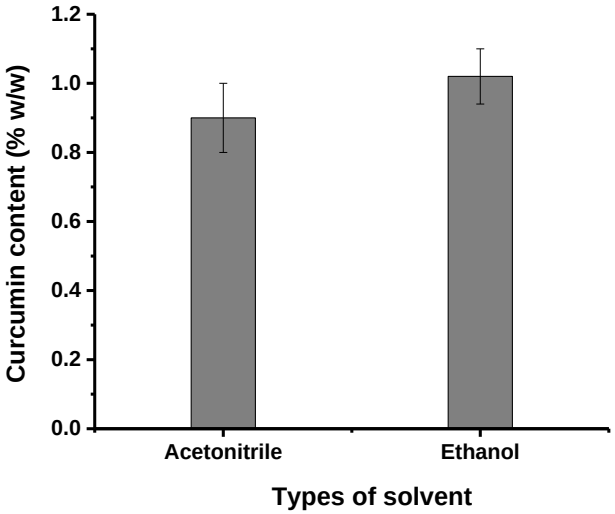

Figure 4.6 Effect of solvent on extraction of curcumin equivalent from turmeric powder sample

Having identified a suitable organic solvent we next explore the effect of sonication on the extraction efficiency. The turmeric powder sample was prepared using the procedure in experimental Section 4.2.2. We investigated the extracted efficiency at different sonication times in the range of 0-20 minute. 10 mg of the sample was weighed prior to addition of 50 mL of ethanol. The sample and solvent were mixed by shaking and then sonicated in an ultrasonic bath for the desired time period. The results are depicted in Figure 4.7 and show that the curcumin equivalent from each sonication time was found to be *ca.* 0.95%w/w - 1.02%w/w. The results show no significant difference in the curcumin extraction efficiency regardless of the sonication time. Accordingly sonication is seen to be pointless and we can simply prepare the sample prior to perform the electrochemical analysis in one step namely mixing the sample with ethanol and shaking rapidly giving a rapid extraction procedure suitable for routine sample analysis.

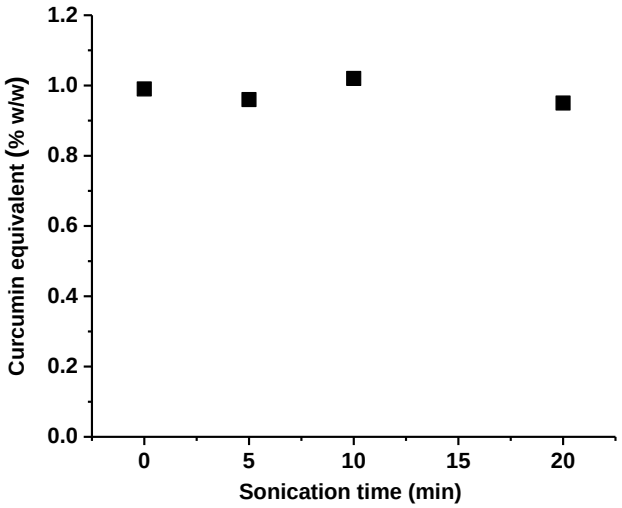

Figure 4.7 Effective curcumin equivalent (%w/w) in turmeric powder at different ultrasonic extractions time from 0 to 20 minutes.

To evaluate the practicality of the developed method, we employed the method to quantify the curcumin equivalent of the turmeric powder sample sourced from a local supermarket. Measurement of the curcumin equivalent in the sample was carried out with minimal sample preparation by simply shaking the sample with ethanol for 1 minute prior to determination of curcumin content using the developed AdsSV method. From the quantification experiment, the curcumin equivalent in sample was calculated to be *ca.* 0.99±0.08%w/w which is consistent with the values reported in the literature using HPLC techniques where the curcumin content in various types of turmeric products is reported to lie between the range of *ca.* 0.5%w/w and 5.7%w/w.[14, 15] Accuracy of the determination was evaluated from the percentage recovery of the sample.[38, 39] Different known amounts of curcumin standard solution were added to separate samples portion before AdsSV analysis. The percentage recovery was calculated based on

$$\%\mathbf{Recovery} = \frac{\mathbf{C_1} - \mathbf{C_2}}{\mathbf{C_{std}}}\mathbf{x100}$$

where C_1 is the concentration of curcumin equivalent in sample added the known amount of standard solution, C_2 is the concentration of curcumin equivalent in sample, and C_{std} is the concentration of standard solution. We found that the recoveries of our method were in the range of 92–108%, indicating good accuracy for the developed method as shown in Table 4.1. The results indicated that the method developed for the determination of curcumin equivalent in real sample using the multiwalled carbon nanotube modified BPPG electrode was accurate and feasible.

Table 4.1 Summary of curcumin equivalent determination in turmeric samples and recoveries

Sample	Original found in sample (μM)	Standard added (μM)	Total found (μM)	Recovery (%)
Extracted curcumin from turmeric powder	5.78	5	10.29±2.1	92
		25	29.37±2.6	94
		50	60.26±2.9	108

4.4 Conclusions

Adsorptive stripping voltammetry has been applied to detection and quantification of curcumin in turmeric samples using multiwalled carbon nanotube modified BPPG electrodes. The voltammetric characteristics were determined. The good linear calibration plot in the range 2-100 μM (R^2 = 0.999) was obtained. The

preparation of a real sample (turmeric powder) for analysis has been simplified to a one-step procedure. This facile, easy method of detection will be likely useful for applications in the food industry.

Bibliography

1. K. Chaisiwamongkhol, K. Ngamchuea, C. Batchelor-McAuley and R. G. Compton, 2017, **29**, 1049-1055.
2. B. Chempakam and V. A. Parthasarathy, in *Chemistry of Spices*, CABI, 2008, pp. 97-123.
3. B. B. Aggarwal and A. B. Kunnumakkara, *Molecular Targets and Therapeutic Uses of Spices: Modern Uses for Ancient Medicine*, World Scientific, 2009.
4. H. P. T. Ammon and M. A. Wahl, *Planta Med*, 1991, **57**, 1-7.
5. M. M. Naidu, B. N. Shyamala, J. R. Manjunatha, G. Sulochanamma and P. Srinivas, *Journal of Food Science*, 2009, **74**, C312-C318.
6. B. B. Aggarwal, A. Kumar and A. C. Bharti, *Anticancer Research*, 2003, **23**, 363-398.
7. Y. Z. Cai, S. Mei, X. Jie, Q. Luo and H. Corke, *Life Sciences*, 2006, **78**, 2872-2888.
8. G. K. Jayaprakasha, L. Jaganmohan Rao and K. K. Sakariah, *Food Chemistry*, 2006, **98**, 720-724.
9. S. Mondal, S. Ghosh and S. P. Moulik, *Journal of Photochemistry and Photobiology B: Biology*, 2016, **158**, 212-218.
10. R. Ravichandran, *Advances in Nanoparticles*, 2013, **2**, 51-59.
11. H. H. Tønnesen and J. Karlsen, *Zeitschrift für Lebensmittel-Untersuchung und Forschung*, 1985, **180**, 132-134.
12. J. Cheng, K. Weijun, L. Yun, W. Jiabo, W. Haitao, L. Qingmiao and X. Xiaohe, *Journal of Pharmaceutical and Biomedical Analysis*, 2010, **53**, 43-49.
13. V. S. Govindarajan and W. H. Stahl, *C R C Critical Reviews in Food Science and Nutrition*, 1980, **12**, 199-301.
14. R. F. Tayyem, D. D. Heath, W. K. Al-Delaimy and C. L. Rock, *Nutrition and cancer*, 2006, **55**, 126-131.
15. G. K. Jayaprakasha, L. Jagan Mohan Rao and K. K. Sakariah, *Journal of Agricultural and Food Chemistry*, 2002, **50**, 3668-3672.
16. S. Dhakal, K. Chao, W. Schmidt, J. Qin, M. Kim and D. Chan, *Foods*, 2016, **5**, 36.
17. V. Ashok, N. Agrawal, A. Durgbanshi, J. Esteve-Romero and D. Bose, *Analytical Methods*, 2015, **7**, 9324-9330.
18. A. M. Syed, M. Qadiruddin and A. Khan, *J. Chem. Soc. Pak*, 1987, **9**, 387.
19. K. Gleason, J. P. Shine, N. Shobnam, L. B. Rokoff, H. S. Suchanda, M. O. S. Ibne Hasan, G. Mostofa, C. Amarasiriwardena, Q. Quamruzzaman, M. Rahman, M. L. Kile, D. C. Bellinger, D. C. Christiani, R. O. Wright and M. Mazumdar, *Journal of Environmental and Public Health*, 2014, **2014**, 730636.
20. K. Sharma, S. S. Agrawal and M. Gupta, *International Journal of Drug Development and Research*, 2012, **4**, 375-380.
21. R. Hiserodt, T. G. Hartman, C. T. Ho and R. T. Rosen, *Journal of Chromatography A*, 1996, **740**, 51-63.
22. Y. Pak, R. Patek and M. Mayersohn, *Journal of Chromatography B: Analytical Technologies in the Biomedical and Life Sciences*, 2003, **796**, 339-346.
23. X. G. He, L. Z. Lin, L. Z. Lian and M. Lindenmaier, *Journal of Chromatography A*, 1998, **818**, 127-132.
24. D. Nematollahi and M. Rafiee, *Journal of Electroanalytical Chemistry*, 2004, **566**, 31-37.
25. G. K. Ziyatdinova, A. M. Nizamova and H. C. Budnikov, *Journal of Analytical Chemistry*, 2012, **67**, 591-594.
26. Z. Stanić, A. Voulgaropoulos and S. Girousi, *Electroanalysis*, 2008, **20**, 1263-1266.

27. P. Daneshgar, P. Norouzi, A. A. Moosavi-Movahedi, M. R. Ganjali, E. Haghshenas, F. Dousty and M. Farhadi, *Journal of Applied Electrochemistry*, 2009, **39**, 1983.
28. A. Peigney, C. Laurent, E. Flahaut, R. R. Bacsa and A. Rousset, *Carbon*, 2001, **39**, 507-514.
29. M. J. Sims, Q. Li, R. T. Kachoosangi, G. G. Wildgoose and R. G. Compton, *Electrochimica Acta*, 2009, **54**, 5030-5034.
30. R. T. Kachoosangi, G. G. Wildgoose and R. G. Compton, *Analyst*, 2008, **133**, 888-895.
31. P. W. Atkins and J. D. Paula, *Atkins' Physical Chemistry*, Oxford University Press, 2010.
32. A. Bard and L. Faulkner, *Electrochemical Methods: Fundamentals and Applications*, John Wiley & Sons, Inc, 2001.
33. E. S. Ong, *Journal of Chromatography B*, 2004, **812**, 23-33.
34. A. Navas Diaz and M. C. Ramos Peinado, *Journal of Agricultural and Food Chemistry*, 1992, **40**, 56-59.
35. W. Wichitnithad, N. Jongaroonngamsang, S. Pummangura and P. Rojsitthisak, *Phytochemical Analysis*, 2009, **20**, 314-319.
36. P. M. Rainey and W. L. Roberts, *The American Journal of Emergency Medicine*, 1993, **11**, 104-108.
37. R. J. Geller, B. R. Ekins and R. C. Iknoian, *The American Journal of Emergency Medicine*, 1991, **9**, 268-270.
38. G. P. Carr and J. C. Wahlich, *Journal of Pharmaceutical and Biomedical Analysis*, 1990, **8**, 613-618.
39. D. R. Jenke, *Journal of Liquid Chromatography & Related Technologies*, 1996, **19**, 737-757.

Chapter 5

Optimisation of Carbon Electrode Materials for Adsorptive Stripping Voltammetry

The previous chapter focussed on the exploitation of multiwalled carbon nanotube modified electrodes for adsorptive stripping voltammetry. In this chapter, different types of carbon electrode materials for adsorptive stripping voltammetry are studied through the use of cyclic voltammetry. Capsaicin is utilised as a model compound for adsorptive stripping voltammetry using basal plane pyrolytic graphite electrodes both unmodified and modified with multi-walled carbon nanotubes, carbon black or graphene nanoplatelets, screen printed carbon electrodes, carbon nanotube modified screen printed electrodes, and carbon paste electrodes. We compare the analytical performance of the different electrodes in terms of sensitivity and limit of detection, concluding that carbon electrodes modified with high surface area material exhibit an improvement of sensitivity. In terms of limit of detection, increasing the electrode surface area however does not improve the detection limit; the limit of detection is similar for all electrodes studied.

The work presented in this chapter has been published in *Applied Materials Today*, 7, (2017), 60-66.[1]

5.1 Introduction

The adsorptive stripping voltammetry technique (AdsSV) has found widespread application in the analytical detection and quantification of a broad range of target analytes.[2-6] It involves the accumulation of target compound(s) onto the surface of an electrode via adsorption as a first step. Once a significant surface coverage has been attained, a potential sweep is performed leading to the oxidation or reduction of the adsorbed analyte(s). Measurement of the charge (or current) from the stripping peak along with suitable calibration gives rise to the quantification of the adsorbate in bulk solution.[7] The electrochemical response of the surface-bound species is thus expected to be highly sensitive to the surface area of the electrode surface and the extent of adsorption.

Carbon electrode materials come in variety of forms and have found extensive application in electrochemical studies.[8] Generally, carbon electrodes possess advantages over other metal electrodes due to their comparatively low cost, wide range of potential windows, and high chemical stability.[9] Well-known carbon allotropes include graphite, graphene, diamond, and fullerenes all of which have been used electrodically. Among these allotropes the most common are based on the graphite structure. Surface treatment and modification are methods of considerable interest at present because they offer the chance to increase surface roughness, surface area or the number of oxygenated functional groups on the electrode surface. Methods of surface treatment include electrochemical[10], thermal treatment[11], microwave-assisted activation[12], plasma treatment[13], and modification with high surface area materials.[14] Some of the aforementioned pre-treatment carbon surface methods may lead to more irreproducible results and is outside of scope of present

work which focuses on carbon electrode materials. In this context, the modification of the surface of electrode with high surface area materials is attractive. Since several breakthrough discoveries in the synthesis and fabrication of nanocarbon materials in the last few decades, there has been increased interest in several forms of these materials including single-walled and multi-walled carbon nanotubes[15, 16], carbon black[17], nanodiamond[18-20], nanohorns[21, 22], and graphene[23, 24]. The AdsSV technique has been reported through the use of different types of carbon based electrodes in applications of electroanalysis which include the carbon materials mentioned above and carbon paste[25-27], as well as screen printed electrodes[4, 28-30]. Carbon nanotubes, rediscovered in 1991 by Iijima[31], are made from a graphite sheet rolled seamlessly, producing tubes of diameter 1-2 nm called singlewalled nanotubes (SWCNTs) whereas multiwalled carbon nanotubes are comprised of several such tubes inside each other having diameter varying from 2 to 50 nm.[32] Carbon black or nanocarbon comprises approximately spherical carbon particles, which typically form aggregates of 10 or more spheres.[33] Various synthetic routes can result in different sizes of carbon black, with primary particles available with nanodimensions.[34] Graphene nanoplatelets belong to the family of graphene materials which exhibit the advantageous properties of graphene including large surface-to-volume ratio and high electron mobility but avoid the poor stability of graphene which agglomerates or restacks via van der Waals interactions.[23, 35-37] These materials are multilayer particles typically comprising 10-30 graphene sheets.[38]

As mentioned carbon paste electrodes are widely used for AdsSV. The carbon paste electrode (CPE) in which carbon is mixed with a liquid binder to form electrodes was first reported by Adams in 1958.[39] After the preliminary report

published by Adams, a huge variety of applications have demonstrated the wide spread applicability of carbon paste electrode in the field of electrochemical analysis.[27, 40] Carbon paste electrodes are interesting due to the ease of their preparation, low background currents (compared to graphite or noble metal electrodes), easily renewed surface, and the feasibility of incorporating different substances into the paste preparation.[41]

The basic requirements for the development of electroanalytical methods include high sensitivity, low detection limit, cost effectiveness as well as ease of use. The electrochemical response from AdsSV is highly dependent on the electrode surface area, as a higher surface area often leads to an improvement of sensitivity. However, in terms of analysis the detection limit is also an important parameter. In voltammetric experiments, the detection limit is sensitive to *both* the magnitude of the faradaic and background capacitative currents.

Because of the importance of capacitance on the limit of detection, the background capacitance is as important as the Faradaic signal when assessing different electrodes. Capacitance originates from the double layer charging of an electrode and is proportional to the electroactive area of the electrode.[42] The double layer capacitance of an electrode can be simply and easily estimated from cyclic voltammograms recorded as a function of scan rate. The charging of the electrodes leads to the capacitative current obtained from the difference between the current measured from the forward and back scans. The relationship between the difference of the capacitative currents (Δi) and scan rates (ν) can be expressed as

$$\Delta i = 2AC\nu \qquad (5.1)$$

where A is the effective surface area of the electrode and C is the electrode capacitance.[43] The relationship from equation 5.1 predicts a linear plot of capacitative current against scan rate. Accordingly the capacitance can be calculated from the slope of such plots.

Kachoosangi *et al.* reported work on the adsorptive stripping voltammetry utilising multiwalled carbon nanotube (MWCNT) modified basal plane pyrolytic graphite (BPPG) electrodes and commercial MWCNT modified SPEs for the detection of capsaicin.[44] Capsaicin contains the 2-methoxyphenol moiety at which electrochemical oxidation occurs. There are several molecules containing this 2-methoxyphenol moiety structural motif for instance vanillin[45], curcuminoids[46], gingerol[47], and hesperidin.[48] In this chapter, we study the adsorptive stripping voltammetry of capsaicin using unmodified and modified basal plane pyrolytic graphite (BPPG) electrodes, screen printed carbon electrodes (SPEs), carbon nanotube modified screen printed electrodes, and carbon paste electrodes. The BPPG electrode is modified by drop-casting with multiwalled carbon nanotubes (MWCNT), carbon black (CB), or graphene nanoplatelets (GNP). Capsaicin is selected as a model system as it is generically representative of large organic molecules which are amenable to study in adsorptive stripping voltammetry on carbon electrodes and, as such, may guide the establishment of general principles. We compare the AdsSV electroanalytical detection sensitivity and limit of detection from these different electrodes and also consider the influence of electrode capacitance. Our aim is to offer guidance in the choice of type of carbon electrode for adsorptive stripping voltammetry, using the capsaicin system as a model.

5.2 Experimental

5.2.1 Chemicals and Apparatus

Capsaicin (8-methyl-N-vanillyl-6-nonenamide) was purchased from Sigma (Lancashire, UK). All solutions were prepared with deionised water of resistivity at 18.2 MΩ cm at 298K (Millipore, USA). The bamboo-like multiwalled carbon nanotubes, b-MWCNTs (30 ± 10 nm diameter, 5–20 μm length, >95% purity) were purchased from NanoLab (Brighton, MA, USA). Graphene nanoplatelets (GNP, 15 μm wide, 6–8 nm thick) were purchased from Strem Chemicals, MA, USA. Nanocarbon (diameter 27 nm ± 10 nm, Monarch 430) was purchased from Cabot Performance. Mineral oil was purchased from Aldrich. The Britton–Robinson buffer, 0.05 M at pH 1.8, was prepared using boric acid (99.5% purity, Aldrich), phosphoric acid (99.99% purity, Aldrich) and acetic acid (99.5% purity, BDH).

A basal plane pyrolytic graphite electrode (BPPGE; 4.7 mm diameter; Le Carbone Ltd, Sussex, UK) was used as a substrate for the modified electrode. A drop-casting method was used for the modification of the electrode by casting 20 μL (4 x 5 μL aliquots)[49, 50] of materials of interest dispersed in acetone (1 mg/1 mL) and then allowing the solvent to evaporate. Note that to prevent any possible evaporation of the solvent in suspensions, all of the suspensions were kept in a fridge over the time range of the experiments.

Carbon paste electrodes were prepared by mixing carbon black (diameter 27 nm ± 10 nm, Monarch 430, Cabot Performance) with mineral oil in a weight ratio of 3:2 using a pestle and mortar. The well-mixed paste was then packed in a holder

made from a Teflon rod with a 3 mm deep cavity and 4.9 mm diameter. A copper wire (not exposed to the solution) made electrical contact with the paste.

5.2.2 Analytical procedure

Electrochemical experiments were performed using a three electrode system in a Faraday cage held at 25 °C using a commercial potentiostat, uAutolab II (Metrohm-Autolab, Netherlands). The electrochemical cell was completed using a saturated calomel electrode, SCE, as the reference electrode (SCE +0.244 V vs. SHE, BASi Inc., Japan) and a platinum mesh 99.99% (Goodfellow, UK) as the counter electrode.

Experiments were conducted by first immersing the electrode (unmodified BPPG electrode, modified BPPG electrode and CPE) in standard solutions of capsaicin with concentration in the range 0.5-60 μM. The accumulation of capsaicin was performed under open-circuit potential conditions with stirring of the solution using a stirrer for 1 minute. After adsorption of the analyte, the electrode was transferred to a blank Britton-Robinson buffer solution of pH 1.8 before commencing the voltammetric scanning step.

Commercially available carbon and carbon nanotube screen printed electrodes with geometric working disc-electrode areas of 4 mm in diameter, a built-in carbon counter electrode and a Ag reference electrode were purchased from Dropsens (C-SPE (DRP-110 Lot: E0013685) and CNT-SPE (DRP-110CNT-160204)). For screen printed electrodes, the accumulation step was performed by dropping 60 μL of a desired capsaicin concentration onto the SPEs and left for 1 minute. The

electrode was then rinsed with deionised water after adsorption step, after which the electrode was allowed to thoroughly dry. A 0.05 M Britton-Robinson buffer was dropped onto the electrode surface for the voltammetric experiments.[44]

5.3 Results and Discussion

5.3.1 Characterisation of commercial screen printed electrodes (SPE) and MWCNT

Prior to their use, the morphology of (A) the commercial carbon screen printed electrode (C-SPE), (B) the carbon materials used to modify their surfaces of C-SPE (CNT-SPE) and (C) the drop casted MWCNT on C-SPE were characterised using a JEOL JSM-6500F Scanning Electron Microscope with an accelerating voltage of 5 kV using a secondary electron imaging mode. Note that SEM images in Figure 5.1 A-C were performed by Dr. Stanislav Sokolov. The carbon materials on the C-SPE, Figure 5.1A, showed a dense deposit of a nanostructured surface, whereas the CNT-SPE (Figure 5.1B) revealed a woven mesh-like of carbon nanotubes. The CNT-SPE shows a more structured surface which may offer a larger effective electrochemical surface area. To compare the morphology of carbon nanotubes on commercial screen printed electrodes and drop-cast modified electrode, MWCNT was drop-casted on the C-SPE which was again imaged using SEM. In Figure 5.1C, the SEM image of drop-cast MWCNT shows that multiwalled carbon nanotubes bundle together randomly and possess a larger tubular structure compared to the nanotubes on the CNT-SPE. The characterisation of graphene nanoplatelets (GNP) and carbon black (CB) are shown in Figure 5.1D[35] and Figure 5.1E[51] respectively.

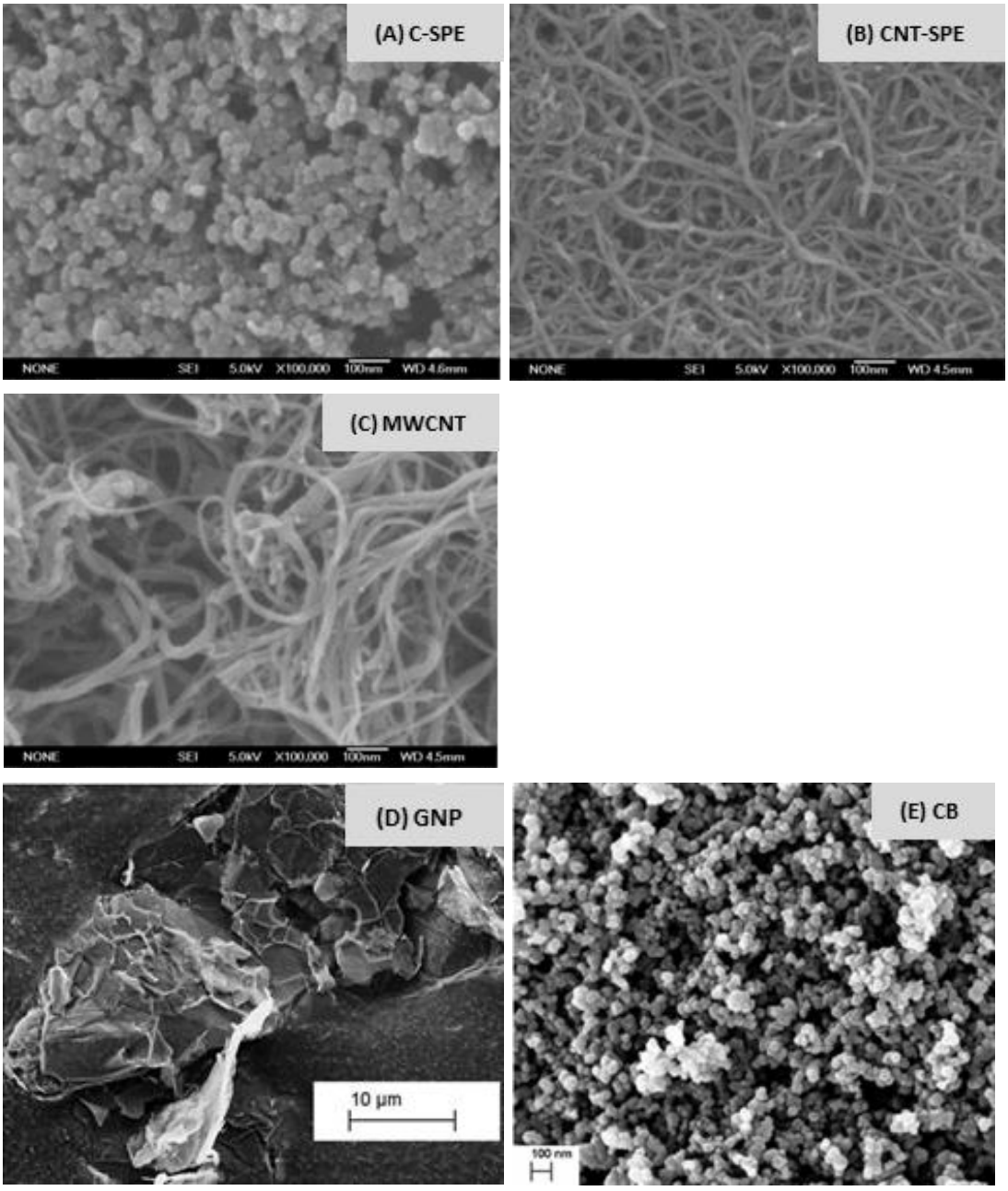

Figure 5.1 SEM images of (A) a commercial carbon screen printed electrode (C-SPE), (B) a commercial carbon nanotube screen printed electrode (CNT-SPE), (C) drop-cast multiwalled carbon nanotubes on a carbon screen printed electrode, (D) graphene nanoplatelets[35], and (E) carbon black[51].

5.3.2 Cyclic voltammetric response of capsaicin

The capsaicin system was used as a model system. Accordingly, we first illustrate and characterise the voltammetric response of capsaicin at a carbon electrode using AdsSV as shown in Figure 5.2. Capsaicin contains the 2-methoxyphenol moiety at which electrochemical oxidation of capsaicin occur which is similar to gingerol in Chapter 3 and curcumin in Chapter 4. Capsaicin was adsorbed on the MWCNT-BPPG electrode from a 50 µM capsaicin in a 0.05 M Britton-Robinson buffer at pH 1.8 under open-circuit conditions for 1 minute. Subsequently the voltammetric response of the electrode was recorded at 100 mV s^{-1}. In the first scan, the electrochemical oxidation of the 2-methoxyphenol moiety in capsaicin is coupled to an irreversible chemical step to form a molecule containing an ortho-benzoquinone unit as shown in the mechanism inset in Figure 5.2. Subsequently in the second scan peaks II and III are observed and correspond to the reversible redox process of the ortho-benzoquinone and catechol couples (C and D inset of Figure 5.2).[44] Qualitatively similar responses were seen from all the electrodes studied except where discussed.

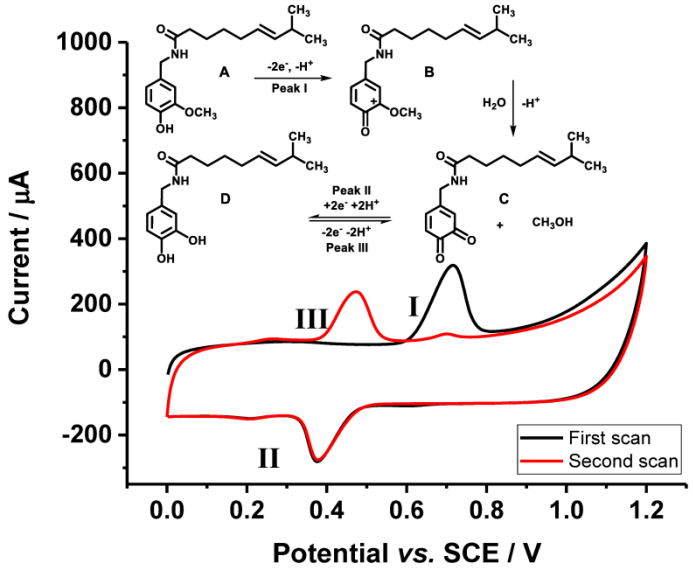

Figure 5.2 The overlaid first and second cyclic voltammograms for the adsorptive stripping voltammetry of 50 µM capsaicin on a MWCNT-BPPG electrode recorded in a 0.05 M Britton–Robinson buffer solution pH 1.8, after open-circuit accumulation for 1 min; scan rate 100 mV s^{-1}. Inset: the proposed electrochemical mechanism of capsaicin

5.3.3 Comparison of the analytical performance of each electrode

In order to compare the analytical performance of each electrode, we conducted adsorptive stripping voltammetry of capsaicin adsorbed from solutions of various concentrations. For unmodified BPPG electrodes, modified BPPG electrodes, and CPE, the experiments were performed by immersing the electrode of interest in capsaicin standard solutions with differing concentrations in the range 0.5-60 μM. The accumulation of capsaicin was performed under open-circuit potential conditions with stirring of the solution for 1 minute. Thereafter, the electrode was transferred to the buffer solution pH 1.8 before commencing the voltammetric scanning step.

The procedure was slightly modified for the SPEs, where 60 μL of the desired capsaicin concentration in the range of 1-30 μM was dropped onto the SPEs and left for 1 minute. Subsequently, the electrode was rinsed with deionised water after accumulation after which the electrode was completely dried before dropping a 0.05 M Britton-Robinson buffer solution of pH 1.8 onto the electrode. The voltammetric responses of each electrode at 100 mV s^{-1} were subsequently recorded as a function of the capsaicin concentration as depicted in Figure 5.3.

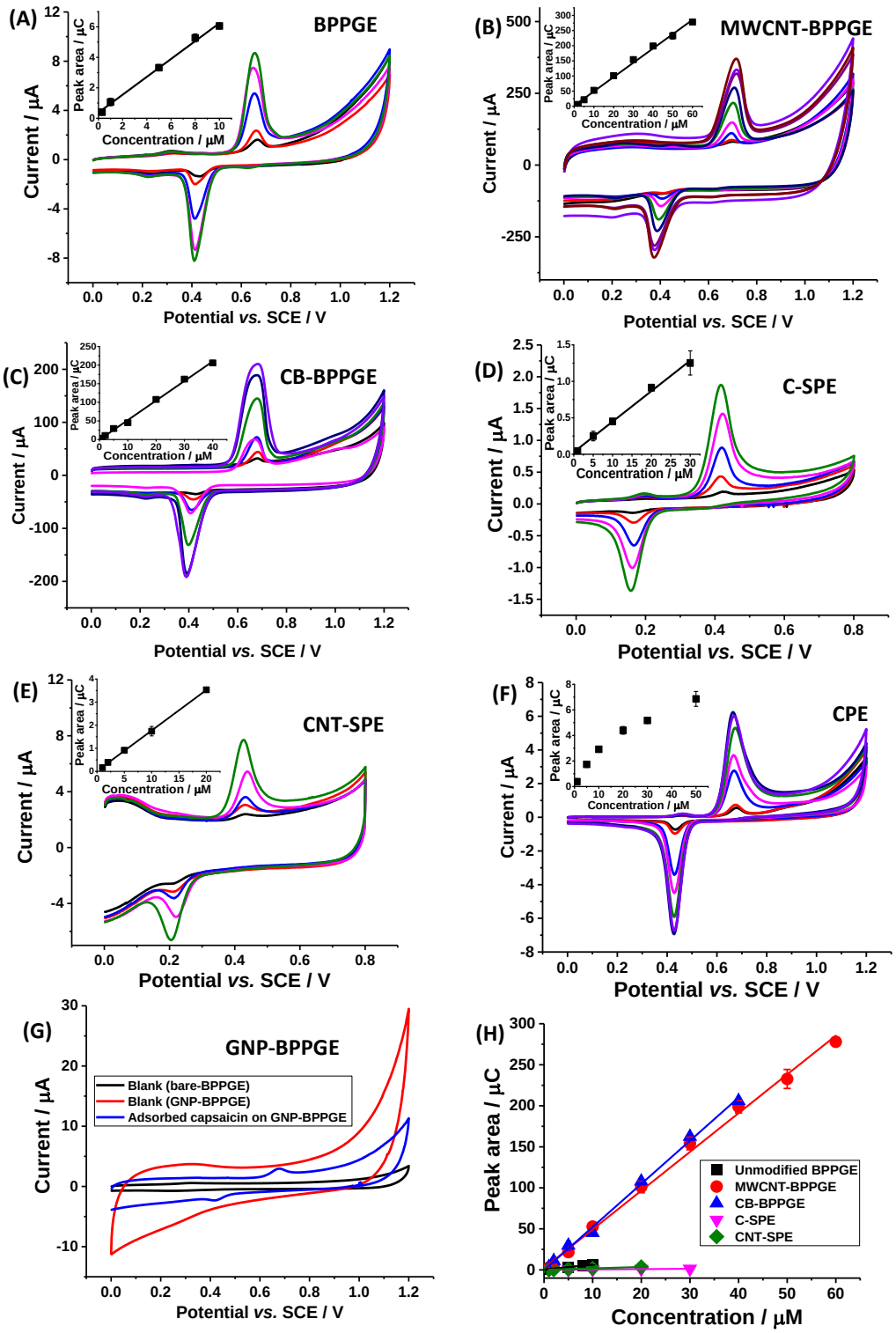

Figure 5.3 The first scans of the adsorptive stripping cyclic voltammetric responses to increasing capsaicin concentrations of (A) unmodified-BPPG electrode, (B) a drop casted multiwalled carbon nanotubes on BPPG electrode (MWCNT-BPPGE), (C) a drop casted carbon black on BPPG electrode (CB-BPPGE), (D) a carbon screen printed electrode (C-SPE), (E) a carbon nanotubes screen printed electrode (CNT-SPE), (F) a carbon paste electrode (CPE) and (G) a drop casted graphene nanoplatelets on BPPG electrode (GNP-BPPGE) at 100 mV s^{-1} in a 0.05 M Britton–Robinson buffer pH 1.8, after open-circuit accumulation for 1 min. Inset: the corresponding calibration curves plot using oxidation peak. A comparison of the corresponding calibration curves of each electrode is shown in (H).

The analytical response of each electrode towards capsaicin was determined by integrating the peak area of oxidative peak of first scan. As shown in the insets of each of Figures 5.3A-F and the summary comparison in Figure 5.3H, the plot of peak area of capsaicin oxidation peak versus capsaicin concentration shows a linear response for each electrode. From this experiment, the sensitivity was obtained from a slope of the relevant calibration plot and the limit of detection was calculated based on $3\sigma/S$ where σ is the standard deviation and S is the sensitivity of the calibration curve[52, 53]. The sensitivity and limit of detection of the different electrodes will be discussed later. In Figure 5.3A-F, a clear and well-defined oxidative peak is exhibited for all types of electrode. This is not found to be the case for the graphene nanoplatelets modified BPPG electrode (Figure 5.3G) as is discussed below.

The BPPG electrodes modified by MWCNT and CB (Figure 5.3B and C) gave a higher magnitude of the signal of the adsorptive stripping voltammetry as compared to an unmodified BPPG electrode (Figure 5.3A). As measured from peak areas of the oxidative peak from 10 μM capsaicin, the voltammetric signals on the MWCNTs and CB modified BPPG electrodes are approximately 10 times greater than from the unmodified BPPG electrode. Likewise, the screen printed electrode modified with carbon nanotubes (CNT-SPE) provides a slight larger signal which is approximately 4 times larger compared to unmodified screen printed electrode (C-SPE). Carbon paste electrodes (CPEs) also give well-defined peaks; however, there is a limited linear range from 1-10 μM which might be ascribed to the limited uptake ability of the paste at high capsaicin concentrations.[54, 55] Considering the GNPs modified BPPG electrode, we found that GNPs did not adhere well to the electrode surface and were easily lost from the BPPG electrode surface during the accumulation process. As can be seen

from Figure 5.3G, the voltammetric responses from GNP modified BPPG electrode (red line) showed a higher capacitance as compared to a bare-BPPG electrode (black line) indicated that some GNP remained on the electrode surface after drop-casting. However, after the adsorption of capsaicin on the modified electrode (blue line in Figure 5.3G) the capacitance decreased and was smaller than expected as compared to the capacitance of the GNP-BPPG electrode before adsorption of capsaicin (red line in Figure 5.3G). The oxidative peak with a small magnitude can be observed at the same potential as the other modified BPPG electrode. This observation suggests that capsaicin can adsorb onto the GNP, but is readily lost.

Next, we considered the surface area and capacitance of the different electrodes studied in this work. The surface area of each electrode was reported in terms of measured surface area or the geometric area. For the modified BPPG electrode with different forms of nanocarbon materials, the effective surface area was calculated from mass of material used in the experiment and its known size and shape (refer to Appendix A1-A3). The geometric area was used for the screen printed electrodes and the carbon paste electrodes by measurement of the diameter of the carbon surface.

In order to determine the capacitance of each electrode, cyclic voltammetry experiments of the electrode without adsorbed capsaicin was conducted in a solution containing only supporting electrolyte (0.05 M Britton-Robinson buffer). Cyclic voltammograms were recorded as a function of scan rates from 25-400 mV s^{-1}. The capacitance was determined using the relation of capacitance and scan rate shown in equation 5.1. The current amplitude difference (Δi) at a potential of 0.6 V (vs. SCE) was plotted as a function of scan rate (Appendix B). From this experiment, the linear

plots were observed passing through the origin and the capacitance of each electrode was calculated from the slope of this plot (Table 5.1). According to Table 5.1, the capacitances of the investigated electrodes were found to lie approximately in the range from 2±0.1 to 470±60 μF. The capacitance of MWCNT and CB modified BPPG electrode are found to be *ca.* 470±60 and 151±16 μF respectively which are larger than the unmodified BPPG electrodes (*ca.* 9±4 μF). Similarly, an unmodified SPE (C-SPE) exhibits a smaller capacitance than a CNT modified SPE namely 2±0.1 μF for the former and 12±3 μF for the latter. Carbon paste electrodes show a low capacitance of 6±2 μF. In terms of specific capacitance, the capacitance per unit area, for an ideal electrode this is typically in the range of 10-40 μF cm^{-2} where the capacitance is likely primarily dependent on the double-layer.[43] Table 5.1 shows that the results for the studied electrodes are roughly the same in the range of 6±1 - 96±23 μF cm^{-2}. Note that unlike true capacitors, where capacitances are independent of the voltage across them, the double layer capacitance is often a function of potential.[43]

Apart from capacitance and specific capacitance, Table 5.1 also summarises the surface area, sensitivity, and limit of detection of each type of electrode. Note that for GNP-BPPG electrodes there is no result reported in Table 5.1 due to the problem of material falling off from the electrode following drop-casting as discussed above. Considering the sensitivity, the MWCNT- and CB- modified BPPG electrodes give a higher sensitivity compared to unmodified BPPG electrode, SPEs and CPE. This distinct high sensitivity when using the MWCNT-BPPG and CB-BPPG electrode is ascribed to the larger surface area of the electrode. It indicates that the higher electrode surface area the greater the current of adsorbed analyte and so the higher sensitivity. Next turning our attention to a screen printed electrode, we compared

two types of commercial SPE namely the carbon screen printed electrodes (C-SPE) and carbon nanotubes modified screen printed electrodes (CNT-SPE). The CNT-SPE

shows a slightly higher sensitivity than C-SPE. This result suggests that a modified screen printed electrode with a high surface area resulting from the CNT surfaces improves the sensitivity. For carbon paste electrodes, the sensitivity is comparable to that obtained from the CNT-SPEs. Note that as we mentioned earlier about the limit of linear range of carbon paste electrode, sensitivity and limit of detection are calculated from the linear range of 1 to 10 μM.

Table 5.1 Summary of the surface area, sensitivity, limit of detection and capacitance of the different types of electrode modification studied

Electrode	Geometric surface area (cm^2)	Sensitivity ($\mu C\ \mu M^{-1}$)	LOD (μM)	Capacitance (μF)*	Specific capacitance ($\mu F\ cm^{-2}$)*
Unmodified BPPG electrode	0.17	0.59	0.24	9 ± 4	52 ± 21
Drop-casted MWCNT-BPPG electrode[a]	19	4.72	0.17	470 ± 60	24 ± 3
Drop-casted CB-BPPG electrode[b]	23	5.26	0.19	151 ± 16	6 ± 0.6
Drop-casted GNP-BPPG electrode[c]	27	-	-	-	-
Carbon screen printed electrode	0.13	0.04	0.20	2 ± 0.1	14 ± 3
Carbon nanotubes screen printed electrode	0.13	0.18	0.41	12 ± 3	96 ± 23
Carbon paste electrode	0.19	0.28	0.40	6 ± 2	30 ± 9

[a]multiwalled carbon nanotubes [b]carbon black [c]graphene nanoplatelets
*n=3

Next we considered the limit of detection. Most importantly the limit of detection obtained from each electrode did not vary significantly. On the basis that we mentioned earlier, the limit of detection can be improved by increasing the signal-to-background ratio. From the result, a modified electrode with a high surface area material exhibits an enhancement of faradaic signal. However, the increase of surface area of electrode is manifested in the larger background signal which is exhibited as larger capacitance values in Table 5.1. These observations indicate that the use of high surface area materials also increases the double layer capacitance. Therefore, the limit of detection does not greatly improve, at least for different carbon based electrodes in the media studied.

5.4 Conclusions

In this work, we have studied the adsorptive stripping voltammetry of capsaicin which is used as a model system to infer general principles for the optimised use of unmodified and modified carbon electrodes where large organic molecules are detected. We have evidenced two important findings with implications for the possible use of different types of carbon electrode for adsorptive stripping voltammetry. First, the magnitude of the signal of adsorptive stripping voltammetry for capsaicin on carbon electrode does not depend greatly on the form of carbon used in the experiments. However, it does depend strongly on the surface area of the materials. Second, we found that increasing the electrode surface area does not improve the limit of detection because the high surface area of electrode concurrently enhances both the adsorptive stripping signals (Faradaic signals) and the capacitance signal (background). Therefore, increasing the electrode surface area with high

surface area materials does not improve the signal-to-background ratio. Thus the limit of detection is not greatly different. In terms of choice of carbon electrode types for adsorptive stripping voltammetry, unmodified and modified BPPG electrode, SPEs and CPE do not exhibit significant differences on the limit of detection. However, in terms of improvement of sensitivity the modified electrodes show the better sensitivity in comparison to the unmodified. It is also possible to suggest in terms of cost effectiveness that carbon black can be proposed as a useful material for modification of electrode which offers similar advantages to multiwalled carbon nanotubes but at close to zero cost.[17]

Bibliography

1. K. Chaisiwamongkhol, C. Batchelor-McAuley, S. V. Sokolov, J. Holter, N. P. Young and R. G. Compton, *Applied Materials Today*, 2017, **7**, 60-66.
2. J. Wang, S. B. Hocevar and B. Ogorevc, *Electrochemistry Communications*, 2004, **6**, 176-179.
3. F. Gutiérrez, G. Ortega, J. L. Cabrera, M. D. Rubianes and G. A. Rivas, *Electroanalysis*, 2010, **22**, 2650-2657.
4. M. Moreno, A. S. Arribas, E. Bermejo, M. Chicharro, A. Zapardiel, M. C. Rodríguez, Y. Jalit and G. A. Rivas, *Talanta*, 2010, **80**, 2149-2156.
5. H. Kuramitz, S. Miyagaki, E. Ueno, N. Hata, S. Taguchi and K. Sugawara, *Analyst*, 2011, **136**, 2373-2378.
6. W. Huang, W. Hu and J. Song, *Talanta*, 2003, **61**, 411-416.
7. J. Wang, in *Analytical Electrochemistry*, John Wiley & Sons, Inc., 2006, DOI: 10.1002/0471790303.ch3, pp. 67-114.
8. R. L. McCreery, *Chemical Reviews*, 2008, **108**, 2646-2687.
9. N. Yang, G. M. Swain and X. Jiang, *Electroanalysis*, 2016, **28**, 27-34.
10. J. Wang, M. Pedrero, H. Sakslund, O. Hammerich and J. Pingarron, *Analyst*, 1996, **121**, 345-350.
11. R. Gusmao, V. Lopez-Puente, I. Pastoriza-Santos, J. Perez-Juste, M. F. Proenca, F. Bento, D. Geraldo, M. C. Paiva and E. Gonzalez-Romero, *RSC Advances*, 2015, **5**, 5024-5031.
12. X. He, Y. Geng, J. Qiu, M. Zheng, S. Long and X. Zhang, *Carbon*, 2010, **48**, 1662-1669.
13. S. C. Wang, K. S. Chang and C. J. Yuan, *Electrochimica Acta*, 2009, **54**, 4937-4943.
14. L. Agüí, P. Yáñez-Sedeño and J. M. Pingarrón, *Analytica Chimica Acta*, 2008, **622**, 11-47.
15. B. Rezaei, N. Askarpour and A. A. Ensafi, *Colloids and Surfaces B: Biointerfaces*, 2013, **109**, 253-258.
16. R. T. Kachoosangi, G. G. Wildgoose and R. G. Compton, *Analytica Chimica Acta*, 2008, **618**, 54-60.
17. T. W. B. Lo, L. Aldous and R. G. Compton, *Sensors and Actuators B: Chemical*, 2012, **162**, 361-368.
18. A. F. Azevedo, M. R. Baldan and N. G. Ferreira, *International Journal of Electrochemistry*, 2012, **2012**, 16.
19. J. B. Zang, Y. H. Wang, S. Z. Zhao, L. Y. Bian and J. Lu, *Diamond and Related Materials*, 2007, **16**, 16-20.

20. L. Chi Hian, K. J. Grehan, C. H. Goeting, R. G. Compton, J. S. Foord and F. Marken, *Electroanalysis*, 2003, **15**, 169-174.
21. N. Karousis, I. Suarez-Martinez, C. P. Ewels and N. Tagmatarchis, *Chemical Reviews*, 2016, **116**, 4850-4883.
22. F. Valentini, E. Ciambella, V. Conte, L. Sabatini, N. Ditaranto, F. Cataldo, G. Palleschi, M. Bonchio, F. Giacalone, Z. Syrgiannis and M. Prato, *Biosensors and Bioelectronics*, 2014, **59**, 94-98.
23. M. Pumera, *Chemical Society Reviews*, 2010, **39**, 4146-4157.
24. L. Wang and M. Pumera, *Applied Materials Today*, 2016, **5**, 134-141.
25. M. C. Ortiz, J. Arcos, J. V. Juarros, J. Lopez-Palacios and L. A. Sarabia, *Analytical Chemistry*, 1993, **65**, 678-682.
26. A. Radi, *Il Farmaco*, 2003, **58**, 535-539.
27. I. Švancara, K. Vytřas, K. Kalcher, A. Walcarius and J. Wang, *Electroanalysis*, 2009, **21**, 7-28.
28. O. Domínguez-Renedo, M. Calvo and M. Arcos-Martínez, *Sensors*, 2008, **8**, 4201.
29. Z. Taleat, A. Khoshroo and M. Mazloum-Ardakani, *Microchimica Acta*, 2014, **181**, 865-891.
30. P. Kanyong, S. Rawlinson and J. Davis, *Sensors and Actuators B: Chemical*, 2016, **233**, 528-534.
31. S. Iijima, *Nature*, 1991, **354**, 56-58.
32. R. R. Moore, C. E. Banks and R. G. Compton, *Analytical Chemistry*, 2004, **76**, 2677-2682.
33. A. I. Medalia and F. A. Heckman, *Carbon*, 1969, **7**, 567-582.
34. A. J. Bard, *Electroanalytical Chemistry: A Series of Advances Volume 17*, Marcel Dekker, New York, 1990.
35. J. Poon, C. Batchelor-McAuley, K. Tschulik and R. G. Compton, *Chemical Science*, 2015, **6**, 2869-2876.
36. T. Gan and S. Hu, *Microchimica Acta*, 2011, **175**, 1.
37. A. Ambrosi, C. K. Chua, A. Bonanni and M. Pumera, *Chemical Reviews*, 2014, **114**, 7150-7188.
38. A. Nieto, D. Lahiri and A. Agarwal, *Carbon*, 2012, **50**, 4068-4077.
39. R. N. Adams, *Analytical Chemistry*, 1958, **30**, 1576-1576.
40. K. Kalcher, J. M. Kauffmann, J. Wang, I. Švancara, K. Vytřas, C. Neuhold and Z. Yang, *Electroanalysis*, 1995, **7**, 5-22.
41. C. Apetrei, I. M. Apetrei, J. A. De Saja and M. L. Rodriguez-Mendez, *Sensors (Basel, Switzerland)*, 2011, **11**, 1328-1344.
42. K. Cinková, M. Clark, S. V. Sokolov, C. Batchelor-McAuley, Ľ. Švorc, R. G. Compton, Electroanalysis 2017, **29**, 1006-1013.
43. A. Bard and L. Faulkner, *Electrochemical Methods: Fundamentals and Applications*, John Wiley & Sons, Inc, 2001.
44. R. T. Kachoosangi, G. G. Wildgoose and R. G. Compton, *Analyst*, 2008, **133**, 888-895.
45. T. R. Silva, D. Brondani, E. Zapp and I. Cruz Vieira, *Electroanalysis*, 2015, **27**, 465-472.
46. D. M. Wray, C. Batchelor-McAuley and R. G. Compton, *Electroanalysis*, 2012, **24**, 2244-2248.
47. K. Chaisiwamongkhol, K. Ngamchuea, C. Batchelor-McAuley and R. G. Compton, *Analyst*, 2016, **141**, 6321-6328.
48. M. J. Sims, Q. Li, R. T. Kachoosangi, G. G. Wildgoose and R. G. Compton, *Electrochimica Acta*, 2009, **54**, 5030-5034.
49. Y. Y. Chan, A. Y. S. Eng, M. Pumera and R. D. Webster, *ChemElectroChem*, 2015, **2**, 1003-1009.
50. A. Y. S. Eng, C. K. Chua and M. Pumera, *Electrochemistry Communications*, 2015, **59**, 86-90.
51. D. Lowinsohn, P. Gan, K. Tschulik, J. S. Foord and R. G. Compton, *Electroanalysis*, 2013, **25**, 2435-2444.
52. D. A. Skoog, *Fundamentals of Analytical Chemistry*, Thomson-Brooks/Cole, 2004.
53. Y. C. Lee, in *Analytical Method Validation and Instrument Performance Verification*, John Wiley & Sons, Inc., 2004, DOI: 10.1002/0471463728.ch3, pp. 27-49.
54. R. Nissim and R. G. Compton, *Chemistry Central Journal*, 2015, **9**, 41.
55. R. Nissim and R. G. Compton, *Analyst*, 2014, **139**, 5911-5918.

Chapter 6

Origin of Oxygen Functionalities on the Surface of Carbon Electrodes

This chapter shifts the focus of this thesis to an investigation of the generation of oxygen-containing functionalities on pristine carbon surfaces. The photosensitivity of the surface modification process is studied both in the dark and under differing light conditions. The results showed the process to be light sensitive, specifically to infra-red radiation. A mechanistic route involving singlet oxygen, $^1O_2$, is proposed and evidenced.

The work presented in this chapter has been published in *Angewandte Chemie*, 57, (2018), 6270-6273.[1]

6.1 Introduction

Carbon-based materials find extensive use as heterogeneous catalysts and catalyst supports. Challengingly, significant variation in the apparent activity of these materials is found to be reported in the literature. Certainly, the presence and diversity – both in terms of identity and concentration – of trace metallic impurities is one important aspect where low amounts heavily influence the electrochemical behaviour of these materials.[2, 3] Further, the surfaces of carbonaceous materials are reactive and "aging" effects leading to differing surface functionalities are documented. A variety of surface oxo groups, most notably quinonyl, hydroxyl, and

carboxyl groups decorated on carbon electrode surface especially on the edge-plane defects have been characterised and reported.[4-7] The presence of these oxygen functionalities alter the behaviour of the material both for electron transfer[8] and provide active sites for catalysing various reactions.[9-11]

Owing to the diverse range of possible surface oxygen containing functionalities a number of mechanistic routes may contribute to their creation. Previous literature has focused theoretically on the interaction of oxygen-containing gas with model graphite structures [12, 13] and in some cases reporting experimental studies at high temperatures.[14, 15]

The route by which surface quinone and hydroxyl groups are formed is of distinct interest. Specifically triplet oxygen ($^3O_2$) is unable to directly participate in Diels-Alder cycloadditions and "ene" type reactions toward singlet state organic molecules.[16] In contrast, singlet oxygen ($^1O_2$) has long been reported to be active. In the 1960s, Foote and Wexler revealed the utility of $^1O_2$ for generating oxygenated hydrocarbons including oxygenation of cyclic dienes and polycyclic aromatic compounds to give 1,4-endoperoxides, in a reaction analogous to the Diels-Alder [4+2] cycloaddition.[17] For olefins containing allylic hydrogen atoms, $^1O_2$ reacts to give allylic hydroperoxides in which the double bond has shifted position a reaction which is analogous to the "ene" reaction.[18]

In this chapter, the mechanistic pathway and the photosensitivity of making oxygen functionality on carbon electrode surfaces under atmospheric temperature and pressure are investigated.

6.2 Experimental

6.2.1 Chemicals and reagents

All chemicals used in this work were of analytical grade and were used as received without further purification. Solutions were prepared using deionized water (Millipore) with a resistivity of 18.2 MΩ cm at 25 °C.

The working solution was prepared using 70% nitric acid to obtain 0.01 M solution. The solution of nitric acid contained 0.1M KCl as supporting electrolyte. The buffer solution were prepared using citric acid/sodium citrate for the pH range 2.5–5.0 and monosodium phosphate/disodium phosphate for the pH range 5.0–9.0. All solutions contained 0.1M KCl as supporting electrolyte. pH buffers were measured using a Hannah pH 213 pH meter with calibration using Duracal buffers (Hamilton) of pH 4.01 ± 0.01, 7.00 ± 0.01, and 10.01 ± 0.01. All pH buffers measurements were carried out in a degassed system where solutions were purged with pure N_2 gas (BOC, Guildford UK) prior to experiments for a minimum of 20 minutes.

6.2.2 Electrochemical instrument and procedure

For the cyclic voltammetry measurements a commercial potentiostat, uAutolab II (Metrohm-Autolab, Netherlands), was used and operated by GPES software. An Edge Plane Pyrolytic Graphite (EPPG) electrode with diameter of 4.0 mm was used as a working electrode throughout the study. The EPPG electrode was made from pieces of highly ordered pyrolytic graphite (HOPG) (Le Carbone Ltd., Sussex, U.K.) and was then set in custom made PTFE housing with an electrical connection made using a stainless steel core. Experiments were conducted at 25°C

within a Faraday cage by using a saturated calomel reference electrode (SCE) and a platinum wire as a counter electrode. For all experiments 100 mVs^{-1} scan rate was used.

The EPPG electrode was polished with alumina powder (Buehler) of decreasing particle size (1.0, 0.3 and 0.05 μm) to refresh surface before doing each experiment.

For the experiment of effect of ambient light study, after polishing the electrode surface, EPPG electrode was exposed to ambient air for 0, 5, 10, 20, 40, 80, and 120 minutes. Subsequently, cyclic voltammetry was recorded in 0.01 M HNO_3 (pH2) contained 0.1 M KCl. In order to study the formation of the surface redox species in aqueous solution, a fresh renewed surface EPPG electrode was immersed in solution of 0.01M HNO_3 (pH 2) for 0, 5, 10, 20, 40, 80, 120 minutes, and overnight and then rinsed with deionised water. All working electrodes were dried by nitrogen before each electrochemical measurement.

For investigation of differing lights effect, EPPG surface was refreshed before exposing to each light condition including infrared, UV, a no light control, and infrared under a nitrogen atmosphere for 0, 10, 20, 40, and 80 minutes. Then, cyclic voltammetry was performed in 0.01 M HNO_3 (pH2) supported with 0.1 M KCl.

6.2.3 Singlet oxygen generation

Singlet oxygen chemiluminescence can be generated by bubbling Cl_2 into alkaline H_2O_2 in a gas washing apparatus. An alkaline H_2O_2 was prepared by mixing 50 mL of 30%H_2O_2 and 12.50 mL of 6 M NaOH. In this work, chlorine gas is generated

by the reaction of $KMnO_4$ and conc. HCl.[19] The generated Cl_2 is directly bubbled through H_2O_2 solution to generate in situ hypochlorite followed by the generation of singlet oxygen (eq. 6.1-6.3)

$$Cl_2 + H_2O_2 \rightleftharpoons H^+ + Cl^- + HOOCl \quad (6.1)$$

$$HOOCl \rightarrow H^+ + Cl^- + O_2 \quad (6.2)$$

The Kasha and Ogryzlo groups[20] reported the red glow accompanying the OCl^- - H_2O_2 reaction that chemiluminescence was attributed to the simultaneous transition of two excited oxygen molecules [O_2, ($^1\Delta_g$)] to the ground state in a two-molecule-one photon process[21]

$$2O_2 (^1\Delta_g) \rightarrow 2O_2 (^3\Sigma_g^-) + h\nu (\sim 630 \text{ nm}) \quad (6.3)$$

From our experiments, a red glow from the reaction mixture was observed. This suggests that we can generate singlet oxygen by using this procedure. Next, the experiment to flow generated singlet oxygen onto EPPG electrode surface was set up by connecting gas from the outlet of the gas washing bottle and directly blew onto electrode surface. Note that the temperature of the reaction rises owing to the exothermic nature of the reaction therefore the reaction vessel was set up in the ice bath to cool down the reaction temperature and to prevent the condensation of water vapour onto the electrode surface.

6.3 Results and discussion

First, functionality on aged[22] edge plane pyrolytic graphite (EPPG) surface was characterised electrochemically. Figure 6.1(A) shows a typical cyclic voltammogram

(CV) in 0.01 M HNO_3 + 0.1 M KCl supporting electrolyte, with peak potentials at 0.293 V and 0.273 V *vs.* SCE for the oxidative and reductive processes.

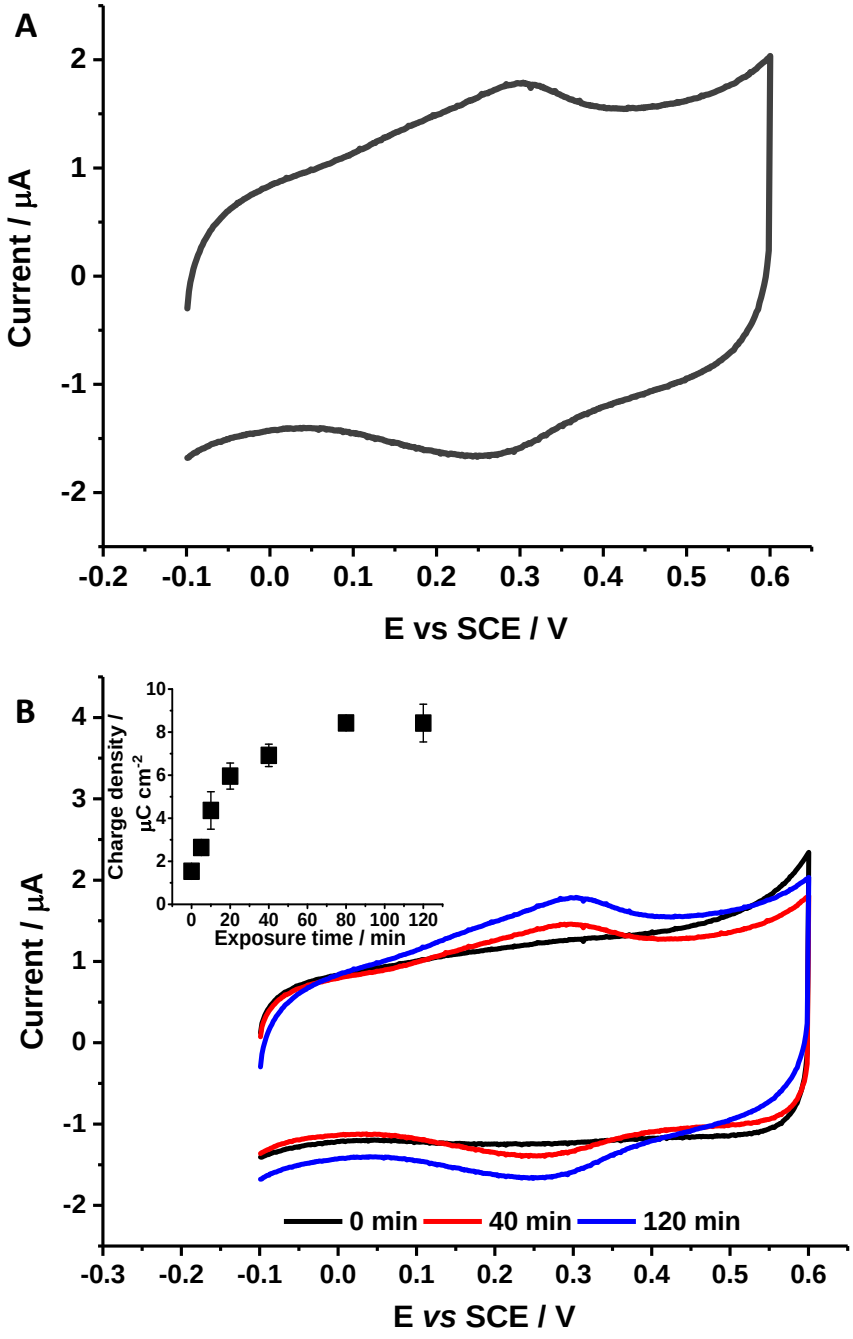

Figure 6.1 (A) Typical CV of an aged EPPG electrode and (B) CV of EPPG electrode after expose to the air for 0, 40, and 120 minutes tested in 0.01 M HNO_3 contained 0.1 M KCl as a supporting electrolyte (pH 2) at a scan rate of 100 mV s^{-1}. Inlay shows the plot of charge per unit area of the oxidative peaks as a function of exposure time (0, 5, 10, 20, 40, 80, 120 minutes). The error bars were obtained from three repeat experiments.

The EPPG electrode surface after fresh renewal was exposed to ambient conditions for 0, 5, 10, 20, 40, 80, 120 minutes. Then, cyclic voltammetry was performed in 0.01 M HNO_3 (pH 2) supported with 0.1 M KCl. As shown in Figure 6.1(B), the presence and magnitude of the voltammetric wave for the redox active species on EPPG electrode surface increases with the exposure time in the air (Inlay Figure 6.1(B)), but with a decreasing rate over time. In order to investigate the formation of the surface redox species in aqueous solution, the EPPG electrode was immersed into a solution of 0.01M HNO_3 (pH 2) + 0.1 M KCl supporting electrolyte immediately after renewal for 0, 5, 10, 20, 40, 80, 120 minutes, and overnight. The results indicate that the process leading to the formation of the surface redox species is inhibited in water. Immersion of the EPPG surface into a solution did not lead to an increase in the magnitude of the redox wave (Figure 6.2).

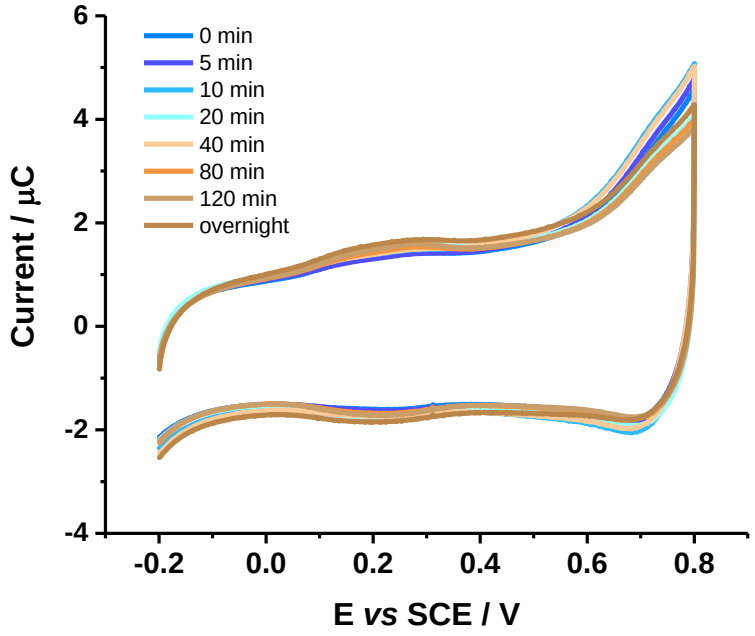

Figure 6.2 Cyclic voltammograms of an EPPG electrode after exposure to the solution of 0.01 M HNO_3 (pH 2) for 0, 5, 10, 20, 40, 80, 120 minutes, and overnight tested in 0.01 M HNO_3+0.1 M KCl supporting electrolyte (pH 2) at a scan rate of 100 mV s^{-1}.

The electrochemical response of redox species on EPPG electrode surface was examined over the pH range from 2.0 to 8.0, as shown in Figure 6.3(A). Cyclic voltammetry was run in an oxidative direction from −0.2 to +0.8 V (*vs* SCE) and reversed to −0.2 V using scan rate of 100 mV s^{-1}. As can be seen from Figure 6.3(A), the voltammogram shifts to more negative potentials as the pH increases. A plot of midpoint potential against pH for the voltammograms at a scan rate of 100 mV s^{-1} is depicted in Figure 6.3(B). For a simple electrochemically reversible voltammograms the midpoint potential obeys the following equation[23]:

$$E_{mid} = E^{\circ}_{formal} - \frac{2.3RTm}{nF} pH \qquad (6.4)$$

where R is the gas constant (8.314 J K^{-1} mol^{-1}), T is the temperature (K), F is the Faraday constant (96485 C mol^{-1}), and m and n are the number of protons and electrons involved in the oxidation, respectively. From equation 6.4, it can be seen that E_{mid} varies by the amount 0.059(m/n) V per pH unit. At pH values in the range 2.0–8.0, the experimental measurement resulted in 0.056 V/pH shift (Figure 6.3(B)), At pH values in the range 2.0–8.0, the experimental measurement resulted in 0.056 V/pH shift (Figure 6.3(B)). The results demonstrate that the process is to be reversible and to involve the transfer of an equal number of electrons and protons, most likely indicating the feature to be due to the presence of quinonyl surface species (or possibly phenolic).

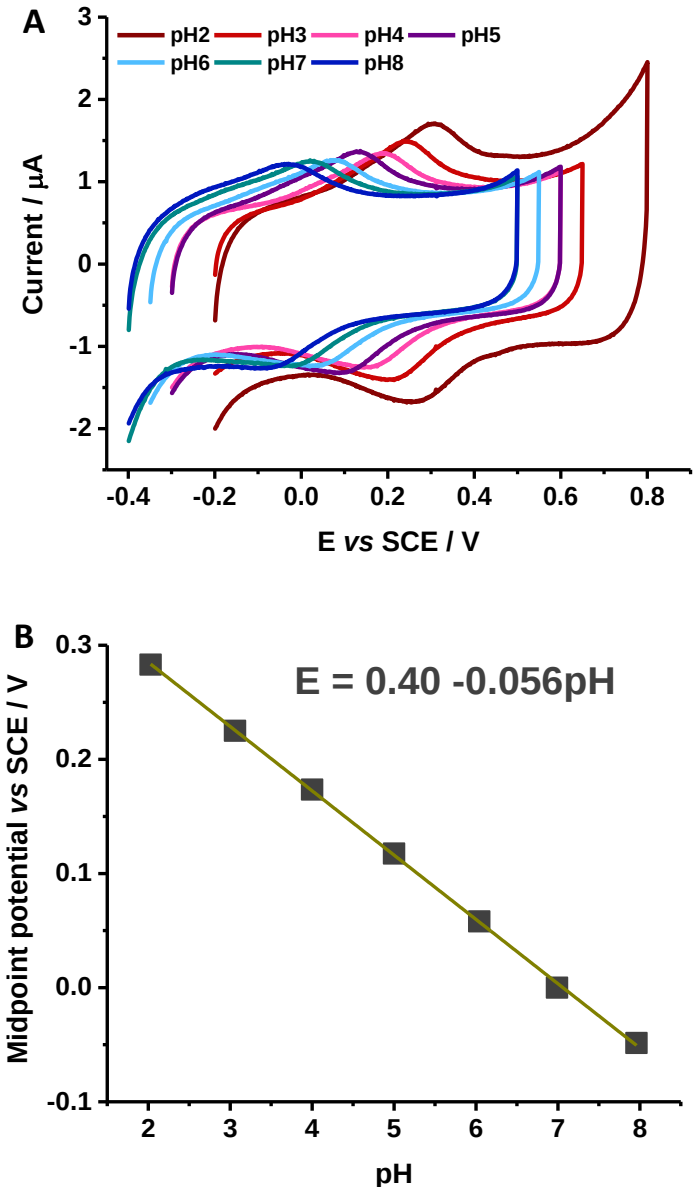

Figure 6.3 (A) Cyclic voltammograms at a scan rate of 100 mV s^{-1} on EPPG electrode in buffer solution, ranging pH from 2 to 8. (B) Calibration plots of midpoint peak potential against pH. All solutions were degassed before performed electrochemical measurements.

Next, X-ray Photoelectron Spectroscopy (XPS) was performed on the electrode surfaces (experimental details and data in Appendix C). All XPS experiments and data analysis were conducted by Dr. Robert G. Palgrave (University College London). XPS detected oxygen at >5 atomic% on all EPPG surfaces, even those measured immediately after polishing. Ar ion depth profiles showed that the oxygen was

confined to the electrode surface and was not present in the bulk. In contrast, highly ordered pyrolytic graphite (HOPG) electrodes showed no detectable levels of surface oxygen in XPS immediately after polishing.[24, 25] This difference is likely due to exposure of the edge planes in EPPG. On the EPPG electrodes, the oxygen signal from the XPS was an order of magnitude greater than that found by electrochemistry; this demonstrates that the redox active species identified electrochemically only corresponds to a small fraction (<10%) of the oxygen present on the EPPG surface (calculation data in Appendix C). This order of magnitude discrepancy between the two values immediately highlights the fact that the electrochemistry is specific to the redox active functionality on the surface whereas the XPS reports on the surface coverage of all surface species. Consequently, in order to progress further the XPS O1s peak will require deconvolution to gain greater specific chemical insight into the surface coverage of the redox active moiety. The magnitude of the whole peak will be subject to a likely error of approximately ±10%.[26] Although deconvolution of an XPS peak is feasible error in the magnitude of the total peak will propagate through plus there will be an additional contribution from the uncertainty inherent in the deconvolution process itself. As further complicating factor, there is no fixed agreement in the literature regarding the assignment of the different peaks to specific surface functional groups. The Figure 6.4 below schematically indicates the ranges over which the different oxygen functionalities have been reported to occur as compared to a O1s XPS peak as measured for a representative carbon surface used in this study. Therefore, assignment of O1s XPS peaks to oxygen functionalities is challenging due to the small chemical shift that exists between different functional groups.[27-32] As found by others [33], we were not able to unambiguously assign the O1s environments to specific chemical environments.

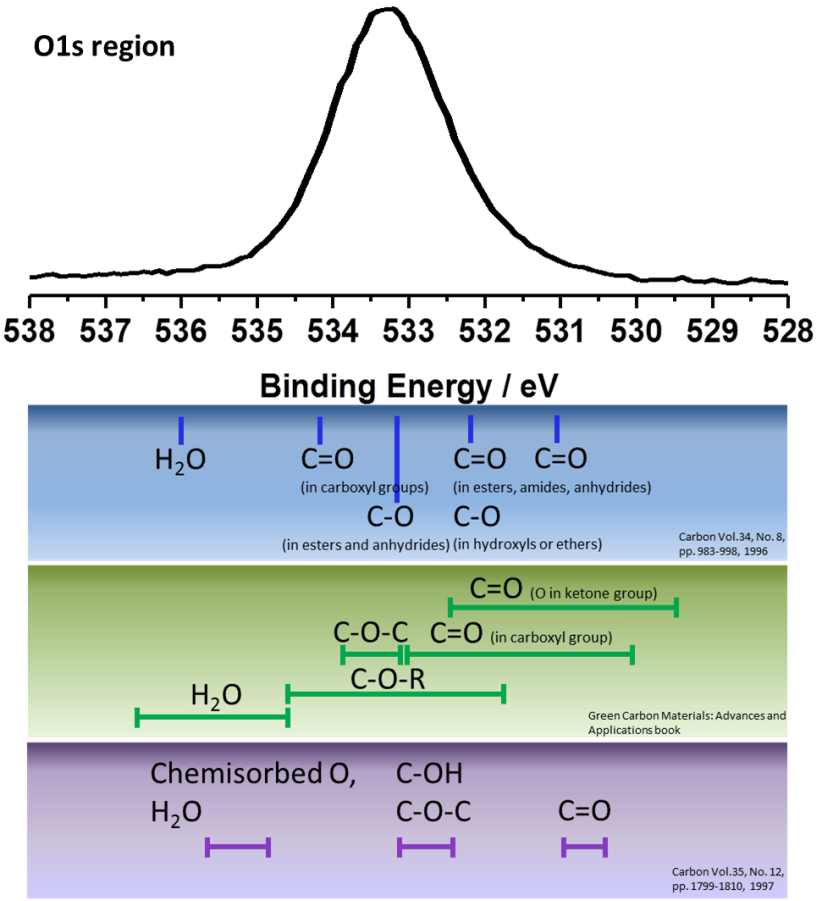

Figure 6.4 O1s region spectrum from EPPG electrode in this work together with peak assignment of different oxygen functionalities reported in the literature.[27-29]

The photosensitivity of the surface modification process was investigated. After surface renewal the EPPG electrode was exposed to differing light conditions. Figure 6.5(A-D) show the cyclic voltammetric profiles of oxygen functionalities on EPPG surface after exposure to infrared, UV, a no light control, and infrared under a nitrogen atmosphere respectively. The electrochemical redox responses show qualitatively similar CV for all cases; however the magnitude of responses with time is different. Note that in this study EPPG electrode is chosen due to its high reactivity

because it is dominated by edge plane sites. The results of other types of graphite electrodes are included in the Appendix D.

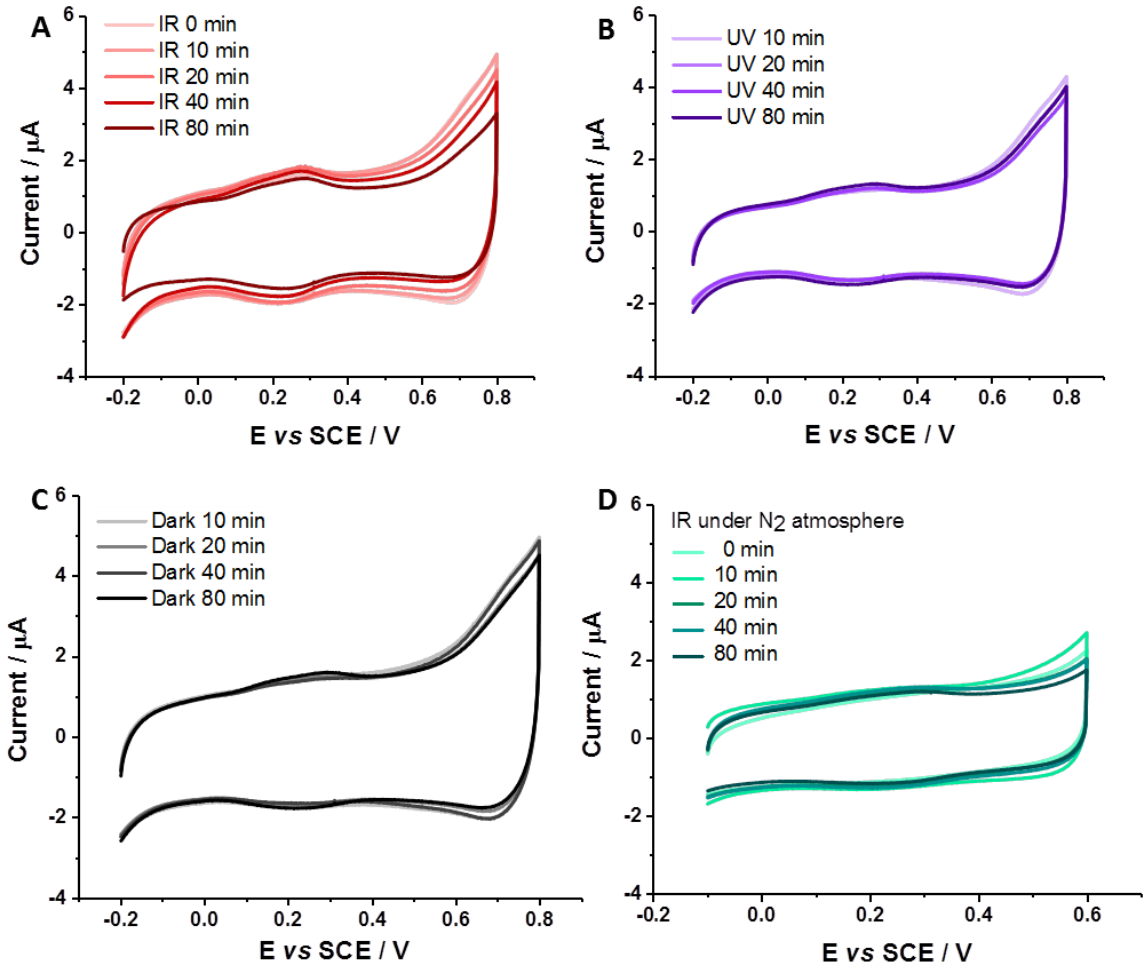

Figure 6.5 Cyclic voltammograms of an EPPG electrode after exposure to different conditions including (A) infrared, (B) UV (365 nm) exposure, (C) control experiment in a dark metal box, and (D) control experiment in IR under a N_2 gas atmosphere tested in 0.01 M HNO_3+0.1 M KCl supporting electrolyte (pH 2) at a scan rate of 100 mV s^{-1}.

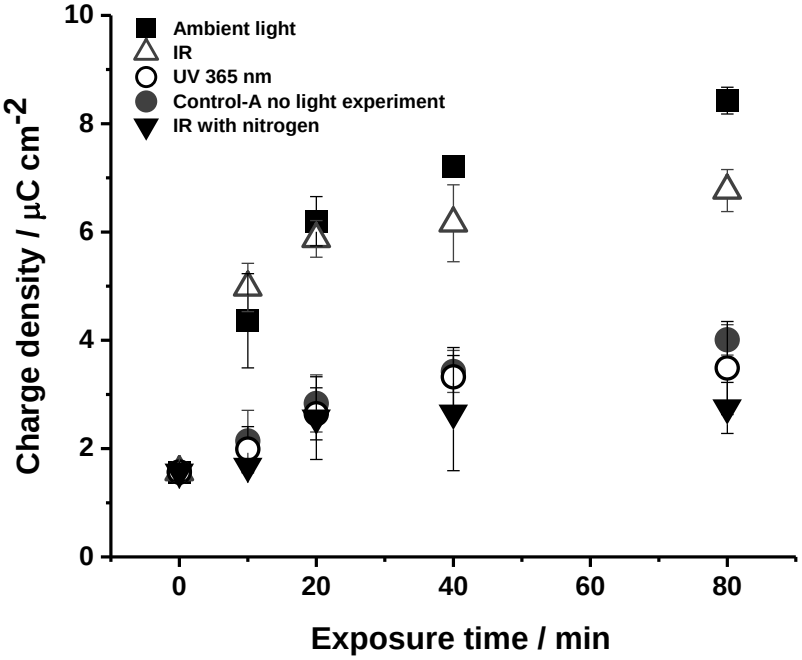

Figure 6.6 Plots of charge densities as a function of exposure time of different conditions including the exposure to normal light (■), IR (△), UV (○), control in dark conditions (●), and control IR under a nitrogen atmosphere (▼).

The effect of different lighting conditions was analysed in terms of the voltammetric charge densities as a function of the exposure time. Figure 6.6 presents these data as a function of exposure time. Note that in the absence of exposure to light the surface coverage of the formed surface redox activity moiety is significantly depleted. Moreover, the charge densities for an electrode exposed to an IR light source were comparable to the electrode being left under ambient conditions. In contrast UV light did not demonstrate an effect on the build-up of oxo groups on the electrode surface; the charge densities were comparable to that of the no light control experiments. This result strongly indicates the involvement of a photochemical process in the aging of the electrode surface and that the photo-sensitivity is predominantly associated with IR wavelengths. A further control experiment was performed where an electrode was exposed to IR light under a nitrogen atmosphere.

The results were comparable to those of the no light control experiment. Such a result is consistent with the aging of the carbon surface being at least partially due to reaction with $^1O_2$.[34] The transition wavelengths from $^3O_2$ to $^1O_2$ are *ca.* 1270 nm and 1070 nm for its vibrational excited states ν=0 and ν=1 respectively.[35-38] The home-fabricated IR coils employed as a broadband IR-generator irradiate a short-wave or near infrared (NIR) with the range from 780 nm to 1400 nm.[39] This range of irradiated wavelengths is a close match to the molecular oxygen transition [$^1\Delta_g$ (ν=1)] ← [$^3\Sigma_g^-$ (ν=0)] and [$^1\Delta_g$ (ν=0)] ← [$^3\Sigma_g^-$ (ν=0)] absorption band. Note that the charge densities of an electrode exposed to ambient conditions show a slightly higher value than under IR conditions, indicating the surface modification likely occurs via multiple parallel pathways under ambient conditions.

To further evidence the involvement of $^1O_2$ in the aging process experiments to generate and expose $^1O_2$ to the electrode surface were made. In this study, the reaction of hydrogen peroxide with in-situ generated hypochlorite was employed to produce $^1O_2$ (experimental details in section 6.2.3). The generation of $^1O_2$ was clearly evidenced by a red chemiluminescence from the reaction.[20] This emission results from an excimer emission formed from two activated oxygen molecules. For the excited oxygen optical transitions $^1\Sigma_g^+ \leftrightarrow {}^3\Sigma_g^-$ and $^1\Delta_g \leftrightarrow {}^3\Sigma_g^-$ radiative half-life in the gas phase is estimated to be 7 sec and 45 min respectively.[40] To investigate an effect of singlet oxygen in the build-up redox species on carbon surface, generated singlet oxygen gas was directly blown onto the electrode surface for 5, 10, 20, and 40 minutes. Control experiments were also performed to compare the effect of singlet oxygen. Three different control experiments were conducted including the flowing of chlorine gas, flowing argon gas through H_2O_2 solution, and leaving the electrode (in a

fume hood) without flowing any gasses. Those control experiments were performed for 5, 10, 20, and 40 minutes (unless otherwise stated) which were the same as in the singlet oxygen experiments so as to allow comparison of the results. Note that chlorine gas was employed to react with hydrogen peroxide for generating singlet oxygen. Chlorine residuals (resulting from the incomplete reaction of Cl_2) might be blown on surface of electrode together with singlet oxygen. Therefore, chlorine gas is taken into account in a control experiment. Control experiments were carried out to ensure that it is not the effect of chlorine gas and hydrogen peroxide, but singlet oxygen.

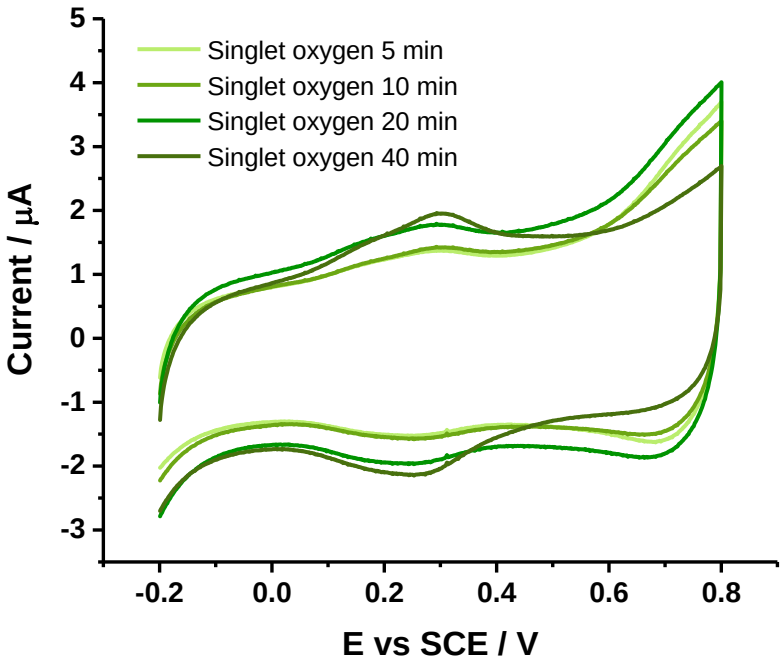

Figure 6.7 Cyclic voltammograms of an EPPG electrode after exposure to singlet oxygen ($^1O_2$) for 5, 10, 20, and 40 minutes tested in 0.01 M HNO_3+0.1 M KCl supporting electrolyte (pH 2) at a scan rate of 100 mV s^{-1}.

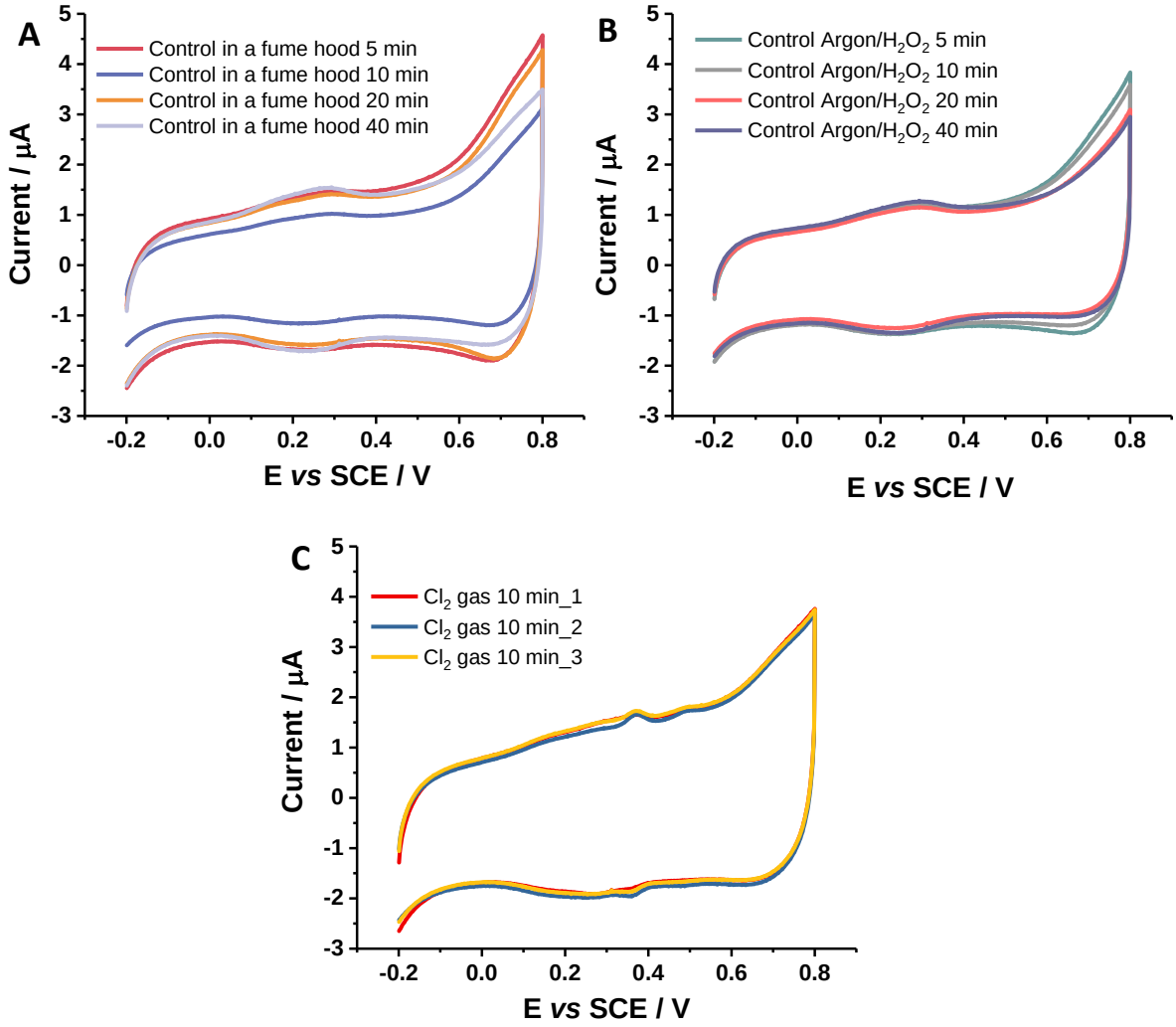

Figure 6.8 CVs of EPPG electrode after exposure to different control experiments including (A) leaving electrode (in a fume hood) without flowing any gasses, (B) flowing argon gas through H_2O_2 solution, and (C) flowing chlorine gas tested in 0.01 M HNO_3+0.1 M KCl supporting electrolyte (pH2) at a scan rate of 100 mV s^{-1}.

Figure 6.7 presents the cyclic voltammetry profiles of redox species on EPPG electrode after exposure to $^1O_2$ gas for different times. All voltammograms of control experiments illustrate in Figure 6.8. Qualitatively similar responses were seen from electrode after exposure to singlet oxygen (Figure 6.7), control experiment in fume hood (Figure 6.8(A)) and flowing argon gas through H_2O_2 (Figure 6.8(B)) but the magnitude of responses with time is different. In contrast, chlorine gas experiments

resulted in a distinctly different voltammetric response of electrode. The results demonstrated that increasing of the surface redox species in electrode surface after flowing gas does not result from the chlorine gas.

The analysed charge densities plotted as a function of exposure time to singlet oxygen and two control conditions is depicted in Figure 6.9. Relatively larger and steadily increasing charge densities are obtained for EPPG electrodes that have been exposed to a flow of $^1O_2$. This result further evidences the likely involvement of $^1O_2$ in generating oxygen functionalities on the graphitic surface.

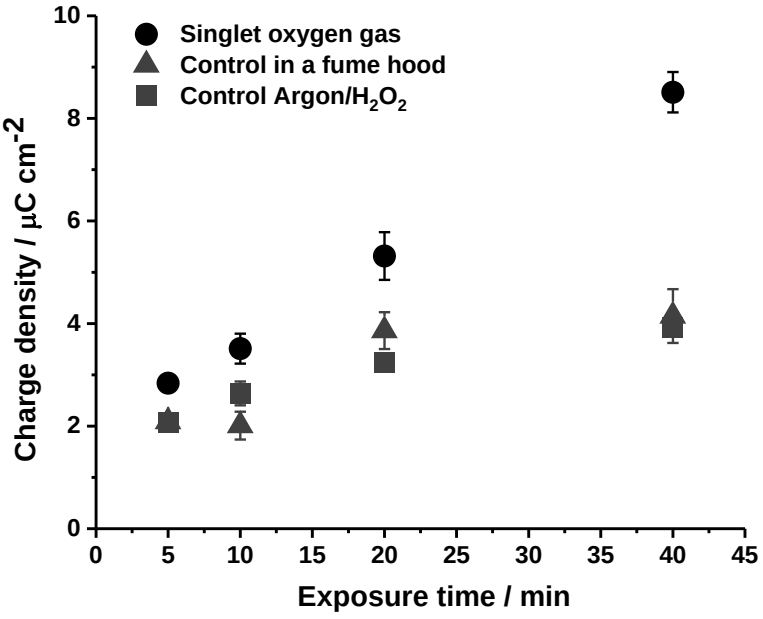

Figure 6.9 Charge densities of oxygen functionalities on electrode surface as a function of exposure time at various exposure conditions.

In view of organic synthesis, typical reaction modes often encountered with $^1O_2$ include Diels-Alder [2+2] and [4+2] cycloadditions and "ene" reactions.[41] This pattern of reactivity is suggestive of the electrophilic character of the $^1O_2$. Accordingly, $^1O_2$ reacts favourably with electron-rich compounds or π-electrons on a

carbon framework.[42] Much literature has reported that $^1O_2$ undergoes oxygenation reactions with naphthalene, anthracene and higher members of the acene series resulting in endoperoxides and/or anthraquinone.[17, 18, 43-45] Considering basic structural units of graphitic materials, edge planes of graphite might be considered as electron-rich zones which preferentially react with $^1O_2$. Specifically, graphitic surface after fresh polishing cannot be perfect idealised structures: there must be "dangling bonds" at the edge. Mechanical renewal of the surface must lead to bond breaking and the generation of dangling bonds or radicals on the graphitic surface. Accordingly, one plausible process for generating oxygen-containing functionalities may arise from a Diels-Alder [2+2] and [4+2] of $^1O_2$ with electron-rich aromatic zones on graphite structures. The proposed mechanism of $^1O_2$ with graphitic surface is shown in Figure 6.10.

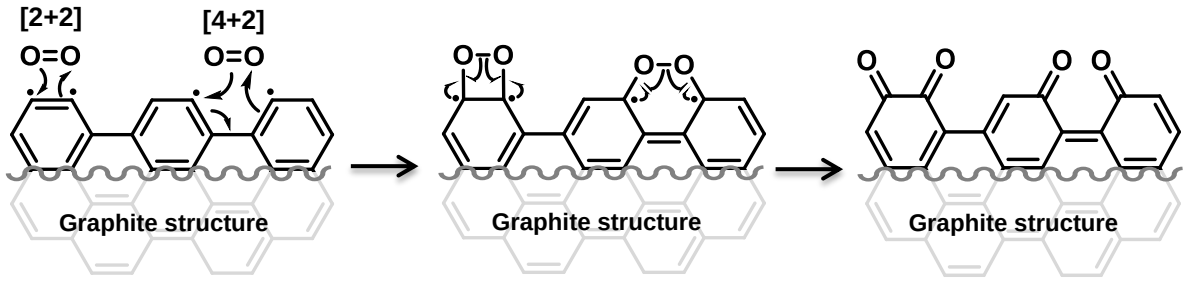

Figure 6.10 Proposed mechanism of singlet oxygen with graphitic structures

How might $^1O_2$ be formed under ambient aerial conditions at the electrode surface? Due to the spin forbidden nature of the transition[34] it is most likely that the graphitic surface is itself acting as a sensitiser. Single-walled carbon nanotubes and fullerenes have been previously reported to be a very effective oxygen sensitiser.[46-48] However, the plausible importance and role of metallic impurities in the graphite material should not be ignored. Metallic or other heavy atom centres may play an important role in the formation of $^1O_2$ due to spin orbit coupling.[49-52]

6.4 Conclusions

In conclusion, by comparing the magnitude of charge densities of redox species on EPPG surfaces, the voltammetric responses of redox species after exposure to normal atmospheric condition and to $^1O_2$ environment are significant higher than the control conditions. This indicates that a plausible origin of oxygen functionality, notably quinone features, on carbon surface is the reaction of $^1O_2$ with the graphite surface.

Bibliography

1. K. Chaisiwamongkhol, C. Batchelor-McAuley, R. G. Palgrave and R. G. Compton, *Angewandte Chemie International Edition*, 2018, **57**, 6270-6273.
2. C. H. A. Wong, C. K. Chua, B. Khezri, R. D. Webster and M. Pumera, *Angew. Chem., Int. Ed.*, 2013, **52**, 8685-8688.
3. C. E. Banks, A. Crossley, C. Salter, S. J. Wilkins and R. G. Compton, *Angew. Chem., Int. Ed.*, 2006, **45**, 2533-2537.
4. R. L. McCreery, *Electroanalytical Chemistry: A Series of Advances*, CRC Press, 1991.
5. M. A. Fryling, J. Zhao and R. L. McCreery, *Anal. Chem.*, 1995, **67**, 967-975.
6. H. Estrade-Szwarckopf, *Carbon*, 2004, **42**, 1713-1721.
7. G. G. Wildgoose, P. Abiman and R. G. Compton, *J. Mater. Chem.*, 2009, **19**, 4875-4886.
8. P. Chen and R. L. McCreery, *Anal. Chem.*, 1996, **68**, 3958-3965.
9. J. L. Figueiredo and M. F. R. Pereira, *Catal. Today*, 2010, **150**, 2-7.
10. M. F. R. Pereira, J. J. M. Órfão and J. L. Figueiredo, *Appl. Catal., A*, 1999, **184**, 153-160.
11. Y. Iwasawa, H. Nobe and S. Ogasawara, *J. Catal.*, 1973, **31**, 444-449.
12. Z. H. Zhu, J. Finnerty, G. Q. Lu and R. T. Yang, *Energy & Fuels*, 2002, **16**, 1359-1368.
13. K. Sendt and B. S. Haynes, *J. Phys. Chem. A*, 2005, **109**, 3438-3447.
14. P. E. Fanning and M. A. Vannice, *Carbon*, 1993, **31**, 721-730.
15. A. Montoya, F. Mondragón and T. N. Truong, *Carbon*, 2003, **41**, 29-39.
16. D. R. Kearns, *J. Am. Chem. Soc.*, 1969, **91**, 6554-6563.
17. C. S. Foote, S. Wexler, W. Ando and R. Higgins, *J. Am. Chem. Soc.*, 1968, **90**, 975-981.
18. C. S. Foote, *Acc. Chem. Res.*, 1968, **1**, 104-110.
19. H. N. Alyea, *J. Chem. Educ.*, 1969, **46**, A218.
20. A. U. Khan and M. Kasha, *J. Am. Chem. Soc.*, 1970, **92**, 3293-3300.
21. B. Z. Shakhashiri and L. G. Williams, *J. Chem. Educ.*, 1976, **53**, 358.
22. Reactive carbon surfaces that are oxidised or reacted by chemicals or moisture in their environment.
23. R. Compton and C. E. Banks, *Understanding Voltammetry*, World Scientific, 2011.
24. X. Ji, C. E. Banks, A. Crossley and R. G. Compton, *ChemPhysChem*, 2006, **7**, 1337-1344.
25. D. J. Morgan, *Surface Science Spectra*, 2017, **24**, 024003.
26. K. R. J. Lovelock, I. J. Villar-Garcia, F. Maier, H. P. Steinrück and P. Licence, *Chem. Rev.*, 2010, **110**, 5158-5190.
27. U. Zielke, K. J. Hüttinger and W. P. Hoffman, *Carbon*, 1996, **34**, 983-998.
28. T. E. Rufford, D. Hulicova-Jurcakova and J. Zhu, *Green carbon materials : advances and applications*, CRC Press Inc., 2014.

29. S. Biniak, G. Szymański, J. Siedlewski and A. Świątkowski, *Carbon*, 1997, **35**, 1799-1810.
30. J. H. Wandass, J. A. Gardella, N. L. Weinberg, M. E. Bolster and L. Salvati, 1987, **134**, 2734-2739.
31. E. Desimoni, G. I. Casella, A. Morone and A. M. Salvi, *Surface and Interface Analysis*, 1990, **15**, 627-634.
32. C. Kozlowski and P. M. A. Sherwood, *Journal of the Chemical Society, Faraday Transactions 1: Physical Chemistry in Condensed Phases*, 1985, **81**, 2745-2756.
33. E. P. Randviir, D. A. C. Brownson, J. P. Metters, R. O. Kadara and C. E. Banks, *Physical Chemistry Chemical Physics*, 2014, **16**, 4598-4611.
34. C. Long and D. R. Kearns, *J. Chem. Phys.*, 1973, **59**, 5729-5736.
35. A. Sivéry, A. Barras, R. Boukherroub, C. Pierlot, J. M. Aubry, F. Anquez and E. Courtade, *J. Phys. Chem. C*, 2014, **118**, 2885-2893.
36. F. Anquez, I. El Yazidi-Belkoura, S. Randoux, P. Suret and E. Courtade, *Photochem. Photobiol.*, 2012, **88**, 167-174.
37. A. A. Krasnovsky and R. V. Ambartzumian, *Chem. Phys. Lett.*, 2004, **400**, 531-535.
38. F. Anquez, A. Sivery, I. El Yazidi-Belkoura, J. Zemmouri, P. Suret, S. Randoux and E. Courtade, in *Singlet Oxygen: Applications in Biosciences and Nanosciences, Volume 1*, The Royal Society of Chemistry, 2016, vol. 1, pp. 75-91.
39. P. Atkins and J. de Paula, *Atkins' Physical Chemistry*, OUP Oxford, 2010.
40. R. M. Badger, A. C. Wright and R. F. Whitlock, *J. Chem. Phys.*, 1965, **43**, 4345-4350.
41. A. Albini and M. Fagnoni, *Handbook of Synthetic Photochemistry*, Wiley, 2010.
42. S. Nonell and C. Flors, *Singlet Oxygen: Applications in Biosciences and Nanosciences, Volume 1* Royal Society of Chemistry, 2016.
43. H. H. Wasserman and D. L. Larsen, *J. Chem. Soc., Chem. Commun.*, 1972, DOI: 10.1039/C39720000253, 253-254.
44. M. A. Fox and S. Olive, *Science*, 1979, **205**, 582-583.
45. H. Maeda, Y. Nanai, K. Mizuno, J. Chiba, S. Takeshima and M. Inouye, *The Journal of Organic Chemistry*, 2007, **72**, 8990-8993.
46. N. Gandra, P. L. Chiu, W. Li, Y. R. Anderson, S. Mitra, H. He and R. Gao, *J. Phys. Chem. C*, 2009, **113**, 5182-5185.
47. T. Murakami, H. Nakatsuji, M. Inada, Y. Matoba, T. Umeyama, M. Tsujimoto, S. Isoda, M. Hashida and H. Imahori, *J. Am. Chem. Soc.*, 2012, **134**, 17862-17865.
48. J. W. Arbogast, A. P. Darmanyan, C. S. Foote, F. N. Diederich, R. L. Whetten, Y. Rubin, M. M. Alvarez and S. J. Anz, *J. Phys. Chem. A*, 1991, **95**, 11-12.
49. C. Schweitzer and R. Schmidt, *Chem. Rev.*, 2003, **103**, 1685-1758.
50. B. F. Minaev and H. Agren, *J. Chem. Soc., Faraday Trans.*, 1997, **93**, 2231-2239.
51. B. F. Minaev, *Russ. Phys. J.*, 1978, **21**, 1205-1209.
52. B. F. Minaev, *Int. J. Quantum Chem.*, 1980, **17**, 367-374.

Chapter 7

Amperometric Micro pH Measurements in Oxygenated Saliva

The previous chapter focussed on the investigation of the origin of oxygen functionality on graphite electrodes. In this chapter, the electrochemically reversible two-electron, two-proton behaviour of the oxo-groups on graphite electrode, specifically the surface quinone group, is utilised for pH analysis. An amperometric micro pH sensor is developed based on the chemical oxidation of carbon fibre surfaces (diameter of 9 μm and length of *ca.* 1 mm) to enhance the population of surface quinone groups for the measurement of salivary pH. A Nernstian response is observed across the pH range 2–8 which is the pH range of many biological fluids. We highlight the measurement of pH in small volumes of biological fluids without the need for oxygen removal and the micro pH electrode is examined by measuring the pH of commercial synthetic saliva and authentic human saliva samples. The results correspond well with those obtained by using commercial glass pH electrodes on large volume samples.

The work presented in this chapter has been published in *Analyst*, 142, (2017), 2828-2835.[1]

7.1 Introduction

Salivary pH measurement has gained attention over the past 10 years due to its possibility as a biomarker for diseases such as anxiety disorder, gingivitis, and tooth decay.[2-6] Among the biological fluids, saliva is one of the most preferable and practical specimens for health monitoring due to the possibility of non-invasive collection, especially in comparison to blood. Most research studies on salivary pH have focussed on oral diseases including dental caries and periodontal (gum) diseases.[6, 7] Salivary pH is normally maintained near neutrality (pH 6.7-7.3). When the pH of the saliva specifically on dental plaque or in dental cavity is below a critical value of 5.5, tooth enamel will demineralise resulting in dental decay. Therefore, pH measurement may readily to identifying active or inactive caries.[8-10]

A great number of methods have been utilised for pH determination including voltammetry[11-13], potentiometry[14-16], and the use of fluorescent agents.[17, 18] The pH of bulk aqueous solutions are easily measured using traditional glass electrodes. However, measuring pH inside a small volume requires an appropriate micro-scale pH probe. In addition in the biological context, a number of disadvantages of the glass electrode have been recognised in terms of the “sodium error” and the “acid error”, the fragility of glass, the large probe size, and the lack of disposability.[19, 20] A normal bulb tip diameter of the commercial glass electrode is 10-12 mm which is not a practicable size for *intra-oral* use, while the smallest bulb tip that is commercially manufactured is 1.3 mm [21]; however, this micro electrode has a high fragility and is non-disposable. To address such limitations of glass electrodes, considerable interest has focused on the design and development of non-glass pH sensors. Examples include voltammetric electrochemical pH sensors utilising a pH sensitive layer of

polymeric films [14, 22], enzymes [23], and organic redox species [24] added to the surface of electrodes. The approach of attaching redox species often involves utilisation of the pH dependence of quinone/hydroquinone (Q/QH_2) redox species.[24, 25] The Nernst equation can be used to quantify the voltammetric of these redox couples,

$$E_{mid} = E^{\circ}_{formal} - \frac{2.3RTm}{nF}pH \qquad (7.1)$$

where m is the number of protons and n is the number of electrons involved in the redox process.[26] Thus assuming a reversible redox process then there is a direct relationship between the peak potential and pH. In particular, for *m* and *n* = 2, slope of *ca.* 60 mV per pH unit is predicted at 25°C.

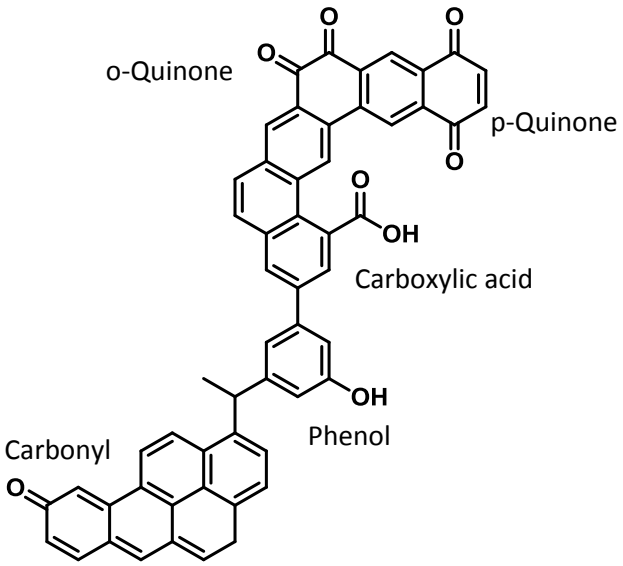

Scheme 7.1 Representation of various functional groups present on graphitic carbon surfaces, adapted from Ref. 27.

In addition to pure graphitic structures, carbon surfaces contain of a great number of different surface functional groups including quinone moieties as shown

in Scheme 7.1.[27, 28] In 2014, Min *et al.* reported using unmodified EPPG and glassy carbon electrodes for pH determination[29, 30], where the pH sensitive nature of intrinsic surface quinone moieties was exploited. In the present work, we extend the concept by enhancing the level of intrinsic quinone groups on a carbon microfibre (*ca.* 5-10 μm) to develop a micro pH sensor for use with limited volumes of biological fluids or in vivo application, focussing specifically on measurements in saliva.

The use of carbon fibres for pH sensing has been reported by several research groups.[12, 31-33] In most cases, chemical compounds containing quinone moieties have been used to modify the carbon fibre surface.[32, 33] Others have reported the use of electrochemical activation of the carbon surface to increase the quinone population.[33] Chemical oxidation of carbon fibre surface is another interesting method for activation of surface functionalities especially quinone groups[34], for example Mathur *et al.* reported the use of potassium permanganate solutions to modify carbon fibres to create quinone functionality.[35] Hitherto, some others oxidants which are oxidising acids, oxygen plasma, and hydrogen peroxide have been reported.[36, 37] However, none have used for measurement of pH in biological media such as saliva.

As aforementioned, the quinone/hydroquinone redox couple can be exploited for pH sensing. However, these species are known to be electrocatalytic towards oxygen reduction.[38-40] Owing to the presence of oxygen in general biological specimens, the use of quinone groups for pH sensing in biological samples contained oxygen could result in an error of measurement arising from mediated oxygen reduction. Consequently, the challenge for this work is to measure pH in oxygenated biological samples, especially for applications in the mouth where it is not possible to remove oxygen from the solutions.

In this chapter, we investigate the use of carbon fibre electrodes for the measurement of salivary pH by highlighting the pH dependence of the reduction of quinone groups on a carbon fibre surface. In addition, we report a simple chemical modification of carbon fibre surface to enhance the population of quinone groups. The voltammetric measurement of different pH buffer solutions is studied using cyclic voltammetry and square wave voltammetry. The present work also demonstrates pH measurement of non-degassed synthetic saliva solutions which we use as a model. The measurement of pH in oxygenated solution performs on the basis for applying to measure the pH in the mouth. Finally, we evidence the capability of the carbon fibre micro-wire electrode to measure pH levels in oxygenated authentic human saliva.

7.2 Experimental

7.2.1 Reagents and solutions

All chemicals used in this work were of analytical grade and were used as received without further purification. Solutions were prepared using deionized water (Millipore) with a resistivity of 18.2 MΩ cm at 25 °C.

The buffer solutions were prepared using citric acid/sodium citrate for the pH range 2.5-5.0 and monosodium phosphate/disodium phosphate for the pH range 5.0-9.0. All solutions contained 100mM KCl as supporting electrolyte. pH buffers were measured using a Hannah pH213 pH meter with calibration using Duracal buffers (Hamiliton) of pH 4.01 ± 0.01, 7.00 ± 0.01, and 10.01 ± 0.01. All pH buffers

measurements were carried out in a degassed system where solutions were purged with pure N_2 gas (BOC, Guildford UK) prior to experiments for a minimum of 20 minutes.

Synthetic saliva (pH 7.5) was prepared with the composition listed in Table 7.1 (AFNOR standard: S90-701).[41, 42] This prepared synthetic saliva solution is designated as *literature synthetic saliva*. 1 M HCl and 1 M NaOH were used for adjusting the pH of literature synthetic saliva to obtain the required pH. *Commercial synthetic saliva* was purchased from Synthetic Urine e.K. manufactured according to a currently standardised production process pursuant to DIN 53160-1.[43] For real saliva samples, informed consent was obtained from all the subjects in this research. Real saliva samples were collected no earlier than 30 minutes after a meal or drink using a salivette sampling device (Sarstedt, Germany). The small cotton swab from salivette was gently chewed for one minute. Recovery of saliva from the swab was carried out by centrifugation of the salivette for 15 min at 2400 rpm. Note that details of the salivette are given in Chapter 2.

Table 7.1 Composition of synthetic saliva (AFNOR standard S90-701)[41, 42]

Chemicals	**Concentration**	
Na_2HPO_4	0.260 g/L	1 mM
KH_2PO_4	0.200 g/L	1.5 mM
$NaHCO_3$	1.500 g/L	18 mM
KSCN	0.330 g/L	3 mM
NaCl	6.700 g/L	115 mM
KCl	1.200 g/L	16 mM

7.2.2 Apparatus

Electrochemical experiments were performed using a three electrode system in a Faraday cage held at 25 °C using a commercial potentiostat, uAutolab II (Metrohm-Autolab, Netherlands). The electrochemical cell was completed using a saturated calomel electrode, SCE, as the reference electrode (SCE +0.244 V *vs.* SHE, BASi Inc., Japan) and a platinum mesh 99.99% (Goodfellow, UK) as the counter electrode. The fabricated carbon fibre microwire electrodes were used as a working electrode (detailed in section 7.2.4 electrode preparation).

7.2.3 Chemical modification of carbon fibre surface

Carbon fibre used in this work was a pitch-based material (9 μm diameter, GoodFellow). The surface of the as-received fibres is coated with 1.0% epoxy in order to enhance their stiffness. The carbon fibre was boiled in acetone for 1 hour to remove the coating and expose the carbon surface.[44] After boiling in acetone, the treated carbon fibre was immersed in room temperature acetone and left to dry.

Chemical modification of carbon fibre surface was carried out and optimised. The de-coated carbon fibre was oxidised with aqueous solution of 0.03 M potassium permanganate at 85°C for 5, 10, 20, and 30 minutes[35] The samples were washed thoroughly with distilled water and then dried in an oven at 60°C for 2 hours.

7.2.4 Electrode preparation

The oxidised carbon fibres were attached to a conducting wire (0.2 mm diameter) of *ca.* 6 cm in length, using electrically conducting silver loaded epoxy

adhesive (RS Components Ltd.) to allow the microfiber working electrode to be connected for electrochemical measurements. The adhesive was set by heat treatment in the oven at *ca.* 80 °C for 20 minutes. The microfiber was then threaded through a plastic pipette tip leaving only the carbon fibre protruding out. The plastic tip was sealed with cyanoacrylate adhesive in order to prevent electrical leakage and the carbon fibre was cut to a length of *ca.* 1 mm.[45]

7.2.5 Electrochemical measurements

A range of pH 2-8 buffer solutions was prepared and their pH measured using a commercial glass electrode prior to experiments. "*Literature synthetic saliva*" was made up and its pH adjusted to obtain a desired pH using 1.0 M HCl or 1.0 M NaOH in the range from 3 to 8.5. The pH range investigated was chosen on the basis that most biofluids will fall within, namely pH 3 to pH 9.[46, 47] A small volume (*ca.* 5 mL) of each solution was transferred to an electrochemical cell. For buffer solutions, the bubbling of nitrogen gas was used to remove dissolved oxygen. Note that for synthetic saliva and real saliva samples, the electrochemical measurements were carried out without degassing the solutions with nitrogen in order to demonstrate the possibility of application to pH measurement in an oral cavity or in vivo. All the electrochemical measurements were performed in a Faraday cage which was thermostatted to maintain a temperature of 25 ± 2 °C. The platinum mesh (counter electrode) was flamed before each experiment to ensure a clean set up. At least 3 experimental scans were carried out for each experiment. For the measurement of cyclic voltammetry, current integration CV was used in this work. Note that in current integration CV the total current is sampled during the whole potential step, while in contrast the current from a normal staircase CV is measured at a specific

moment during the step. In systems involving time dependent process and surface species, there is a difference between the voltammetric responses for a reversible redox process from staircase CV and current integration CV.[48] Specifically the voltammetric response of surface bound species may be completely unobservable via staircase CV if the reaction takes place at the very beginning of a step or at different point that the current is sampled. In this work, the surface quinone redox reaction is the process of interest. Therefore, current integration CV was used in all cyclic voltammetry experiments to avoid any problems from missing or reducing current measurements from a surface bound reaction.

7.3 Results and discussions

In the following, first, chemical modification of a carbon fibre is optimised to obtain a procedure which maximises the surface coverage of quinone functionality. Second, the voltammetric measurement of buffer solutions is studied in a degassed system using both cyclic voltammetry and square wave voltammetry employing the modified fibres as electrodes. Lastly, the carbon fibre micro-wire electrode is used to measure the pH of synthetic saliva and applied to human saliva samples.

7.3.1 Chemical modification of carbon fibre surface

As discussed above, carbon substrates intrinsically exhibit quinone moieties on their surfaces. Cyclic voltammograms of unmodified carbon fibres were recorded in 0.01 M HNO_3 (pH 2.2) with 100 mM KCl as a supporting electrolyte at 100 mV s^{-1} (Figure 7.2). The voltammetric response shows oxidation/reduction peaks for the

quinone/hydroquinone (Q/QH_2) redox couple. Specifically an oxidation peak potential occurs at 0.196 V and a reduction peak potential is seen at *ca.* 0.127 V *vs*. SCE. However, the magnitude of the peak from an *unmodified* carbon fibre is very small (0.46 nA and 0.07 nA for the oxidation and reduction peaks respectively). This suggests that the population of quinone groups on the unmodified carbon fibre is low. Therefore, the following seeks to increase the surface coverage of quinone moieties through the chemical oxidation of the carbon fibre surface. Several oxidants, including oxygen plasma, oxidising acids (HNO_3, H_2SO_4, and H_3PO_4), potassium permanganate ($KMnO_4$), hydrogen peroxide (H_2O_2), have been reported previously [35-37].

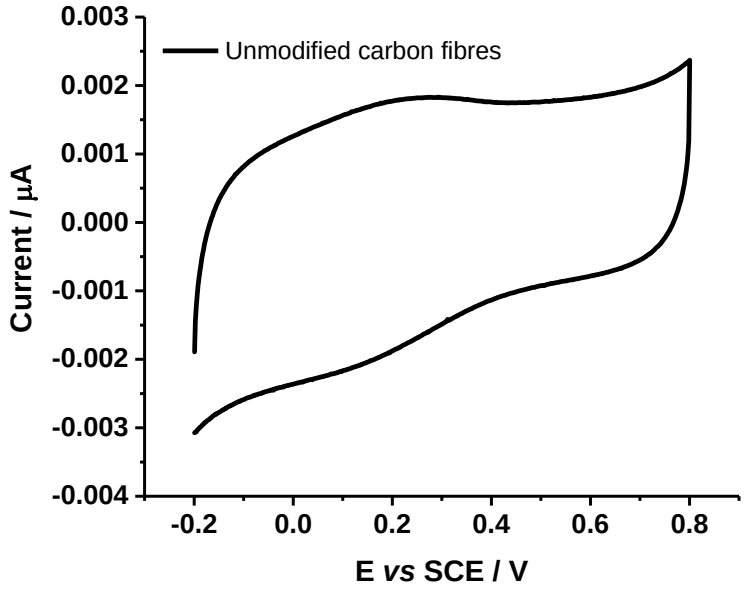

Figure 7.2 CV of unmodified pitch-based carbon fibre (micro-wire electrode) in 0.01 M HNO_3 + 100 mM KCl supporting electrolyte at scan rate of 0.1 Vs^{-1}.

In this work, $KMnO_4$ was chosen as oxidising agent to modify the carbon fibre surface due to the simple chemical procedure involved compared to other strong oxidising acids. The modification of carbon fibre surface was accomplished by simply oxidising its surface in aqueous 0.03 M $KMnO_4$ solution. Note that this concentration

of $KMnO_4$ was reported by Mathur *et al.* for oxidation of polyacrylonitrile-based carbon fibre [35]. Oxidation of the carbon fibre generates structural defects which contain oxygen functional groups.[35, 36, 49]

In order to obtain the best conditions for the modification of carbon fibre surface, an optimisation of the time of oxidation was made. Briefly, carbon fibres were boiled in aqueous 0.03 M $KMnO_4$ solution at 85 °C for 5, 10, 20, and 30 minutes. After the modification process, the micro-wire electrodes were constructed as described in section 7.2.4.

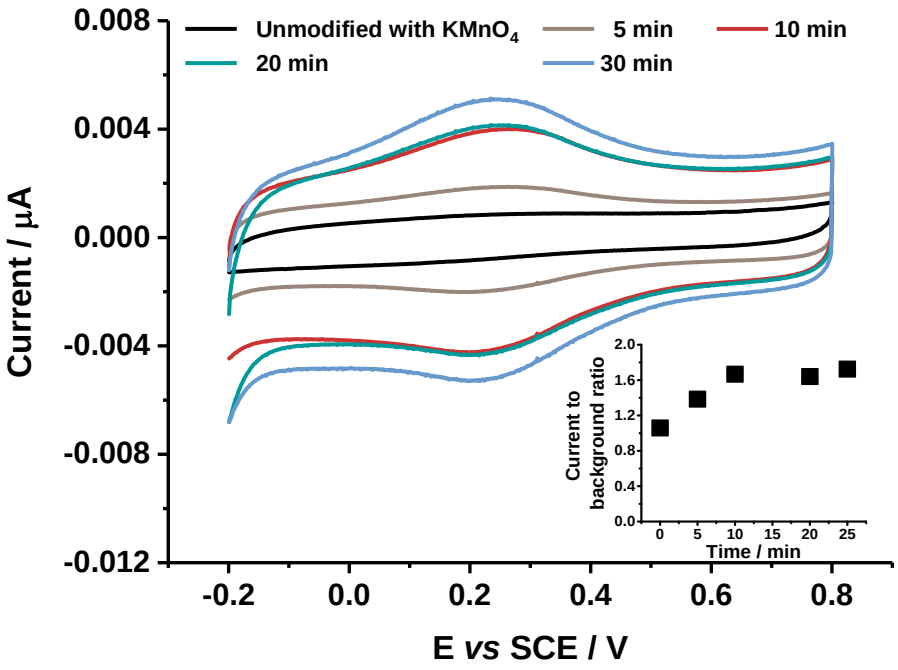

Figure 7.3 Optimisation of the chemical modification time in aqueous solution of 0.03 M $KMnO_4$. CVs at unmodified and modified carbon fibre electrodes in 0.01 M HNO_3 in 100 mM KCl supporting electrolyte (pH 2.2) at a scan rate of 0.1 V s^{-1}. Inset is plotted the current to background ratio as a function of modification time.

The voltammetric responses of the carbon fibre micro-wire electrodes before and after treatment in $KMnO_4$ were evaluated in 0.01 M HNO_3 (pH 2.2) with 100 mM KCl as supporting electrolyte at 0.1 V s^{-1}. Figure 7.3 shows the overlaid CVs of the unmodified carbon fibres compared with the $KMnO_4$ modified carbon fibres. Well-defined peaks were obtained in all cases. The magnitude of the peak current was observed to increase as a function of the modification time. However, not only does the peak current increase, so also does the background capacitative response. In order to select the optimal oxidation time, the current to background ratio was considered. As shown in an inset of Figure 7.3, on increasing the oxidising time from 0 to 10 minutes, the current to background ratio enhanced significantly. For longer oxidation times the current to background ratio slightly increased. Specifically, the current to background ratio reaches a near plateau at *ca.* 10 minutes. Therefore, 10 minutes oxidation time was selected as the preferred chemical modification for the carbon fibre surface. Note that, it is known that $KMnO_4$ prepared in acid (such as H_2SO_4) is a stronger oxidising agent, and so we tried to modify the carbon surface using $KMnO_4$ prepared in different concentrations of H_2SO_4. Accordingly the modification of the carbon fibre surface was also carried out for 10 minutes in 0.03 M $KMnO_4$ solution prepared in low concentrations (range of 5-20 mM H_2SO_4) or concentrated H_2SO_4 (18 M) and cyclic voltammograms recorded in 0.01 M HNO_3 with 100 mM KCl as a supporting electrolyte at 100 mV s^{-1} (Figure 7.4). At low concentrations of H_2SO_4 (5-20 mM), the results show that the current to background ratio did not greatly improve (Inset Figure 7.4). For a modification of carbon fibre in $KMnO_4$ prepared in concentrated H_2SO_4 (18 M), the carbon fibre surface was destroyed. Consequently, the mild conditions of aqueous $KMnO_4$ solution was utilised as the chemical oxidising agent.

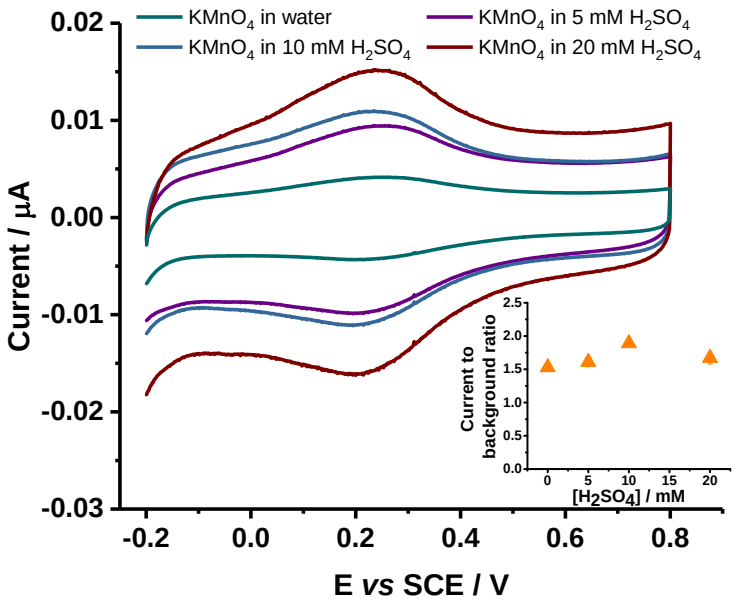

Figure 7.4 CVs at carbon fibre electrodes after modification in $KMnO_4$ prepared in different concentrations of H_2SO_4 tested in 0.01 M HNO_3 in 100 mM KCl supporting electrolyte (pH 2.2) at a scan rate of 0.1 V s^{-1}. Inset is current to background ratio as a function of sulphuric acid concentration.

The reproducibility and stability of micro-wire electrodes were also investigated. A reproducibility of responses between three different constructed micro-wire electrodes shows a small standard deviation (±0.006 V), indicating a good reproducibility of the electrodes (Figure 7.5(A)). In terms of stability of electrodes, we performed the CV measurements of the same micro-wire electrode over multiple scans. The oxidation potential, reduction potential, and midpoint potential remained at same position of each potential, showing the excellent stability of micro-wire electrode as shown in Figure 7.5(B).

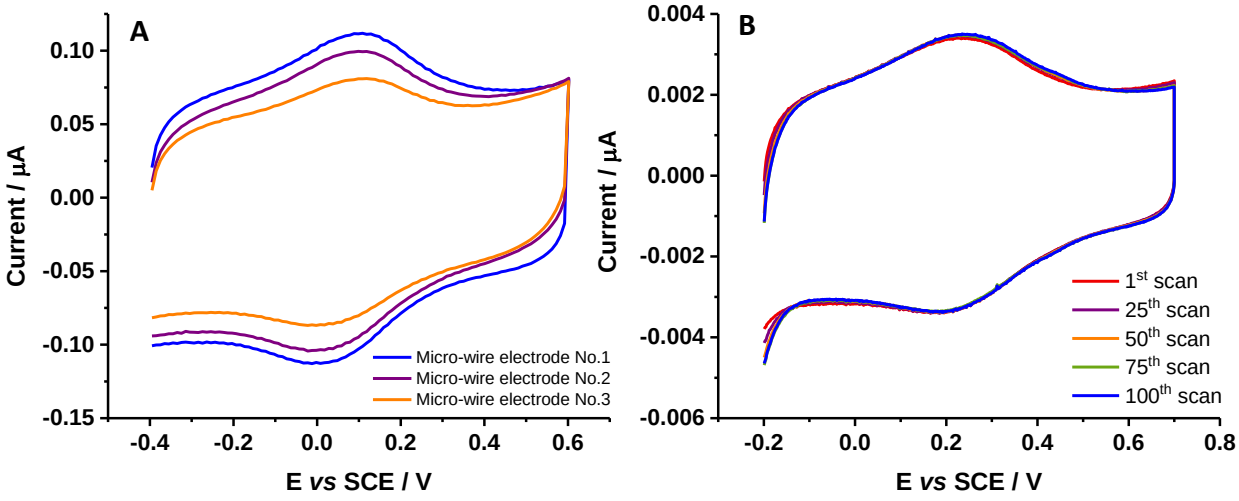

Figure 7.5 (A) CVs in literature synthetic saliva (pH 5.0) at three different micro-wire electrodes at scan rate of 4 V s^{-1}. (B) CVs in 0.01M HNO_3 supported with 0.1M KCl (pH 2.2) at the same micro-wire electrode with multiple scans at scan rate of 0.1 V s^{-1}.

7.3.2 Voltammetric measurement of the pH of buffer solutions

The quinone/hydroquinone redox couple on carbon fibre surfaces was investigated for voltammetric pH measurements. Cyclic voltammetry in a range of buffer solutions in the presence of 100 mM KCl supporting electrolyte was performed using the carbon fibre micro-wire electrodes. The CV response was first measured from -0.2 V to +0.7 V for a buffer solution of pH 2 at a scan rate of 0.1 V s^{-1}, and then the potential window was adjusted as a function of the pH. The cyclic voltammetric response for quinone groups on the carbon fibre surface was recorded in solutions of pH 2 – 8. All measurements in this section were performed in a degassed system by bubbling nitrogen gas to remove dissolved oxygen in solutions; measurements without degassing are discussed later in the chapter. Fig. 7.6(A) shows the overlaid

cyclic voltammograms of quinone groups on carbon fibre electrodes in different pH buffer solutions at scan rate of 0.1 V s^{-1}. It can be observed that by increasing pH, peak potentials shift in the cathodic direction towards more negative values. For analysis of the data, the oxidation, reduction, and midpoint potentials were all noted. The corresponding plots against pH are shown in Figure 7.6(B). The gradient of the slopes were 68.8±1.3 mV, 61.5±1.7 mV, and 65.3±1.3 mV per pH reflecting an almost Nernstian response corresponding to a two-electron, two-proton electrochemical process.

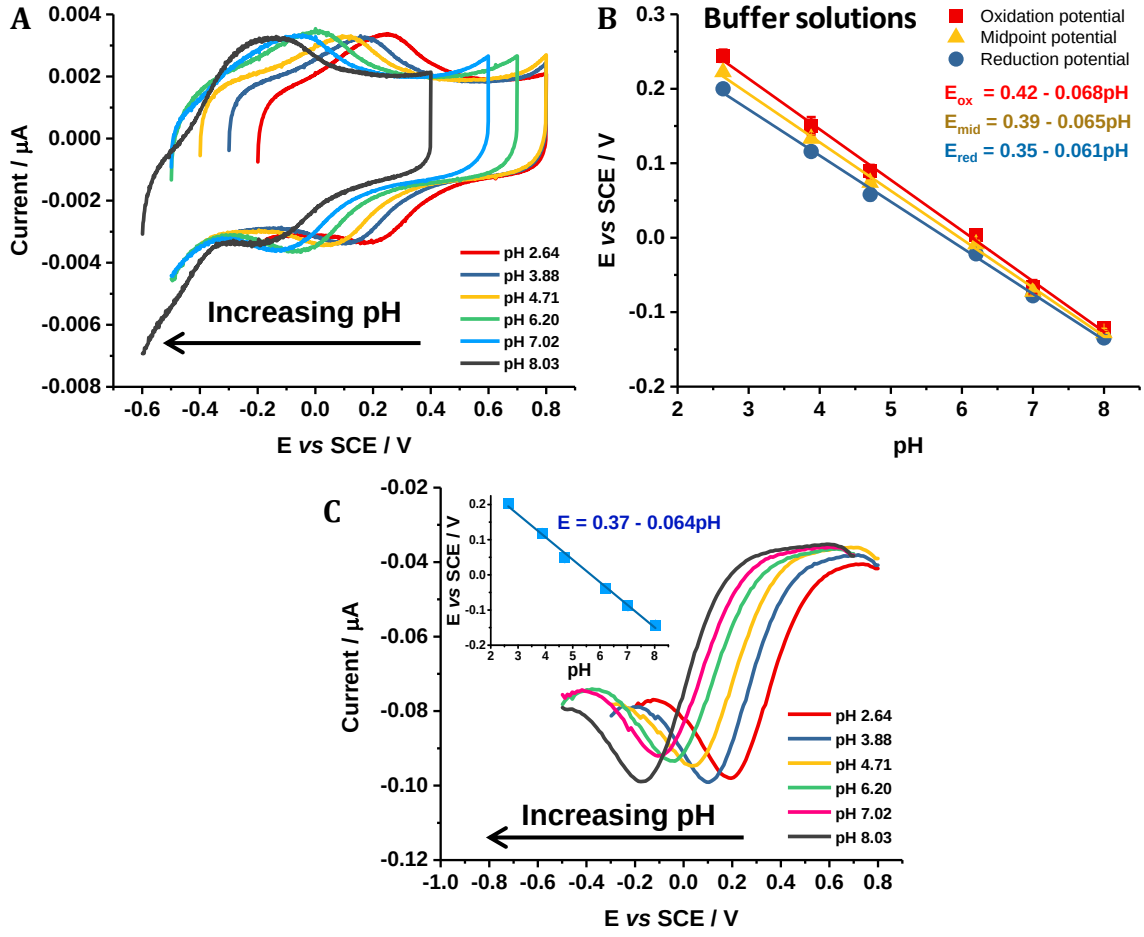

Figure 7.6 Quinone peaks in cyclic voltammetry at a scan rate of 0.1 V s^{-1} (A) and quinone reduction peaks in square wave voltammetry (C) on chemical modified pitch-based carbon fibre obtained in buffer solutions, ranging in pH from 2 to 8. Calibration plots of peak potential against pH obtained from CV (B) and SWV (inset of (C)). All of the buffer solutions were degassed before the performed electrochemical measurement.

After performing cyclic voltammetry and observing a linear response between the peak potential and pH, further studies using square wave voltammetry (SWV) were carried out using optimised SWV parameters: frequency 75 Hz, step potential 10 mV, and amplitude 100 mV, over the entire pH range studied. As can be seen in Fig. 7.6(C), a single SWV peak was observed by scanning from positive to negative potential. It can be observed that the peak potentials shift in the cathodic direction towards more negative potentials on increasing the pH. By measuring the reduction peak potentials and plotting against pH, a linear response was obtained in the pH 2-8 range, as shown in the inset of Fig. 7.6(C). The gradient of the slope was 64.6±2.0 mV per pH, consistent with the Nernst equation for a temperature of 25 °C for a two-proton, two-electron process. From this, we can see that both CV and SWV can be exploited for measurement of pH in buffer solutions.

7.3.3 Investigating the measurement of pH in saliva

7.3.3.1 pH measurement of synthetic saliva

Synthetic saliva was prepared according to the composition and concentrations specified in literature [41, 42] (‘*literature synthetic saliva’*). To partially mimic the use of the micro-wire electrode in situations such as in the mouth or in vivo, we performed CV in solutions without removing dissolved oxygen. We first carried out CV in *literature synthetic saliva* of pH 7.9 at scan rate of 0.1 V s^{-1} to observe the surface quinone behaviour in solutions without any degassing. An oxygen reduction was observed while the surface quinone oxidation/reduction peaks also appeared as shown in Figure 7.7 (red line). The slight overlaying of the two peaks can

be observed as revealed by comparison with deoxygenated buffer (blue line). Quinone groups present on the surface of carbon electrode have been known under certain conditions to catalyse oxygen reduction.[38-40] Consequently, this together with the peak due to direct reduction of the oxygen at the carbon surfaces overlapping with the quinone signal may result in the error of peak potential measurement if CV at 0.1 V s^{-1} is used for the pH measurement.

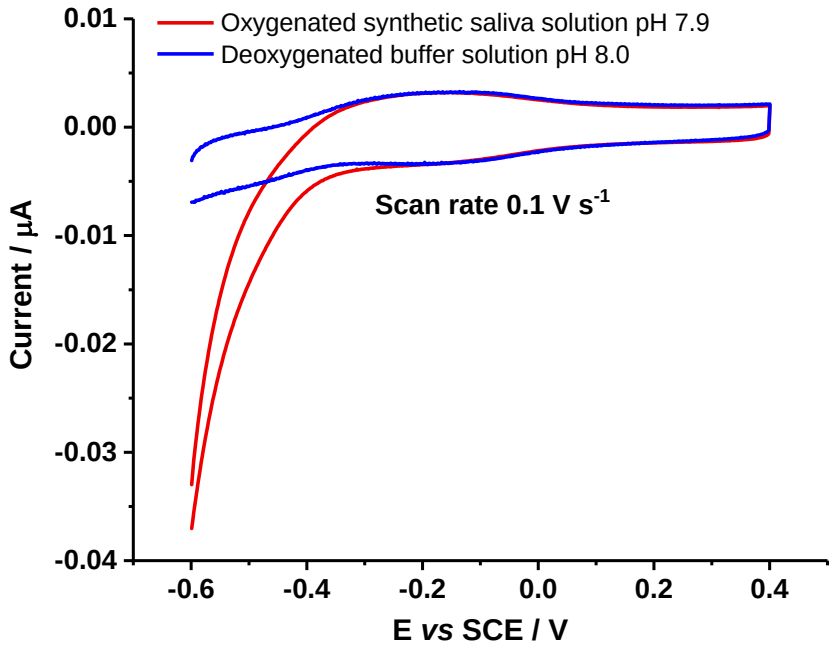

Figure 7.7 CV of chemical modified carbon fibre in literature synthetic saliva pH 7.9 without degassing compares (red line) with CV of chemical modified carbon fibre in buffer solution with degassing (blue line) at scan rate of 0.1 V s^{-1}, showing a presence of oxygen reduction in oxygenated solution (red line).

To address this problem, pH measurement in *'literature synthetic saliva'* without degassing using a micro-wire electrode was next investigated through a variable scan rate study. Different scan rates (0.1 – 8 V s^{-1}) were applied to *'literature synthetic saliva'* at pH 7.9 without degassing. The aim was to remove the influence of the oxygen reduction. Figure 7.8 shows overlaid CVs of micro-wire electrode in

literature synthetic saliva at different scan rates. The figure shows no oxygen reduction at the high scan rate in the potential range presented (0.5 – 8 V s^{-1}). This indicates that interference from oxygen reduction on micro-wire electrode can be effectively avoided by using high voltammetric scan rates. This reflects both the irreversibility of the O_2/H_2O_2 couple and the likely "outrunning" of any catalytic reduction of oxygen mediated via the quinone. Note that the oxygen reduction process is electrochemically irreversible and hence shifts to more negative potentials with increasing scan rates in contrast to the electrochemically reversible quinone reduction. Therefore, interference from the oxygen reduction can be removed by using high scan rates without disturbing quinone signals. We also note that such a procedure is unlikely to be successful when applied to electrode of macroscopic proportions. For further studies, measurements of pH in saliva were all carried out using scan rate of 4 V s^{-1}.

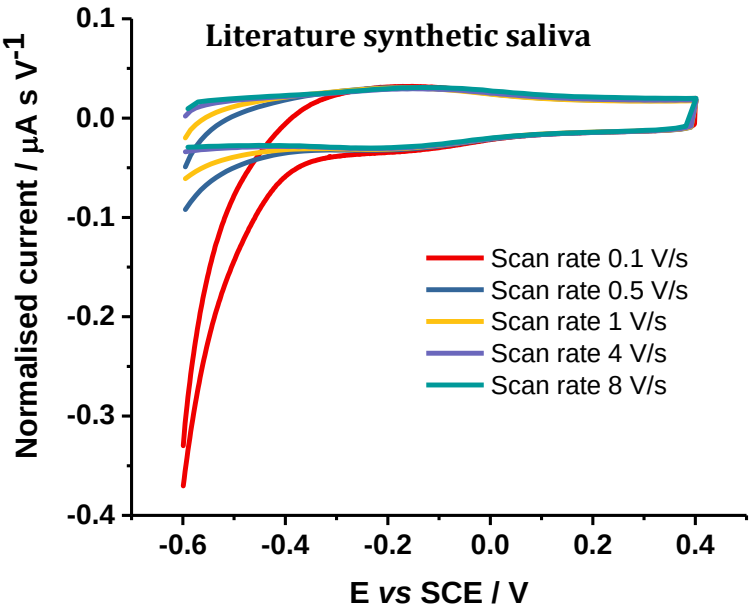

Figure 7.8 CVs of chemical modified carbon fibre in prepared synthetic saliva of pH 7.93 without degassing at different scan rates, showing a removal of oxygen reduction at high scan rates.

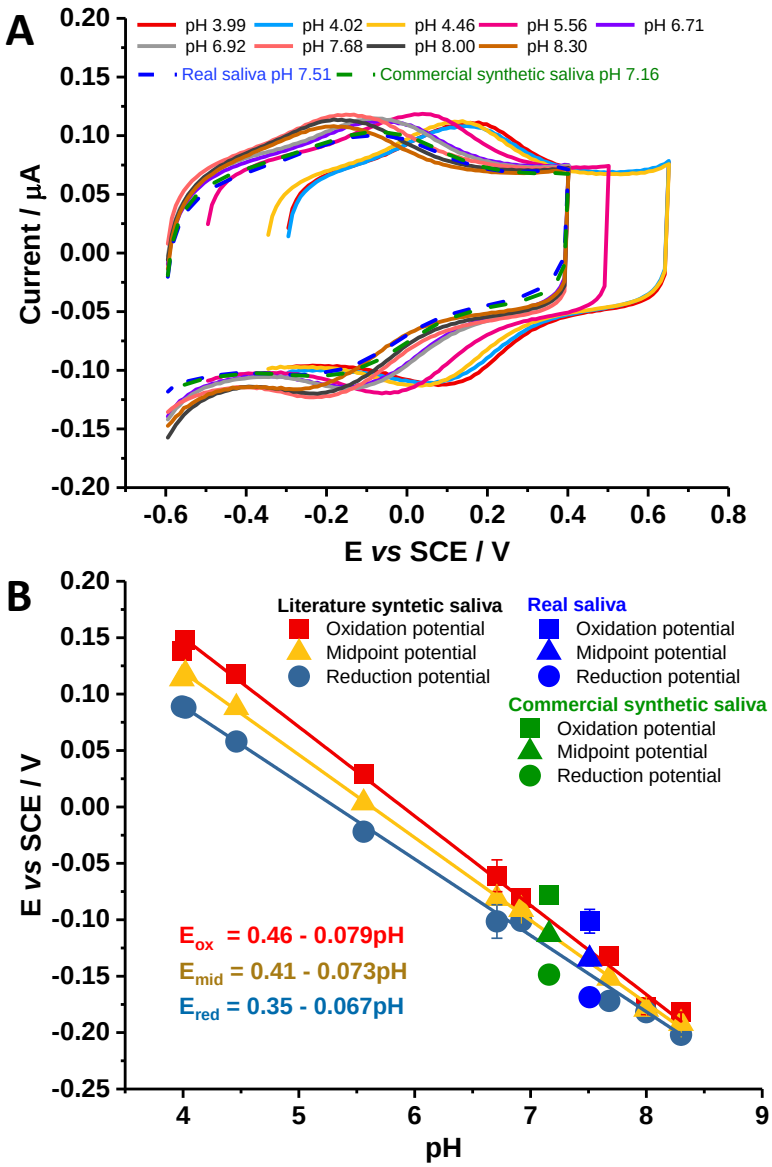

Figure 7.9 (A) CVs of chemical modified pitch-based carbon fibre in prepared synthetic saliva pH ranging from 3.99 to 8.30 (solid line), with real saliva and commercial synthetic saliva (dash line) at a scan rate of 4 V s^{-1}. (B) Calibration plots of peak potential against pH in prepared synthetic saliva without degassing, including results of real saliva and commercial synthetic saliva.

Using the higher scan rate for pH measurement in *'literature synthetic saliva'* without degassing, varying pHs of this synthetic saliva were tested at the micro-wire electrode (Figure 7.9(A) solid line). Well-defined cyclic voltammograms were obtained from the whole range of pH from 3.99 to 8.30. The oxidation, reduction, and midpoint potential were measured and plotted against pH. The linear response from

the plot of peak potential against pH was observed from all three lines as shown in Figure 7.9(B). The gradients obtained from oxidation, reduction, and midpoint potential were 79.1±2.4 mV, 67.7±1.8 mV, and 73.4±1.4 mV per pH unit respectively. These shifts in the voltammetric peak position are greater than that predicted by the Nernst equation. However, this most likely arises due to the quinone voltammetric waveshape as a function of pH, leading to a greater apparent shift in the peak position at the higher scan rates.

7.3.2.2 pH measurements in authentic human saliva

Having investigated the voltammogram response of the quinone modified carbon fibre electrodes for pH measurement of *'literature synthetic saliva'* at different pH values, here application of the micro-wire electrode to measure pH was next applied to *'commercial synthetic saliva'* and *'real saliva samples'*. The pH of these saliva solutions were measured using a commercial glass electrode before voltammetric measurements. The CVs of the micro-wire electrode were recorded in commercial synthetic saliva (pH 7.16) and real saliva samples (pH 7.51) at scan rate of 4 V s^{-1} without degassing. The dashed lines in Figure 7.9(A) show well-defined CVs from both types of saliva solution. Again, the oxidation, reduction, and midpoint potentials were measured. The obtained potential values were plotted against pH and were shown in the same calibration plots as the 'literature synthetic saliva' (Figure 7.9(B)). Good agreement is seen especially for the midpoint potential.

In Table 7.2 the results of pH measurements on commercial synthetic saliva and authentic human saliva are given. The determinations were performed both with a micro-wire electrode and a glass electrode. The pH values of the saliva sample using

a micro-wire were calculated from the midpoint potential and pH. The good agreement between the results from the two electrodes is obtained.

Table 7.2 Determinations on saliva samples with a glass electrode and a micro-wire electrode

Saliva	Glass electrode	Micro-wire electrode (This work)
Commercial synthetic saliva	7.16±0.04	7.19±0.08
Authentic human saliva	7.51±0.05	7.48±0.07

7.4 Conclusions

In summary, by chemical modification of carbon fibre surface, The pH measurement in oxygenated biological samples, synthetic saliva and real saliva in this case, was performed using high scan rate CV to remove the influence of any oxygen reduction reaction catalysed by surface quinone or the overlapping direct oxygen reduction. In particular, the micro-wire was validated for pH measurements in real saliva. Specifically, in this work we illustrated a proof of concept of using surface quinones on micro-wire electrode for pH sensing in authentic human saliva. Note that to realise a fully 'micro device', an electrochemical system without an external reference but with an internal reference (such as a ferrocene modified carbon fibre surface) might be further investigated.[24]

Bibliography

1. K. Chaisiwamongkhol, C. Batchelor-McAuley and R. G. Compton, *Analyst*, 2017, **142**, 2828-2835.
2. J. M. Yoshizawa, C. A. Schafer, J. J. Schafer, J. J. Farrell, B. J. Paster and D. T. Wong, *Clinical microbiology reviews*, 2013, **26**, 781-791.
3. N. Rathnayake, S. Åkerman, B. Klinge, N. Lundegren, H. Jansson, Y. Tryselius, T. Sorsa and A. Gustafsson, *PLoS ONE*, 2013, **8**, e61356.
4. S. Baliga, S. Muglikar and R. Kale, *Journal of Indian Society of Periodontology*, 2013, **17**, 461-465.
5. B. Sandin and P. Chorot, *Psychophysiology*, 1985, **22**, 226-230.
6. C. Seethalakshmi, R. C. J. Reddy, N. Asifa and S. Prabhu, *Journal of Clinical and Diagnostic Research : JCDR*, 2016, **10**, ZC12-ZC14.
7. A. Yamunadevi, J. Dineshshankar, S. Banu, N. Fathima, N. Ganapathy, T. Yoithapprabhunath, T. Maheswaran and V. Ilayaraja, *Journal of Natural Science, Biology and Medicine*, 2015, **6**, 295-299.
8. S. Hojo, M. Komatsu, R. Okuda, N. Takahashi and T. Yamada, *Journal of Dental Research*, 1994, **73**, 1853-1857.
9. J. A. Aas, A. L. Griffen, S. R. Dardis, A. M. Lee, I. Olsen, F. E. Dewhirst, E. J. Leys and B. J. Paster, *Journal of Clinical Microbiology*, 2008, **46**, 1407-1417.
10. W. J. Loesche, *Microbiological Reviews*, 1986, **50**, 353-380.
11. M. Amiri, E. Amali, A. Nematollahzadeh and H. Salehniya, *Sensors and Actuators B: Chemical*, 2016, **228**, 53-58.
12. M. A. Makos, D. M. Omiatek, A. G. Ewing and M. L. Heien, *Langmuir*, 2010, **26**, 10386-10391.
13. J. Phair, L. Newton, C. McCormac, M. F. Cardosi, R. Leslie and J. Davis, *Analyst*, 2011, **136**, 4692-4695.
14. T. Inoue, T. Baba and A. Yuchi, *Electroanalysis*, 2011, **23**, 536-542.
15. A. E. Musa, F. J. del Campo, N. Abramova, M. A. Alonso-Lomillo, O. Domínguez-Renedo, M. J. Arcos-Martínez, M. Brivio, D. Snakenborg, O. Geschke and J. P. Kutter, *Electroanalysis*, 2011, **23**, 115-121.
16. C. Zuliani, G. Matzeu and D. Diamond, *Electrochimica Acta*, 2014, **132**, 292-296.
17. H. R. Kermis, Y. Kostov and G. Rao, *Analyst*, 2003, **128**, 1181-1186.
18. M. Kneen, J. Farinas, Y. Li and A. S. Verkman, *Biophysical Journal*, 1998, **74**, 1591-1599.
19. D. A. Skoog, *Fundamentals of Analytical Chemistry*, Thomson-Brooks/Cole, 2004.
20. M. Dole and B. Z. Wiener, *Transactions of The Electrochemical Society*, 1937, **72**, 107-127.
21. Fisherscientific, https://www.fishersci.co.uk/, (accessed May, 2017).
22. R. A. Webster, F. Xia, M. Pan, S. Mu, S. E. C. Dale, S. C. Tsang, F. W. Hammett, C. R. Bowen and F. Marken, *Electrochimica Acta*, 2012, **62**, 97-102.
23. R. M. Greenway, S. J. Gardiner, A. L. Hart and J. Dunlop, *Biosensors and Bioelectronics*, 1994, **9**, 457-461.
24. L. Xiong, C. Batchelor-McAuley and R. G. Compton, *Sensors and Actuators B: Chemical*, 2011, **159**, 251-255.
25. G. G. Wildgoose, M. Pandurangappa, N. S. Lawrence, L. Jiang, T. G. J. Jones and R. G. Compton, *Talanta*, 2003, **60**, 887-893.
26. R. G. Compton and C. E. Banks, *Understanding Voltammetry (2nd ed.)*, World Scientific, 2011.
27. R. L. McCreery, *Electroanalytical Chemistry: A Series of Advances Volume 17*, ed. A.J. Bard, Marcel Dekker, New York, 1990.
28. K. T. Kawagoe, J. B. Zimmerman and R. M. Wightman, *J Neurosci Methods*, 1993, **48**, 225-240.
29. M. Lu and R. G. Compton, *Analyst*, 2014, **139**, 2397-2403.
30. M. Lu and R. G. Compton, *Analyst*, 2014, **139**, 4599-4605.
31. X. Zhang, B. Ogorevc and J. Wang, *Analytica Chimica Acta*, 2002, **452**, 1-10.
32. A. McLister, N. Lowry, A. Anderson, J. McHugh and J. Davis, *Fibers and Polymers*, 2015, **16**, 2294-2297.
33. A. Anderson, J. Phair, J. Benson, B. Meenan and J. Davis, *Materials Science and Engineering: C*, 2014, **43**, 533-537.
34. H. Kahlert, *Journal of Solid State Electrochemistry*, 2008, **12**, 1255-1266.
35. R. B. Mathur, J. Mittal, O. P. Bahl and N. K. Sandle, *Carbon*, 1994, **32**, 71-77.

36. L. B. Nohara, G. Petraconi Filho, E. L. Nohara, M. U. Kleinke and M. C. Rezende, *Materials Research*, 2005, **8**, 281-286.
37. C. A. Frysz and D. D. L. Chung, *Carbon*, 1997, **35**, 1111-1127.
38. K. Tammeveski, K. Kontturi, R. J. Nichols, R. J. Potter and D. J. Schiffrin, *Journal of Electroanalytical Chemistry*, 2001, **515**, 101-112.
39. M. S. Hossain, D. Tryk and E. Yeager, *Electrochimica Acta*, 1989, **34**, 1733-1737.
40. A. Sarapuu, K. Vaik, D. J. Schiffrin and K. Tammeveski, *Journal of Electroanalytical Chemistry*, 2003, **541**, 23-29.
41. K. Elagli, M. Traisnel and H. F. Hildebrand, *Electrochimica Acta*, 1993, **38**, 1769-1774.
42. F. C. Giacomelli, C. Giacomelli and A. Spinelli, *Journal of the Brazilian Chemical Society*, 2004, **15**, 541-547.
43. Synthetic-Urine, http://www.synthetic-urine.de/en/products/synthetic-human-body-fluids/synthetic-saliva-according-to-din-53160-1.html, (accessed May, 2017).
44. C. M. Pike, C. P. Grabner and A. B. Harkins, *Journal of Visualized Experiments : JoVE*, 2009, DOI: 10.3791/1040, 1040.
45. J. Ellison, C. Batchelor-McAuley, K. Tschulik and R. G. Compton, *Sensors and Actuators B: Chemical*, 2014, **200**, 47-52.
46. J. Chamberlain, *The Analysis of Drugs in Biological Fluids 2nd Edition*, CRC press, 1995.
47. A. Waugh and A. Grant, *Ross and Wilson Anatomy and Physiology in Health and Illness – Twelfth edition*, Churchill Livingstone, 2014.
48. H. A. Heering, M. S. Mondal and F. A. Armstrong, *Analytical Chemistry*, 1999, **71**, 174-182.
49. C. L. Mangun, K. R. Benak, M. A. Daley and J. Economy, *Chemistry of Materials*, 1999, **11**, 3476-3483.

Chapter 8

An Amperometric method for blood pH sensing

In this chapter, amperometric pH sensing in samples of sheep's blood is investigated. Initially, the surface quinones on graphite electrodes were employed for the study. However, in terms of signal size and the lack of robustness of the developed electrodes, micro-disc carbon fibre electrodes appeared to be less than optimal to use for study in biological samples with complex matrices such as blood (Refer to Appendix E). This led to further investigation using a metal/metal oxide system for pH sensing. Specifically, the study and exploitation of iridium oxide electrodes for amperometric pH sensing in sheep's blood were carried out, shown to be superior, and are described in this chapter. The iridium oxide electrodes are made by electrodeposition of iridium oxide onto an iridium micro-disc electrode from an alkaline solution of iridium(III) oxide. The response of the electrode is studied in aqueous solutions and authentic samples of sheep's blood employing both cyclic voltammetry and square wave voltammetry. Uncertainties of pH measurement in blood samples via cyclic voltammetry (±0.07 pH units) were improved by a factor of two using square wave voltammetry (±0.03 pH units). Limitations of amperometric pH sensing in blood samples are considered as caused by the uncertainty of the required reference measurements (via a conventional glass electrode) and also the use of matrix-free and low ionic strength buffers to calibrate a standard glass electrode for the measurement of blood pH.

The work presented in this chapter has been published in *Analyst*, 144, (2019), 1386-1393.[1]

8.1 Introduction

pH is probably the most frequently measured chemical parameter due to its importance in many areas including environmental monitoring, medical diagnosis, and quality control in food industry.[2-4] As recommended by IUPAC, pH is defined in terms of the single ion activity of the hydrogen ion in solution

$$\mathrm{pH} = -\log a_{H^+} = -\log(m_{H^+}\gamma_{H^+}/m^{\ominus})$$

in which a_{H^+} is the relative (molality basis) activity and γ_{H^+} is the activity coefficient of the hydrogen ion (H^+) at the molality m_{H^+}, and $m^{\ominus}$ is the standard molality (1 mol kg^{-1}).[5] It is noteworthy that the IUPAC-recommended definition of pH has been mentioned and argued as an ambiguous definition of the measured quantity. A detailed description of the historical development of pH and the complexity of pH measurement appears in a review by de Levie.[6] The activity coefficient of individual ions cannot be defined uniquely or measured.[7] From thermodynamic studies of electrolytic solutions one always obtains mean activity coefficients ($\gamma_{\pm}$) for combinations of ions. The validity of the experimentally derived values of the single ion activities is still under dispute. Significant work has focussed on the estimation of the single ion activity coefficients of H^+ and Cl^- from the mean activity of HCl, on the basis of the hydration model.[8, 9] In 2011, Sakaida *et al.* proposed the experimental procedure to estimate the values of individual ion activity of H^+ and Cl^- to the extent of the accuracy of the liquid junction potential which is the use of ionic liquid salt bridge.[10] The experimental values show the fairly good agreement with the recent theoretical predictions extending of Debye-Huckel theory proposed by Fraenkel.[11, 12] Although considerable literature reported an experimental estimation and a

theoretical prediction of single ion activities, IUPAC-recommendation of the single ion activity for the pH in aqueous solutions is based on the Harned cell.[5] The Harned cell (a hydrogen electrode and silver/silver-chloride electrode in a cell without a liquid junction) is a primary method of measurement in order to incorporate pH determinations into the SI system, based on a well-defined measurement equation in which all of the variables can be determined experimentally.[13] The activity coefficient is estimated by help of the Debye-Hückel theory. All measurements are restricted to samples with ionic strength ≤ 0.1 mol kg^{-1}.[14, 15] At higher ionic strength (I > 0.1 mol kg^{-1}), the activity coefficient cannot be evaluated by the Debye-Hückel limiting law leading to an uncertain value of the activity of hydrogen ion. In terms of biological fluids, it is noteworthy that the ionic strength of blood is normally about 0.15 M. [16, 17] Consequently, pH measurements in blood samples become operationally defined. The measured values depend on the measurement procedure and have their own uncertainty. In terms of practical usage, the use of low ionic strength buffer to calibrate a glass electrode for high ionic strength solution pH measurements may lead to an erroneous reading from a pH meter and this value might not be a true representation of the measurand.

In this chapter, we focus on using an iridium oxide electrode for amperometric pH measurement of blood. This system is selected due to its long history of being developed and repeatedly used as potentiometric pH sensors in other applications.[18-21] In order to generate an iridium oxide layer on a conducting metal, iridium oxide can be deposited (a) thermally [22-24], (b) by sputtering [25, 26], (c) by sol-gel method [27], or (d) electrochemically.[28-30] The characteristics of iridium oxide are generally sensitive to its structure and composition, which depend on the fabrication method and

conditions. Thermally and sputtering prepared iridium oxide give dry oxide films or anhydrous films that are less hydrous than electrochemically prepared iridium oxide deposited from an aqueous solution. Overviews of different preparation methods were provided by Huang *et al.*[31], Kakooei *et al.*[32], and Yao *et al*.[22] Consequently, it is important to investigate how accurate and precisely we can define pH using this system. Note that the accuracy is the closeness between a measured value and true value of measurand, while precision is the closeness of agreement between independent measurements of a quantity under the same condition without reference to a theoretical or true value. In this chapter, the iridium oxide electrodes are made by electrodeposition of iridium oxide onto iridium micro-disc electrode and are tested in aqueous solutions of variable pH and in authentic samples of sheep's blood. Cyclic voltammetry and square wave voltammetry are employed to study the limitations of amperometric pH sensing of blood.

8.2 Experimental

8.2.1 Electrode preparations

Paint deposition. An iridium wire (100 μm in diameter, GoodFellow, UK) was insulated using cathodic electrophoretic paint (Clearclad HSR, LSV Coating, UK). The paint coating procedure was adapted from Ellison *et al*.[33] The wire was held vertically in a centre of a conducting metal cell with a diameter of 1 cm. A constant DC voltage of 30 V was applied for 2 min between the iridium wire and the metal cell. After deposition, the iridium wire was then heated at 120 °C for 30 minutes to cure the deposited insulating film. Repeated deposition and cure steps were performed 3

times to obtain insulated electrodes. The thickness of paint coating layers was 18.3±2.6 μm (n=3) as evaluated from microscope imaging.

Iridium oxide deposition. The iridium containing deposition solution was prepared according to the method described by Baur *et al.*[34] and Salimi *et al.*[35] The preparation of this solution consists of two steps. The first step is the formation of the diaquatetrachloroiridate(III) ion ($Ir(H_2O)_2Cl_4^-$) from K_3IrCl_6. To prepare *ca.* mM solutions of $IrCl_6^{3-}$, potassium hexachloroiridate(III) (K_3IrCl_6) (Aldrich) is dissolved in 0.1M HCl and the solution is heated at 80-85°C for 2 h:

$$IrCl_6^{3-} + 2H_2O \xrightarrow[85°C,\ 2h]{0.1M\ HCl} Ir(H_2O)_2Cl_4^- + 2Cl^-$$

At this point, the prepared solution is reportedly stable and can be stored for several months.[34] The second step is the formation of iridium(III) oxide from $Ir(H_2O)_2Cl_4^-$ by making the solution of $Ir(H_2O)_2Cl_4^-$ basic according to the following reaction:

$$2Ir(H_2O)_2Cl_4^- + 8NaOH \longrightarrow Ir_2O_3{\bullet}xH_2O + (7\text{-}x)H_2O + 2OH^- + 8NaCl$$

Prior to addition of the base, oxygen must be removed from the acidic solution of $Ir(H_2O)_2Cl_4^-$ due to the instability of iridium(III) oxide under oxygen. After a thorough degassing with nitrogen gas, the pH of solution is raised to 10.5-11.5 by adding 0.1M NaOH, and this solution is used for the deposition of iridium oxide onto the iridium wire micro-disc electrode.

An insulated iridium wire was cut at the tip to generate a micro-disc electrode. Then the clean electrode was immersed in the deposition solution containing 1mM iridium(III)complexes and the potential cycled from +0.2 to +1.2 V at scan rate of 50

mV s^{-1} for 15 cycles (unless stated otherwise). Cyclic voltammograms of consecutive scans showed an increasing of the currents suggesting of the formation of an electroactive deposit on the electrode surface (Appendix F). The formation of iridium(IV) oxide layers is initiated electrochemically at the surface of iridium micro-disc electrode based on the following reaction which is modified from Baur and Spaine's work.[34]

$$Ir_2O_3 \bullet xH_2O_{(aq)} + 2OH^- + (x\text{-}1)H_2O \longrightarrow 2[IrO_2 \bullet xH_2O]_{(s)} + 2e^-$$

After deposition, the iridium micro-disc electrodes modified with iridium oxide films were cleaned with deionised water and dried with nitrogen gas.

8.2.2 Chemicals and reagents

All chemicals and reagents used were of analytical grade. Solutions were prepared using deionised water (Millipore, resistivity at 18.2 MΩ cm at 25 °C). Buffer solutions were prepared using citric acid/sodium citrate for the pH range 2.5–5.0 and monosodium phosphate/disodium phosphate for the pH range 5.0–9.0. All solutions contained 100 mM KCl as supporting electrolyte. The pH values of buffers were measured using a HACH LANGE Sension+ PH31 pH meter calibrated using standard buffers of pH 4.01 ± 0.01, 7.00 ± 0.01, and 10.01 ± 0.01. Defibrinated sheep's blood was purchased from TCS Biosciences Ltd, UK and the pH adjusted using vapour withdrawal carbon dioxide gas (BOC, Guildford UK). Carbon dioxide gas was bubbling into sheep's blood samples for a few seconds to adjust the pH and the pH of the samples was recorded.

8.2.3 Apparatus

Electrochemical measurements were performed using a μAutolab II potentiostat (Metrohm-Autolab BV, Utrecht, Netherlands). A standard three electrode set up was used, consisting of a saturated calomel reference electrode (SCE +0.244 V vs. SHE, BASi Inc., Japan) and a platinum wire counter electrode, and an iridium oxide micro-disc working electrode. The electrochemical set up was thermostated in a Faraday cage at a constant value of 25.0 ± 0.2 °C.

8.3 Results and discussion

In the following sections, the electrodeposition of iridium oxide onto an iridium micro-disc electrode is demonstrated for use as a blood pH sensing probe. Defibrinated sheep's blood is used as a model for biological samples in general and blood samples in particular. Note that defibrinated sheep's blood is the blood without fibrin protein; fibrin is *mechanically* removed without the use of anticoagulants or other additives. First, the pH response of the iridium oxide layers on iridium micro-disc electrodes is studied in buffer solutions. Second, the voltammetric responses of the developed probe in sheep's blood are investigated via both cyclic and square wave voltammetry. Last, the scope and limitations of amperometric pH sensing in blood samples are critically considered.

8.3.1 pH response of the iridium oxide layers on iridium micro-disc electrodes in *buffer* solutions

The iridium oxide electrode was investigated for voltammetric pH measurement. Cyclic voltammetry in a range of buffer solutions in the presence of 0.1M KCl supporting electrolyte was conducted using an iridium oxide micro-disc electrode. The voltammetric response was measured from 0.0 V to +0.8 V for a buffer solution of pH 2 at a scan rate of 100 mV s^{-1}. The potential window was adjusted as a function of pH accordingly to accommodate the shift in potential and to best observe the response of the oxidation and reduction peak. The CVs of iridium oxide supported on the iridium micro-disc electrode was recorded in buffer solutions of pH 2-8. Figure 8.1 shows the results over the pH range 2-8. The inset of Figure 8.1 depict plots of the oxidation, reduction and midpoint potentials *vs.* pH for iridium micro-disc electrode modified with iridium oxide films; the slope of the linear shown is about 62.7±1.2, 57.5±1.2, and 67.9±1.5 mV per pH for midpoint potential, oxidation/reduction peak potentials respectively. The values obtained by extrapolating to pH 0, of midpoint potential, oxidation and reduction peak potentials are 596±7, 613±7, and 579±9 mV respectively.

Three possible redox processes have been reported by Pourbaix[36, 37] to be involved in the pH dependent redox response of an iridium oxide electrode as

$$Ir_2O_3 + 6H^+ + 6e^- \rightleftharpoons 2Ir + 3H_2O \quad (8.1)$$

$$IrO_2 + 4H^+ + 4e^- \rightleftharpoons Ir + 2H_2O \quad (8.2)$$

$$2IrO_2 + 2H^+ + 2e^- \rightleftharpoons Ir_2O_3 + H_2O \quad (8.3)$$

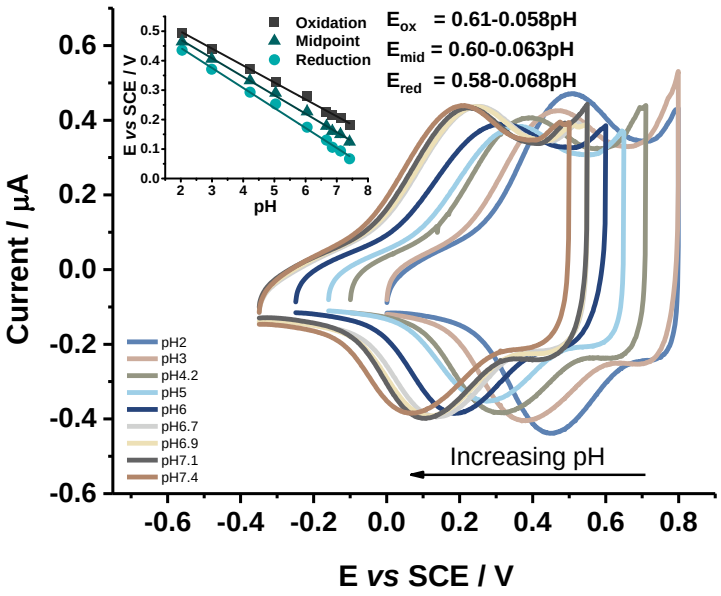

Figure 8.1 Cyclic voltammetry responses of iridium oxide on iridium micro-disc electrode at different pH of *buffer* solutions; scan rate of 100 mV s^{-1}. Inset shows the variation of potential *vs* pH.

and the Nernst equation is

$$E = E^0 - 2.303\frac{mRT}{nF}pH \qquad (8.4)$$

where m and n are number of protons and electrons involved in the redox process, respectively. The theoretical standard electrode potential (E^0) given by Pourbaix[36, 37] for each equilibrium is identical with a value of 926 mV vs SHE or 681 mV vs SCE. From equation 8.1-8.3 Nernstian responses have an expected slope of 59 mV/pH at 25°C. This type of response is reported for anhydrous iridium oxide film resulting from procedures involving heat-treatment or sputtering processes.[24, 38] For the electrochemically grown iridium oxide, this process results in amorphous films with varying hydration and possibly the presence of a hydrated oxyhydroxide.[39] Many redox reactions are possible between the reduced and oxidised forms of oxide and oxyhydroxide where the exact stoichiometric composition of hydrous film is difficult

to determine. The general equilibria investigated by Burke *et al.*[40] and Olthuis *et al.*[39] were

$$[-Ir^{IV}-(OH)_x-Ir^{IV}-]_n + 2ne^- + 3nH^+ \leftrightarrow [-Ir^{III}-(OH)_{x-3}\cdot 3H_2O-Ir^{III}-]_n \quad (8.5)$$

$$Ir_2O(OH)_3O_3^{3-} + 2e^- + 3H^+ \leftrightarrow 2Ir(OH)_2O^- + H_2O \quad (8.6)$$

The equilibrium (8.6) indicates that the theoretical sensitivity for this process predicts a shift in the equilibrium potential of 88.7 mV per pH unit (at 25°C). Moreover, the varying stoichiometric compositions of the hydrous film give rise to a super-Nernstian response ranging from 61 mV pH^{-1} to 90 mV pH^{-1} and electrodes that exhibit super-Nernstian slopes are generally assumed to have a mixed iridium oxide composition and be operating under a correspondingly mixed reaction mechanism.[18, 41, 42]

In terms of accuracy of pH measurement in buffer solutions using iridium oxide modified iridium micro-disc electrodes, to evaluate the measurement uncertainty, a linear regression was applied. The linear plot of midpoint potentials of iridium oxide tested in aqueous buffer solutions against pH (inset of Figure 8.1) was used to calculate uncertainties of pH measurement in buffer. Standard deviation of potential values deviated from the linear plot were calculated and converted to a pH unit using the calibrated sensitivity of the linear plot (Appendix G1). According to the estimation, uncertainties of pH measurement in buffer using iridium oxide electrode were found to be approximately ±0.1 pH units. This value is consistent with the literature where previous work has reported an accuracy of developed iridium oxide electrodes tested in aqueous solutions to be in the range of 0.02 – 0.2 pH units obtained from potentiometric measurement.[19, 43, 44] Note that in these literature

reports the reading from the glass electrode against which solutions are themselves calibrated was assumed to be absolute. However, as with any analytical technique the use of a glass electrode for the measurement of pH also has its own uncertainty. Significant work has been focussed on the assessment of uncertainty of pH measurements using glass electrode.[45-48] The main errors that limit the accuracy of pH measurement are errors arising from the standard buffers and from junction potentials which limit the accuracy with the glass electrode to *ca.* ±0.02 pH units.[49, 50] Apart from the limitations from the uncertainty of pH measurement of the glass electrode in buffer solutions, quantitative interpretation of measured pH values is limited to dilute aqueous solutions of simple solutes. This requirement results in limitations of the glass electrode for use in non-aqueous media, suspensions, colloids, and aqueous solutions of ionic strength greater than 0.1 mol kg^{-1}. Note that the uncertainty of pH measurement of the glass electrode used in this study was found to be *ca.* ±0.01 pH units for aqueous buffer solutions and *ca.* ±0.02 pH units for sheep's blood samples. Briefly the uncertainty of pH the measurement using a glass electrode is determined by measuring pH of solutions either buffer or sheep's blood 10 times and the standard deviation of the measured values is calculated (Appendix G2).

8.3.2 Investigating the measurement of pH in *sheep's blood* samples

8.3.2.1 Cyclic voltammetric measurement of pH in sheep's blood

Having demonstrated the pH dependence of iridium oxide film voltammetric response from measurements in buffer solutions, the capabilities of the iridium oxide electrode for blood pH sensing were investigated by studying the electrode in sheep's

blood of different pH values. First the cyclic voltammetric response of iridium oxide at iridium micro-disc electrode in sheep's blood is considered. A sample of defibrinated sheep's blood was used as received without dilution. Carbon dioxide gas was employed to control and alter the pH of the sample. Iridium oxide electrode was set up in a cell together with a glass electrode to perform real time pH monitoring. The electrode was cleaned by DI water and dried between tests. The CV response was first measured from -0.5 V to +0.5 V for a sheep's blood solution of pH 7.4-7.5 at a scan rate of 100 mV s^{-1}, then the potential window was adjusted as a function of the pH. According to the first test in sheep's blood, the CV measured in sheep's blood shown in Figure 8.2 is more distorted compared to the CV tested in aqueous buffer solution.

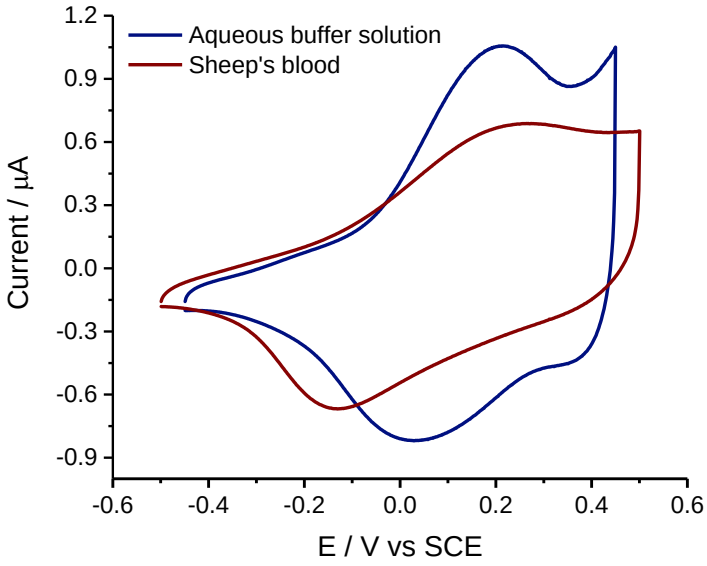

Figure 8.2 Comparison of cyclic voltammetric responses of 0.1M phosphate buffer (pH7.4) and sheep's blood (pH 7.5) at iridium oxide on iridium micro-disc electrode; scan rate of 100 mV s^{-1}.

In order to investigate a possible improvement of the peak to peak separation, the thickness of iridium oxide film was varied by changing the number of deposition

cycles. Deposition procedure was described in section 8.2.1. Briefly, the iridium micro-disc electrode was dipped in the deposition solution and the potential cycled from +0.2 V to +1.2 V at scan rate of 50 mV s^{-1} for 2, 5, 8, 15, and 30 cycles. The CV responses of iridium oxide on iridium micro-disc electrode were measured in sheep's blood. As thickness of the iridium oxide layer increases by increasing the number of deposition cycles, the obtained cyclic voltammograms tested in sheep's blood became less "reversible", as shown in Figure 8.3. The peak separation (ΔE_p) values were 240mV, 200mV, 266mV, 284mV and 295 mV for 2, 5, 8, 15, and 30 deposition cycles respectively. Considering the peak to peak separation and the definition of the peak, 5 deposition cycles was chosen as an optimal condition to prepare iridium oxide film in this study.

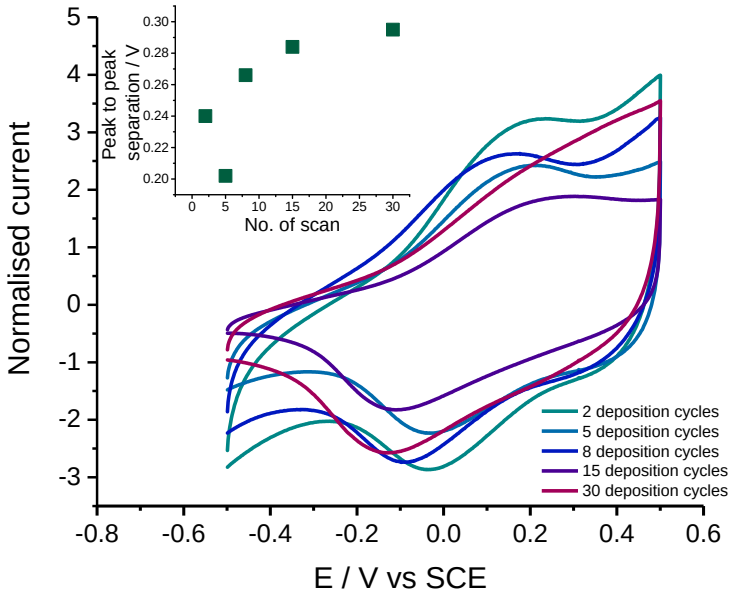

Figure 8.3 Optimisation of iridium oxide thickness varying by differing number of scans (2, 5, 8, 15, and 30 scans). Normalised cyclic voltammetry response of electrodeposition of iridium oxide on iridium micro-disc electrode of *sheep's blood* samples; scan rate of 100 mV s^{-1}. Inset: plot of peak to peak separation against number of electrodeposition cycles.

After the optimisation of iridium oxide thickness, the cyclic voltammetric response for iridium oxide on the iridium micro-disc electrode was recorded in sheep's blood solutions of pH 6.5-7.5. Figure 8.4(A) shows the overlaid representative CVs of iridium oxide supported on the iridium micro-disc electrode in sheep's blood solutions of different pH at a scan rate of 100 mV s^{-1}. It can be observed that by increasing the pH, peak potentials shift in the cathodic direction towards more negative values. The oxidation, reduction, and midpoint potentials were recorded (n=22). The plots of peak potentials against pH monitored by the pH meter are shown in Figure 8.4(B). The gradients of the slopes were 90.4±4.6, 81.2±7.7, and 99.5±8.6 mV per pH unit for midpoint potential, oxidation/reduction peak potentials respectively. The uncertainty of the pH measurement from the midpoint potential is ±0.07 pH unit calculated using the same method as mentioned in section 8.3.1 (see Appendix G1).

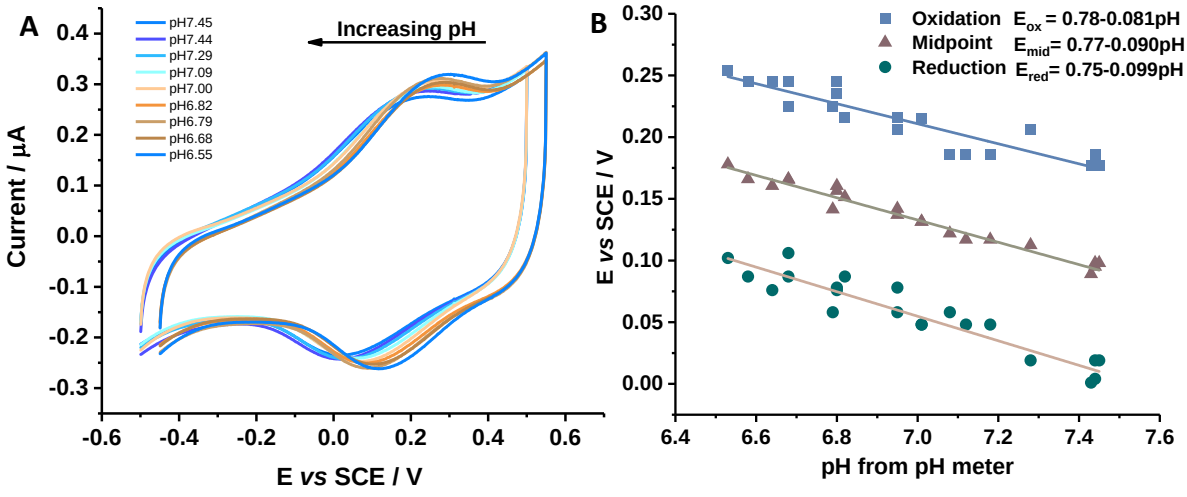

Figure 8.4 (A) Cyclic voltammetry responses of iridium oxide on iridium micro-disc electrode with varying pH of *sheep's blood* samples ranging from 6.5 to 7.5. (B) Plots of potentials against pH value reading from pH meter.

Considering voltammetric responses obtained in sheep's blood, the peaks were not as well defined as, and are more distorted in comparison with, the CVs of buffer solutions. This leads to difficulty in determining the peak position which may cause uncertainty of peak measurement. In terms of peak to peak separation as mentioned earlier the obtained CV tested in sheep's blood became less "reversible" with a peak to peak separation of *ca.* 200 mV compared to CV of electrode tested in buffer solutions where peak to peak separation is 50 mV. The peak to peak separation is larger in sheep's blood partly because the presence of complex matrix in blood may have an effect on the electron transfer process of Ir/IrOx electrode.

Considering the apparent standard electrode potential of the redox reaction ($E^{0'}$),[51, 52] the y-intercepts at pH = 0 of linear plot of midpoint potential *vs* pH indicated that $E^{0'}$ was 596±7 mV vs SCE for electrodes studied in buffer solutions (Inset Figure 8.1). However, the intercepts from plots of midpoint potentials against pH from CVs tested in sheep's blood were 765±32 mV (Figure 8.4(B)). Possibilities of the differences of $E^{0'}$ may cause by irreproducibility of the electrochemical measurements or a matrix effect of the blood samples. To study the reproducibility of the electrochemical measurements, iridium oxide electrodes were tested in buffer and sheep's blood again to study the reproducibility of measurements in different samples. Considering $E^{0'}$ for electrodes studied in buffer solutions, values were slightly shifted between experiments to experiments in the range of 586±4 mV – 596±7 mV (data shown in Appendix G3). However, the y-intercept from the sheep's blood samples experiments shifted in the range of 752±39 – 817±47 mV. This result shows that the differences of $E^{0'}$ value is not caused by the irreproducibility of the electrodes, but by a matrix effect of blood samples, probably specific chemical or

medium effects as reflected in the proton activity coefficient. Electrodes in this work were stored in ambient air and can be used within a period of month. Note that the magnitude of the peaks decreases with storage time, but the peak positions do not change. To examine possible fouling effects on the electrodes, the electrodes were repeatedly tested in blood samples. On completion of the blood sample testing cyclic voltammograms were re-measured in aqueous buffer solution (pH=2). They were essentially identical to those obtained before the use of electrode in blood pH sensing experiments suggesting the reusability and robustness of the electrode.

8.3.2.2 Square wave voltammetric measurement of pH in sheep's blood

Having investigated the pH measurement of sheep's blood using cyclic voltammetry, square wave voltammetry (SWV) was next utilised to determine whether this technique can be employed to improve the measurement uncertainty. Owing to the ability of SWV to improve signal-to-noise ratios relative to those of in particular, cyclic voltammetry, one may expect an improvement of defined peaks facilitating peak position measurements.[53] The optimisation of SWV in sheep's blood sample including frequency, step potential, and amplitude was performed to obtain best quality square wave voltammetry for sheep's blood pH measurements (Appendix H). The optimised SWV parameters (frequency 15 Hz, amplitude 10 mV, and step potential 1 mV) were used to measure the pH of sheep's blood. SWV was conducted in variable pH of sheep's blood adjusted pH by bubbling carbon dioxide gas into blood samples (as above). The glass electrode and the iridium oxide probe were immersed in blood samples to monitor the pH of the solution simultaneously.

Therefore, electrochemical measurements data (peak potential) obtained are reported relative to the pH monitored by the pH meter. Square wave voltammetry scans were initially to increasingly positive potentials to obtain an oxidative peak and then scans were reversed in direction. Representative square wave voltammograms of iridium oxides in variable sheep's blood pH solutions are shown in Figure 8.5(A) and 8.5(B). A single SWV peak was seen in both scan directions. It can be observed that the peak potentials shift in a cathodic direction towards more negative potentials on increasing the pH both for oxidative and reductive scans. For analysis of the data, the oxidation/reduction peak potentials and midpoint potential of iridium oxide supported on iridium micro-disc electrode were all recorded (n=19). The plots of potentials against pH reading from pH meter are shown in Figure 8.5(C). The gradients of the slopes were 101.3±3.2, 82.0±4.2, and 120.8±3.0 mV per pH unit for midpoint potential, oxidation/reduction peak potentials respectively. In terms of an uncertainty of pH measurement in sheep's blood using iridium oxide electrode, the same method as mentioned in section 8.3.1 and Appendix G1 was applied. The uncertainty from midpoint potential was calculated to be ±0.03 pH unit which is an improvement of a factor of two compared to results from cyclic voltammetry. Moreover, the uncertainty from the glass pH meter itself is ±0.02 pH unit. The improvement of the pH measurement by using SWV is evidenced in terms of sensitivity and uncertainty of pH measurement.

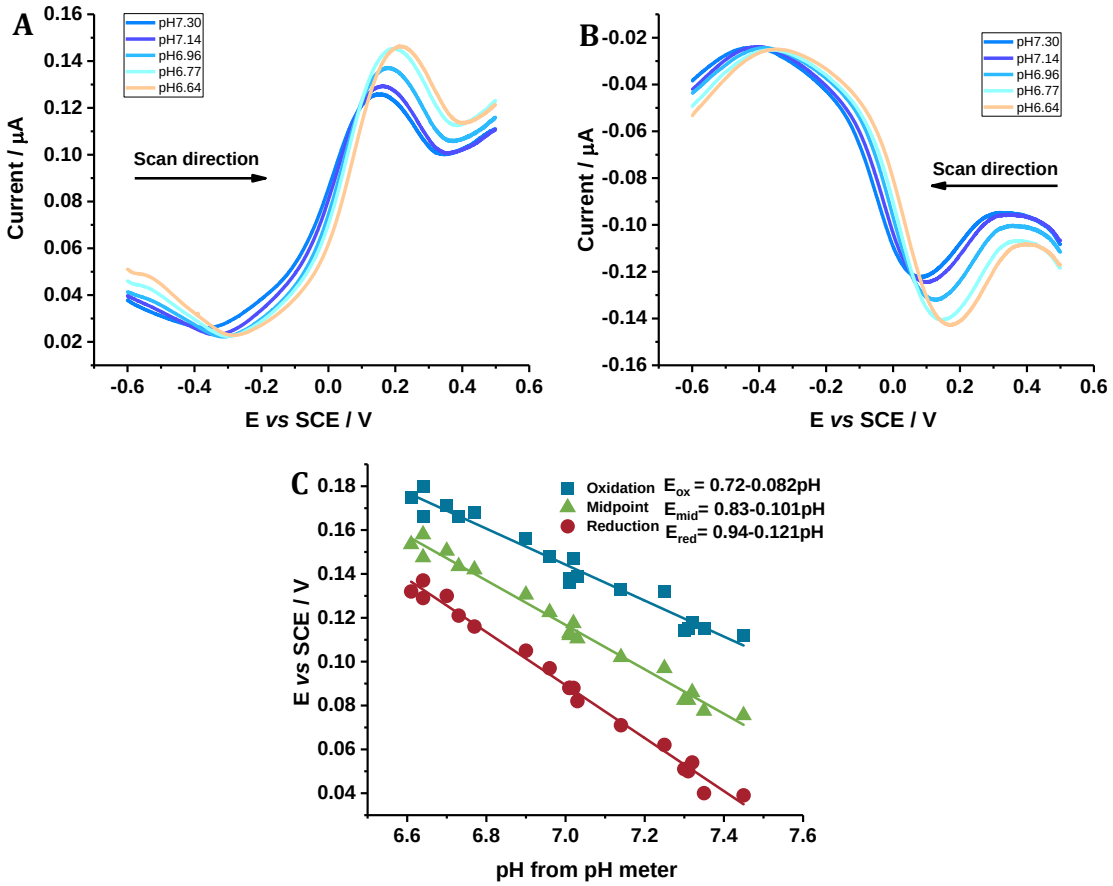

Figure 8.5 Square wave voltammetry (frequency 15 Hz, step potential 1 mV, and amplitude 10 mV) response of iridium oxide on iridium micro-disc electrode with varying pH of *sheep's blood* samples ranging from 6.5 to 7.5 (A) oxidation and (B) reduction. (C) Plots of potentials against pH value reading from pH meter.

8.3.3 Limitations of amperometric pH sensing in sheep's blood

Having investigated the measurement of pH in sheep's blood samples employing both CV and SWV, limitations of amperometric pH sensing in blood are next considered. First, precision of pH measurement of sheep's blood using a standard glass electrode is considered because of its use as a reference pH value for our developed method. Fundamentally, the absolute value of pH is not defined under

these conditions. Due to the definition of pH, the activity coefficients of individual ions cannot be defined uniquely or measured. Consequently, one cannot accurately know the pH value. Note that the accuracy is the closeness between a measured value and true value of measurand, therefore to assess the accuracy of measurement the true value is required. However, according to the way of measurement we can tell how precisely we can define the pH of sheep's blood from measurement. Note that as mentioned in section 8.3.1 an uncertainty of pH measurement of sheep's blood using a glass electrode in this study is about ±0.02 pH units. In consequence, precision of our developed method for pH measurement is considered next. The present findings show that an uncertainty of pH measurement in sheep's blood using CV is ±0.07 pH units and can be reduced to ±0.03 pH units using SWV. However, the apparent uncertainty of our measurements should also consider the uncertainty of reference measurement (glass electrode) and the uncertainty from our method. Because both methods have their own uncertainty, therefore, the apparent uncertainty is necessarily more than what we obtain from any new method itself. Uncertainties reported in this work assumed that pH reading from the pH meter was absolute. Moreover, another important point to consider is the effect of the matrix in different samples both in terms of buffers versus blood and also blood sample to blood sample. There are the practical difficulties in using matrix-free buffers of low ionic strength to calibrate a glass electrode for blood pH measurement. Consequently, pH readings when measuring the pH of blood might not be an exact value of blood pH. To address the problem of using matrix-free buffers to calibrate a standard glass electrode, standard reference buffer solution(s) of synthetic biological fluids or blood samples in particular may need to be developed to reduce error in the measured values.

Furthermore, development and testing of a suitable model for the activity coefficients of acid-base components in such a blood medium needs to be considered.

8.4 Conclusions

An iridium oxide electrode supported on an iridium micro-disc electrode is used as a pH probe for studying amperometric blood pH measurements. We have evidenced the possibility of iridium oxide electrode as a blood pH sensing. The scope and limitations of amperometric pH sensing in real blood samples resulting in an uncertainty of pH measurement are considered as follows: First, to estimate an uncertainty of our proposed method, the uncertainty of reference measurements which is a conventional glass electrode need to be taken into account because both methods have their own uncertainty. This may lead to a higher of the apparent uncertainty than the uncertainty obtained from any new method itself. Second, the effect of the matrix in samples can cause an uncertain measurement resulting from the use of matrix-free and low ionic strength buffers to calibrate a standard glass electrode for measurement of high matrix blood pH.

Bibliography

1. K. Chaisiwamongkhol, C. Batchelor-McAuley and R. G. Compton, *Analyst*, 2019, **144**, 1386-1393.
2. V. M. C. Rérolle, C. F. A. Floquet, M. C. Mowlem, D. P. Connelly, E. P. Achterberg and R. R. G. J. Bellerby, *TrAC Trends in Analytical Chemistry*, 2012, **40**, 146-157.
3. Y. M. Dong, E. I. F. Pearce, L. Yue, M. J. Larsen, X. J. Gao and J. D. Wang, *Caries Research*, 1999, **33**, 428-436.
4. X. Zhang, Y. Lin and R. J. Gillies, *Journal of nuclear medicine : official publication, Society of Nuclear Medicine*, 2010, **51**, 1167-1170.
5. R. P. Buck, S. Rondinini, A. K. Covington, F. G. K. Baucke, M. A. Brett Christopher, M. F. Camoes, M. J. T. Milton, T. Mussini, R. Naumann, K. W. Pratt, P. Spitzer and G. S. Wilson, *Pure and Applied Chemistry*, 2002, **74**, 2169-2200.

6. R. de Levie, *Electrochimica Acta*, 2014, **135**, 604-639.
7. P. Hünenberger and M. Reif, *Single-ion Solvation: Experimental and Theoretical Approaches to Elusive Thermodynamic Quantities*, Royal Society of Chemistry, 2011.
8. R. G. Bates, B. R. Staples and R. A. Robinson, *Analytical Chemistry*, 1970, **42**, 867-871.
9. R. H. Stokes and R. A. Robinson, *Journal of the American Chemical Society*, 1948, **70**, 1870-1878.
10. H. Sakaida and T. Kakiuchi, *The Journal of Physical Chemistry B*, 2011, **115**, 13222-13226.
11. D. Fraenkel, *Molecular Physics*, 2010, **108**, 1435-1466.
12. D. Fraenkel, *The Journal of Physical Chemistry B*, 2011, **115**, 557-568.
13. H. S. Harned and B. B. Owen, *The physical chemistry of electrolytic solutions*, Reinhold Pub. Corp., 1950.
14. R. G. Bates, *Determination of pH; theory and practice*, Wiley, New York, 1973.
15. P. Debye and E. Hückel, *Physikalische Zeitschrift*, 1923, **24**, 185-206.
16. A. K. Covington and R. A. Robinson, *Analytica Chimica Acta*, 1975, **78**, 219-223.
17. M. Rasia and A. Bollini, *Biochimica et Biophysica Acta (BBA) - Biomembranes*, 1998, **1372**, 198-204.
18. S. R. Ng and D. O'Hare, *Analyst*, 2015, **140**, 4224-4231.
19. S. A. M. Marzouk, S. Ufer, R. P. Buck, T. A. Johnson, L. A. Dunlap and W. E. Cascio, *Analytical Chemistry*, 1998, **70**, 5054-5061.
20. J. Park, M. Kim and S. Kim, *Sensors and Actuators B: Chemical*, 2014, **204**, 197-202.
21. M. L. Zamora, J. M. Dominguez, R. M. Trujillo, C. B. Goy, M. A. Sánchez and R. E. Madrid, *Sensors and Actuators B: Chemical*, 2018, **260**, 601-608.
22. S. Yao, M. Wang and M. Madou, *Journal of The Electrochemical Society*, 2001, **148**, H29-H36.
23. Y. Sato, K. Ono, T. Kobayashi, H. Wakabayashi and H. Yamanaka, *Journal of The Electrochemical Society*, 1987, **134**, 570-575.
24. M. Wang, S. Yao and M. Madou, *Sensors and Actuators B: Chemical*, 2002, **81**, 313-315.
25. S. F. Cogan, T. D. Plante and J. Ehrlich, *Conference proceedings : ... Annual International Conference of the IEEE Engineering in Medicine and Biology Society. IEEE Engineering in Medicine and Biology Society. Annual Conference*, 2004, **6**, 4153-4156.
26. M. J. Tarlov, S. Semancik and K. G. Kreider, *Sensors and Actuators B: Chemical*, 1990, **1**, 293-297.
27. C. M. Nguyen, S. Rao, X. Yang, S. Dubey, J. Mays, H. Cao and J.-C. Chiao, *Sensors (Basel, Switzerland)*, 2015, **15**, 4212-4228.
28. P. VanHoudt, Z. Lewandowski and B. Little, *Biotechnology and Bioengineering*, 1992, **40**, 601-608.
29. Y. Kazusuke, *Japanese Journal of Applied Physics*, 1989, **28**, 632.
30. H. A. Elsen, C. F. Monson and M. Majda, *Journal of The Electrochemical Society*, 2009, **156**, F1-F6.
31. W. D. Huang, H. Cao, S. Deb, M. Chiao and J. C. Chiao, *Sensors and Actuators A: Physical*, 2011, **169**, 1-11.
32. S. Kakooei, M. C. Ismail and B. Ari-Wahjoedi, *Int. J. Mater. Sci. Innovat*, 2013, **1**, 62-72.
33. J. Ellison, S. Eloul, C. Batchelor-McAuley, K. Tschulik, C. Salter and R. G. Compton, *Journal of Electroanalytical Chemistry*, 2015, **745**, 66-71.
34. J. E. Baur and T. W. Spaine, *Journal of Electroanalytical Chemistry*, 1998, **443**, 208-216.
35. A. Salimi, M. E. Hyde, C. E. Banks and R. G. Compton, *Analyst*, 2004, **129**, 9-14.
36. M. Pourbaix, J. Van Muylder, N. d. Zoubov and c. Centre belge d'étude de la, *Atlas d'équilibres Thermodinamiques à 25° C*, Gauthier-Villars et Cie, Paris, 1963.
37. A. J. Bard, R. Parsons, J. Jordan, P. International Union of and C. Applied, *Standard potentials in aqueous solution*, M. Dekker, New York, 1985.
38. S. Ardizzone, A. Carugati and S. Trasatti, *Journal of Electroanalytical Chemistry and Interfacial Electrochemistry*, 1981, **126**, 287-292.
39. W. Olthuis, M. A. M. Robben, P. Bergveld, M. Bos and W. E. van der Linden, *Sensors and Actuators B: Chemical*, 1990, **2**, 247-256.
40. L. D. Burke, M. E. Lyons, E. J. M. O'Sullivan and D. P. Whelan, *Journal of Electroanalytical Chemistry and Interfacial Electrochemistry*, 1981, **122**, 403-407.
41. S. Carroll and R. P. Baldwin, *Analytical Chemistry*, 2010, **82**, 878-885.
42. L. D. Burke, J. K. Mulcahy and D. P. Whelan, *Journal of Electroanalytical Chemistry and Interfacial Electrochemistry*, 1984, **163**, 117-128.
43. A. N. Bezbaruah and T. C. Zhang, *Analytical Chemistry*, 2002, **74**, 5726-5733.

44. M. L. Hitchman and S. Ramanathan, *Analyst*, 1988, **113**, 35-39.
45. R. P. Buck, S. Rondinini, A. K. Covington, F. G. K. Baucke, M. A. Brett Christopher, M. F. Camoes, M. J. T. Milton, T. Mussini, R. Naumann, K. W. Pratt, P. Spitzer and G. S. Wilson, *Journal*, 2002, **74**, 2169.
46. G. Meinrath and P. Spitzer, *Microchimica Acta*, 2000, **135**, 155-168.
47. P. Spitzer, *Accreditation and Quality Assurance*, 2001, **6**, 55-60.
48. P. Spitzer, R. Eberhardt, I. Schmidt and U. Sudmeier, *Fresenius' Journal of Analytical Chemistry*, 1996, **356**, 178-181.
49. I. Leito, L. Strauss, E. Koort and V. Pihl, *Accreditation and Quality Assurance*, 2002, **7**, 242-249.
50. D. C. Harris, C. A. Lucy, H. University of North Carolina at Chapel and C. Department of, *Quantitative chemical analysis*, Freeman Custom Publishing, New York, NY, 2016.
51. M. L. Hitchman and S. Ramanathan, *Talanta*, 1992, **39**, 137-144.
52. M. L. Hitchman and S. Ramanathan, *Electroanalysis*, 1992, **4**, 291-297.
53. C. M. A. Brett and A. M. O. Brett, *Electrochemistry : principles, methods, and applications*, Oxford University Press, Oxford, 1993.

Chapter 9

Overall conclusions

This thesis has developed electrochemical sensors for applications in food analysis and for medical diagnosis.

First, electrochemical methods for gingerol and curcumin detection were successfully developed and utilised for the voltammetric determination of these compounds in standard and real spice samples. The extraction of compounds of interest from real sample is simplified to a facile methodology resulting in a time-saving sample preparation. These rapid and easy-to-use methods will be useful for quality control applications in food industry and have been licensed to the company Zimmer & Peacock.

Different types of carbon materials for adsorptive stripping voltammetry were studied using cyclic voltammetry for a comparison as to their relative suitability in electrochemical sensing. Several forms of carbon materials and carbon electrodes are used in this study. The analytical performances; sensitivity and limit of detection of each electrode were compared. Insights into the optimisation of carbon electrode materials for adsorptive stripping voltammetry show that the *sensitivity* of responses depends strongly on the surface area of electrodes but much less on the type of carbon material. However, increasing the electrode surface area does not improve the *limit of detection*. This is because the increasing of surface area simultaneously enhances both the signals of adsorptive stripping peak (Faradaic signals) and capacitative current (non-Faradaic signal or background) resulting in an unchanged signal-to-background ratio.

The mechanism of generation of surface quinone functionality on edge plane pyrolytic graphite electrode was also investigated. The results show that the process of making quinone on pristine carbon surfaces is photosensitive especially to IR radiation. A mechanistic route involving singlet oxygen, $^1O_2$, was proposed and evidenced.

Another application of electrochemical detection considered in this thesis is for medical diagnosis. Sensors for pH measurement in saliva were developed with a view to dental caries identification. A pH sensitive micro-sized sensor was developed by using a carbon fibre electrode for the diagnosis of tooth decay via local measurements of pH. The surface quinone presence on the micro-wire electrode offers a simple pH amperometric pH sensor. The applications in human saliva without the need for oxygen removal are also highlighted.

Finally, the application for pH measurement in blood samples was investigated. An iridium oxide electrode was exploited for pH sensing in blood sample (sheep's blood). Uncertainties of pH measurement in sheep's blood were improved by using square wave voltammetry compared to cyclic voltammetry. This study considered the limitations of amperometric pH measurements in blood samples including the uncertainty of the required comparative reference measurements (via a conventional glass pH electrode) and also the use of matrix-free and low ionic strength buffers to calibrate a standard glass electrode for the measurement of blood pH, leading to uncertainties of measurements.

In summary, the results discussed in this thesis emphasise the potential of the electrochemical method for use in the food industry and by the clinical community as an alternative and simple analytical approach. Underpinning this work in fundamental studies, we first established general principles to offer guidance in the

optimal choice of carbon electrodes for AdsSV in different applications. Second, the reaction mechanism of atmospheric oxygen with a carbon electrode surface was evidenced to provide a possible pathway of generating surface quinone functionality.

Appendix A

A1 Calculation of the surface area of multiwalled carbon nanotubes on the BPPG electrode used in Chapter 3 - 5

Bamboo-like multiwalled carbon nanotubes (MWCNT) possess a *ca.* 30 nm diameter as provided by the supplier NanoLab and are *ca.*1.4 g cm^{-3} in density.[1]

In order to estimate the surface area of each material, first, the total volume of material casted on the BPPG electrode was calculated.

We had 20 x 10^{-3} mg of MWCNT on the bare BPPG electrode.

According to

$$\text{Density} = \frac{\text{Mass}}{\text{Volume}} \quad (1)$$

$$\text{Volume} = \frac{20 \text{ x } 10^{-6} \text{ g}}{1.4 \text{ g cm}^{-3}} \quad (2)$$

The total volume of MWCNT on the BPPG electrode was 1.4 x 10^{-5} cm^3.

MWCNT has cylindrical shape, thus we can calculate surface area of 1 nanotube from $2\pi rh$ and volume of 1 nanotube from $\pi r^2 h$.

Surface area of 1 NP = $2\pi rh$

= $2 \times \pi \times (15 \times 10^{-7} cm) \times (15 \times 10^{-4} cm)$

= $1.4 \times 10^{-8} cm^2$

Volume of 1 NP = $\pi r^2 h$

$$= \quad \pi \times (15 \times 10^{-7} cm)^2 \times (15 \times 10^{-4} cm)$$

$$= \quad 1.1 \times 10^{-14} cm^3$$

Number of nanotubes on the electrode $= \quad \frac{Total\ volume}{Volume\ of\ 1\ NP}$

$$= \quad \frac{1.4 \times 10^{-5} cm^3}{1.1 \times 10^{-14} cm^3}$$

$$= \quad 1.4 \times 10^9\ nanotubes$$

Total surface area = Surface area of 1 NP x Number of nanotubes

$$= \quad (1.4 \times 10^{-8} cm^2) \times (1.4 \times 10^9 nanotubes)$$

= 19.6 cm^2

The estimated surface area of MWCNT we used on the modified electrode is *ca.* 20 cm^2.

A2 Calculation of surface area of Carbon Black on the BPPG electrode used in Chapter 5

Carbon black (CB) particles are *ca.* 27 nm in diameter and have a density of *ca.*1.7-1.9 g cm^{-3}.[2]

In order to estimate the surface area of each material, first, the total volume of carbon black casted on the BPPG electrode was calculated.

We had 20 x 10^{-3} mg of CB on the bare BPPG electrode.

According to

$$\text{Density} = \frac{\text{Mass}}{\text{Volume}} \qquad (1)$$

$$\text{Volume} = \frac{20 \text{ x } 10^{-6} \text{ g}}{1.9 \text{ g cm}^{-3}} \quad (2)$$

The total volume of CB on the BPPG electrode was 1.1 x 10^{-5} cm^3.

CB has spherical shape, thus we can calculate surface area of 1 nanoparticle from $4\pi r^2$ and volume of 1 nanoparticle from $\frac{4}{3}\pi r^3$.

Surface area of 1 NP = $4\pi r^2$

= $4 \times \pi \times (13.5 \times 10^{-7} cm)^2$

= $2.29 \times 10^{-11} cm^2$

Volume of 1 NP = $\frac{4}{3}\pi r^3$

= $\frac{4}{3} \times \pi \times (13.5 \times 10^{-7} cm)^3$

= $1.03 \times 10^{-17} cm^3$

Number of particles on the electrode = $\frac{Total\ volume}{Volume\ of\ 1\ NP}$

= $\frac{1.1 \times 10^{-6} cm^3}{1.03 \times 10^{-17} cm^3}$

= $1.1 \times 10^{12}\ particles$

Total surface area = Surface area of 1 NP x Number of particles

= $(2.29 \times 10^{-11} cm^2) \times (1.1 \times 10^{12} particles)$

= 25.2 cm^2

The estimated surface area of CB we used on the modified electrode is *ca.* 25 cm^2.

A3 Calculation of the surface area of Graphene Nanoplatelets on the BPPG electrode used in Chapter 5

A Graphene nanoplatelet (GNP) is 7.1 nm thick and 16.5 μm wide with *ca.* 2.1 g cm^{-3} in density which is provided in Strem Company's specification sheet and experimentally derived results of Poon *et al*.[3]

We had 20 x 10^{-3} mg of GNP on the bare BPPG electrode.

According to

$$\text{Density} = \frac{\text{Mass}}{\text{Volume}} \quad (1)$$

$$\text{Volume} = \frac{20 \text{ x } 10^{-6} \text{ g}}{2.1 \text{ g cm}^{-3}} \quad (2)$$

The total volume of GNP on the BPPG electrode was 9.5 x 10^{-6} cm^3.

We assume that GNP has a cylindrical shape with top and bottom surfaces. Thus we can calculate the surface area of 1 nanoplatelet from 2πrh and also calculate the surface area of circular shape of the top and bottom of a platelet from πr^2. The volume of one nanoplatelet is calculated from $\pi r^2 h$.

Surface area of 1 NP = $2\pi rh + 2\pi r^2$

$$= [2 \times \pi \times (8.25 \times 10^{-4} cm) \times (7.10 \times 10^{-7} cm)]$$

$$+[2 \times \pi \times (8.25 \times 10^{-4} cm)^2]$$

$$= 4.28 \times 10^{-6} cm^2$$

Volume of 1 NP = $\pi r^2 h$

$$= \quad \pi \times (8.25 \times 10^{-4} cm)^2 \times (7.10 \times 10^{-7} cm)$$

$$= \quad 1.52 \times 10^{-12} cm^3$$

Number of platelets on the electrode $= \quad \frac{Total\ volume}{Volume\ of\ 1\ NP}$

$$= \quad \frac{9.5 \times 10^{-6} cm^3}{1.52 \times 10^{-12} cm^3}$$

$$= \quad 6.3 \times 10^6\ platelets$$

Total surface area = Surface area of 1 NP x Number of platelets

$$= \quad (4.28 \times 10^{-6} cm^2) \times (6.3 \times 10^6 platelets)$$

$$= \quad 27\ cm^2$$

The estimated surface area of GNP we used on the modified electrode is 27 cm^2.

Bibliography

1. Q. Zhang, J. Liu, R. Sager, L. Dai and J. Baur, *Composites Science and Technology*, 2009, **69**, 594-601.
2. D. Lowinsohn, P. Gan, K. Tschulik, J. S. Foord and R. G. Compton, *Electroanalysis*, 2013, **25**, 2435-2444.
3. J. Poon, C. Batchelor-McAuley, K. Tschulik and R. G. Compton, *Chemical Science*, 2015, **6**, 2869-2876.

Appendix B

Estimated capacitance of the electrode used in Chapter 5

In order to determine the capacitance of each electrode used in Chapter 5, CV experiments were conducted and recorded as a function of scan rates from 25-400 mV s^{-1} in a solution of 0.05 M Britton-Robinson buffer solution (pH 1.8). The capacitance was determined employing the relation of capacitance and scan rate shown in equation 5.1 in Chapter 5. The current amplitude difference (Δi) at a potential of 0.6 V (vs. SCE) was plotted as a function of scan rate. The capacitance of each electrode was calculated from the slope of the linear plot.

B1 Unmodified basal plane pyrolytic graphite electrode (Unmodified-BPPGE)

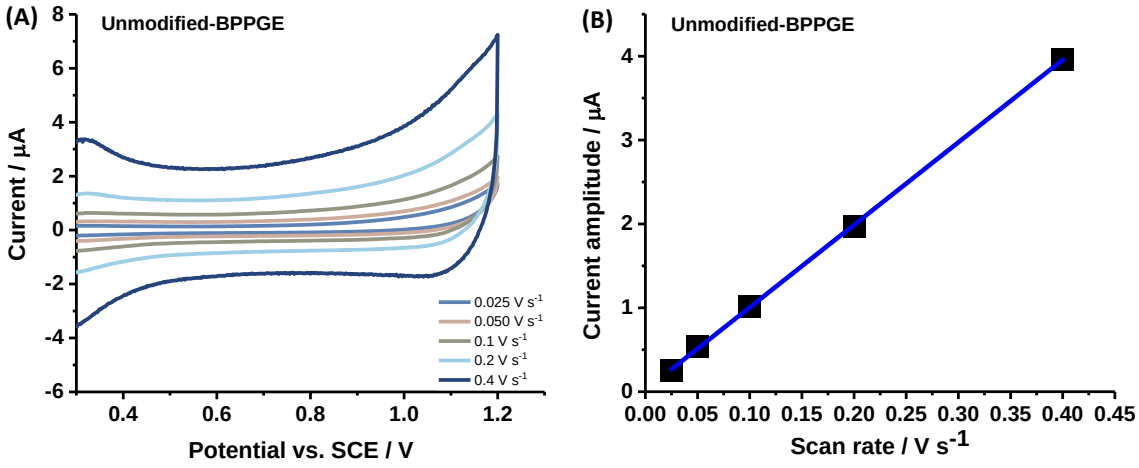

Figure B1 (A) CVs in 0.05 M Britton-Robinson buffer solution (pH 1.8) at bare BPPG electrode in different scan rates (25-400 mV s^{-1}). (B) A linear plot of current amplitude difference (Δi) collected at a potential of 0.6 V (vs. SCE) as a function of scan rate.

B2 Multiwalled carbon nanotubes modified basal plane pyrolytic graphite electrode (MWCNT-BPPGE)

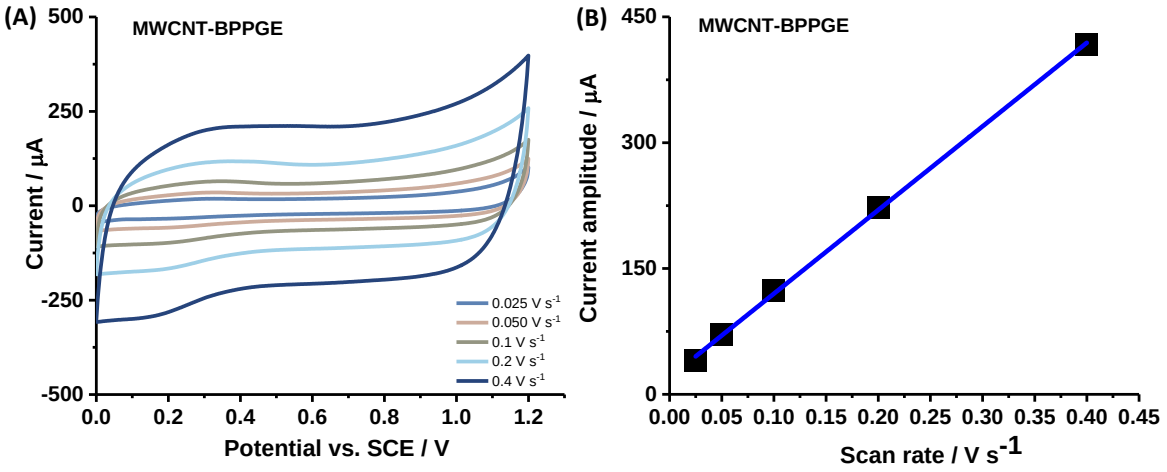

Figure B2 (A) CVs in 0.05 M Britton-Robinson buffer solution (pH 1.8) at MWCNT modified BPPG electrode in different scan rates (25-400 mV s^{-1}). (B) A linear plot of current amplitude difference (Δi) collected at a potential of 0.6 V (vs. SCE) as a function of scan rate.

B3 Carbon black modified basal plane pyrolytic graphite electrode (CB-BPPGE)

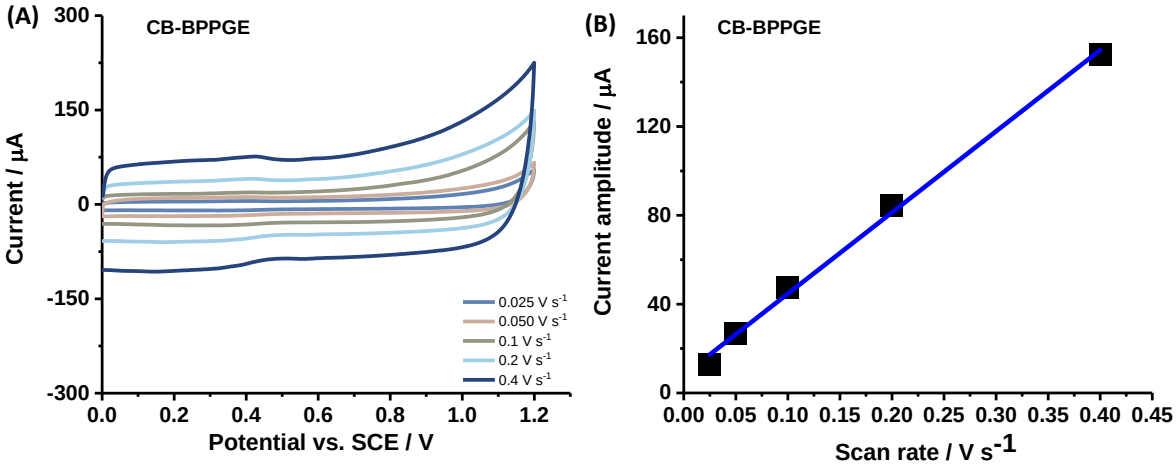

Figure B3 (A) CVs in 0.05 M Britton-Robinson buffer solution (pH 1.8) at CB modified BPPG electrode in different scan rates (25-400 mV s^{-1}). (B) A linear plot of current amplitude difference (Δi) collected at a potential of 0.6 V (vs. SCE) as a function of scan rate.

B4 Carbon screen printed electrode (C-SPE)

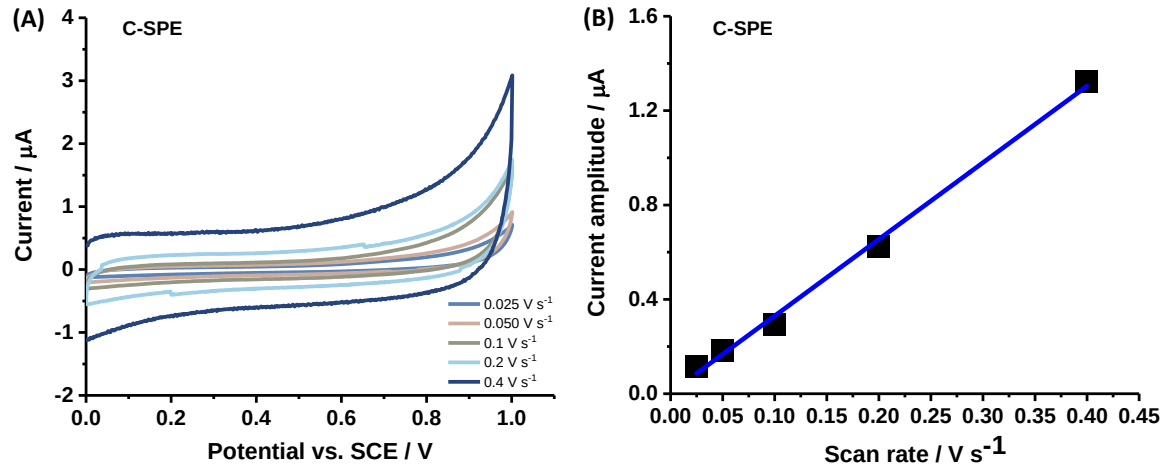

Figure B4 (A) CVs in 0.05 M Britton-Robinson buffer solution (pH 1.8) at carbon screen printed electrode in different scan rates (25-400 mV s^{-1}). (B) A linear plot of current amplitude difference (Δi) collected at a potential of 0.6 V (vs. SCE) as a function of scan rate.

B5 Carbon nanotubes modified screen printed electrode (CNT-SPE)

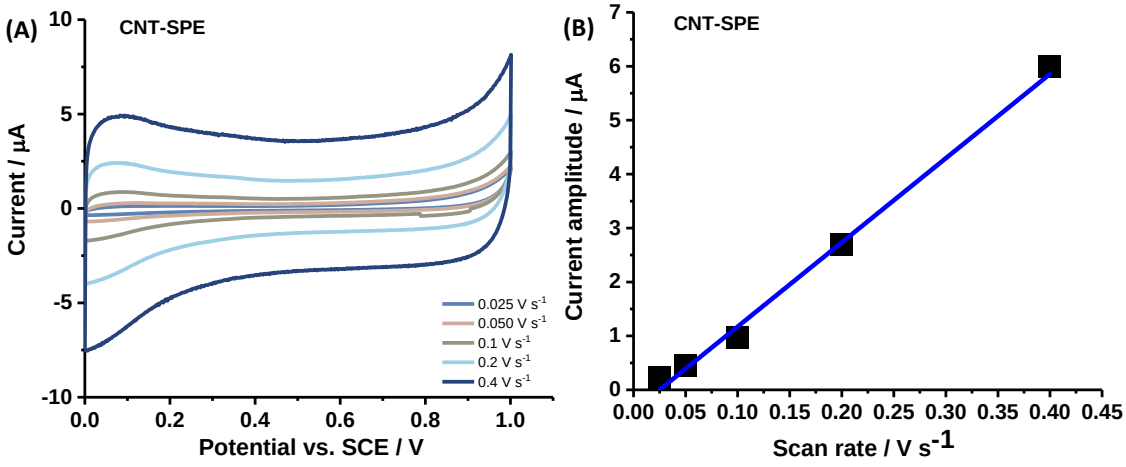

Figure B5 (A) CVs in 0.05 M Britton-Robinson buffer solution (pH 1.8) at carbon nanotubes screen printed electrode in different scan rates (25-400 mV s^{-1}). (B) A linear plot of current amplitude difference (Δi) collected at a potential of 0.6 V (vs. SCE) as a function of scan rate.

B6 Carbon paste electrode (CPE)

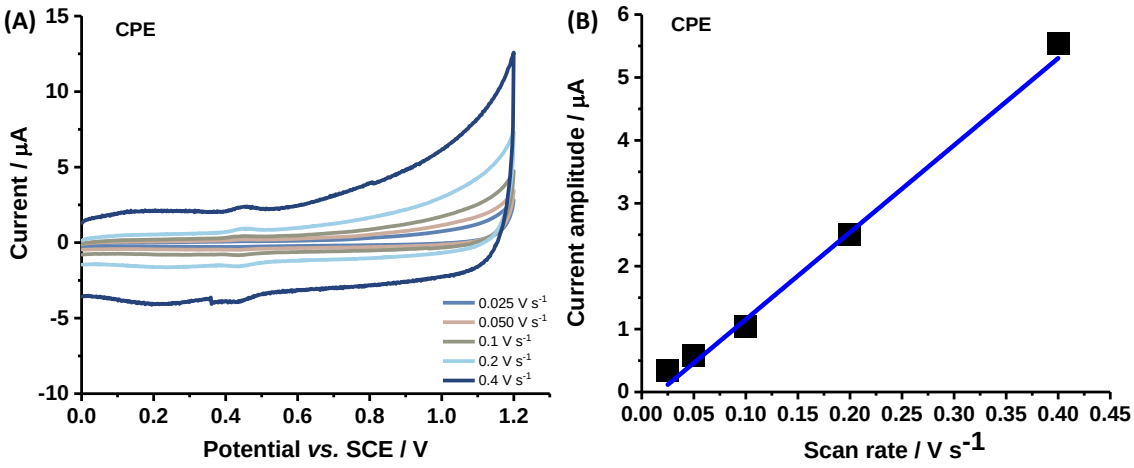

Figure B6 (A) CVs in 0.05 M Britton-Robinson buffer solution (pH 1.8) at carbon paste electrode in different scan rates (25-400 mV s^{-1}). (B) A linear plot of current amplitude difference (Δi) collected at a potential of 0.6 V (vs. SCE) as a function of scan rate.

Appendix C

X-ray photoelectron spectroscopy (XPS) study of the EPPG surface in Chapter 6

All XPS experiments and data analysis were conducted by Dr. Robert G. Palgrave.

X-ray photoelectron spectroscopy (XPS) was measured using a Thermo Fisher Scientific Theta Probe spectrometer, with a base pressure of 5×10^{-10} mbar and utilizing monochromated Al K alpha radiation (1486.6 eV). The analysis area was defined by the X-ray spot size which was 400 μm. Photoelectron kinetic energy was measured using a hemispherical analyser operated in constant analyser energy (CAE) mode with pass energy of 50 eV for high resolution spectra and 200 eV for survey spectra. The electron lens axis is 50° from the sample normal, and photoelectrons are accepted over an angular range of 60°. A 2D position sensitive detector was used. A dual beam (electron and Ar ion) charge compensation device was used to prevent charging of the sample surface. In situ etching was carried out using monoatomic Ar ion beam operated at 3000 V. Samples were polished in air and placed into the loadlock after 0, 40, 120 and 1440 minutes of air exposure. The '0 min' sample was loaded and evacuated to <1 mbar in less than 30 s from the end of the polishing process.

Figure C1 shows the representative of XPS data of EPPG electrode samples. The survey scans relevant to EPPG electrodes are reported in Figure C1(A). XPS analysis revealed the samples predominantly show carbon and oxygen with small

(<0.5 atomic%) amounts of N, Si and Al. The oxygen content relative to carbon varied between 6.8%-16.8% as shown in Table C1. High resolution scan of C1s and O1s from electrodes exposed to air for various times are illustrated in Figure C1(B) and (C) respectively. Argon ion etching significantly reduced the measured oxygen content of the surface (Figure C2), indicating that the oxygen rich layer is limited to the top few nanometers of the electrode. After 160 s of the etching to a depth of approximately 40 nm, the oxygen O1s signal drops below the detection limit of XPS as can be seen in Figure C2 and C3.

Table C1 Oxygen content relative to carbon from XPS analysis of all samples

Exposure time / min	**%Oxygen content**
0	6.8%-12.4%
40	8.1%-10.2%
120	6.9%-8.3%
1440	7.2%-16.8%

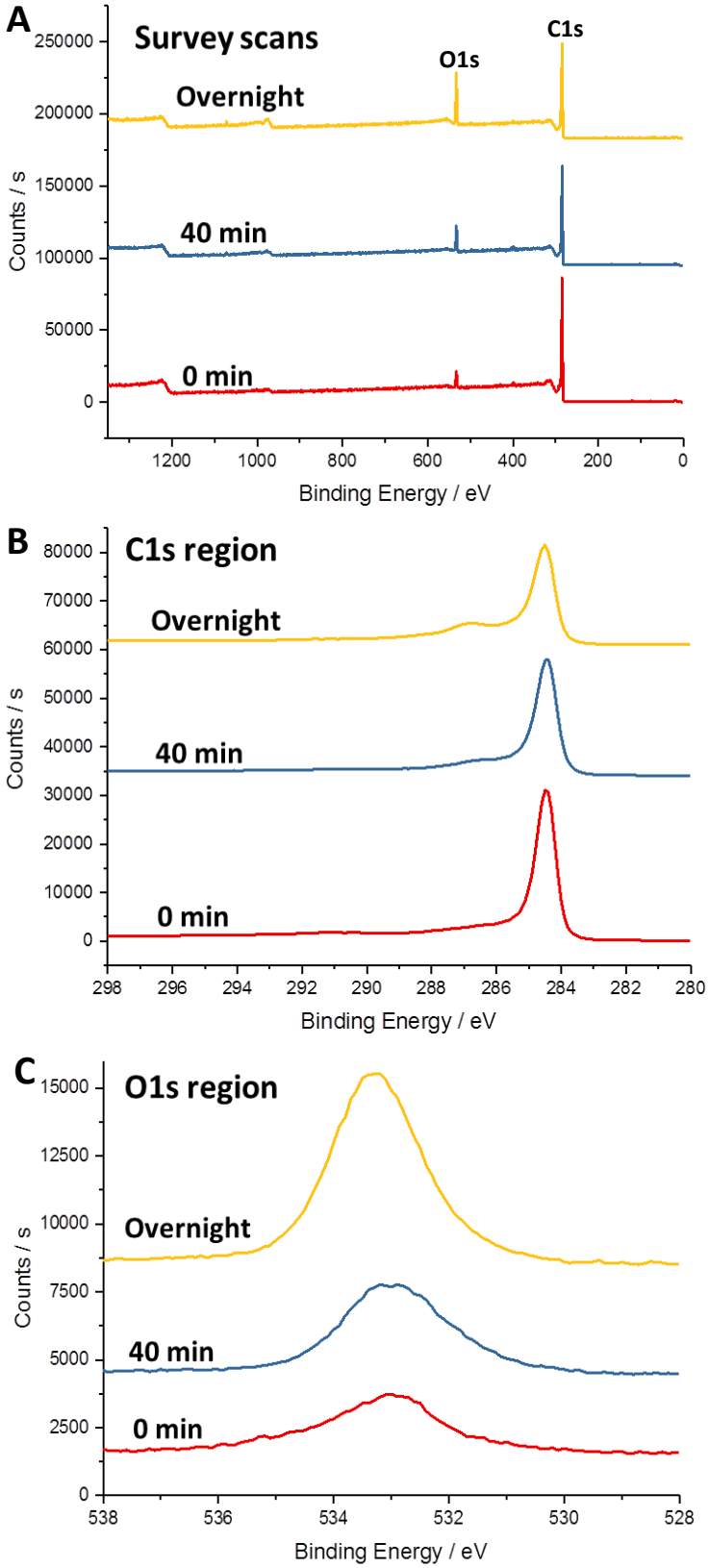

Figure C1 XPS spectra of survey scans, carbon 1s region, and oxygen 1s region of EPPG electrodes after exposed to ambient light conditions for 0 min, 40 min, and overnight.

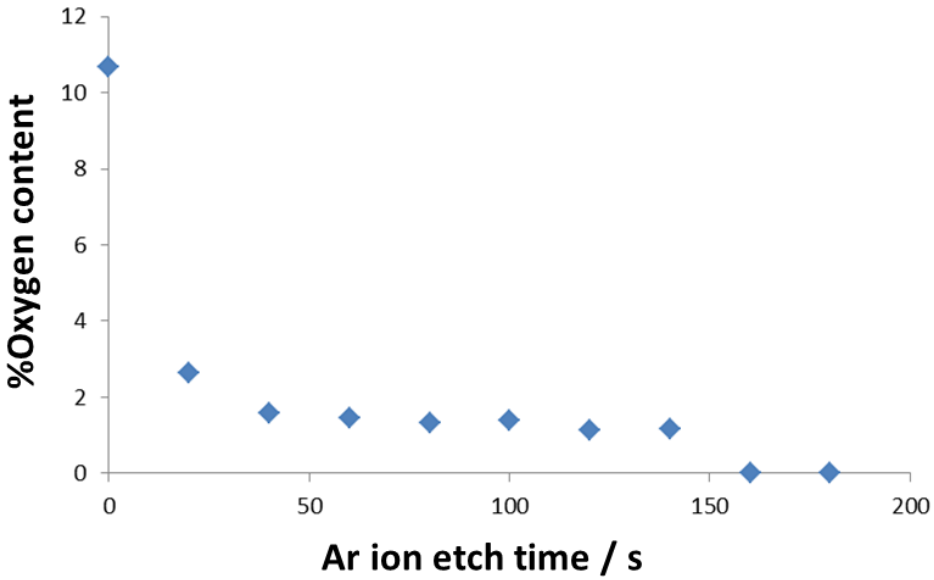

Figure C2 Percentage of oxygen content as a function of argon etching time

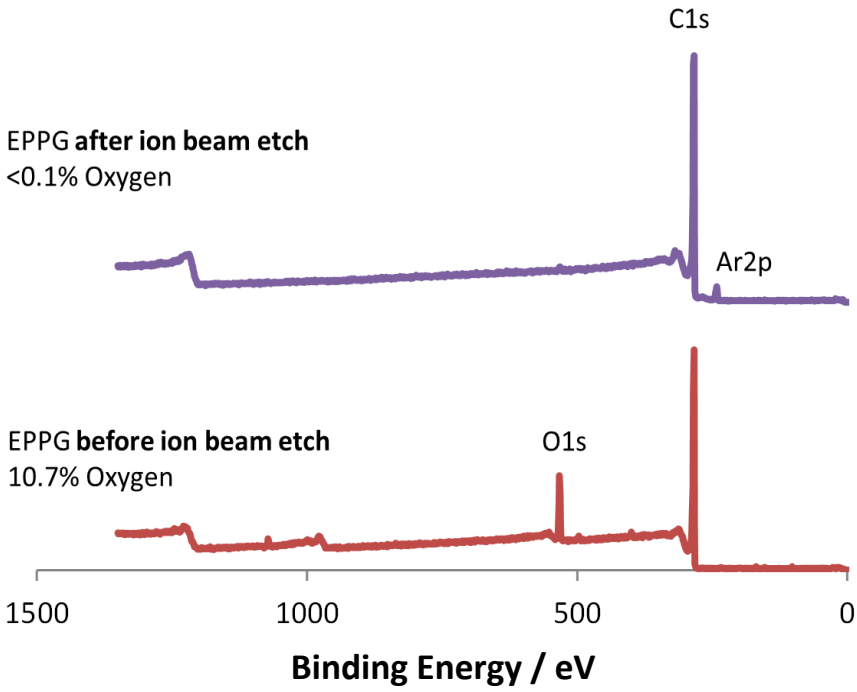

Figure C3 XPS spectra of survey scans before and after argon ion etching experiment

Although making a quantitative comparison between the XPS and electrochemical data is not easy, through comparison of the magnitude of the oxygen

O1s XPS response to that of the carbon C1s signal an estimation of the oxygen surface content as measured via XPS can be made. Based on the Ar ion etching data (Figure C2), we use a model of an oxygen rich overlayer with a pure carbon substrate. The inelastic mean free path, λ, of C1s and O1s electrons are calculated using the method of Seah *et al.* [1] to be approximately 1.9 and 1.7 nm respectively. For simplicity, a constant λ was assumed for both C1s and O1s electrons of 1.8 nm. The intensity of photoelectron emission from a depth of d is given by:

$$I(d) = I_0\, e^{\left(-\frac{d}{\lambda cos\theta}\right)}$$

where θ is the emission angle, equal to 50° in this measurement, and I_0 is the inherent photoemission intensity.[2] Using a model of an overlayer, A, and a substrate, B, it follows that the intensity of photoemission from the overlayer, I_A, as a proportion of the total photoemission, I_0, is given by:

$$\frac{I_A}{I_0} = 1 - e^{\left(-\frac{t}{\lambda cos\theta}\right)}$$

where t is the thickness of the overlayer. Assuming that the oxygen is confined within the top unit cell of the electrode, we take t to be 0.7 nm. Using the values for λ and θ stated above, we calculate that the overlayer provides 45.4% of the total photoemission signal.

Taking the density of the oxygen rich overlayer to be equal to that of the bulk graphite then the effective number of atoms sampled by XPS is estimated as follows:

Estimation of oxygen surface coverages on an EPPG electrode from XPS results

Density of graphite: 2.266×10^6 g m^{-3}

Thickness of oxygen containing overlayer: ~ 0.7 nm

Atomic mass of carbon: 12.01 g mol^{-1}

Therefore,

$$\text{Number of carbon atoms} = \frac{(2.266\ \text{g cm}^{-3})\text{x}\ (7\text{x}10^{-8}\text{cm})}{12.01\ g\ mol^{-1}}\ x\ (6.02x10^{23}\ atom\ mol^{-1})$$

$$= 7.95\text{x}10^{15}\ \text{atoms cm}^{-2}$$

The number of atoms in the overlayer is $7.95\text{x}10^{15}$ atoms cm^{-2}

From XPS analysis, the measured oxygen to carbon ratio varies between 6.8% - 16.8%. Assuming that all the oxygen exists in the 0.7 nm overlayer, which as calculated above provides 45.4% of the photoemission signal, then the oxygen concentration in this overlayer ranges from 14.9-37.0%. Consequently, the estimated surface coverage of the oxygen is found to be approximately $1.19\text{x}10^{15}$ – $2.94\text{x}10^{15}$ oxygen cm^{-2}. If in fact the oxygen rich overlayer is thicker than 0.7 nm then the concentrations calculated above will decrease, so these represent upper limits. Assuming the surface redox active species to be a quinone i.e. with two oxygen per molecule and that all surface oxygen functionality in quinoidal then the estimated surface coverage of the electroactive species is $5.95\ \text{x}10^{14}$ – $1.47\text{x}10^{15}$ oxygen cm^{-2}.

In comparison the electrochemically measured quinone surface coverage (Γ) is calculated based on Faraday's 1st law

$$Q = \Gamma nFA$$

where Q is the charge transfer during redox reaction of quinone functionality on EPPG electrode surface, n is the number of electrons transfer per molecule which is equal to 2, F is Faraday constant (96485 C mol^{-1}), and A is the total surface area of electrode (*ca.* 0.126 cm^2). Thus, the surface coverage (Γ) of quinones on an EPPG electrode surface is estimated to be in the range of $0.48\ \text{x}\ 10^{13}$ - $2.79\ \text{x}\ 10^{13}$ molecules cm^{-2}. This order of magnitude discrepancy between the two values immediately

highlights the fact that the electrochemistry is specific to the redox active functionality on the surface whereas the XPS reports on the surface coverage of all surface species. Consequently, although XPS demonstrates the presence of oxygen functionality on the carbon surface and that the functionality changes in composition and amount as a function of time and between different carbon samples, ultimately the specificity of electrochemical technique to redox active species means that correlation between the two techniques is not feasible. In conclusion, the XPS data demonstrates that the redox active species studied electrochemically only correspond to a relatively small fraction of the oxygen functionality on the carbon surface.

Bibliography

1. M. P. Seah and W. A. Dench, *Surf. Interface Anal.*, 1979, **1**, 2-11.
2. S. Tougaard, *Journal of Electron Spectroscopy and Related Phenomena*, 2010, **178-179**, 128-153.

Appendix D

Cyclic voltammogram of a surface quinone on a BPPG and a glassy carbon electrode surface

Other types of graphite electrodes including basal plane pyrolytic graphite electrode (BPPG) and glassy carbon (GC) were used to conduct the experiments under ambient light condition. The BPPG electrode and glassy carbon (GC) electrode were polished with alumina powder (Buehler) of decreasing particle size (1.0, 0.3 and 0.05 μm) to refresh surface before doing each experiment. The BPPG electrode was exposed to an ambient light for 0, 5, 10, 20, 40, 80, and 160 minutes after polishing the electrode surface. For glassy carbon electrode, the electrode was left in ambient conditions for 0 minute and long period of exposure time (overnight). Cyclic voltammetry was recorded in 0.01M HNO_3 (pH 2) supported with 0.1 M KCl.

Figure D1 illustrates voltammograms with increasing time exposed to an ambient light. The result of BPPG electrode under ambient light condition shows that analysed charge densities increase with exposure time (Inset Figure D1(A)). So, there is a trend with exposure time under an ambient light condition. However, its maximum charge densities are far lower than that of EPPG electrode under the same conditions (Chapter 6). This result is consistent with the lower number of edge plane sites on basal plane compared to edge plane carbon. For glassy carbon electrode, there is no strong signal of oxygen functionalities as shown in Figure D1(B). This is also compatible with the number of edge plane sites on glassy carbon electrode which are again far lower than an edge plane electrode.

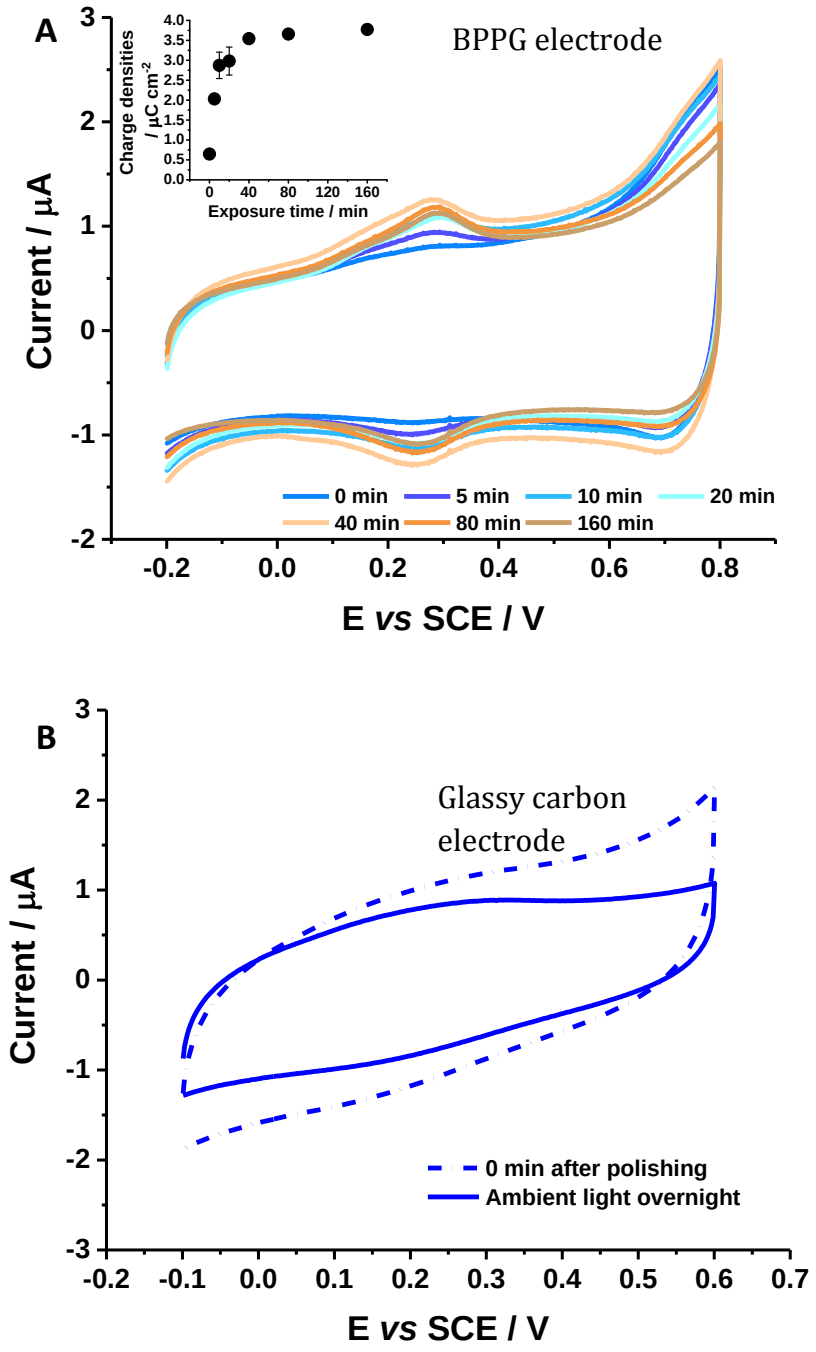

Figure D1 (A) Cyclic voltammograms of oxygen functionalities on BPPG electrode after exposure to the air for 0, 5, 10, 20, 40, 80, and 160 minutes tested in 0.01 M HNO_3+0.1 M KCl supporting electrolyte (pH 2) at a scan rate of 100 mV s^{-1}. Inset of (A) shows the plot of charge densities of the oxidative peaks as a function of exposure time. (B) Cyclic voltammograms of a glassy carbon electrode immediately measured after polishing and after exposure to ambient air overnight tested in 0.01 M HNO_3+0.1 M KCl supporting electrolyte (pH 2) at a scan rate of 100 mV s^{-1}.

Appendix E

Quinone signals on a micro-disc carbon fibre electrode

The Carbon fibre micro-wire was developed as an accurate and reliable pH sensing electrode in Chapter 7, in particular for the application of pH sensing in saliva. Nevertheless, the wider use of these electrodes is limited by their fragility and the difficulty of renewing or cleaning the electrode surface. Specifically, the Carbon fibre micro-wire used in Chapter 7 was a single Carbon fibre which was connected to a conducting wire and supported within a pipette tip as a holder. The Carbon fibre itself protruded through the tip of a holder to a length of ca. 1 mm. This led to difficulty with handling of the electrode during the electrochemical study and in storage. Accordingly, a different design was developed to overcome this problem and enhance the robustness of Carbon fibre based electrodes for pH sensing in biological fluids in general but especially in blood samples for possible in vivo study. Specifically, the Carbon fibre was insulated with electrophoretic paint and supported with an electrically insulating Kapton tape forming a Carbon fibre electrode which is more robust and easier to handle as shown in Figure E1 where the assembly is cut to expose fresh discs of carbon as needed, thus replacing the former cylindrical design by a disc.

Electrode fabrication

First, carbon micro-electrodes were fabricated by attaching a single 9 μm diameter carbon fibre (Goodfellow Cambridge Ltd.) to a conducting metal wire using silver epoxy (RS Components Ltd.) conductive adhesive. The adhesive was set by heating for 20 minutes at approximately 80°C. Second, the carbon fibre electrodes

were insulated using cathodic electrophoretic paint (Clearclad HSR, LVH Coating, UK). The carbon fibre was immersed in the paint which was placed in a conducting metal cell with a diameter of 1 cm. A voltage of 25 V was then applied between the cell and the carbon fibre for 2 minutes. The electrode was removed from the metal cell and cured at 120°C for 30 minutes. Finally, the insulated carbon fibre electrodes were sealed with the electrically insulating Kapton tape to support a single carbon fibre. The electrode tip was cut using a razor blade to expose a new active carbon fibre micro-disc electrode.

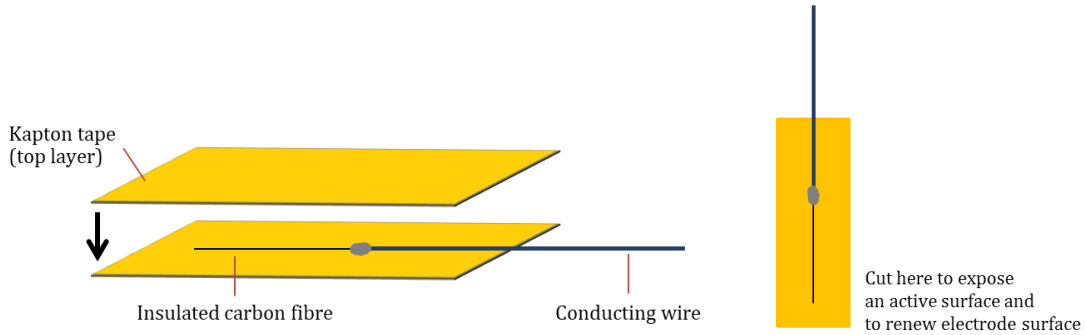

Figure E1 A schematic of insulated carbon fibre supported in Kapton tape.

Electrochemical procedure

A standard three electrode setup was used for experiments and the micro-disc carbon fibre was used as a working electrode. A platinum wire was used as a counter electrode and a saturated calomel electrode (SCE, potential E=+0.244V versus standard hydrogen electrode) was used as a reference electrode.

Results and discussion

The electrochemical response of quinones on the electrode surface was examined over the pH range from 2.0 to 7.5, as shown in Figure E2 (A). Cyclic

voltammetry was scanned in an oxidative direction from -0.1 to +0.6 V (vs SCE) and reversed to -0.1 V using scan rate of 100 mV s^{-1}. As can be seen from Figure E2 (A), quinone oxidation/reduction peaks were obtained and the voltammograms shift, as expected, to more negative potentials as the pH increases. A plot of the oxidative peak potential, reductive peak potential and midpoint potential against pH is depicted in Figure E1 (B). The gradient resulted in a 52.3±2.0, 52.3±0.2, and 52.2±3.8 mV/pH for midpoint potential, oxidation/reduction peak potentials respectively showing sub-Nernstian responses.

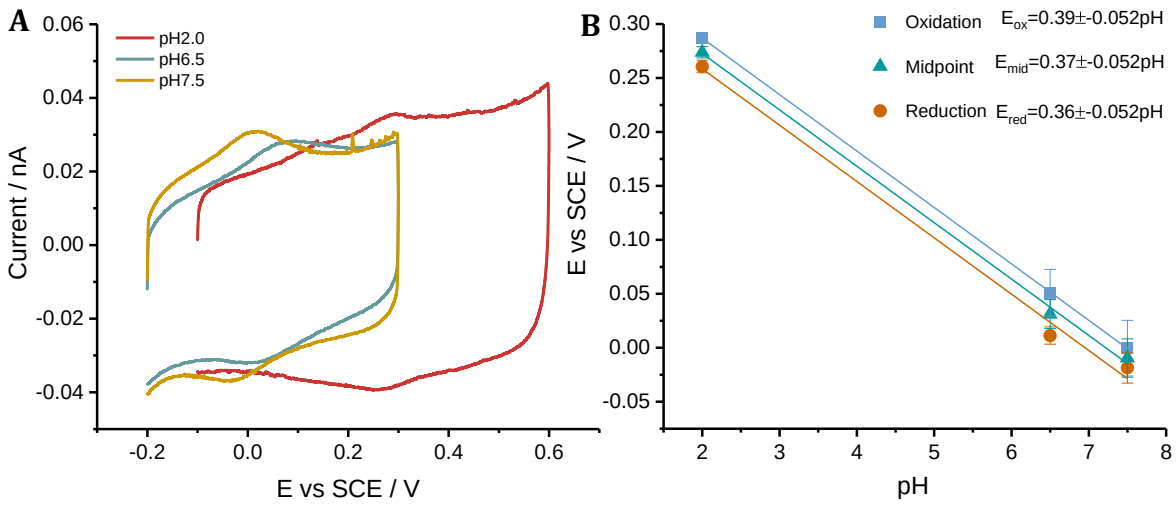

Figure E2 (A) Cyclic voltammograms of quinone oxidation/reduction peaks on carbon fibre micro-disc electrode obtained in pH buffered solution supported with 0.1M KCl including 0.01M HNO_3 (pH2.1), citrate buffer (pH6.5), and phosphate buffer (pH7.5) solutions. (B) Plots of peak potentials against pHs.

Having examined the electrochemical responses of the quinones on the Carbon fibre micro-disc, the developed electrode was evaluated further in terms of practical use. The Carbon fibre supported with flexible Kapton tape results in a more

robust electrode in terms of the use of the electrode in an electrochemical set up as compared to the use of a Carbon fibre without any support. However, there are two difficulties arising from the use of micro-disc electrodes supported by Kapton tape. First, the electrochemical signals of the quinones on the surface of micro-disc electrode are low and variable as can be seen from the voltammograms, especially at higher pH around 6.5-7.5 which is the range of pH in most biological fluids. Three different electrode surfaces were generated by cutting using a razor blade and tested in phosphate buffer solution (pH 7.5). The CVs of the quinone oxidation/reduction peaks on the Carbon fibre micro-disc electrodes are overlaid and depicted in Figure E3 showing the variations of quinone signals from each electrode. The variability of signal magnitude may cause by the variation of the quinone populations on each part of the Carbon fibre. The low magnitude of signal may lead to an error of peak position measurements resulting in a higher uncertainty of pH measurements.

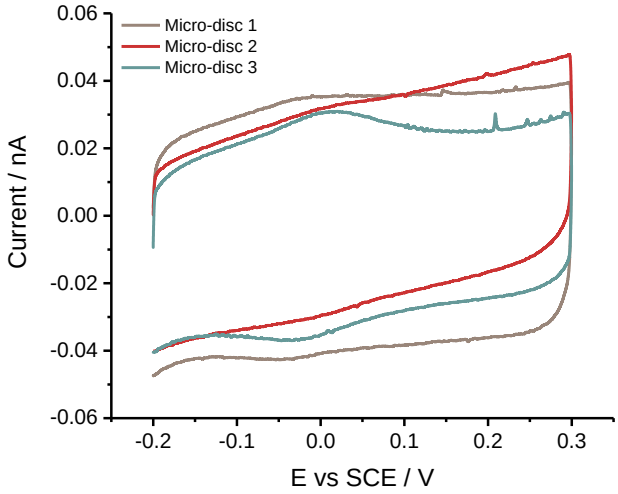

Figure E3 Three overlaid cyclic voltammograms of quinone oxidation/reduction peaks on three carbon fibre micro-disc electrodes obtained in phosphate buffer (pH7.5) solutions.

The second difficulty of using this design of electrode is a high possibility of breaking the electrode during the electrode surface renewal process. The developed electrode is easily renewable by slicing the end of electrode using a razor blade to regenerate the electroactive area. However, this method of electrode surface regeneration was found to lead to broken electrodes. Due to the fragility of the Carbon fibre itself, the cutting causes disconnection of carbon fibre from the contact wire at some point along the electrode. As the disconnection point cannot be seen by naked eye, a microscope was used to investigate. Figure E4 shows microscope images of a Kapton sealed carbon fibre micro-disc electrode in good condition (Figure E4(A)) and with a crack in the carbon fibre (Figure E4(B)). These cracks were found to lead to disconnection.

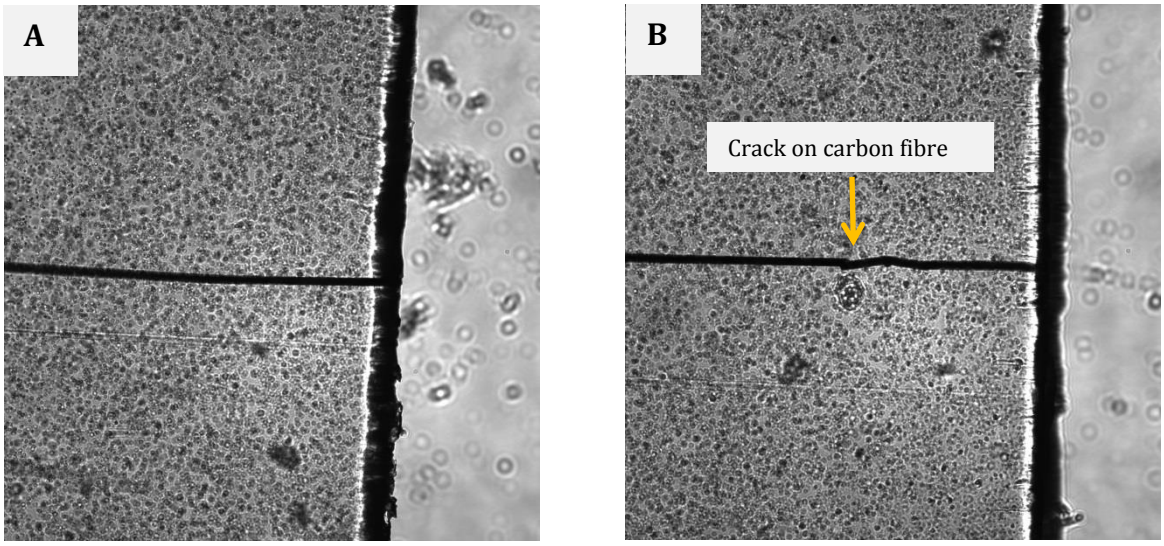

Figure E4 Microscope images for carbon fibre (diameter 9 μm) sealed in Kapton tape. (A) An image of a working carbon fibre and (B) carbon fibre with crack after surface renewal (pointed by yellow arrow).

In summary, a cylindrical carbon micro-wire electrode as employed in Chapter 7 may be used for pH measurement in blood samples. However, for in vivo study the

micro-wire electrode was considered to be too fragile. Accordingly, the carbon micro-disc electrode developed in this study showed an advantage in terms of its ease of handling. However, in terms of signal size and variation, the quinone signals on Carbon micro-disc electrode were small in comparison with a Carbon micro-wire electrode partly as a result of its smaller surface area of electrode leading to lower quinone populations. The small signal size can lead to a difficulty in using a Carbon micro-disc for pH measurement in blood due to the presence of the more complex matrix of blood as compared to saliva. Finally, the regeneration of electrode surface by slicing at the edge of electrode sometimes caused a disconnection of carbon fibre with a conducting wire resulting in breaking of the electrodes. Therefore, the alternative investigation and exploitation of a metal/metal oxide system for pH sensing was developed as described in Chapter 8.

Appendix F

Electrodeposition of iridium oxide onto iridium micro-disc electrode

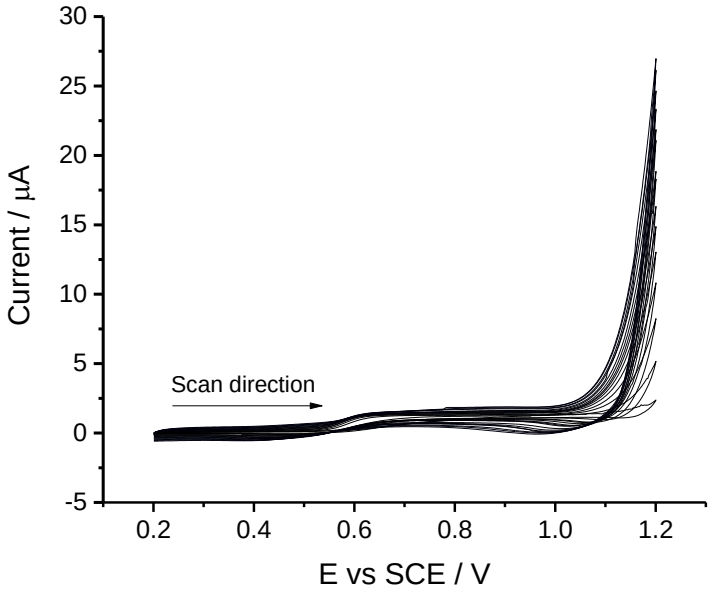

Figure F1 Cyclic voltammograms (15 cycles) at the iridium micro-disc electrode in a deposition solution containing 1.0 mM K_3IrCl_6 (pH = 11.5); scan rate 50 mV s^{-1}.

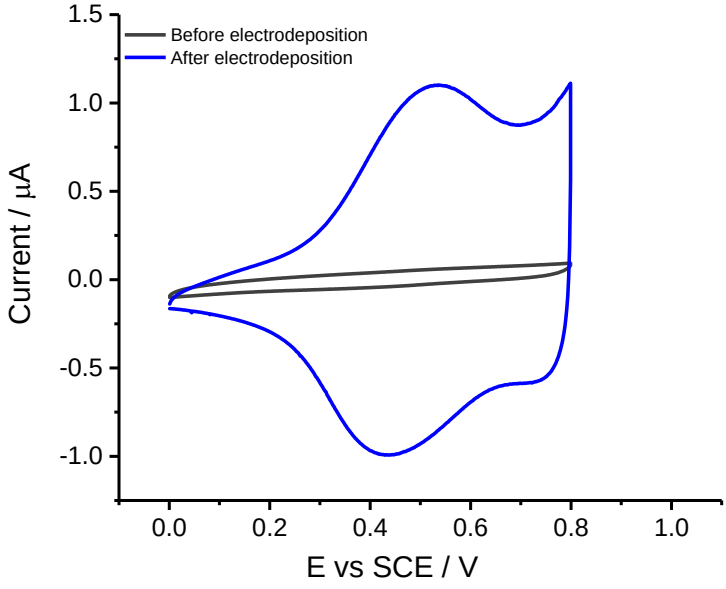

Figure F2 Cyclic voltammograms of bare and iridium oxide modified the iridium micro-disc electrode in 0.01M HNO_3 + 0.1M KCl (pH 2); scan rate 100 mV s^{-1}.

Appendix G

G1 Estimation of uncertainty of pH measurements using an iridium oxide electrode and a glass electrode as a reference pH value

G1.1 Uncertainty of pH measurements of aqueous buffer solutions using cyclic voltammetry

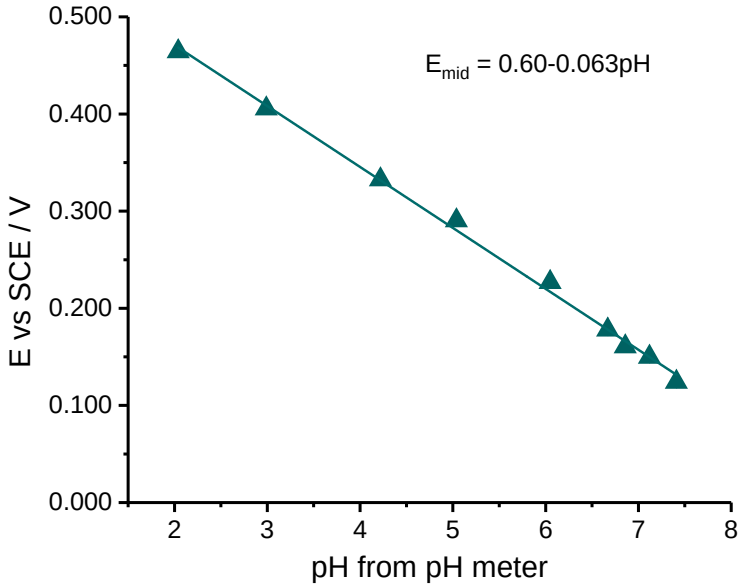

Figure G1 Plot of midpoint potentials from CV of iridium oxide on iridium micro-disc electrode in aqueous buffer solutions at variable pH against pH reading from pH meter.

pH from pH meter	Midpoint potential-measurement (E_{meas}) / V	Midpoint potential-calculation (E_{calc}) / V	$\Delta E=E_{meas}-E_{calc}$ / V	Standard deviation of ΔE / V
2.04	0.465	0.468	-0.004	0.006
2.99	0.406	0.409	-0.003	
4.22	0.333	0.332	0.001	
5.04	0.288	0.280	0.007	
6.05	0.225	0.217	0.008	
7.12	0.152	0.150	0.002	
7.41	0.127	0.132	-0.005	
6.67	0.181	0.178	0.003	
6.86	0.161	0.166	-0.005	
2.04	0.465	0.468	-0.004	
2.99	0.406	0.409	-0.003	
4.22	0.333	0.332	0.001	
5.04	0.293	0.280	0.013	
6.05	0.229	0.217	0.012	
7.12	0.148	0.150	-0.002	
7.41	0.122	0.132	-0.010	
6.67	0.175	0.178	-0.003	
6.86	0.160	0.166	-0.006	
2.04	0.465	0.468	-0.004	
2.99	0.406	0.409	-0.003	
4.22	0.333	0.332	0.001	
5.04	0.288	0.280	0.007	
6.05	0.225	0.217	0.008	
7.12	0.152	0.150	0.002	
7.41	0.127	0.132	-0.005	
6.67	0.181	0.178	0.003	
6.86	0.161	0.166	-0.005	

Conversion of standard deviation (V) to pH units

Considering slope of the linear plot of midpoint potentials of iridium oxide on iridium micro-disc electrode in aqueous buffer solutions using cyclic voltammetry at variable pH against pH reading from pH meter as shown in Figure G1,

Slope is 0.063 V per 1 pH units

Therefore, 0.006 V is $\frac{1}{0.063} \times 0.006 = 0.095$ pH units

G1.2 Uncertainty of pH measurements of sheep's blood using cyclic voltammetry

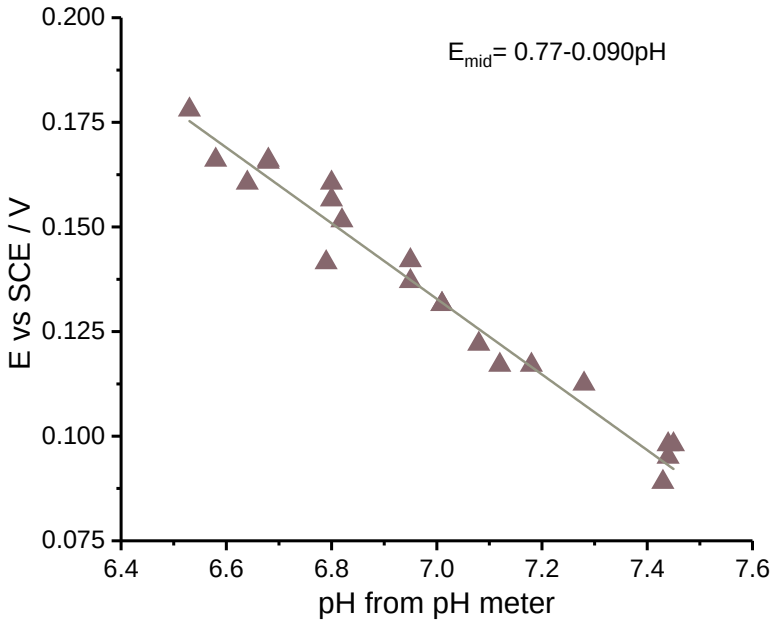

Figure G2 Plot of midpoint potentials from CV of iridium oxide on iridium micro-disc electrode in sheep's blood sample at variable pH against pH reading from pH meter.

pH from pH meter	Midpoint potential-measurement (E_{meas}) / V	Midpoint potential-calculation (E_{calc}) / V	$\Delta E=E_{meas}-E_{calc}$ / V	Standard deviation of ΔE / V
7.15	0.103	0.119	-0.017	0.006
6.79	0.142	0.152	-0.010	
6.64	0.161	0.165	-0.005	
6.58	0.166	0.171	-0.005	
7.43	0.089	0.094	-0.005	
7.01	0.132	0.132	0.000	
6.8	0.157	0.151	0.006	
6.68	0.166	0.162	0.004	
7.44	0.095	0.093	0.002	
7.28	0.113	0.108	0.005	
7.01	0.132	0.132	0.000	
6.8	0.161	0.151	0.010	
6.53	0.178	0.175	0.003	
7.45	0.098	0.092	0.006	
7.08	0.122	0.126	-0.004	
6.82	0.152	0.149	0.002	
6.68	0.166	0.162	0.004	
7.44	0.098	0.093	0.005	
7.18	0.117	0.117	0.000	
7.12	0.117	0.122	-0.005	
6.95	0.142	0.137	0.005	
6.95	0.137	0.137	0.000	

Conversion of standard deviation (V) to pH unit

Considering slope of the linear plot of midpoint potentials of iridium oxide on iridium micro-disc electrode in sheep's blood samples using cyclic voltammetry at variable pH against pH reading from pH meter as shown in Figure G2,

Slope is 0.090 V per 1 pH units

Therefore, 0.006 V is $\frac{1}{0.090} \times 0.006 = 0.067$ pH units

G1.3 Uncertainty of pH measurements of sheep's blood using square wave voltammetry

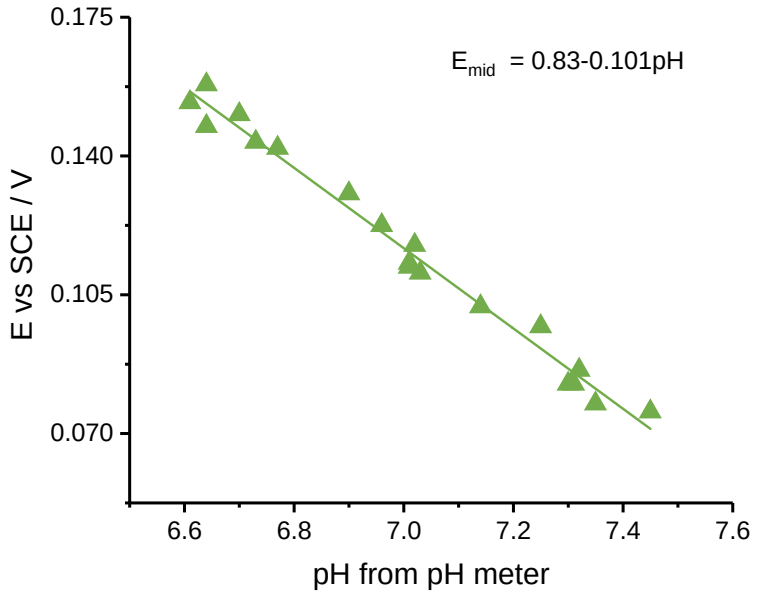

Figure G3 Plot of midpoint potentials from SWV of iridium oxide on iridium micro-disc electrode in sheep's blood sample at variable pH against pH reading from pH meter.

pH from pH meter	Midpoint potential-measurement (E_{meas}) / V	Midpoint potential-calculation (E_{calc}) / V	$\Delta E=E_{meas}-E_{calc}$ / V	Standard deviation of ΔE / V
7.32	0.086	0.084	0.002	0.0035
7.14	0.102	0.103	-0.001	
6.96	0.123	0.121	0.002	
6.77	0.142	0.140	0.002	
6.64	0.158	0.153	0.005	
7.35	0.078	0.081	-0.004	
7.01	0.112	0.116	-0.004	
7.30	0.083	0.086	-0.004	
7.03	0.111	0.114	-0.003	
6.73	0.144	0.144	-0.001	
6.61	0.154	0.156	-0.003	
7.45	0.076	0.071	0.004	
7.01	0.113	0.116	-0.003	
6.64	0.148	0.153	-0.006	
6.70	0.151	0.147	0.003	
7.31	0.083	0.085	-0.003	
7.02	0.118	0.115	0.003	
7.25	0.097	0.091	0.006	
6.90	0.131	0.127	0.004	

Conversion of standard deviation (volts) to pH unit

Considering slope of the linear plot of midpoint potentials of iridium oxide on iridium micro-disc electrode in sheep's blood samples using square wave voltammetry at variable pH against pH reading from pH meter as shown in Figure G3,

Slope is 0.101 V per 1 pH units

Therefore, 0.0035 V is $\frac{1}{0.101} \times 0.0035 = 0.034$ pH units

G2 Estimation of uncertainties of using a conventional glass electrode for pH measurements in aqueous buffer solutions and in sheep's blood samples

No. of measurements	Buffer			Sheep's blood		
1	2.03	4.95	9.08	7.50	7.27	7.18
2	2.01	4.93	9.07	7.49	7.27	7.18
3	2.01	4.93	9.05	7.53	7.27	7.13
4	2.01	4.93	9.07	7.53	7.30	7.15
5	2.00	4.93	9.07	7.54	7.31	7.13
6	2.00	4.92	9.07	7.55	7.31	7.18
7	2.00	4.92	9.06	7.53	7.32	7.16
8	2.00	4.92	9.07	7.52	7.32	7.17
9	2.00	4.92	9.07	7.52	7.31	7.18
10	2.00	4.92	9.07	7.53	7.31	7.19
Mean	2.01	4.93	9.07	7.52	7.30	7.17
Standard deviation	0.01	0.01	0.01	0.02	0.02	0.02

G3 Study of variability of apparent standard electrode potential of electrodes studied in buffer solutions and in sheep's blood

A) Aqueous buffer solutions

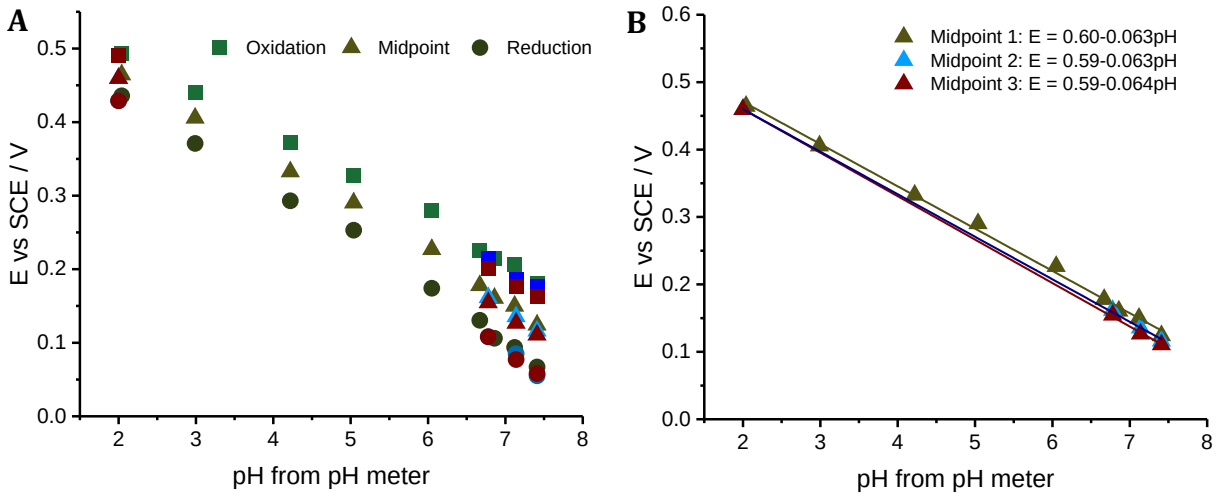

Figure G4 Reproducibility of cyclic voltammetry measurements of our IrOx pH sensor in buffer solutions (A) plots of all values including oxidation, reduction, and midpoint potentials and (B) enlarged plots of midpoint potential.

B) Sheep's blood

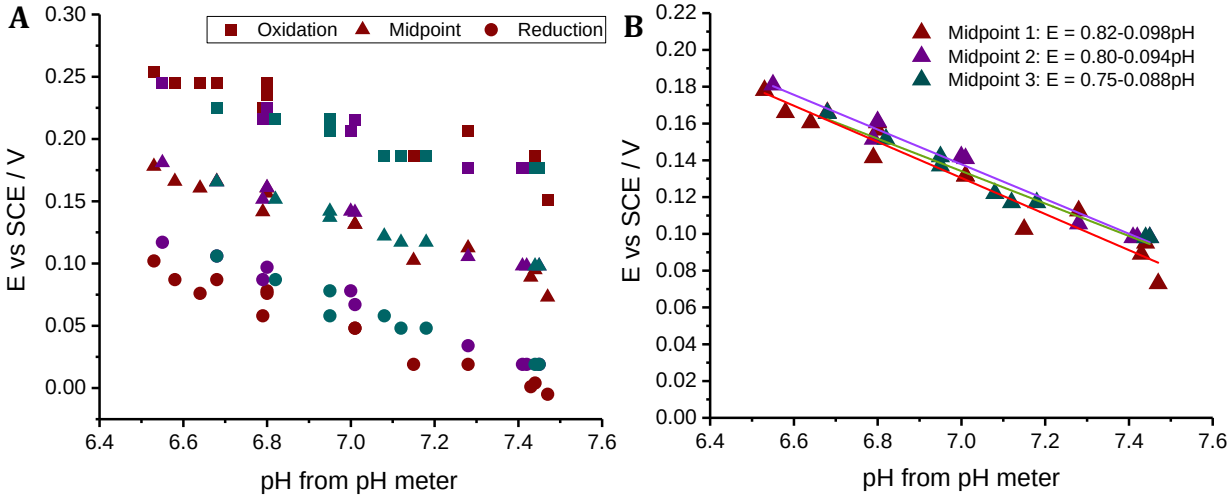

Figure G5 Reproducibility of cyclic voltammetry measurements of our IrOx pH sensor in sheep's blood samples (A) plots of all values including oxidation, reduction, and midpoint potentials and (B) enlarged plots of midpoint potential.

Appendix H

Optimisation of square wave voltammetric parameters in sheep's blood sample

To obtain best quality square wave voltammetry for pH measurements in sheep's blood, the optimisation of SWV in sheep's blood sample including frequency, step potential, and amplitude was investigated. The results of the optimisation studies are shown in Figures H1-H4 where the optimal parameters were chosen using the value of current to background ratio. The optimised SWV parameters (frequency 15 Hz, amplitude 10 mV, and step potential 1 mV) were used to measure the pH of sheep's blood.

H1 Optimisation of frequency

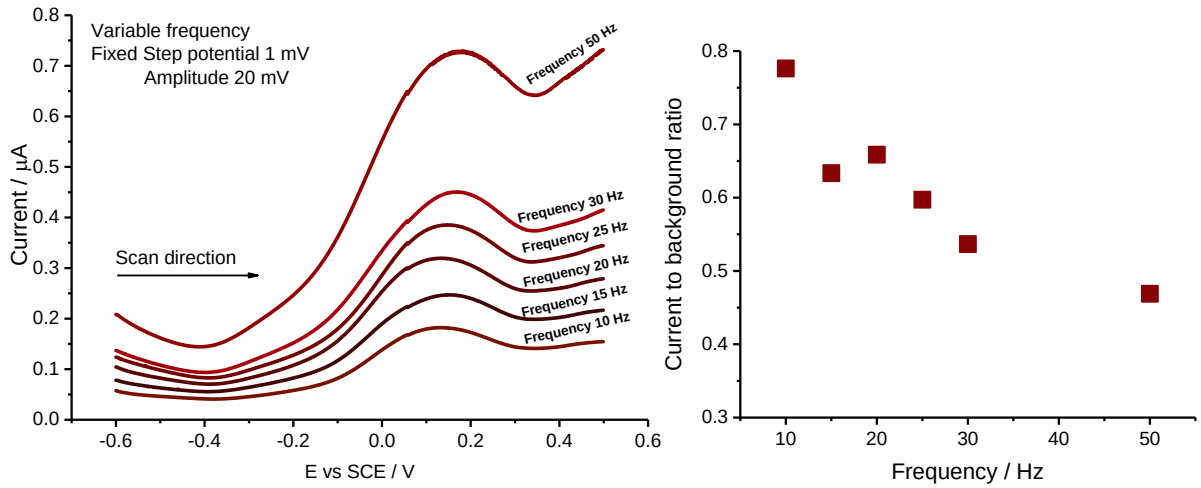

Figure H1 Effect of the frequency parameter on the SWV signal tested in sheep's blood samples, performed with step potential and amplitude fixed at 1 mV and 20 mV respectively.

H2 Optimisation of amplitude

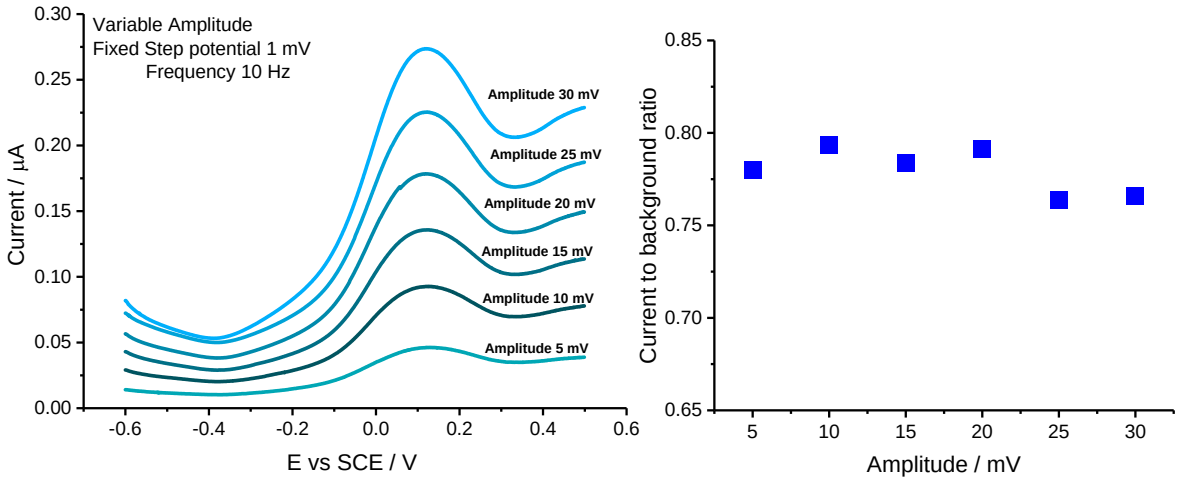

Figure H2 Effect of the amplitude parameter on the SWV signal tested in sheep's blood samples, performed with step potential and frequency fixed at 1 mV and 10 Hz respectively.

H3 Optimisation of step potential

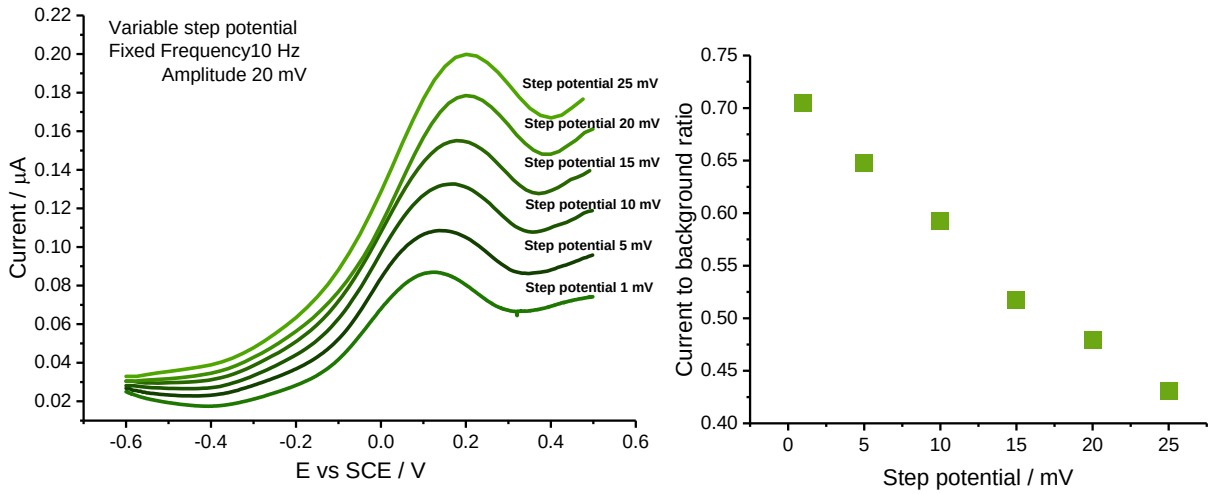

Figure H3 Effect of the step potential parameter on the SWV signal tested in sheep's blood samples, performed with frequency and amplitude fixed at 10 Hz and 20 mV respectively.

H4 Optimisation of frequency

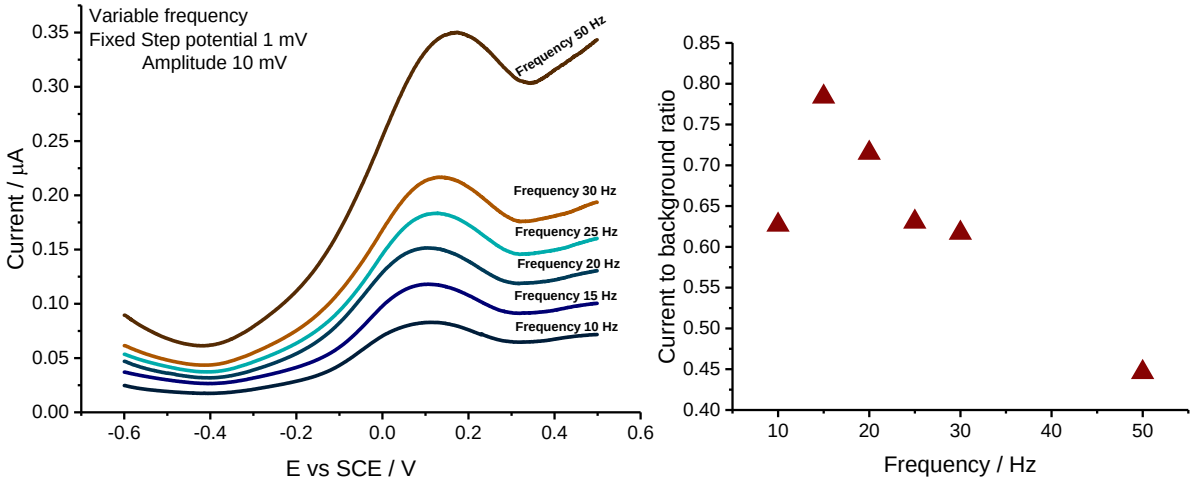

Figure H4 Effect of the frequency parameter on the SWV signal tested in sheep's blood samples, performed with step potential and amplitude fixed at 1 mV and 10 mV respectively.